2008

Repair of corroded steel beam using CFRP

Meiling Chen
University of Windsor

Repair of corroded steel beam using CFRP

By

MEILING CHEN

A Thesis
Submitted to the Faculty of Graduate Studies
through
the Department of Civil and Environmental Engineering
in Partial Fulfillment of the Requirements for
the Degree of Master of Applied Science at the
University of Windsor

Windsor, Ontario, Canada

2008

Your file Votre référence
ISBN: 978-0-494-42288-5
Our file Notre référence
ISBN: 978-0-494-42288-5

ABSTRACT

Many steel structures were built during World War I and II. More than twenty percent of steel bridges in the USA are structurally deficient. The cost for rehabilitation in most cases is far less than the cost of replacement. Moreover, the rehabilitation generally takes less time than replacement. Due to the limited methods available to mitigate this problem, new materials were explored in recent years to adopt cost-effective technique to address this issue.

This thesis focuses on the use of Carbon Fiber Reinforced Polymer (CFRP) sheets as a competitive technique to restore the capacity of surface corroded steel beam. Rehabilitation was achieved by bonding the CFRP fabrics on to the corroded area of the bottom flange of steel beams. A series of tests and finite element analyses were also conducted.

Results showed that the ultimate load capacity of the rehabilitated structures can be restored using this method; however, ductility reduces.

DEDICATION

To the one who showed me where to seek

Pushed and persevered, week after week

To those who helped me reach my best

To those who aided in my quest

Many thanks to you

I bid you adieu

ACKNOWLEDGEMENTS

This project was carried out under the supervision and guidance of Dr. S. Das to whom I am profoundly grateful for his kindness, endless constructive commentary, and valuable suggestions, continuous support, and encouragement throughout my studies. Dr. Das devoted his time and sincere efforts to provide all necessary research facilities for this work.

I would like to express my appreciation to the committee members: Dr. N. Zamani and Dr. M. K. S. Madugula for their constructive suggestions to improve this thesis.

The acknowledgment also goes to all technical staff: Lucian Pop, Patrick Seguin, and Matthew St. Louis for their assistance in laboratory work.

A special thanks goes to the BASF, who donated part of the total CFRP materials needed in this project.

At the last, I would like to thank my family, especially Patrick, for their constant support and encouragement. Special thanks are also given to all my friends, especially Xin Wu, Roy Chen, and Chochos.

TABLE OF CONTENTS

LIST OF TABLES

LIST OF FIGURES

1 INTRODUCTION

1.1 General

Advanced composites have been used since World War II. The carbon fiber reinforced polymer (CFRP) was first used in the military during 1950s (Hollaway, 1993). Currently due to its incomparable strength-to-weight ratio, CFRP is used extensively for products needs to achieve lightweight and durable products, such as applications in aerospace, automotive fields. In the recent past, the CFRP has been introduced to civil engineering infrastructure. Because of the high strength-to-weight and stiffness-to-weight ratio, CFRP is widely used in corrosion and fatigue repair, strengthening, etc.

1.2 Statement of problem

The Federal Highway Administration (FHWA) of the United States of America (USA) has developed a program to rate bridges on the nation's highways through biannual inspection. At the end of 2005, 21.5% of the steel bridges are classified as structurally deficient (US DOT, 2005). Similar bridge inventory in Canada is not available. However, the Province of British Columbia alone owns over 700 structures that are classified as steel bridges (Tam and Stiemer, 1996). The significant temperature fluctuations and extensive use of deicing salts cause serious corrosion in a large number of existing bridges.

Corrosion repair with steel plate is the most common and conventional method. Although this method is effective, other serious problems could be introduced to the steel structure, such as fatigue problem, future galvanic corrosion, and additional dead load to the structure. Recently, Carbon Fiber Reinforced Polymer (CFRP) and other fiber polymers have been introduced in corrosion repair. This repairing method does not affect structure's fatigue life, and does not increase the dead weight as much as the conventional repair method does.

Significant studies were conducted on use of CFRP composite for rehabilitation and strengthening of existing concrete structures. However, only a few studies were undertaken on repair of corroded steel members and steel structures using CFRP composites.

1.3 Objectives and scope

The present research was initiated to examine the rehabilitation technique of surface corroded steel beams using carbon fibre reinforced polymer (CFRP) sheets. Consequently, the following are the primary objectives of this research project:

(a) To study if the load carrying capacity of beam with corrosion on its bottom flange can be restored to the level of virgin (undamaged) beam using CFRP fabric (sheet).

(b) To determine the changes in the ductility due to the repair and rehabilitation.

(c) To model the structural behaviour of rehabilitated corroded beam using finite element (FE) method.

(d) To determine the influence of depth and length of the corrosion on the required thickness of CFRP using the FE model developed.

The scope of the current project was limited to the W200x21 steel beam. A total of nine full-scale tests on W200x21 steel beams were carried out.

The numerical simulations of the full-scale corroded steel beam rehabilitated with CFRP sheets were performed using ABAQUS, a commercially available finite element analysis software package. The primary objective of the numerical tool was to be able to predict behaviour similar to that observed in the full-scale beam tests. The other objective was to expand the database in order to obtain information when repairing the corroded steel beams with different lengths and depths of corrosion.

1.4 Organization of thesis

The thesis is broken into five major chapters and two other small chapters: the first chapter (Introduction, Chapter 1) and the very last chapter (Summary and Conclusions and Recommendation, Chapter 7). Chapter 2 summarizes the findings obtained from the literature on the issues, such as previous studies on corrosion repair with CFRP, debonding issue, and galvanic corrosion of carbon and steel. Chapters 3 and 4 discuss the full-scale test program and the results obtained from the tests. In the following two

chapters, that is, in Chapters 5 and 6, numerical modeling of the full-scale tests and the comparison of behavior obtained from experiments and numerical simulations are discussed. A parametric study was also included in Chapter 6.

2 LITERATURE REVIEW

2.1 General

The Federal Highway Administration (FHWA) of the United States of America (USA) has developed a program to rate bridges on the nation's highways through biannual inspection (US DOT, 2004a). At the end of 2005, a total of 595,605 bridges were in use in the United States. There are 190,850 bridges, roughly one third, utilizing steel as the main carrying structural element. Of the steel bridges, 21.5% are classified as structurally deficient (US DOT, 2005). It should be noted that these numbers do not include bridges designed specifically for railroads and pedestrians (U.S. DOT, 2004)). The primary reasons for deterioration of the bridges include corrosion, fatigue, increase in dead load, and permitted live load (Tavakkolizadeh and Saadatmanesh, 2001 a).

Similar bridge inventory in Canada was not able to be found. However, the Province of British Columbia alone owns over 700 structures that are classified as steel bridges (Tam and Stiemer, 1996). The significant temperature fluctuations and extensive use of deicing salts cause serious corrosion in a large number of existing bridges (See Figure 2.1 for detail).

Corrosion is one of the major factors affecting the long-term serviceability of steel bridges. There are five main forms of corrosion: general corrosion, pitting corrosion, crevice corrosion, stress corrosion, and galvanic corrosion. General corrosion is a general loss of surface material and is most frequently seen. Pitting corrosion mostly occurs in high stress areas. This type of corrosion could be dangerous, because the corrosion extends into the metal while showing little sign of corrosion on the surface. Crevice corrosion is caused by low concentrations of dissolved oxygen, such as underneath peeling paint. Stress corrosion occurs when metal is under tensile stress and in a corrosive environment. Galvanic corrosion is degradation of a metal by an electrochemical reaction with its environment (Kayser and Nowak, 1989). Corrosion reduces the cross-sectional area of bridge members and weakens the structural elements. The corroded areas of structural elements need to be repaired such that they are able to provide full services that they were designed for.

2.2 Corrosion Repair

There are many different methods available for repairing of corroded members. Corrosion repair with steel plate is the most common used conventional method. Recently, Carbon Fiber Reinforced Polymer (CFRP) and other fiber polymers have been introduced in corrosion repair. This section presents a literature review of the subject and highlights the main differences between corrosion repair with steel plate and with CFRP.

2.2.1 Corrosion Repair with Steel

Corrosion repair with steel is involves by welding or bolting a piece of steel plate or flat onto the corroded steel element after cleaning out the corrosive products. Although this method is effective, due to lack of quality control of welds, rivets and bores and the introduction of large initial discontinuities, fatigue problems become the major issue for these structures. In cold regions, low temperatures decreases the toughness of the steel, which can lead to brittle failures (Tavakkolizadeh and Saadatmanesh, 2001a). Another concern is welding and bolting as it couples two piece of metals together, and forming a concentration cell leading to future galvanic corrosion. Moreover, this method often results in stress concentration and thermal locked-in residual and these stresses further weaken the system (Matta et al., 2005).

2.2.2 Corrosion Repair with CFRP

Significant studies were conducted on use of CFRP composites for rehabilitation of concrete structures. The studies were directed to strengthening of structures in shear (Harajli and Soudki, 2003), in flexural (Lamanna et al., 2004), and in bond behavior (Soudki and Sherwood, 2003). However, only a few studies were undertaken on repair of corroded steel structure using CFRP composite.

Corrosion repair with CFRP composite involves epoxy bonding of the CFRP composite to steel after cleaning the corroded steel. There are two forms of CFRP composite. One is CFRP dry fabric, also known as CFRP wrap or CFRP fabric, and the other one is CFRP laminate, also as known as CFRP plate or CFRP strip. CFRP dry fabric is flexible, and can be wrapped around structural members. Polymer (adhesive) is required to apply the CFRP dry fabric on the job site to produce the CFRP composite and bond

the CFRP dry fabric to the structural. CFRP laminate is pre-manufactured CFRP composite; there is no air content in the polymer resin, thus ensuring the highest quality. When the cross-section is same, CFRP laminate generally contains more CFRP fabric than CFRP composite made out with CFRP dry fabric. Unlike repairing concrete using CFRP, CFRP laminate is commonly used to repair steel structure, because steel has a higher tensile elastic modulus than concrete. CFRP dry fabric can also be used for repair of steel structure, but many layers are required.

Since no welding or bolting is required when repairing with CFRP laminate, steel structures repaired with CFRP is expected not to affect structure's fatigue life (Tavakkolizadeh and Saadatmanesh, 2001a). Due to the lightweight of CFRP, it creates savings on labor, machine and application time. However, the cost of CFRP materials is much higher than steel plates; therefore, the cost of CFRP materials is offset by these savings. Repair with CFRP laminate may be more expensive than steel plate. However, the process as a whole is still economically comparable as to the conventional method of repairing with steel. Since the weight of CFRP is much lighter, using CFRP materials to repair does not increase dead weight as much as steel plate does.

2.2.3 Previous studies on corrosion repair with CFRP

A series of tests on corrosion repair using CFRP laminates on four full-scale corroded girders was conducted by Gillespie et al. (1996a, 1996 b, and 1997). Gillespie et al. (1996a, 1996 b, and 1997) conducted large-scale tests on two 6.4 m long corroded steel girders, with 40% loss in the tension flange and 29% stiffness loss. The girders were repaired by bonding CFRP laminates to the two faces of the corroded flange of the girder (Figure 2.2). The study indicated that the flexural strength and stiffness increases were significant (100% and 25%, respectively). The repaired girder achieved the desired load level without any failure of the adhesive. The load deformation curve (Figure 2.3) also shows that the girder exhibited good ductile behavior with large plastic deformations.

In a study conducted by Tavakkolizadeh and Saadatmanesh (2001b), the effectiveness of CFRP for repairing damaged steel-concrete composite beams was investigated. 21.4 mm, 42.7 mm or 85.5 mm depth cuts were made in the beam by a 1.27 mm blade at the mid-span on both sides of the bottom flange to simulate 25, 50, and 100 percent area

loss of the flange. One, three, and five layers of CFRP fabric sheet(s) covered 3.95 m of the bottom flange, while the span of the steel beam was 4.78 m. The CFRP sheet was 75 mm wide, and placed side by side on the steel girder. Figure 2.4 shows the test setup, Figure 2.5(b) and (c) shows the cross section view and corrosion detail. Figure 26, 27 and 28 shows the load deformation curves for the 25% loss and one-layer, 50% loss and three-layer, and 100% loss and five-layer repairing system respectively. The ultimate flexural load capacity of the girders increased by 20, 80, and 10 percent for damaged beams of 25, 50, and 100 percent with one, three, and five layers of CFRP layers respectively. The technique restored the elastic stiffness of the girder to 91, 102, and 86 percent of the virgin girder for damaged beams of 25, 50, and 100 percent with one, three, and five layers of CFRP layers respectively. The post-elastic stiffness of the girder also increased 21, 19 and 32 times as compared with the virgin girder.

Liu et al. (2001) notched a 100 mm (4 in) section from one side of the tension flange of a Metric W310x21 (Imperial W12x14) girder to simulate the loss of steel area in the flange due to corrosion. The girder was repaired with a 100 mm (3.94 inch) wide by 1.4 mm (0.055 inch) CFRP laminate covering the full length and quarter length of the beam. The girder was then tested with a point load applied at the mid-span (three point bending) until failure occurred (Figure 2.9). Figure 2.10 shows the load vs. deformation curves. The unit1, unit2, unit3, and unit 4 represent the virgin beam, the corroded beam, retrofit with full length of CFRP, and retrofit with quarter length of CFRP, respectively. The experimental results obtained from this study showed an increase in bending stiffness and plastic load carrying capacity of corroded steel members can be achieved from the application of CFRP laminates to the tension flange of corroded steel members. The failure mode was peeling off the CFRP laminates. The peeling occurred at the termination point along the length of CFRP laminates. The ductility of the retrofitted system is less than the virgin beam. The mid span deflection is about 1/120, 1/240 and 1/360 of the clear span for virgin beam, repaired with full length of CFRP, and repaired with quarter length CFRP respectively.

Miller et al. (2001) used CFRP laminate to repair a corroded bridge girder. The girder of the bridge experienced bending stiffness loss in the range of 13% to 32%. The bridge corroded fairly uniform along the length of each girder with the majority of section loss occurring in the tension flange and web. Repair was done by bonding a

single layer of 5.3 mm thick CFRP laminate covering the whole length of the inner and outer faces of the tension flange (Figure 2.11). The elastic stiffness of the four repaired girders increased from 10% to 37%. The average ultimate bending capacity increased by 21%. A field repair was also conducted by them to check the applicability of the repair method in the field. Six 5.3 mm thick CFRP plates were bonded side by side to cover the entire inner flange face. To evaluate the effectiveness of the strengthening scheme, diagnostic load tests were performed before and after the application of the CFRP plates. The test measured strain at the center of the inner face of the tension flange of the girder as a three-axle dump truck was driven in the right traffic lane (above the girder) with the driver's side wheels on the marked lane line. Figure 2.12 shows the test result. Comparison of the strain for the pre- and post-load tests revealed a reduction of 11.6% in strain; it is an increase of 11.6% in flexural stiffness.

A total of 10 scaled-model steel-concrete composite beams (steel beam-concrete slab system) were tested by Al-Saidy et al. (2004). Corrosion was simulated by removing 50% and 75% of their bottom flange and then repaired by adding CFRP plate to restore their original strength. Two types of repairing methods were used. The first repairing method involved bonding of CFRP plate to the bottom of the web (Figure 2.13a). This method is suitable for the flange that is all corroded. In the second repair method, CFRP laminate was bonded to the bottom flange (Figure 2.13b). All beams were tested in four-point bending static loading, see Figure 2.14 for test setup. The load deformation curves for all the specimens are in Figure 2.15, 2.16, and 2.17. The following notation was adopted to describe the specimen in the load deformation curves. Undamaged beams are designated with "U", while the designation for damaged beams starts with the letter "D". In the damage control beam "D" was used alone to indicated that no repair was installed. In repaired beams, the letter "D" is followed by two numbers that indicated the percentage of damage to the bottom flange. For example, "50" means that 50% of the original bottom flange area was removed ("damaged"). This number is followed by a letter-number combination such as "R1" to reflect the repair scheme used. This combination is followed by a letter and two numbers, such as "E29" to reflect the modulus of the elasticity in ksi of the CFRP plate being used. The result indicate that the strength of damaged beams can be fully restored to its original, undamaged state with the use of CFRP plates, however, only about 50% of the the

elastic flexural stiffness can only be restored. In addition, ductility is slightly reduced with the addition of CFRP plates.

2.3 Debonding Issue

After steel reaches its yielding point, the steel can no longer carry any additional load and undergoes plastic deformation. However, the behavior of CFRP material is linearly elastic to failure. Therefore, the steel beam strengthens with the use of CFRP, after the steel has yielded, the additional load will transfer through the bond to the CFRP until failure occurs either due to debonding of CFRP or due to the rupture of the CFRP ruptures. Several studies using experiments and finite element analysis showed that the bond is one the weakest link for this type system. (Gillespie et. al. 1996 a, b; Edberg et al. 1996; Sen et. al. 1995 and 2001).

The most commonly used CFRP in the 90s was less than 60% as stiff as steel (Sen et. al., 1995) (Figure 2.18). This means, before the steel yields, CFRP will deform more than steel under the same load. The likelihood of a cohesive failure in the adhesive is where there is shear and peeling stress concentrations, which is most likely near the two ends of the CFRP laminate. Considering surface preparation alone is not expected to solve this problem. Sen et al. (2001) used additional bolts to augment the load transfer capacity of the epoxy adhesive in their experiments. Use of small and large quantities of bolts was also suggested to minimize the magnitude of localized stress concentrations and to reduce the tendency for transverse CFRP laminate fractures. It was also suggested that CFRP laminates with stiffness close to that of steel be used to minimize debonding problem. The debonding issue for steel repairing will not take places as long as the steel behavior elastically. (Sen et al., 2001). However, after the steel has yielded, the debonding issue is raised again as the steel is expected to deform rapidly compared to the CFRP.

Transfer of load from beam to CFRP occurs through shear mechanics of the epoxy. The shear forces in the epoxy are large relative to the bending forces and large curvatures are generally present. However, for large girders, the span length causes shear forces to be small relative to bending forces and large curvatures at the midpoint. To prevent this failure mode in large girders, tape the composite over a sufficient length (Gillespie et al. 1996 a).

Peel stress occurs when a CFRP composite is being lifted or peeled from the steel and takes places at the edges of the CFRP composite. The CFRP laminate should be beveled to a 45 degree angle at all terminations to reduce the peel stresses. This is a typical procedure for composite joints and has proven to effectively limit peel stresses (Vinson and Sierakowski, 1987). Two other methods to reduce the peel stress problem were also suggested. Liu et al. (2001) suggested application of Glass Fiber Re-enforced Polymer (GFRP) sheets to the longitudinal laminates. The GFRP sheets need to be wrapped around the tension flange and part of the web. Sen et al., (1995) used three piece steel clamps to hold the bottom flange and CFRP laminates.

The possion ratio of CFRP is in the range of 0.2 to 0.4. The possion ratio of steel is approximately 0.3. The different in poisson ratio can cause edge failures. This problem can be easily solved by using CFRP laminates with Poisson ratios in the primary to transverse direction, similar to that of steel. (Gillespie, 1996 a).

2.4 Galvanic corrosion of carbon and steel

Galvanic corrosion occurs when two dissimilar metals are electrochemically coupled, welded, or bolted. It is assumed that the galvanic corrosion occurs if there is direct contact between a CFRP material and steel (Tavakkolizadeh, and Saadatmanesh, 2001 a). Several studies were performed to understand dependence of corrosion rates on various factors. It was found that the galvanic corrosion was directly related to the thickness of the epoxy coating (Tavakkolizadeh, and Saadatmanesh, 2001 a). Corrosion testing in both seawater and a deicing salt solution was conducted and the following was found: (i) A 0.1mm thin film of epoxy was used, the corrosion rate would decrease by seven and five percent. (ii) Using 0.25mm of epoxy, the corrosion rate decreased by twenty-one and twenty-three percent respectively. (iii) Sizing agents also decrease the galvanic corrosion rate of CFRP's. It was proven that acetone was the most effective solvent for removing the sizing agent, and lowered the corrosion rate by fifty percent. (iv) By using a nonconductive layer of fabric between CFRP's and steel, such as E-Glass, can electrically insulate the two materials from each other and prevent galvanic corrosion (Tavakkolizadeh, and Saadatmanesh, 2001 a, b; Liu et al. 2001; Gillespie et al. 1996). Thus, direct contact between CFRP and steel needs to be avoided. Since fibers on both strips are covered by an epoxy resin matrix, during manufacturing

or application process, the direct contact between CFRP fabric and steel surface is expected not to be present (Nozaka et al. 2005). As a result, the galvanic corrosion is minor, and can be ignored.

2.5 Composite materials

2.5.1 General

Composite materials are engineered materials made from two or more constituents with significantly different physical or chemical properties, which remain separate and distinct within the finished structure. A composite is a combination of a matrix (such as polyester, vinyl ester, nylon, epoxy, and phenolic) and reinforcement (such as glass, carbon, or other reinforcing material). The matrix material surrounds the reinforcement, to maintain the reinforcing material in its proper positions. The matrix material also distributes the load evenly over the reinforcing agent, in order to achieve a higher ultimate load capacity than either the matrix or reinforcing material alone. Composite materials may also contain filers, additives, and core materials to adjust the final product. (Wikimedia Foundation Inc., 2007c)

Composite materials have been widely used in every day life for centuries. For example, concrete can be a composite material, using steel and aggregate to reinforce the cement. Other examples include plasterboard, plywood, and white cast iron. Although most of the composite materials are not formed naturally, some do exist such as wood, mother of pearl, and bone.

2.5.2 Fiber Reinforced Polymer (FRP)

Fiber reinforced polymer (FRP) uses several polymers for the matrix, and different kinds of fibers to reinforce. The FRP is typically referred to by the name of its reinforcing fiber (such as CFRP stands for Carbon Fiber Reinforced Polymer). The polymer of choice is usually epoxy, but other plastics, such as polyester or vinyl ester, are also sometimes used. Due to the wide variety of matrix and reinforcement materials available, composite material can be designed to provide a wide range of mechanical properties including tensile, flexural, impact and compressive strengths in order to satisfy the special needs for different projects. (Wikimedia Foundation Inc., 2007b)

2.5.3 Advantages of FRP

Other than the well-known and incomparable strength-to-weight ratio, FRP has shown incredible resistance to environmental factors, such as: (a) Freeze and thaw; (b) Ultra-Violet protection; (c) Chemical and temperature changes; and (d) Fire resistance. FRP materials have low water absorption ability and therefore, they are able to resist the damaging effects of freezing water expansion. FRPs can be fabricated with a surface layer containing a pigmented gel coating or have an UV inhibitor included as an additive to the composite matrix to resist weathering and UV light. FRP can be specially formulated to provide long-term resistance to nearly every chemical and temperature environment. As a result, FRP can be fabricated such that it is able to withstand the effects of de-icing salt and/or saltwater spray from the ocean. FRP material can be built with special fire resistant resins to make the FRP composite fire resistant.

2.5.4 Carbon Fiber

Carbon fiber, as shown in Figure 2.19, is made out of long, thin fibers of carbon and transferred into graphite. A common method of making carbon fiber is the oxidation and thermal pyrolysis of polyacrylonitrile (PAN). PAN is the raw material commonly used to make carbon fiber, which usually contains 93-95% of Carbon. PAN has long chain molecules, and when heated in the correctly, molecules bond side by side, forming a single round fiber. Pitch or Rayon can also be used to manufacture lower quality carbon fiber. The carbon fiber can be further heated to achieve higher mechanical property values. When heated in the range of 1500 to 2000 ° C (carbonization), the highest tensile strength (5650MPa) carbon fiber can be produced, while a higher modulus of elasticity (531GPa) can be produced between 2500 to 3000 ° C (graphitizing). Carbon fibers are separated into different categories based on the modulus elasticity: standard modulus (250GPa), intermediate modulus (300Gpa), and high modulus (>300Gpa). CFRP's are generally anisotropic materials. This means, CFRP's have different stiffness's and other mechanical properties depending on which direction the force or moment is applied. (Wikimedia Foundation Inc., 2007a)

2.5.5 Epoxy

Epoxy is a thermosetting epoxide polymer that cures when mixed with a catalyzing agent, also known as a hardener. Epoxy can be designed to meet almost any application. It can be used on wood, glass, metal, stone, and some plastics. It can be flexible or rigid when cured, fast setting or extremely slow. Epoxy has an unrivaled heat and chemical resistance compared to common adhesives. The epoxy and catalyst should be mixed carefully to avoid small air bubbles from entering the mix, since the strength will reduce significantly when air bubbles are present. (Wikimedia Foundation Inc., 2007d)

Epoxy is formed by oxygen, hydrogen, and Carbon atoms. There is one epoxy group at each end of the epoxy molecule (See Appendix I for details). When mixing with the proper catalyst, an exothermic reaction will occur, resulting in the epoxy and catalyst molecules cross-linking together. The energy required to break the covalent bond occurring during the reaction is enormous, which in turn creates an epoxy matrix resistant to high stress.

2.5.6 Applications of CFRP

Modern advanced composites have been used since World War II. CFRP was first used in the military during 1950s (Hollaway, 1993). Currently due to its incomparable strength-to-weight ratio, CFRP is used extensively for producers needs to achieve lightweight and durable products. It has many applications in aerospace, automotive fields, as well as boats, tripods, laptops, and fishing rods. It also has applications in the production of bicycles, especially high-end racing bicycles, because of its vibration absorbing ability.

CFRP has been introduced to civil infrastructures recently. Because of the high strength-to-weight and stiffness-to-weight ratio, CFRP is widely used in corrosion and fatigue repair, strengthening, etc. Furthermore, CFRP can extend its applications to wrapping around beams in order to limit shear stresses.

2.6 ASTM Standards

Theoretically carbon fibre should have same strength in tension and compression. However, CFRP composite is weak in compression because of air voids and other defects presents in CFRP products. CFRP is used to repair or strengthen material in the tension zone. As a result, the tensile properties of CFRP and epoxy are the key factor for the user when choosing a CFRP composite strengthening system for a project. In most cases, the tensile property is established by the manufacture. The following section shows the ASTM international standard testing methods for both CFRP laminate and epoxy.

2.6.1 Standard tensile test for CFRP

ASTM D3039/D 3039M - 00 (ASTM 2006a) standard recommends a test method to determine tensile properties of polymer matrix composite materials. The test specimen should be 250 mm in length by 15 mm wide with 138 mm gauge length. The thickness of the specimen is depending on the thickness of the CFRP. Because CFRP strips are very thin, four special tabs are required for gripping the specimen by the test machine, and to transfer the load into the specimen (Figure 2.20). The tab was made of GFRP board of electro sonic and model # 64p44we. Each specimen had four tabs of 56mm x 15mm attached to CFRP using epoxy. By use of a tab with lesser bevel angels provides smooth transition into the coupon. Control of fiber alignment is critical in this test. When fiber alignment is improper, some fibers may break earlier than others, causing the actual cross-section to be reduced, resulting the measured prosperities lower than the actual value. This test is a strain controlled test; the standard rate is $0.01 min^{-1}$.

2.6.2 Standard tensile test for epoxy

The standard test method for tensile properties of plastics as recommended in ASTM D638-03 (ASTM 2006f) is used to establish the tensile strength of the epoxy. The test specimen shall conform to the dimensions shown in Figure 2.21. The speed of the test need to be 5 mm/min ± 25% while the nominal strain rate is 0.1 mm/mm x min. Tensile strength is calculated by dividing the maximum load in Newton (or pounds-ft) by the original minimum cross-sectional area of the specimen. Percent elongation, modulus of elasticity, secant modulus, and Poisson's ratio can also be determined from this test.

2.6.3 Standard shear stress test for epoxy

Shear stress is created by two surfaces sliding over each other. Shear stress distributed across the bond in an entirely different way (See Figure 2.22 for details). In the following section, a standard testing method for lap shear of FRP (ASTM, 2006e) is discussed.

The standard testing method for lap shear adhesion of fiber reinforced plastic (FRP) bonding is the testing of lap shear bond strengths, using composite materials such as FRP's bonded to steel. The dimension of the coupon sample is 25.4 mm by 101.6 mm (1 inch x 4 inch). The nominal thickness of the bonding is 0.76 mm (0.03 inch) (See Figure 2.23 for detail). The specimen loading rate need to be 13 mm (0.5 inch)/min. A minimum of five lap shear samples need to be tested. Individual peak load values in kPa (or psi) and average maximum and minimum values are recorded, as well as the test temperature, bond conditions, and failure type.

2.6.4 Standard test method for cleavage and peel stress

Cleavage stress occurs when a ridge joint is forced opened at one end (See Figure 2.24). Peel stress occurs when a flexible substrate is being lifted or peeled from the other substrate (See Figure 2.25). The stress distribution for cleavage and peel stresses are similar, mostly concentrated at one end (See Figure 2.26). There are two common test methods to determine the cleavage/peel stress. These two methods are discussed in the following sections.

2.6.5 Standard test method for strength properties of adhesives in cleavage peel by tension loading

This method determines the strength properties of adhesives in cleavage peel by tension loading and gives information as to the performance of substrate/adhesive combinations under cleavage/peel forces (ASTM, *2006c).* The test specimens is 25.4 mm (1 inch) wide by 177.3 mm (7 inch) long, but bonded only over approximately 76 mm (3 inch) of the length. (See Figure 2.27 for detail) 20-guage steel gripping wires are inserted in the unbounded end, and then attached to the testing machine jaws. The load is applied at a constant speed of 12.7 mm (0.5 inch)/min. A minimum of 10 test specimens for

each adhesive is required. The cleavage/peel resistance is measured over at least a 50.8 mm (2 inch) length of the bond line after the initial peak.

2.6.6 Standard test method for climbing drum peel for adhesives

This method is more complicated. The test is done by clamping the assembly in a universal test machine (see Figure 2.28) to determine the peel resistance of adhesive bonds between relatively flexible and rigidly adhered bonds; and the relatively flexible facing of a sandwich structure and its core. (ASTM, 2006d).

2.6.7 Standard tensile test for steel

ASTM E 8M-04 (ASTM, 2006b) specifies the standard test method for determining tensile properties of metallic materials. The test specimen shall be conformed to the dimensions shown in Figure 2.29. The thickness of the specimen is dependent on the thickness of the material. The speed of testing should be set for strain rate in between 0.05 and 0.5 m/m/min. Yield strength, ultimate strength, percent Elongation, modulus of elasticity, and Poisson's ratio are determined from this test.

2.7 Summary

Corrosion is a common problem for steel bridges and can occur anywhere on the steel member, such as the flange (Figure 2.30), web (Figure 2.31) and in between connections (Figure 2.32). The most common types of corrosion for steel beams are general corrosion, crevice corrosion, and galvanic corrosion.

Lots of research has been done repair and rehabilitation on concrete. But only a few studies are on steel. In previous studies on steel, uses of CFRP to repair corrosions of real bridges or simulated corrosions of the flange have been looked at. Strength and stiffness of the steel member have increased significantly. However, some of the corrosion simulations are very aggressive, such as removing 75% of the tension flange. This will most likely not occur in a real life situation because the bridge should be inspected regularly. No study in current literature did surface repair on general corrosion.

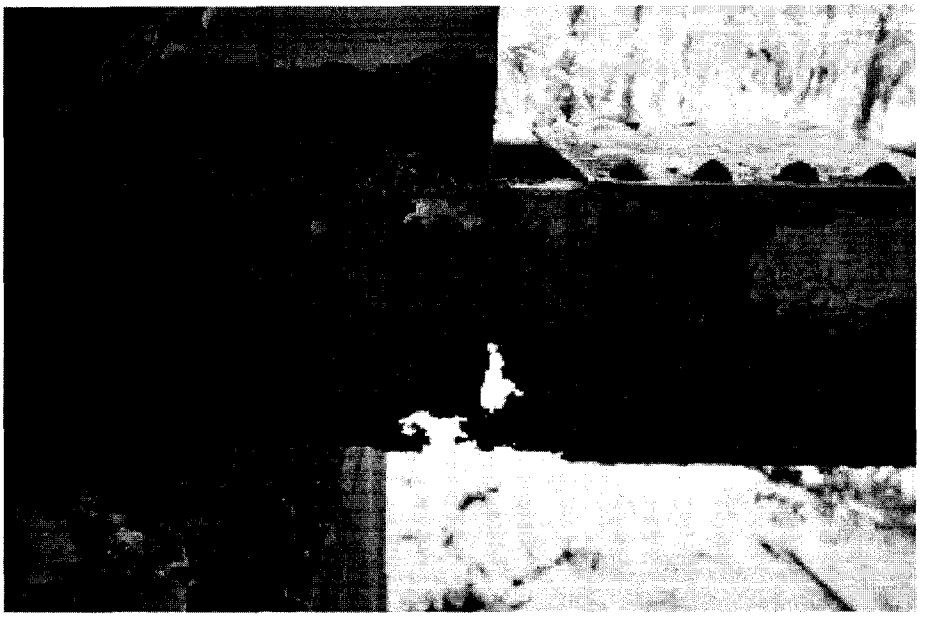

Figure 2.1: Corroded bridge (Conor Watkins, 2006)

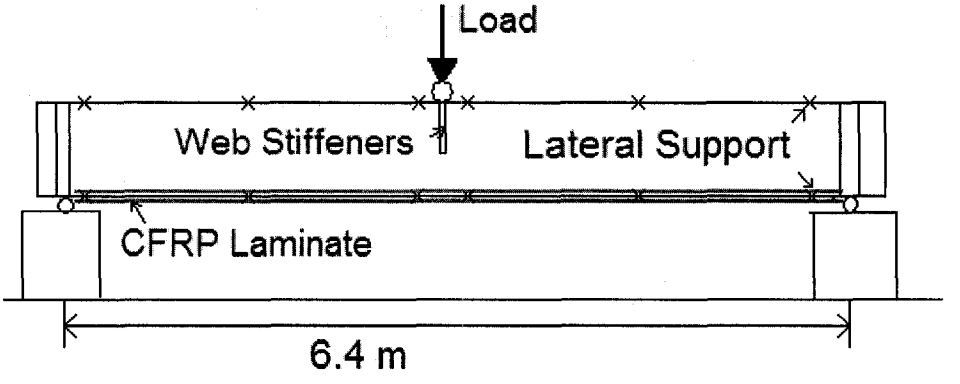

Figure 2.2: Test setup (Gillespie et al. ,1996a, 1996b, and 1997)

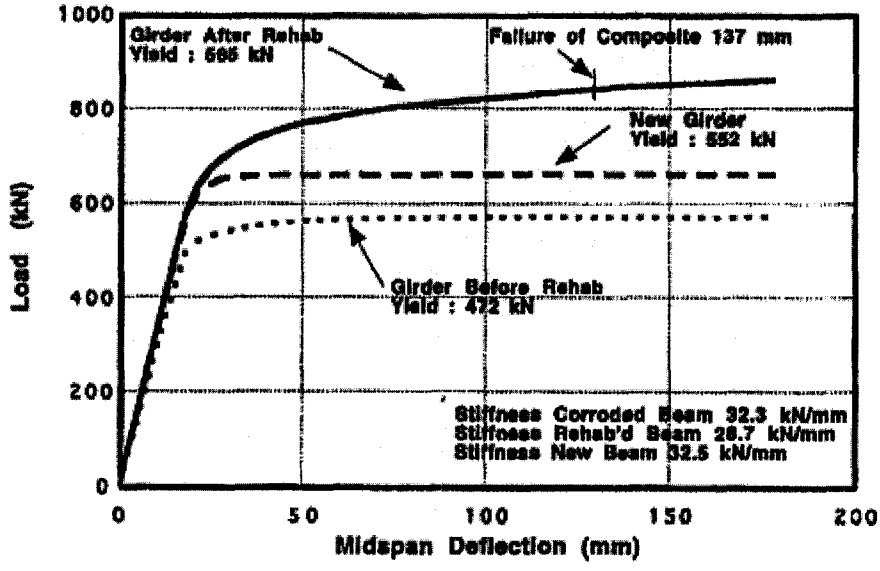

Figure 2.3: Load-deformation curve (Gillespie et al. ,1996a, 1996b, and 1997)

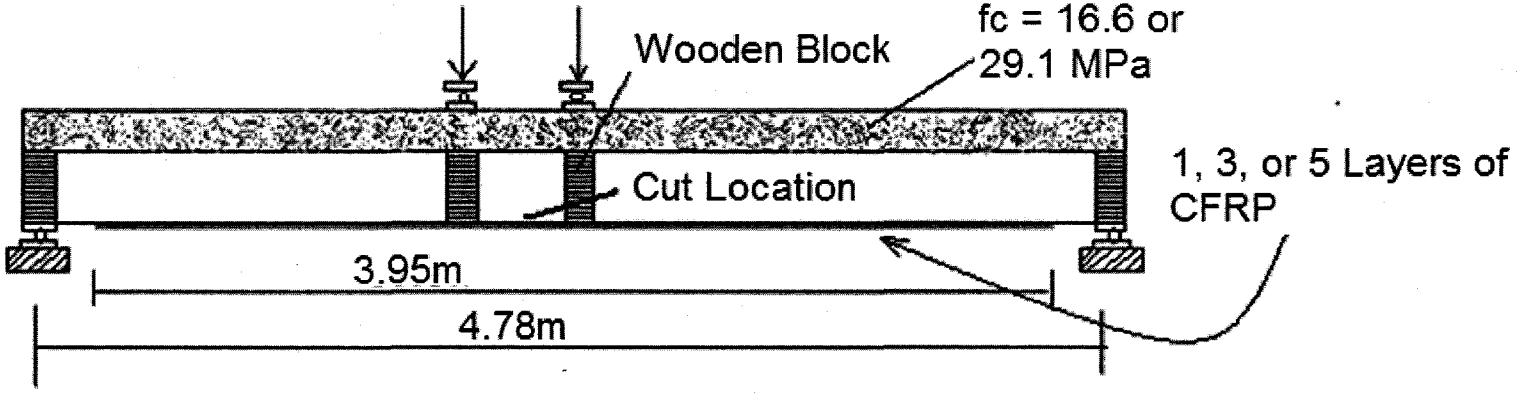

Figure 2.4 : Test setup (Tavakkolizadeh et al., 2001b)

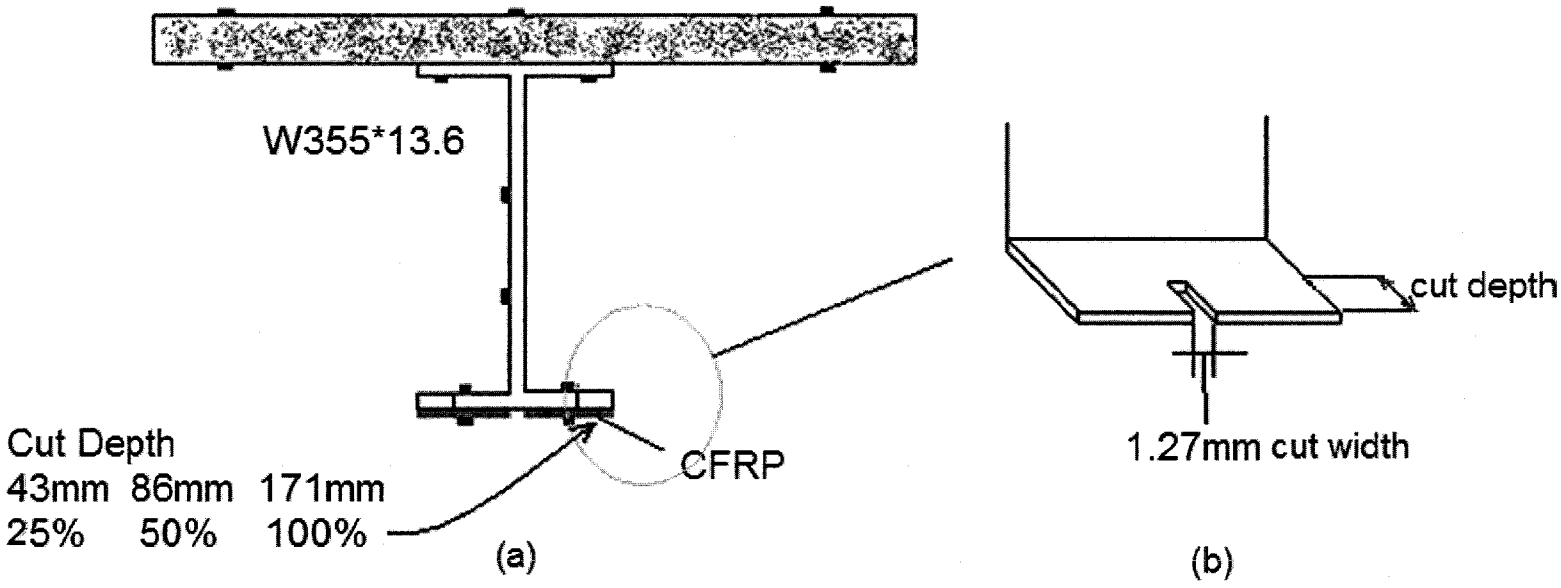

Figure 2.5(a): Cross sectional view
(b): Corrosion detail

(Tavakkolizadeh et al., 2001b)

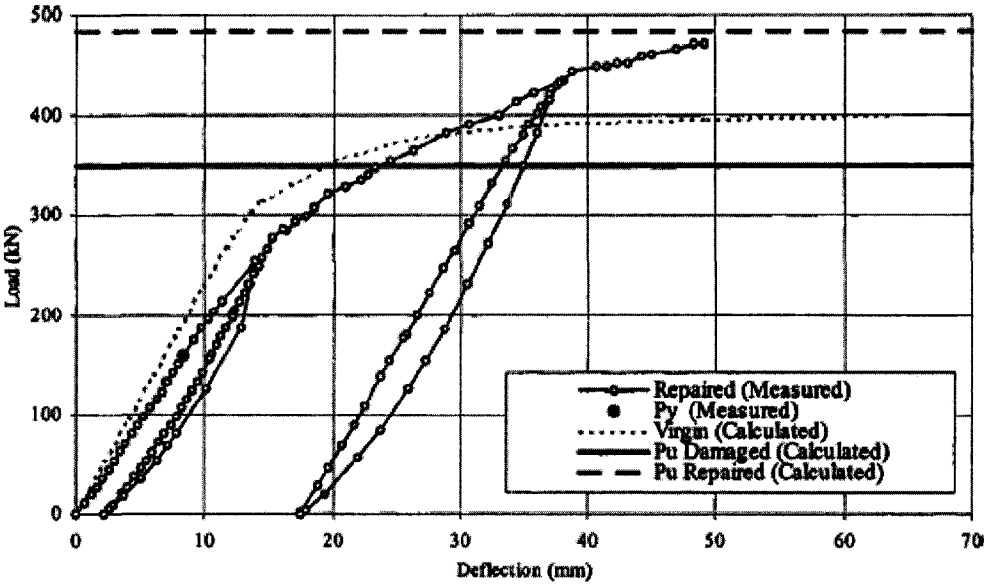

Figure 2.6: Load versus deflection of girder with 25% loss in flange area and repaired with one layer of CFRP sheet (Tavakkolizadeh and Saadatmanesh, 2001b)

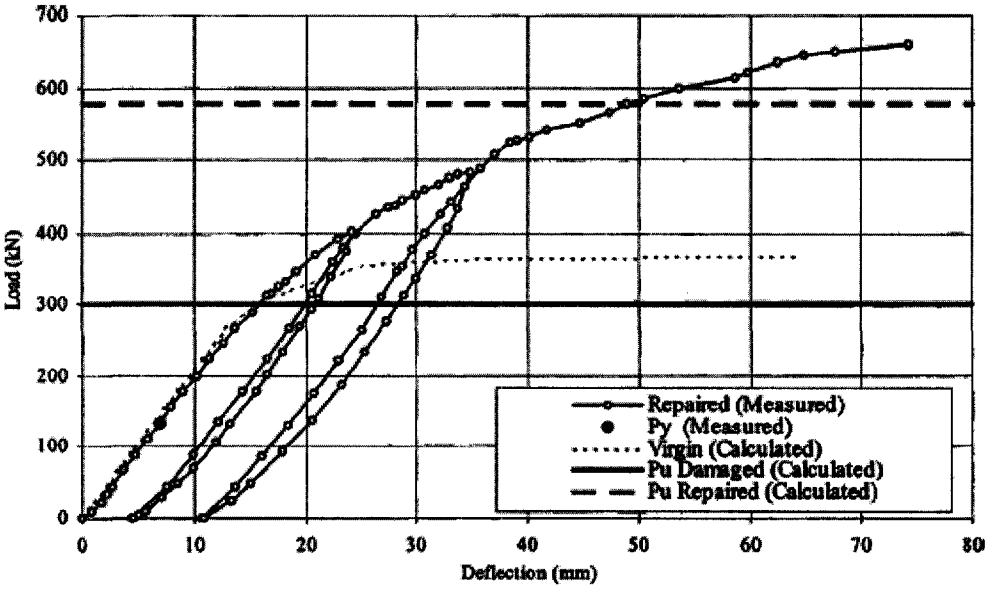

Figure 2.7: Load versus deflection of girder with 50% loss in flange area and repaired with three layers of CFRP sheet (Tavakkolizadeh and Saadatmanesh, 2001b)

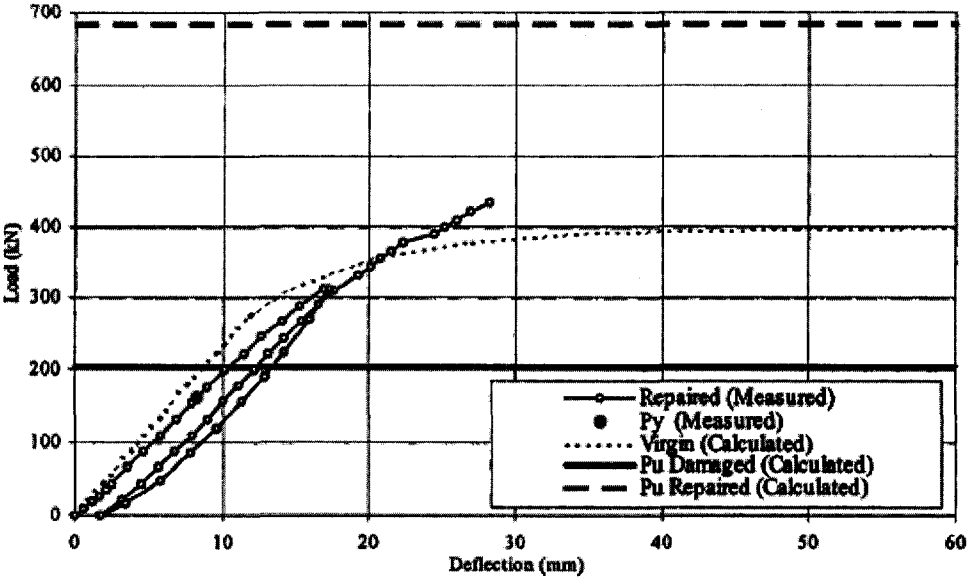

Figure 2.8: Load versus deflection of girder with 100% loss in flange area and repaired with five layers of CFRP sheet (Tavakkolizadeh and Saadatmanesh, 2001 b)

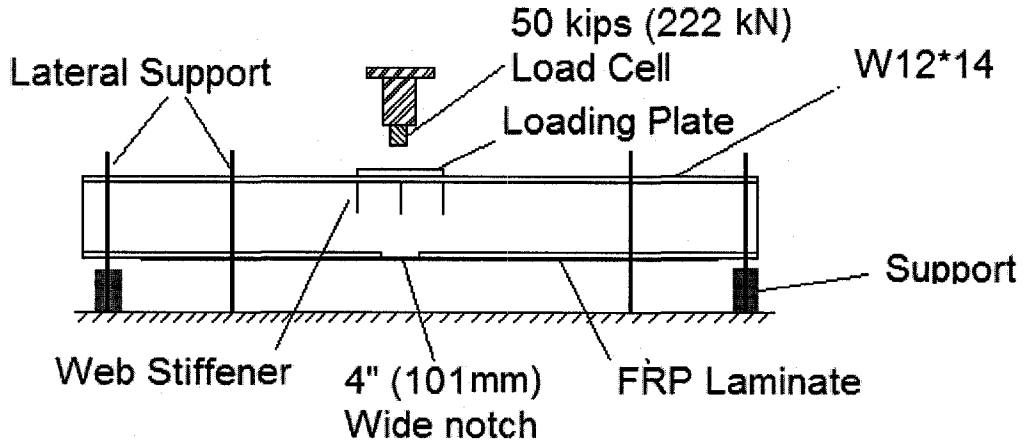

Figure 2.9: Test set-up (Liu et al., 2001)

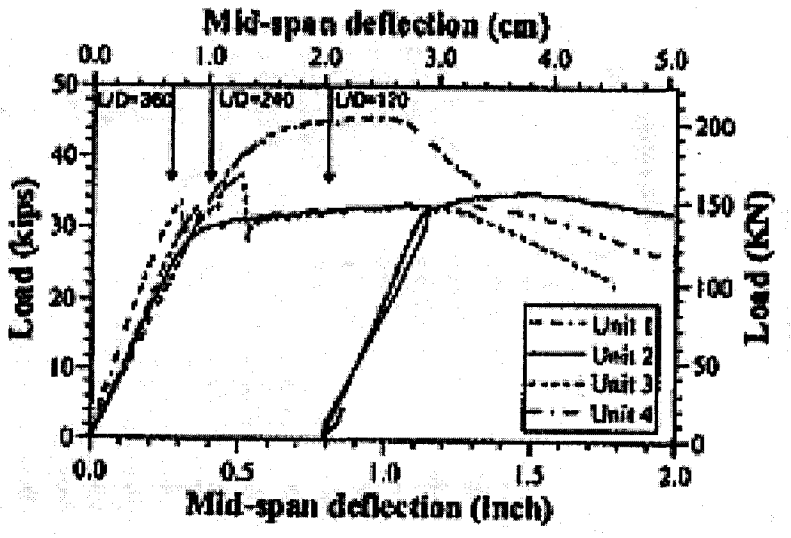

Figure 2.10: Load vs. deformation curve (Liu et al., 2001)

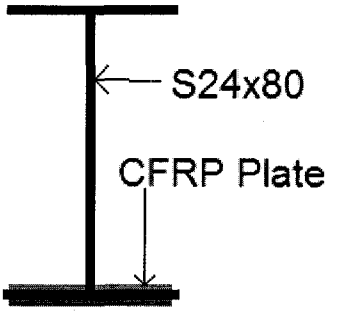

Figure 2.11: Cross section view (Miller et al., 2001)

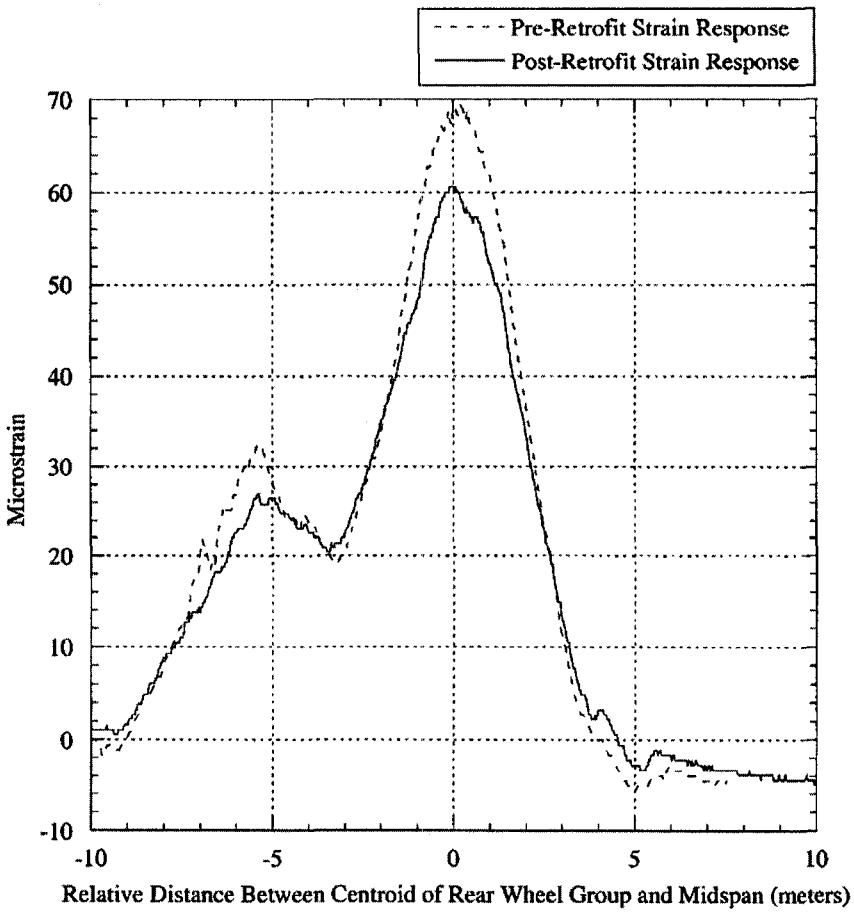

Figure 2.12: Comparison of pre- and post-retrofit tension strain in girder G5 (Miller et al. , 2001)

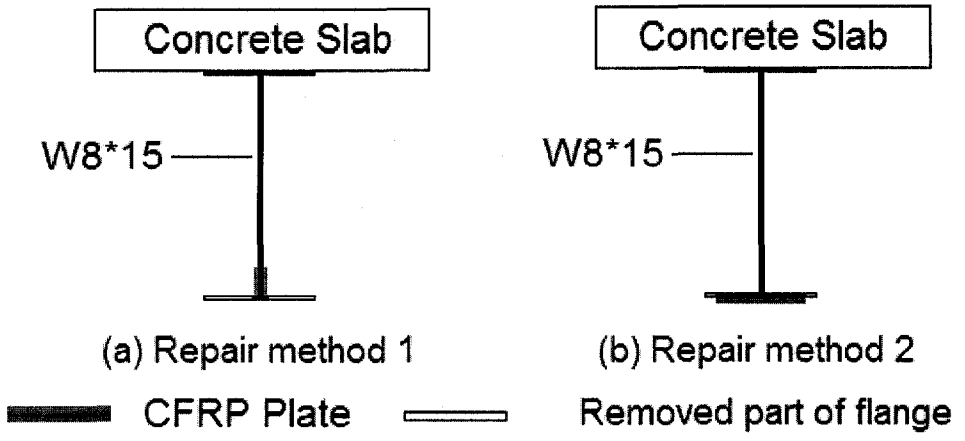

Figure 2.13 (a): Repair method 1
(b): Repair method 2
(Al-Saidy et al. ,2004)

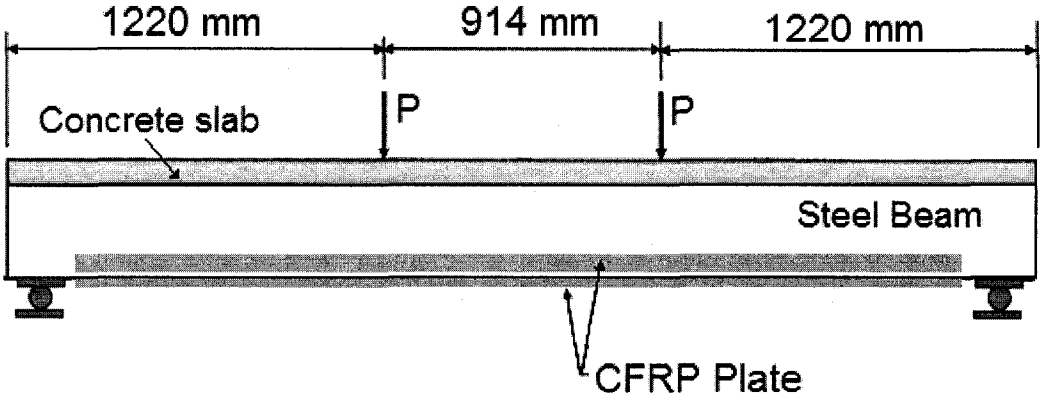

Figure 2.14: Test set up (Al-Saidy et al. ,2004)

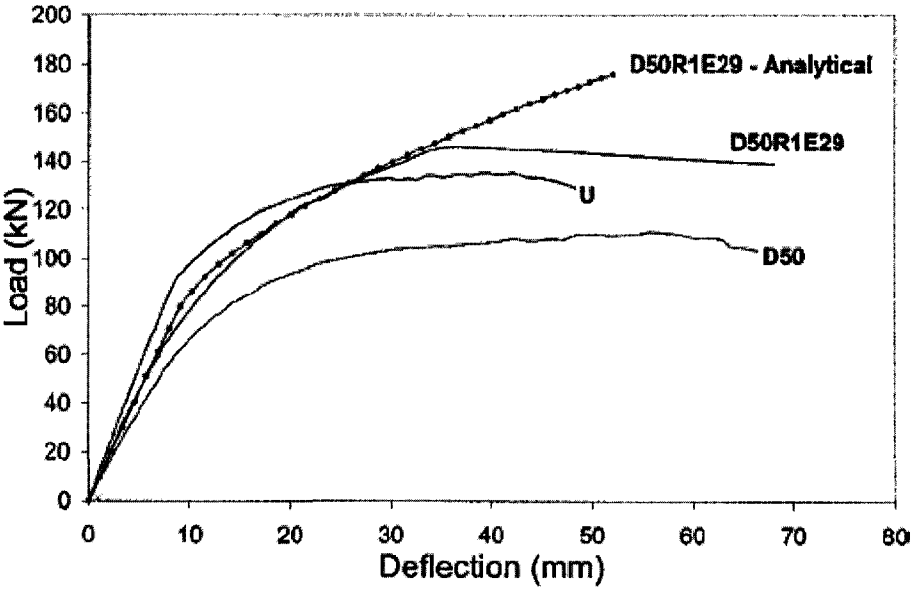

Figure 2.15: Comparison of measured midspan deflection in Beams U, D50, and D50R1E29 (Al-Saidy et al. ,2004)

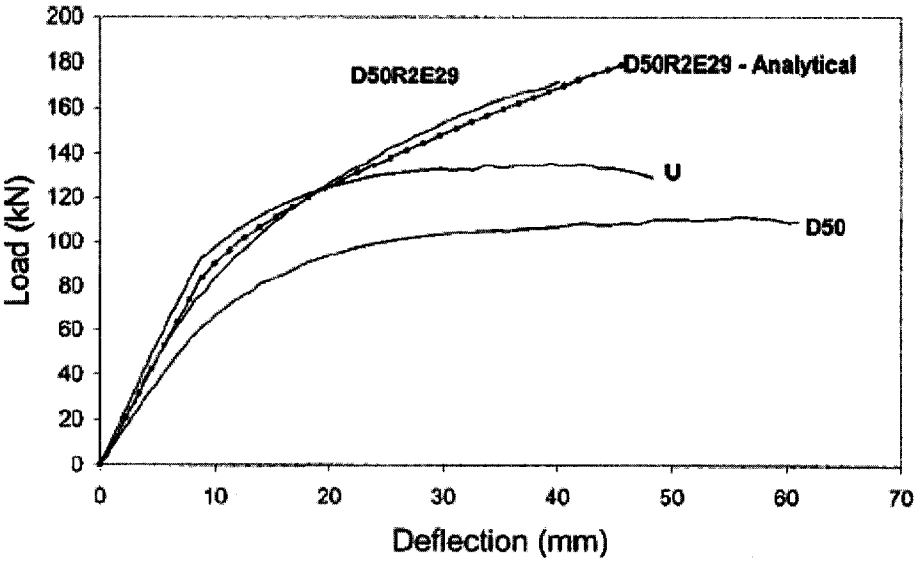

Figure 2.16: Comparison of measured midspan deflection in Beams U, D50, and D50R2E29 (Al-Saidy et al. ,2004)

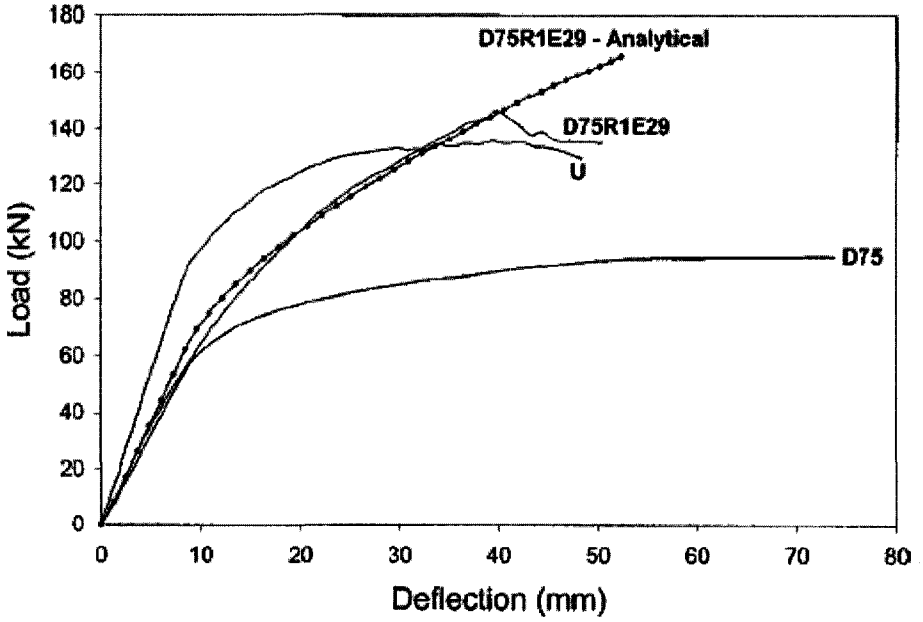

Figure 2.17: Comparison of measured midspan deflection in Beams U, D75, and D75R1E29 (Al-Saidy et al. ,2004)

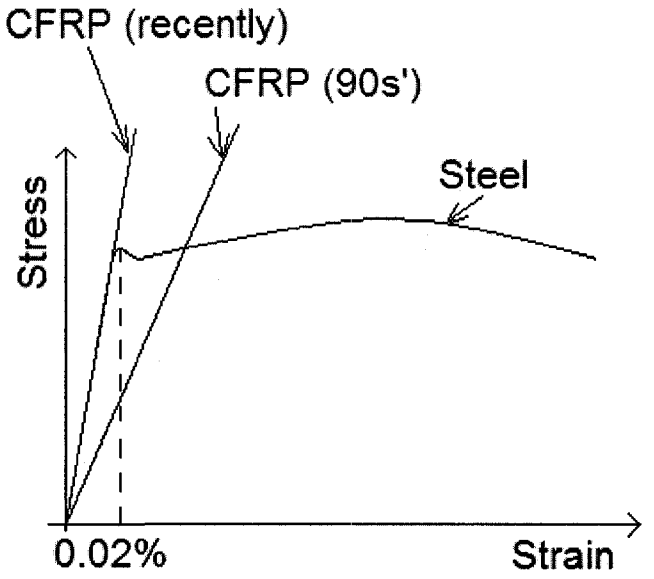

Figure 2.18: Typical CFRP and steel stress vs. strain behavior

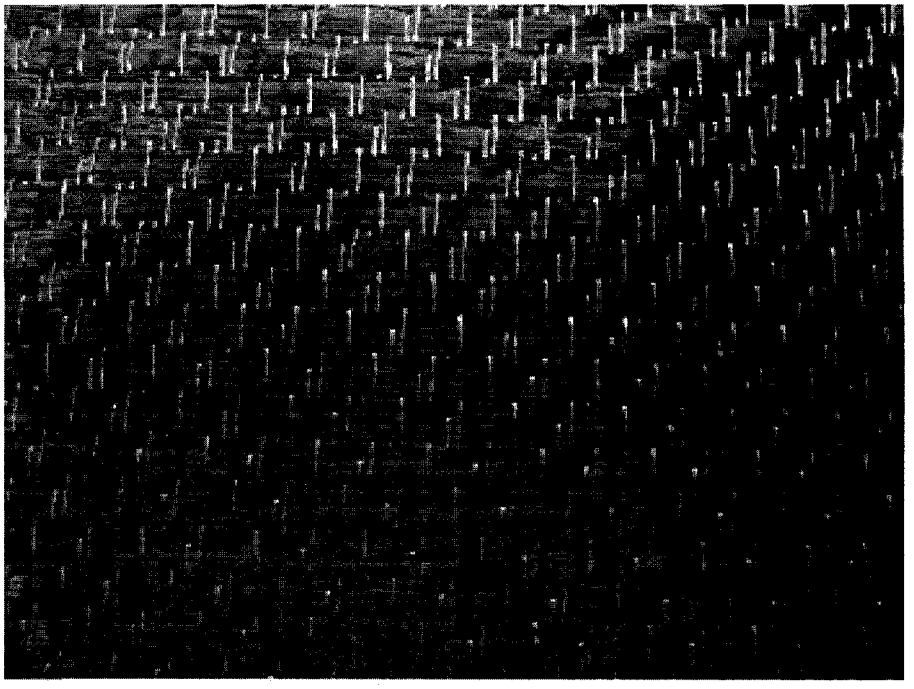

Figure 2.19: Carbon fiber dry fabric (sheet)

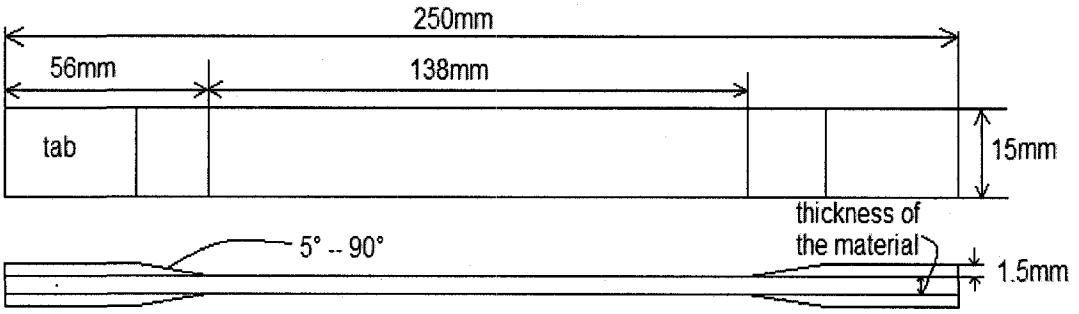

Figure 2.20: Tension test specimen sketch - D3039/D 3039M - 00
(ASTM, 2006a)

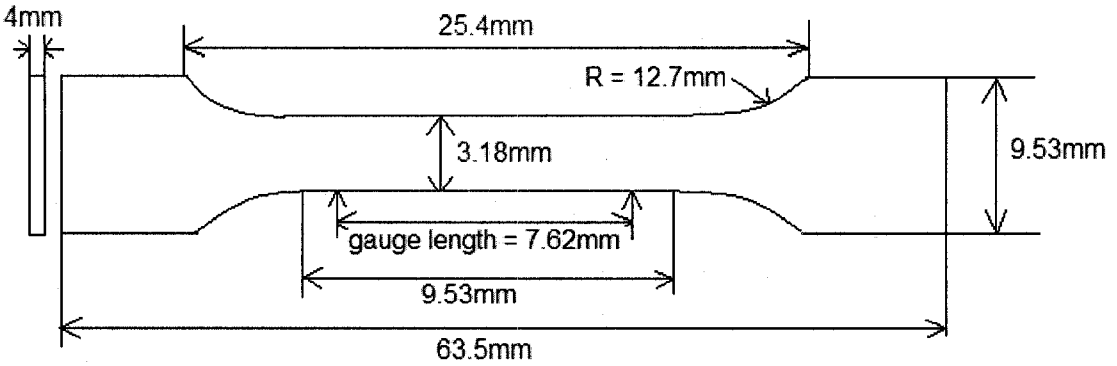

Figure 2.21: Specimen dimension for non-rigid plastic – ASTM D638-03 (ASTM, 2006f)

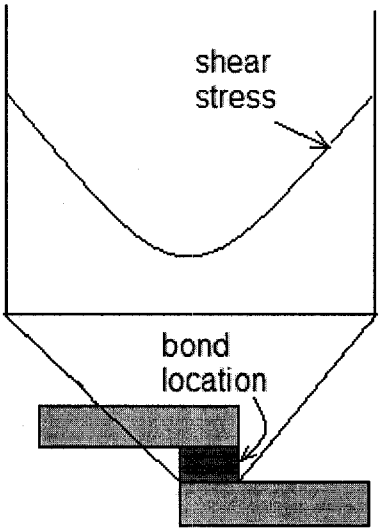

Figure 2.22: shear stress distribution (Plexus Structural adhesive, 2006)

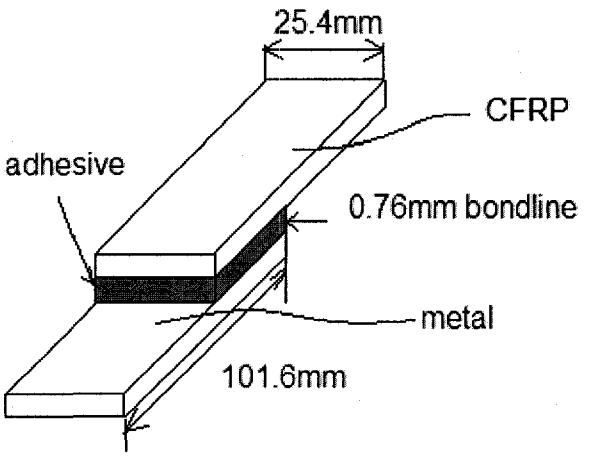

Figure 2.23: Lap shear overlay – ASTM D5868-01
(ASTM, 2006e)

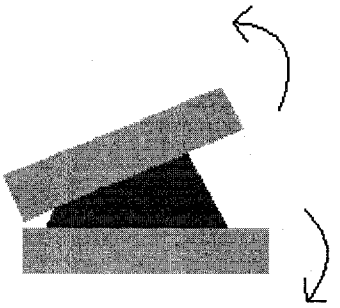

Figure 2.24: Cleavage stress
(Plexus Structural adhesive, 2006)

Figure 2.25: Peel stress
(Plexus Structural adhesive, 2006)

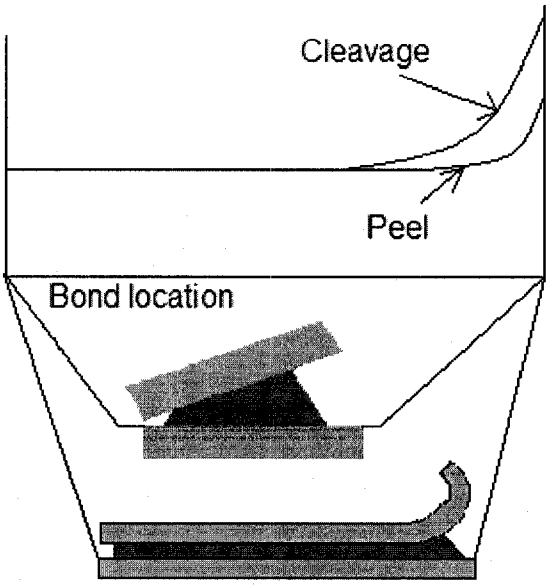

Figure 2.26: Cleavage and peel stress distribution
(Plexus Structural adhesive, 2006)

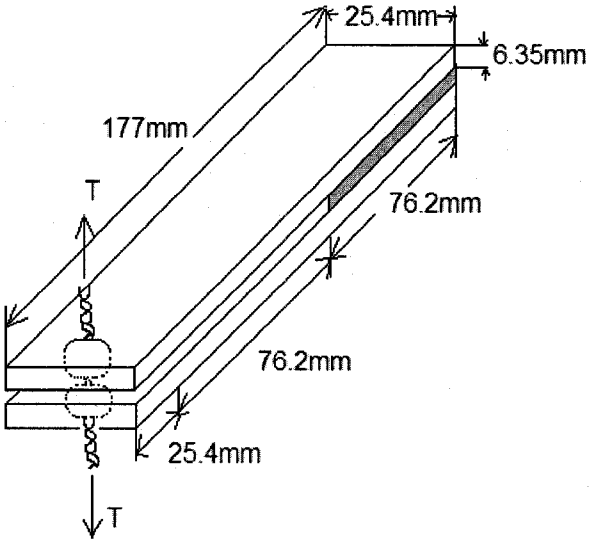

Figure 2.27: Cleavage peel test specimen – ASTM D3807-98
(ASTM, 2006c)

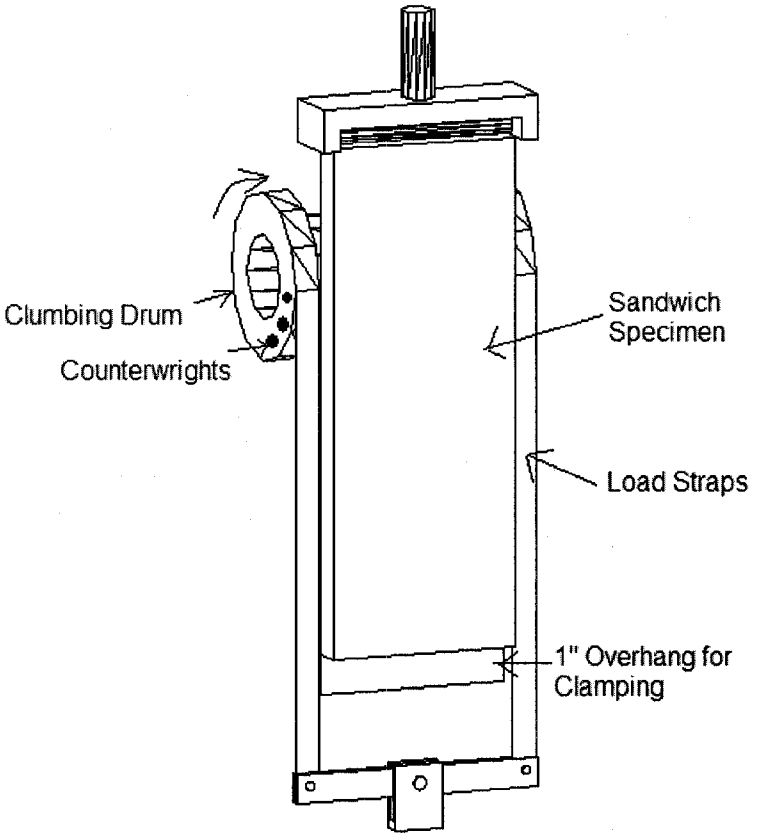

Figure 2.28: Assembly of peel apparatus – ASTM D1781-98

(ASTM, 2006d)

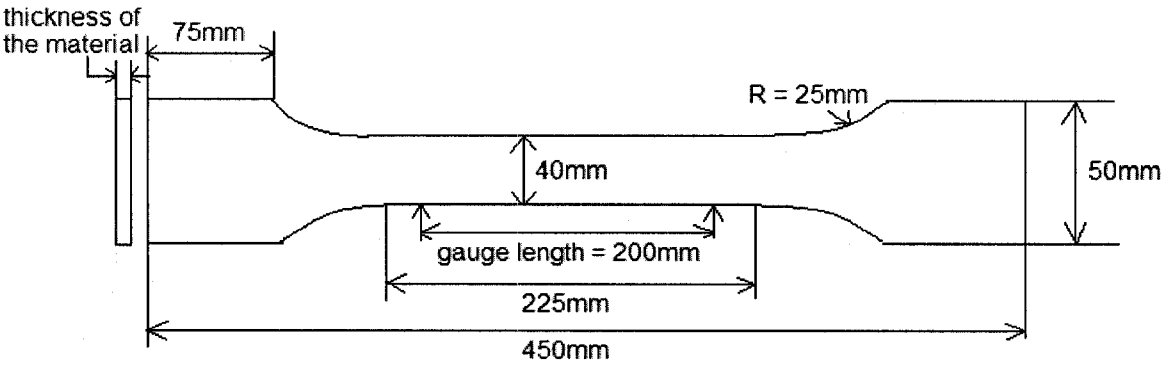

Figure 2.29: Specimen dimension for metallic materials (Plate type) – ASTM E 8M-04

(ASTM, 2006b)

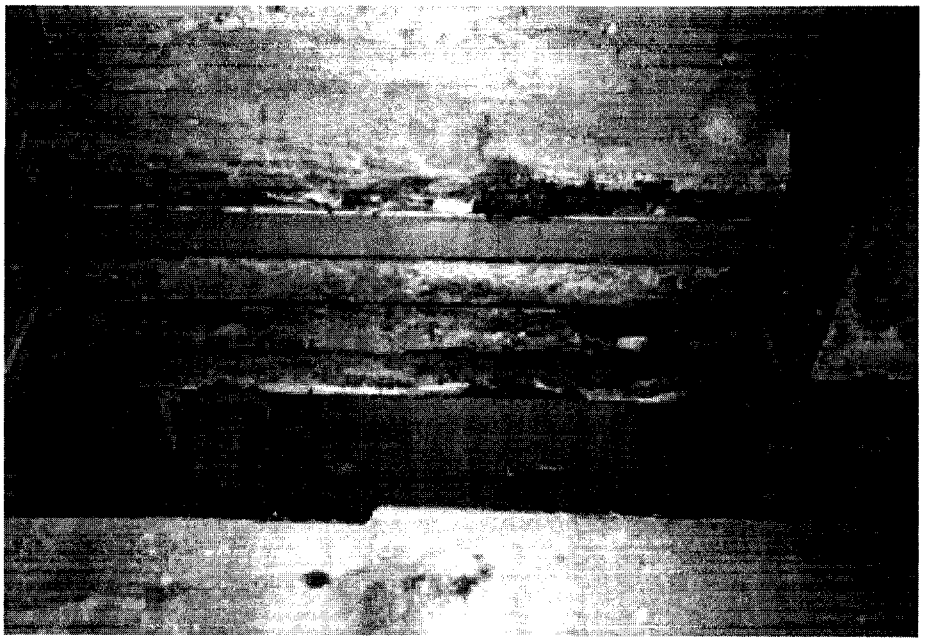

Figure 2.30: Corrosion on the flange
(US DOT, 2004b)

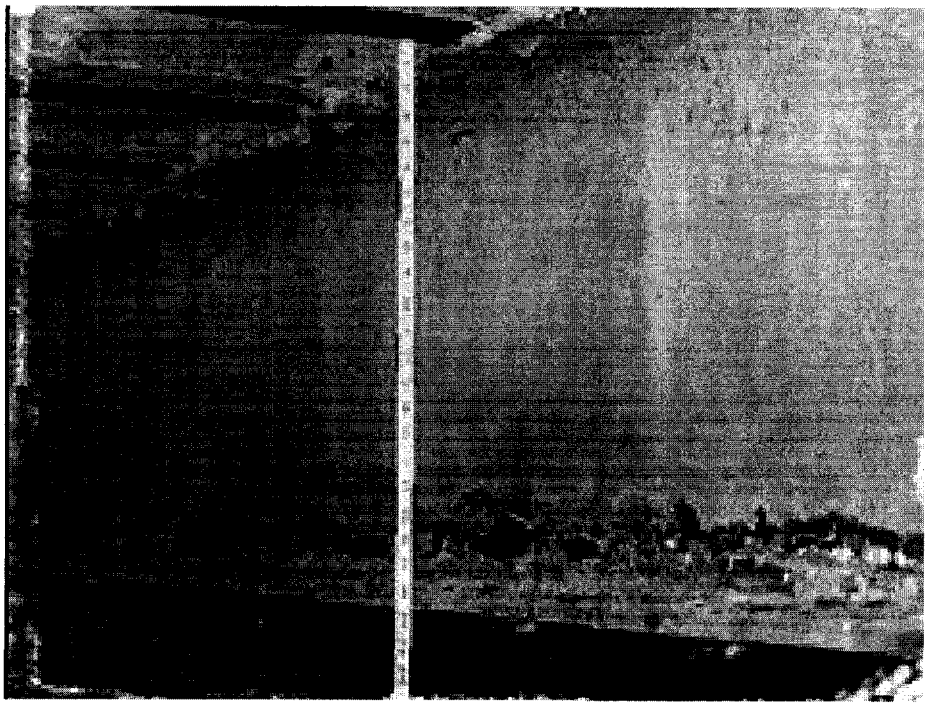

Figure 2.31: Corrosion on the web
(Network, 2000)

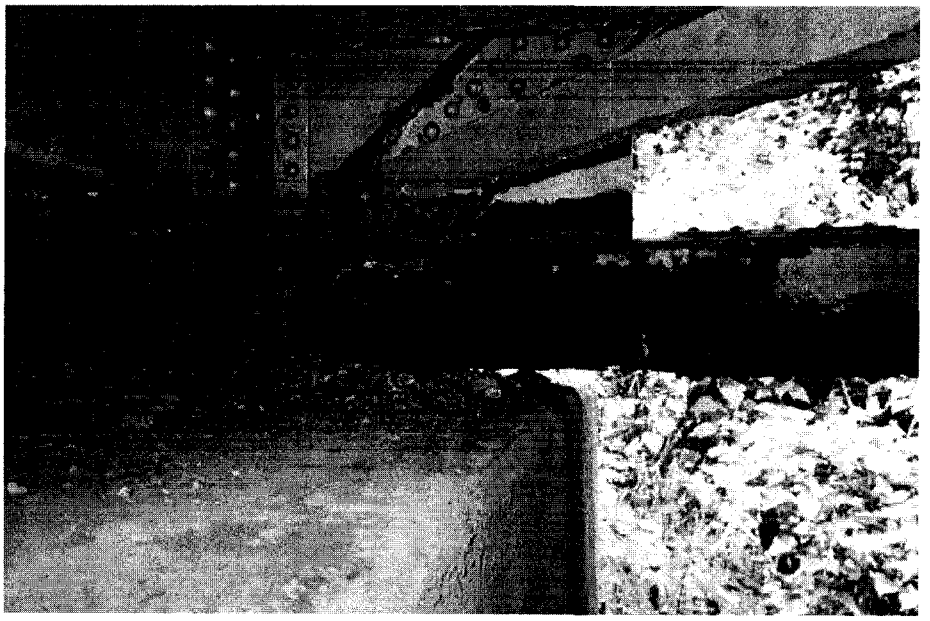

Figure 2.32: Complicated joints, hard for water to evaporate, corrosion between connections (Conor Watkins, 2006)

3 EXPERIMENTAL PROGRAM

3.1 Introduction

The object of the experimental study was to examine the rehabilitation technique of surface corroded steel beams using carbon fiber reinforced polymer (CFRP) sheets.

The experimental program, consisting of ten steel wide flanged I-shaped beam specimens, was set to evaluate the effectiveness of the CFRP sheets used as an external reinforcement for the rehabilitation of the surface corroded steel beams. This chapter describes the test specimens (configuration, materials, and fabrication), instrumentation, experimental setup, procedure for a three point bending test, and the rehabilitation scheme using CFRP sheets were used in this study.

3.2 Experimental Program

Ten specimens were designed, fabricated, and tested in the University of Windsor Structure Laboratory. Table 3.1 summarizes the primary variables for the specimens. The test specimens are called using specific identification labels. The following names/labels were used to describe the specimen. The TS, CV, CC, and RC denote Trial specimen, Control Virgin (uncorroded) specimen, Control Corroded specimen, and Rehabilitated Corroded specimen, respectively. For rehabilated specimens, longer labels (names) were required. For example, for specimen RC-W67-T2.4-G1, W67 and T2.4 denote width, and thickness of the CFRP were 67 mm and 2.4 mm, respectively. The last letter G1 indicates that the specimen belongs to group one. All specimens, excluding the trial specimen (TS), were divided into two groups. There were four specimens in Group1, which included CV-G1, CC-G1, RC-W67-T2.4-G1, and RC-W133-T2.4-G1. The Group2 contained five specimens, which are: CV-G2, CC-G2, RC-W133-T2.4-G2, RC-W133-T1.2-G2, and RC-W133-T0.6-G2.

3.3 Description of Test Specimen

All the specimens were 1800 mm long and made of standard wide flange I-shaped cross-section W200x21matric (W8x14 Imperial) (Figure 3.1). The center to center support length of the specimens was 1600 mm.

3.3.1 Detail of the corrosion

The surface corrosion was simulated by machining the bottom flange of the beam. The corrosion was introduced at the mid-length of the outer face of the bottom flange (Figure 3.2). A circular arc shaped 100 mm long corrosion was machined (Figure 3.3). HAAS TOOLROOM MILL TM1 machine was used to make the corrosion (Figure 3.4). The plan view of the corrosion was trapezoidal and could not be made rectangular because the beam flange is not perfectly level, the actual flange slightly tilted (Figure 3.5). Figure 3.6 is a photo of a corrosion and Figure 3.7 is the plan view of the corrosion. Figure 3.8 is the three-dimensional sketch of the corrosion. The length of the corrosion was 100 mm long in the longitudinal direction of the beam (direction-3) at the edge of the flange and 80 mm long at the web-flange connection. The width of the corrosion was 64 mm along the width of the beam (in direction-1) as shown in Figure 3.7. The corrosion spread over the half of the flange width. Thus, the corrosion was symmetrical about the mid-span of beam in direction-3, but was unsymmetrical in direction-1. Variation of corrosion depth in direction-3 was between 4 mm at its mid-length to no corrosion at ends (Figure 3.8). Variation in direction-1 was from 4 mm at the edge of flange to 2.6 mm at the web-flange corner. Figures 3.9 and 3.10 show the details of two-dimensional cross-section view of the corrosion at the outer edge of the flange and at the web-flange intersection, respectively.

3.3.2 Details of trial virgin specimen (TS)

The trial specimen (TS) was placed on a pin support on one end and roller support on the other end with a 1600 mm clear (center to center) span. Two U shaped steel frames were welded to the stiff wide beam at 610 mm from center to avoid any sudden lateral movement of the beam (Figure 3.11 and 3.12). The U shaped steel frame is 30mm away from the specimen flanges. A three point bending load was applied on the TS specimen until it failed. The specimen failed in lateral torsion buckling. Four linear potentiometers (LP) were used to acquire the deformation history of the beam. The location of the LP can be seen in Figure 3.11. Figure 3.12 shows a picture of the test set up for this specimen, while Figure 3.13 shows the specimen after failure. Figure 3.13(b) shows the flange buckling under the load and Figure 3.13(c) shows the lateral torsion buckling.

The load-deformation behavior for this specimen is shown in Figure 3.14. This specimen yielded at a load of 170 kN (shown by point Y) and 7.4 mm vertical deformation at its mid-span. The vertical deformation in this figure was measured through LP8 (Figure 3.11). The ultimate load (shown by point U) was 180.7 kN and the deformation was 9.33 mm. Figure 3.15 shows the deformation response obtained from LP7, LP8, and LP9 at 40 kN, 140 kN, 160 kN, 170 kN, and end of loading process. The specimen deformed slowly until it reached its ultimate load (U), then deformed rapidly while the load dropped. The deformation was almost symmetric about load application point along direction-3 until ultimate load (180.7 kN) was applied. However, the deformation became unsymmetrical before end of loading process because of lateral torsion buckling. Figure 3.16 is the load and mid-span lateral deformation curve, which shows after reaching the ultimate load, the specimen deformed laterally rapidly. The deformation was recorded through LP5 (Figure 3.11). The location of the salient points identified by Y, U, and F in Figure 3.14 and Figure 3.16, are the yield point, ultimate load point, and failure load point, respectively.

The failure mode for specimen TS was lateral torsion buckling shown in Figure 3.13, even though calculation (Appendix II) shows that the specimen was not expected to fail in lateral torsion buckling. The reason of the lateral buckling for this specimen seems to be that the load was not probably applied perfectly in the center, and there was no lateral support to prevent the torsion. The top flange underneath the load also buckled. Therefore, for specimens in groups 1 and 2, lateral supports (LS) were provided to prevent lateral torsion buckling. Steel round blocks (SB) were also used between top and bottom flanges to avoid the flange buckling under the load application point.

3.3.3 Details of the Group 1 specimens

Four lateral supports (LS) and two steel round blocks (SB) were installed on each side of specimen for all specimens of group 2. The LS for both top and bottom flanges were located at 180 mm and 610 mm away from the mid-length (Figure 3.17). Two types of lateral supports were used. The first type (Type 1) of LS was built by welding a 100 mm high x 75 mm wide x 10 mm thick steel plate to an angle (L51x51x7.9). The LS were then bolted against strong steel column (Figure 3.18). This LS is shown by ✳ in Figure 3.17. The other type (Type 2) of LS was made using

300 mm high x 100 mm wide x 30 mm thick steel plates. The plates were welded to U shaped steel frames and then the U shaped frames were welded to the wide beam (Figure 3.19). They were located at 610 mm on either side of beam's mid-length (shown by ✕ in Figure 3.17). The SB were installed at 110 mm away from the beam's mid-span where there were no strain gauges (shown by ● in Figure 3.17). When this location was infeasible due to strain gauges, the SB were installed 140 mm away from center (Figure 3.17). The steel blocks were 30 mm in diameter (Figure 3.20).

All the specimens in group1 failed due to web buckling, some less severe than others. Consequently, web stiffeners (WS) were used in all specimens of group 2. Furthermore, a flange stiffener (1000 mm long x 110 mm wide x 6 mm thick steel plate) was also welded on to the top of the beam to avoid flange buckling under the load.

3.3.4 Details of the Group 2 specimens

Two WS (180 mm long x 60 mm wide x 8 mm thick steel plates) were welded either side of the web at the center of the steel beam, for all specimens of group2 (Figure 3.21). A steel plate of 1000 mm long x 110 mm wide x 6 mm thick was welded to top flange of each specimen of group 2 to avoid the top flange from buckling (Figure 3.22). LS and SB used for specimens of group 1 were used in all specimens of group 2 as well.

3.4 Material Properties

The materials used in the tests include steel, epoxy(Saturant), filler putty, primer, and CFRP dry fabric.

3.4.1 Steel

The steel beam used in this study was of W350 grade steel. They were purchased separately from the Victoria Steel Corporation and the Border Steel Ltd. located in Windsor, Ontario. Eight coupon specimens (Figure 3.23) were cut from these steel beams. Four coupon specimens from the beams purchased from the Victoria Steel Corporation, and remaining four from the beam purchased from the Border Steel Ltd. Tensile tests were conducted on coupon specimens according to ASTM E 8M-04

(ASTM, 2006b) as described in section 2.6.7, to obtain their material behaviors. A 300 kN (both tension and compression) capacity Tinus Olsen Universal Testing Machine was used for these tests (Figure 3.24). Figure 3.25 shows a failed steel coupon specimen. Figure 3.26 and Figure 3.27 show the strain vs. stress relationships obtained from the tensile material tests of Victoria steel and Border steel, respectively. The following notations were adopted in Figures 3.26 and 3.27 to describe the specimen. Victoria means the coupon specimen was cut from a beam purchased from Victoria Steel Corporation, Border means the coupon specimen was cut from a beam purchased from Border Ltd. Following Victoria or Border, is a letter-number notation, W# or F#. W and F, denote whether the coupon specimen was cut from the web (W) or from the flange (F) of the beam. The number denote the number of the specimen. Therefore, Victoria-W1 denotes the first coupon specimen cut from the web of the beam purchased from Victoria Steel Corporation.

The average of the modulus of elasticity was calculated to be 219.3 GPa and the first yield and ultimate stress were 420.7 MPa and 552.06 MPa as shown in Table 3.2.

3.4.2 Composite materials

The composite strengthening system used in the tests was the MBrace composite strengthening system, which is manufactured by The Chemical Company, BASF and Sikawrap Hex dry fabric (230c) manufactured by Sika Canada Inc. The composite strengthening system includes MBrace Primer, MBrace Putty, MBrace Saturant, and MBrace CFRP dry fabric (CF 160).

MBrace Primer is a low viscosity polyamine cured epoxy. MBrace Primer is the first component applied to a substrate in order to create a high bond base coat for the MBrace system (BASF 2006b). MBrace Putty is a high viscosity epoxy paste, which is used to even out small defects and create a smooth surface for MBrace system to be applied (BASF 2006c). MBrace Saturant is a low viscosity epoxy that is used to impregnate and reinforce MBrace dry fabric (CF 160) and bond CFRP on the steel substrate (BASF 2006d). MBrace Primer, Putty, and Saturant are all with different viscosities for various uses. Each one is a two-components epoxy (resin and hardener), with a mix ratio of 3:1 (resin to hardener) by volume. MBrace CF160 is composed of a high strength carbon fiber dry fabric. The carbon fibers are held in a unidirectional

alignment with glass fiber (BASF 2006a). MBrace CF160 needs to be impregnated and reinforced by the MBrace Saturant. Once the MBrace system is fully installed on the beam, it acts as an externally bonded CFRP reinforcement system to increase the strength and structural performance of the beams. Material properties for MBrace composite strengthening system reported by the Manufacture are listed in Table 3.3.

Due to the unavailability of the MBrace CF160 dry fabric during last phase of test program, Sikawrap Hex 230c was used to repair specimens of group3. Sikawrap produces several dry fabric products , however Sikawrap Hex 230c was chosen for this study because its ultimate (fracture) tensile strength and elastic modulus were similar to those of MBrace CF160. See Table 3.3 for material properties for Sikawrap Hex 230c. Since thickness of Sikawrap Hex 230c is thinner than MBrace CF160, more numbers of layers of Sikawrap Hex 230c was necessary to achieve the equivalent thickness of the MBrace CF160.

3.4.3 Carbon Fiber Reinforced Polymer tensile test

Two different CFRP tensile coupon specimens were prepared and tested to determine the mechanical properties of MBrace CF160 CFRP. The quasi-static tensile tests were conducted as recommended by ASTM D3039/D 3039M - 00 (ASTM 2006a) standard, as discussed in section 2.6.1. The tensile coupons specimen from group 1 was made from MBrace CF160 composite and the coupon specimens for other group was made from MBrace CF160 dry fabric. Tabs with 15° bevel angle, which was made out of E-GFRP (E-glass fiber reinforced polymer) board produced by Electro Sonic (model # 64p44we) were attached to the end of coupon specimens using MBrace Saturant to provide a soft interface and grip. A 300 kN capacity (both tension and compression) Tinus Olsen Universal Testing Machine was used to apply the tension load (Figure 3.28). Figures 3.29 and 3.30 show the coupon specimens before and after the test. Figure 3.31 and 3.32 show the strain vs. stress relationships for CFRP laminate and CFRP dry fabric specimens, respectively. The following notations were adopted in Figures 3.31 and 3.32 to describe the specimen. The letter W indicates that the coupon specimen was made from MBrace CFRP composite, and the letters W/O means the coupon specimen was made from MBrace dry CFRP fabric. Following W or W/O, is a number notation, denote the number of the specimen. Therefore, W1 denotes the first coupon specimen made from MBrace CFRP composite (laminate). The average of the

tensile modulus for CFRP laminate was obtained as 243 GPa while The manufactures specifies a value of 227 GPa. Note, the carbon fiber specimen W1 was first loaded to 60 kN, reloaded, and then loaded to fail.

As mentioned in section 1.6.1, fiber alignment is critical in these tests, especially for dry fabric. When there is no epoxy (Saturant) to distribute the load evenly among fibers, some fibers break before others, decreasing the effective area of the cross section, resulting in the reduction of the modulus of elasticity. The average of the tensile modulus of the CFRP dry fabric was calculated by taking the slope of each curve between 50 kN and 400 kN loads, where all the curves are essential linear and very similar. The average of the tensile modulus for CFRP dry fabric was obtained as 224 GPa ((230+190+252)/3).

Due to the high variation in test data obtained from dry CFRP fabric specimens as shown in Figure 3.32, the data was not used in this study.

3.4.4 Shear stress test of epoxy

Three coupons were tested according to ASTM D5868-01 (ASTM, 2006e), Section 2.6.3. A 300 kN capacity (both tension and compression) Tinus Olsen Universal Testing Machine was used for the test. Figure 2.23 shows a sketch of the specimen. Steel flat and CFRP laminate were bonded with the MBrace Saturant epoxy. The steel flats were cut out from the flange of the steel beam purchased from the Victoria Steel Corporation, the dimensions of the steel flat were 101.6 mm long x 25.4 mm wide x 6.4 mm thick. The CFRP laminate was made by saturating a large piece of MBrace CF 160 dry fabric with MBrace Saturant. After cured in room temperature for seven days, the CFRP laminate was cut into 101.6 mm long x 25.4 mm wide pieces. The thickness of the CFRP laminate was 0.79 mm. The nominal thickness of the bond was 0.76 mm. It was controlled by putting the cut CFRP laminate on top of a 110 mm long x 25.4 mm wide x 7.16 mm aluminum flat while curing as shown in Figure 3.33. Figure 3.34 shows the failed shear coupon specimens. A linear potentiometer (LP) with 200 mm (8 in.) gauge length was used to measure the vertical movement of the lower crosshead of the testing machine, which is equal to the deformation of the specimen. Figure 3.35 shows the stress vs. strain curves obtained from the test. The S# was adopted in Figures 3.35 to describe the specimen. The letter S means it is a Shear

stress epoxy coupon specimen, and the number denotes the specimen number. The average of ultimate shear stress was calculated to be 14.6 MPa.

3.5 Rehabilitation Method

Any successful rehabilitation depends on the proper preparation of the structural element. This section includes surface preparation, resin constituent materials and their mixing, and method of application of CFRP to corroded steel beams.

3.5.1 Surface preparation

One of the most important steps in a successful rehabilitation of a structural member is the surface preparation of the repaired structural component. Therefore, careful attention was given to prepare the steel surface before application of CFRP fabrics.

1. The surface was sand blasted using 12-20 mesh industrial coarse sand to a "white metal" finish (Figure 3.36) to ensure good bonding between CFRP and steel surface.
2. After sand blasting, the steel beam was cleaned by compressed air.
3. A thin layer of MBrace Primer was then applied to the surface to penetrate the pore structure of the steel substrates and to provide a high bond base coat (Figure 3.37).
4. The corrosion was filled by using either MBrace Putty (Figure 3.38) or layers of small piece of CFRP fabric (Figure 3.39) to ensure a smooth surface (Table 3.1). Only one specimen (RC-W67-T2.4-G1) was filled the corrosion with MBrace putty. For all other rehabilitated specimens, short pieces (100-95 mm long) of CFRP fabric (several layers) were used instead.

3.5.2 Saturating resin preparation

Correct proportioning and proper mixing are important when using epoxy resin systems. Improper preparation of the resin can lead to premature debonding of CFRP laminate, resulting in the loss of composite action.

Sever defects may be introduced to the system during mixing. Air can be drawn into the resin during mixing and remain as small air bubbles, which can reduce the strength of the composite system significantly. Improper mixing can result in chemical

inconsistency, meaning that some regions contain high percentages of hardener, while others may contain no hardener at all. The efficiency of the resin system depends on the appropriate use of the mix ratio of the chemicals (epoxy ingredients). Errors in the mixing ratio can result in under-cure.

The two components of the epoxy resin were mixed manually; since small quantity of epoxy resin was required. Attention was paid to the mix ratio (3:1 by volume of Part A and Part B) to ensure the proper mixing of epoxy. Mixing was performed at a slow rate to avoid drawing an excessive amount of air into the matrix. The mixing was continued for a minimum of three minutes to ensure thorough and proper mixing.

3.5.3 Application of CFRP

1. The CFRP sheet was cut into the required size.
2. Once the epoxy was mixed, it was applied to both surfaces of the CFRP sheets using a paint roller to ensure the CFRP was saturated (impregnated) properly with epoxy (Figure 3.40).
3. Subsequently, the saturated CFRP was applied on the beam and the epoxy resin was applied again onto the surface of the CFRP.
4. These steps were repeated for every single layer of CFRP wrap and CFRP cross wrap.
5. After applying the CFRP wraps and cross wraps, a layer of thin plastic sheet and a layer of cardboard on top of plastic sheet were placed and clamped with large paper clips (Figure 3.41). This ensured the CFRP composite finished surface was smooth after curing, making it easier to apply strain gauges on the cured finished CFRP composite. The beams were left at room temperature for 7 days to cure before the test.

Thickness of the CFRP wraps for various specimens was varied because, for specimen RC-W67-T2.4-G1, RC-W133-T2.4-G1, and RC-W133-T2.4-G2, 2.4 mm thick CFRP sheets were bonded to the outer face of the bottom flange (which means three layers of MBrace CF160 or eight layers of Sikawrap Hex 230c). For specimen RC-W133-T1.2-G2, 1.2 mm thick CFRP sheets were used (which means four layers of Sikawrap Hex 230c). For specimen RC-W133-T0.6-G2, 0.6 mm thick CFRP sheets were used (which means two layers of Sikawrap Hex 230c). The lengths of CFRP sheets varied

by six mm from one layer to the next (for example, first layer was 1000 mm long, second layer was 994 mm long, and third layer was 988 mm long), to avoid the stress concentration at CFRP termination points. The width of the CFRP wrap was 67 mm for RC-W67-T2.4-G1 (Figure 3.42) and 133 mm for all the other RC specimens (Figure 3.43). CFRP laminates were installed with the fibers oriented in the beam's latitudinal direction (direction-3).

Subsequently, CFRP cross wraps (fiber oriented along the width of the beam, direction-1) were applied to the beam using the same CFRP application method. Five 50 mm wide cross wraps were applied on specimen RC-W67-T2.4-G1 with a 212.5 mm clear spacing in between (Figure 3.44). For the rest of the repaired corroded (RC) specimens, a 200 mm wide cross wrap was applied at the center (on the corrosion) and three 70 mm wide cross wraps on each side of the corrosion (Figure 3.45). The clear distance between each cross wraps was 70 mm. When MBrace CF160 was used, one layer of the dry fabric formed each cross wrap; and when Sikawrap Hex 230c was used, two layers of the dry fabric formed each cross wrap.

3.6 Instrumentation

The instruments used in these tests were: strain gauges (3 mm and 13 mm gauge length) to measure strain in steel and CFRP, linear potentiometers to measure beam's deflections, a manual hydraulic pump along with a 445 kN (100 kips) capacity loading jack, universal donut shaped load cell of 445 kN (100 kips) capacity, and two universal donut shaped load cells of 222 kN (50 kips) capacity to obtain the applied loads and reactions.

3.6.1 Strain gauges

The strain gauges (SG) used in this study was purchased by the OMEGA Engineering INC located in Unite Kingdom. The SGs used on steel surface was Model SGD-3/350-LY11. This SG is 3.2 mm long x 2.5 mm wide grid area, 350 ohms resistance, $\pm$0.25% tolerance, and 2.01% gauge factor. The SGs used on CFRP composite was Model SGD-13/1000-LY11. This model has 13 mm long x 7.2 mm wide grid area, 1000 ohms resistance, $\pm$0.35% tolerance, and 1.99% gauge factor.

SGs were used to study the composite action and load transfer between steel and CFRP composite. No SG was used on the CV specimen. For the specimen CC-G1, seven SGD-3/350-LY11 SGs were used. Figure 3.46 shows the locations of the SGs for specimen CC-G1. Two SGs (number 6 and 7) were installed at the center of the inner side of the bottom flange, one in the lateral direction (direction-1, shown by ▬), one in the longitude direction (direction-3, shown by •). Another two SGs (number 4 and 5) were installed at the same locations as SG6 and 7,but on the top surface of bottom flange (Figure 3.46). One SG (number 1) was applied in direction-3 at the mid-span on the bottom face of top flange, and two SGs (number 2 and 3) were applied on the web in direction-3. For each of the RC (rehabilated corroded) beams, five SGD-3/350-LY11 SGs were installed to the top surface of the bottom flange (shown by S1, S2, S3, S4, and S5 in Figure 3.47). Five SGD-13/1000-LY11 SGs were installed on the surface of CFRP at the same position of the SGD-3/350-LY11 SGs (shown as C1, C2, C3, C4, and C5 in Figure 3.47). For the specimen CC-G2, five SGD-3/350-LY11 SGs were applied at the same locations as was for RC specimens. Effect was made to locate SG S1 and SG C1 on the same vertical axes (direction 2) and same for others as well. However, it was impossible to achieve that and it is believed that locations for CFRP strain gauges (C1, C2, C3, C4, and C5) and its corresponding steel strain gauges (S1, S2, S3, S4, and S5) were not exactly on the same vertical aces (direction 2)

The surface of the steel beam/CFRP composite was grinded using a pneumatic grinder, and then rubbed with "MCA-1 M" Preparation Conditioner A. Then, the surface was rubbed again using "MN5A-1" Neutralizer. M-Coat A air-cruing polyurethane coating was applied to the surface of the steel/CFRP composite to accelerate the bonding. The SG was installed to the steel or CFRP composite surfaces using "M-Bond 200" adhesive. A polyethylene sheet was applied over the SG and pressed for approximately one minute to ensure the proper bonding. After making sure that the SG was securely bonded and would not detach from the applied surface, the polyethylene sheet was removed. Lastly, the gauge terminal was soldered with the conductors of the lead wire cable and coated using "M-Bond adhesive (catalyst-c)". All strain gauges were tested and checked thoroughly before and after repairing using a digital ohmmeter. Vishay Ltd. manufactured all the chemicals mentioned in this paragraph.

3.6.2 Linear potentiometers (LP)

Deflections at three points on the bottom surface of beam's bottom flange and one point on the vertical face of bottom flange of the steel beam were continuously monitored using linear potentiometers (LP) (Figure 3.48). The three LPs on the bottom surface of bottom flange had 10 cm (4 in.) stroke while the other one had 5 cm (2 in.) stroke. They were pre-calibrated in order to find the gauge factor.

3.6.3 Loading system

The load was applied by a manual hydraulic pump through a loading jack of 445 kN (100 kips) capacity. Figure 3.49 shows a sketch of the test setup. The capacity of the loading jack was 100 tons. Load data were acquired by the data acquisition system through the universal load cell. The load was applied by the 100 tons loading jack. The load was then transferred to the bearing plate, which is 700 mm long x 132 mm wide x 12 mm thick, and acted at the top center of the beam as marked before (Figure 3.50).

The specimen was supported on pin and roller supports (Figure3.49). The reaction was at the supports were recorded through two 50 kips load cells (Figure 3.49). The load cells were installed on to stiff wide beams as shown in Figure 3.51. All load cells were calibrated using 600 kN capacity (both tension and compression) Tinus Olsen Universal Testing Machine. Figure 3.52 to 3.54 show the calibration curve for each load cell.

3.6.4 Data acquisition system

The model of the analog input module was Data Scan 7021, manufactured by Adept Scientific located in England. Each of the modules had eight channels. Four analog input modules were connected in the data acquisition system. A total 8, 14, 13 and 18 data channels were required to collect the data for the CV, CC-G1, CC-G2, and fixed RC specimens respectively. The local measurement speed was set to be one reading per second. Data collection was facilitated using Dalite software, recording all readings electronically into a computer file (Figure 3.55).

3.6.5 Test set-up

Test setup is shown in Figure 3.49 and 3.50. After the CFRP composite air-dried for seven days, the location of the support, loading point, linear potentiometers (LP), lateral support, and steel round blocks were marked. The specimen was then placed on the pin and roller supports (Figure 3.49).

Steel angles were connected to the frame to support the LPs, which were adjusted and placed at their marked positions. All instruments (strain gauges, linear potentiometers, load cells) were checked and connected to the data acquisition panel, which was connected to the computer to record all readings. Figure 3.56 and 3.57 show the sketch of test set up of specimens of group1 and group2, respectively. The load was applied until the specimen failed. Figure 3.58 to Figure 3.75 illustrate the testing process for all group 1 and 2 specimens.

3.7 Summary

This chapter described the specimens (configuration, materials, and fabrication), instrumentation, experimental setup, loading procedure, and the rehabilitation scheme using CFRP laminates.

Table 3.1: Test matrix

Group		1				2				
	TS	CV-G1	CC-G1	RC-W67-T2.4-G1 (4 layers)	RC-W133-T2.4-G1 (4 layers)	CV-G2	CC-G2	RC-W133-T2.4-G2 (4 layers)	RC-W133-T1.2-G2 (2 layers)	RC-W133-T0.6-G2 (1 layers)
Corrosion			Y	Y	Y		Y	Y	Y	Y
Bearing plate under jack	Y	Y	Y	Y	Y	Y	Y	Y	Y	Y
Lateral supports		Y	Y	Y[1]	Y	Y	Y	Y	Y	Y
Steel round blocks		Y	Y	Y	Y	Y	Y	Y	Y	Y
Web stiffeners						Y	Y	Y	Y	Y
Flange stiffener						Y	Y	Y	Y	Y
Filler (Putty)				Y						
Filler (CFRP)					Y			Y[2]	Y[2]	Y[2]
2.4 mm thick CFRP sheets (67mm wide)				Y						
2.4 mm thick CFRP sheets (133 mm wide)					Y			Y[2]		
1.2 mm thick CFRP sheets (133 mm wide)										Y[2]
0.6 mm thick CFRP sheets (133 mm wide)									Y[2]	
Cross wraps (50 mm wide)				Y						
Cross wraps (200 mm and 70 mm wide)					Y			Y[2]	Y[2]	Y[2]

[1] 75mm wide lateral supports were provided only on the top of the flange, see Figure 3.50 for details
[2] Sikawrap Hex 230c was used instead of MBrace CF160

Table 3.2: Mechanical properties of steel beam

	Modulus of Elasticity (GPa)	Ultimate Stress (MPa)	First Yield Stress (MPa)
Victoria 1	256	530	417
Victoria 2	239	537	438
Victoria 3	180	533	432
Victoria 4	219	540	447
Border 1	181	543	432
Border 2	247	573	436
Border 3	232	602	447
Border 4	201	558	457
Average	219	552	438

Average E from Victoria = 224 GPa
Average E from Border = 225 GPa

Average yield strength from Victoria = 535GPa
Average yield strength from Border = 569 GPa

Average ultimate strength from Victoria = 434GPa
Average ultimate strength from Border = 443 GPa

Table 3.3: Material properties for composite strengthening system as reported by manufacture

Material	Tensile Strength (MPa)	Tensile Modulus (GPa)	Poisson Ratio	Ultimate Rupture Strain	Flexural Strength (MPa)	Flexural Modulus (GPa)	Thickness (mm/layer)
MBrace Primer[1]	14.5	0.717	0.48	40%	24.1	0.595	N/A
MBrace Putty[2]	12	1.8	0.48	7%	26.2	0.895	N/A
MBrace Saturant[3]	54	3.0	0.40	3.5%	138	3.724	0.67
MBrace CF 160[4]	3800*	227	N/A[6]	1.67%	N/A[6]	N/A[6]	0.79
Sikawrap Hex 230c[5]	3450*	231	0.246	1.5%	N/A[6]	N/A[6]	0.29

* The ultimate tensile strength measured in primary direction of CFRP laminate

[1] BASF (2006, b)
[2] BASF (2006, c)
[3] BASF (2006, d)
[4] BASF (2006, a)
[5] Sika Canada Inc. (2007)
[6] N/A means not available.

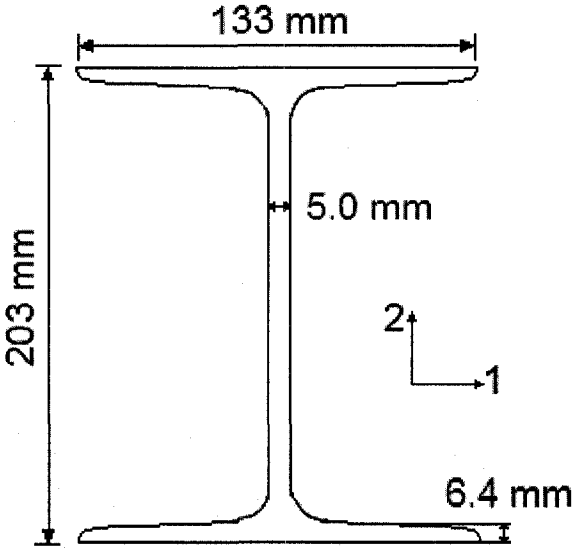

Figure 3.1: Cross-section of W200x21 beam

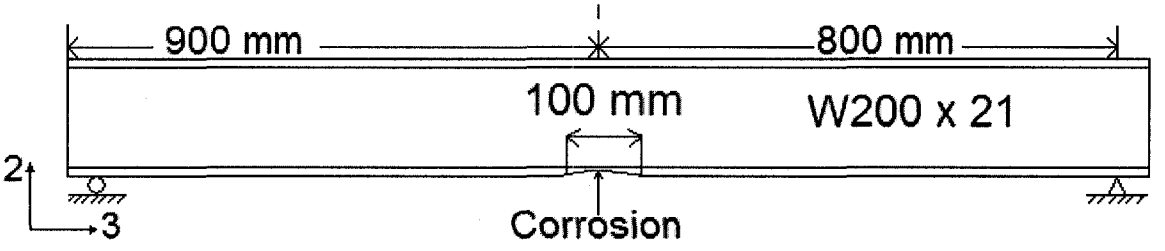

Figure 3.2: Location of the corrosion

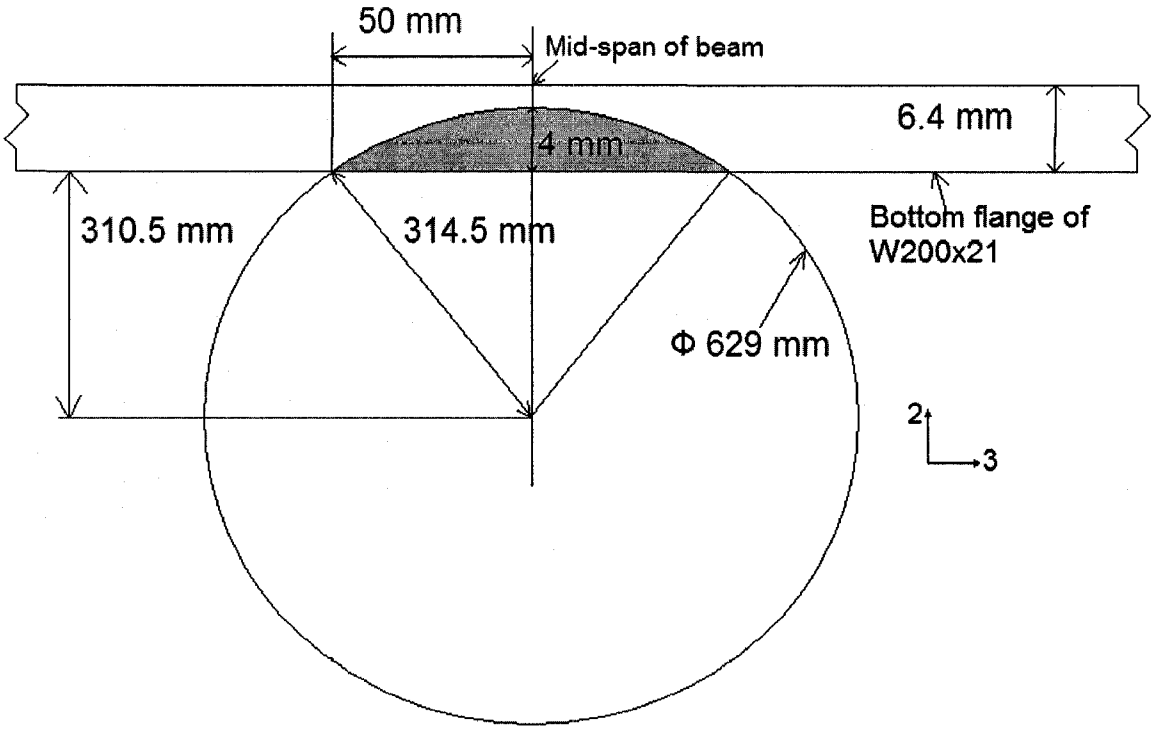

Figure 3.3: Detail of the corrosion geometry (cross-sectional view)

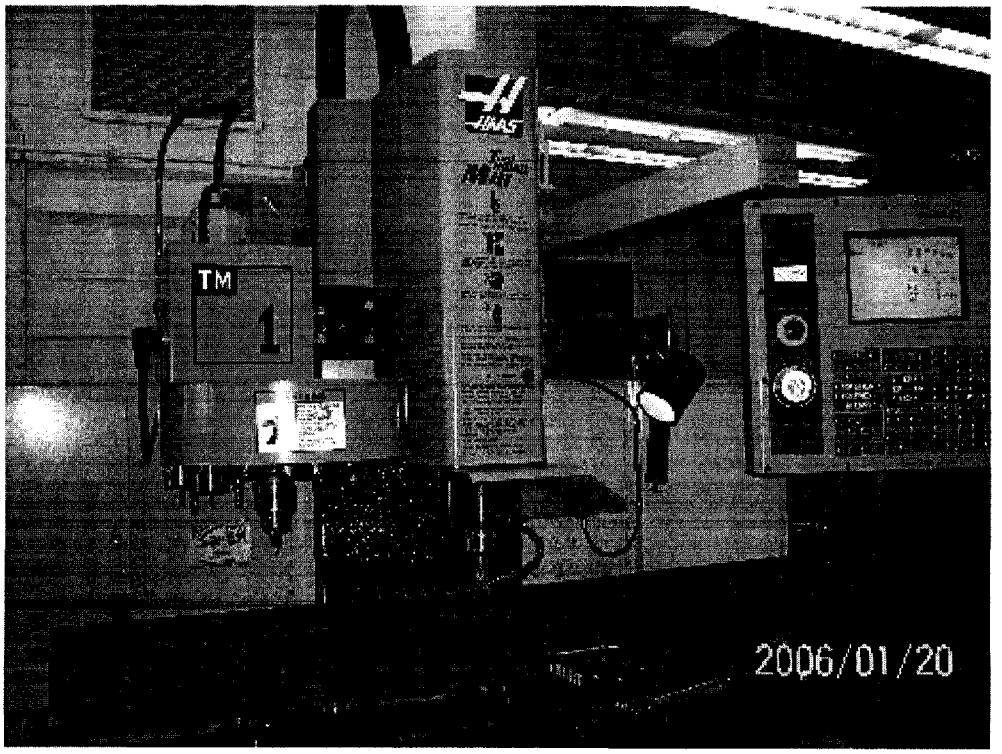

Figure 3.4: HASS TOOL ROOM MILL TM1 machine

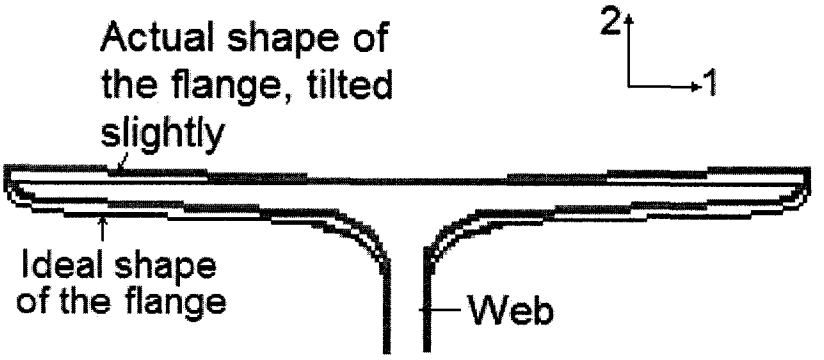

Figure 3.5: Actual shape of the flange

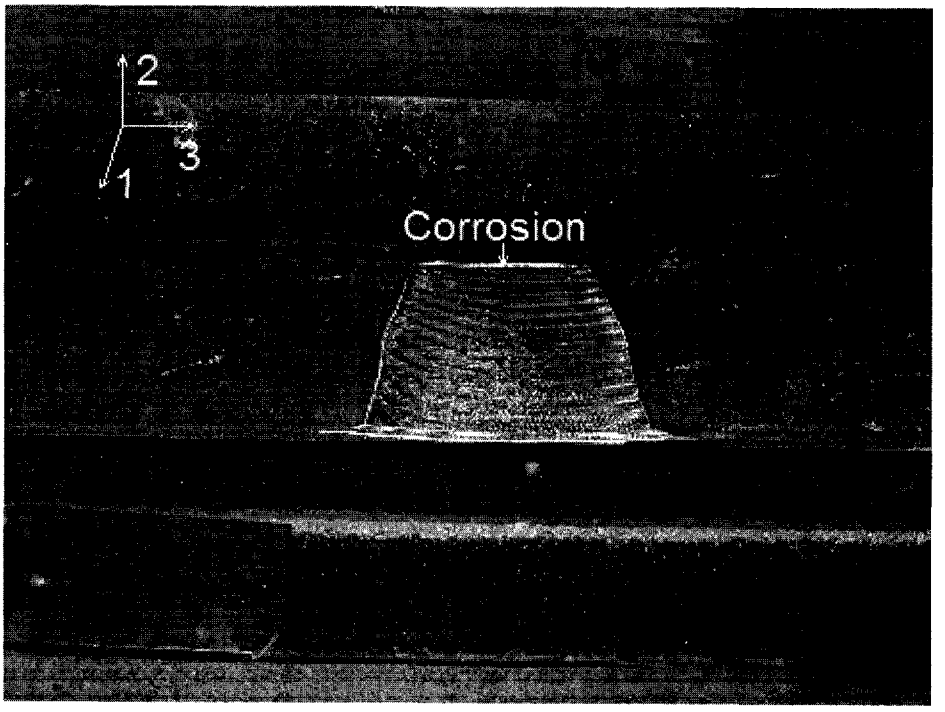

Figure 3.6: Photo of the corrosion (plan view)

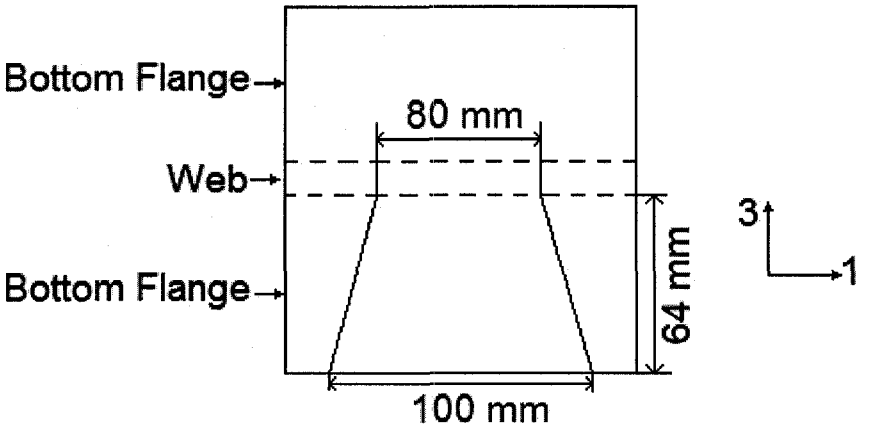

Figure 3.7: Plan view of the corrosion

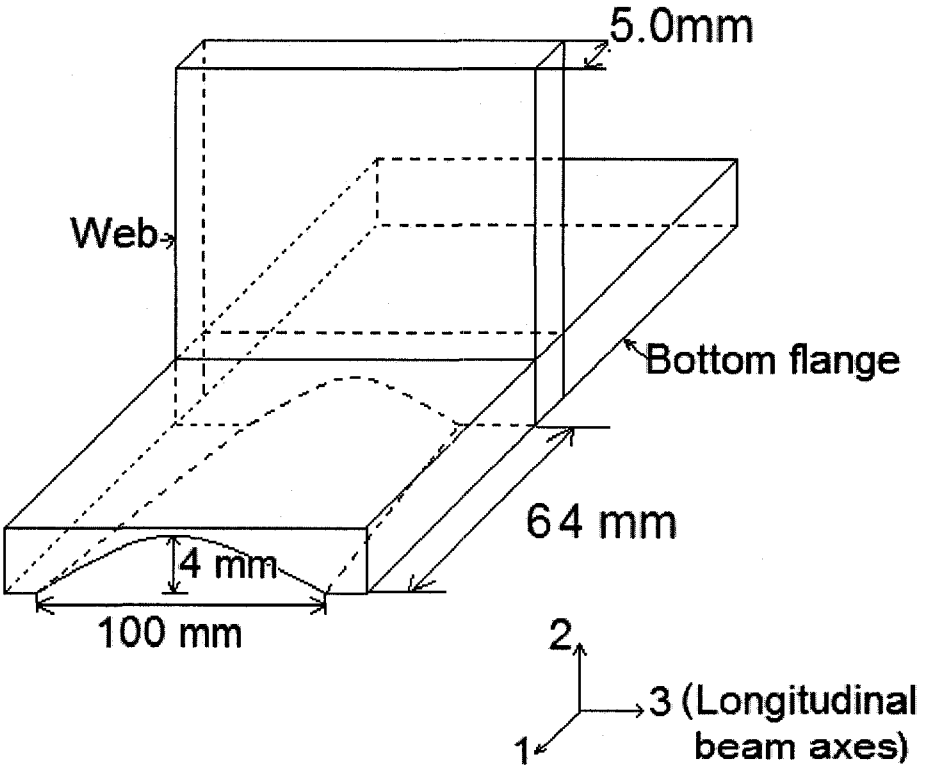

Figure 3.8: Three-dimensional sketch of the corrosion

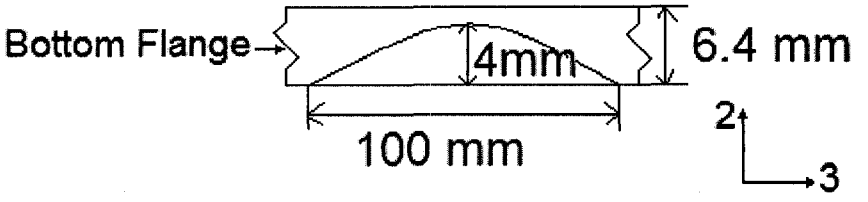

Figure 3.9: Two-dimensional view of the corrosion at the outer edge of the flange

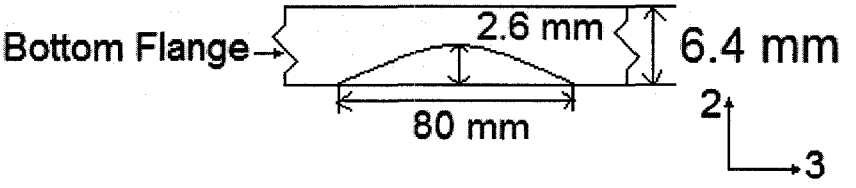

Figure 3.10: Two-dimensional view of the corrosion at the web-flange intersection

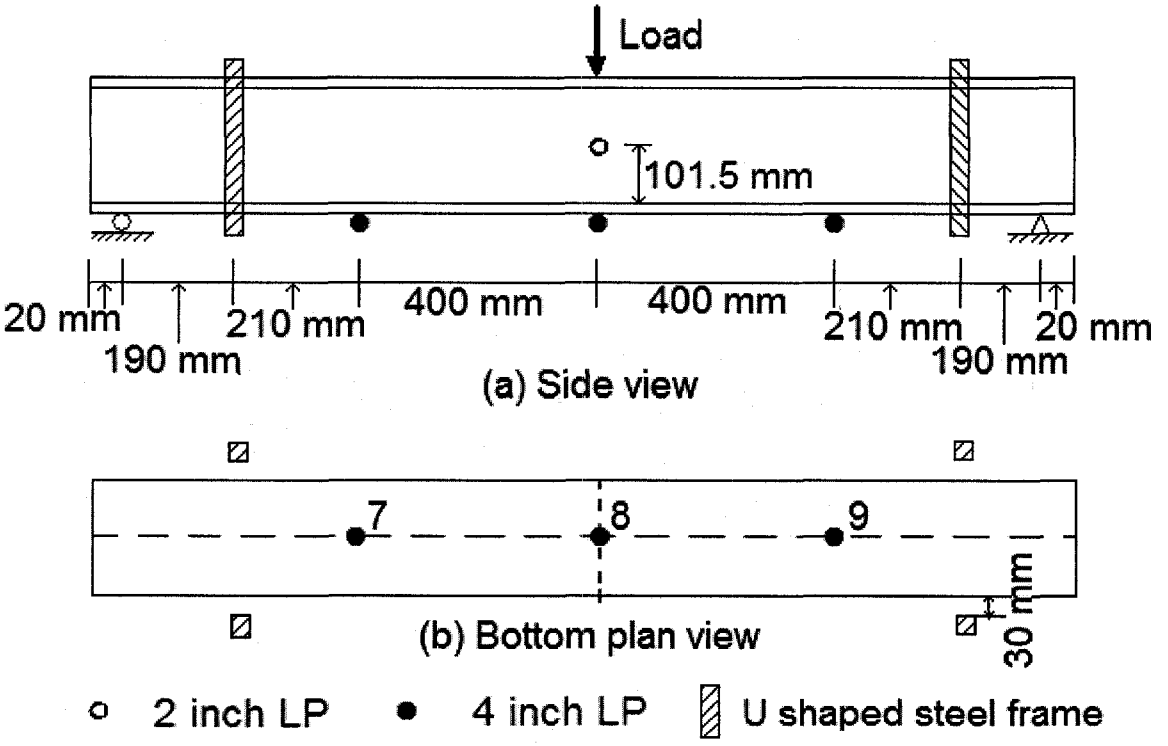

Figure 3.11: A sketch of test setup for TS
(a) Side view
(b) Bottom plan view

Figure 3.12: Test setup for TS

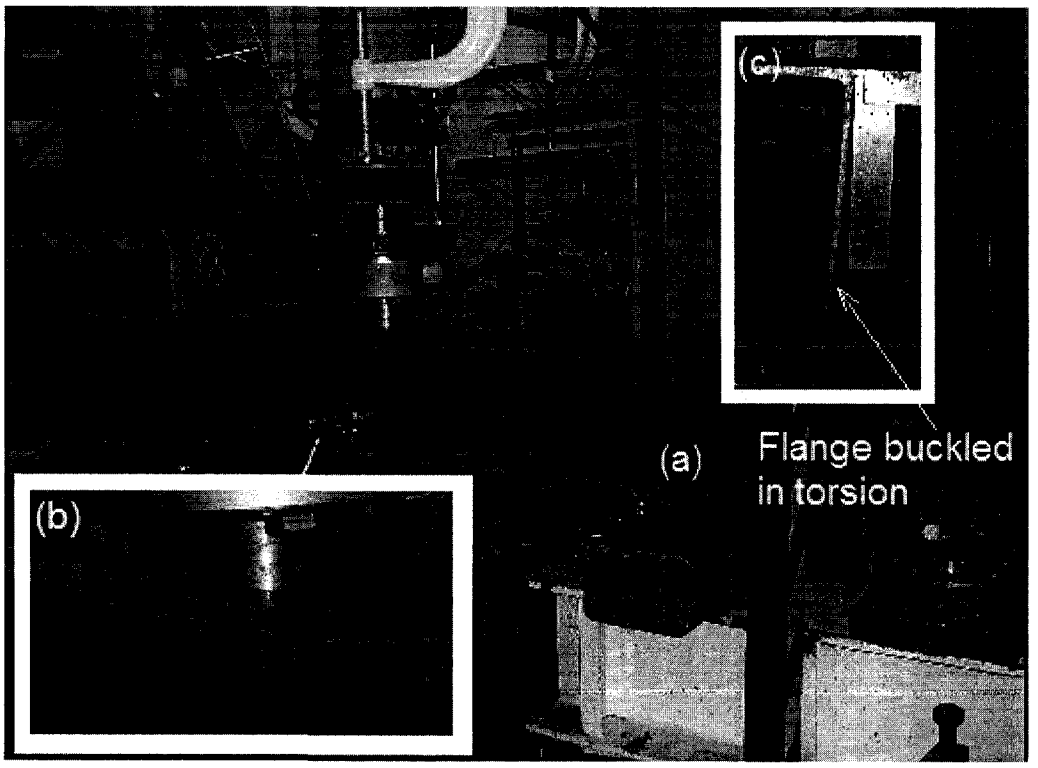

Figure 3.13: (a) Specimen TS after completion of test
(b) Flange buckled under the load
(c) Side view of the beam shows lateral torsion buckling

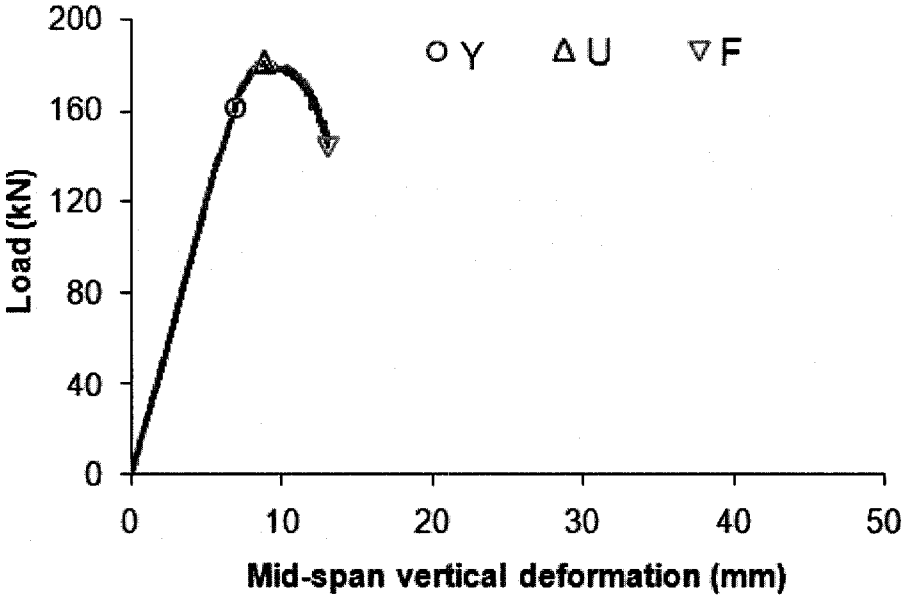

Figure 3.14: Load vs. mid span vertical deformation for TS

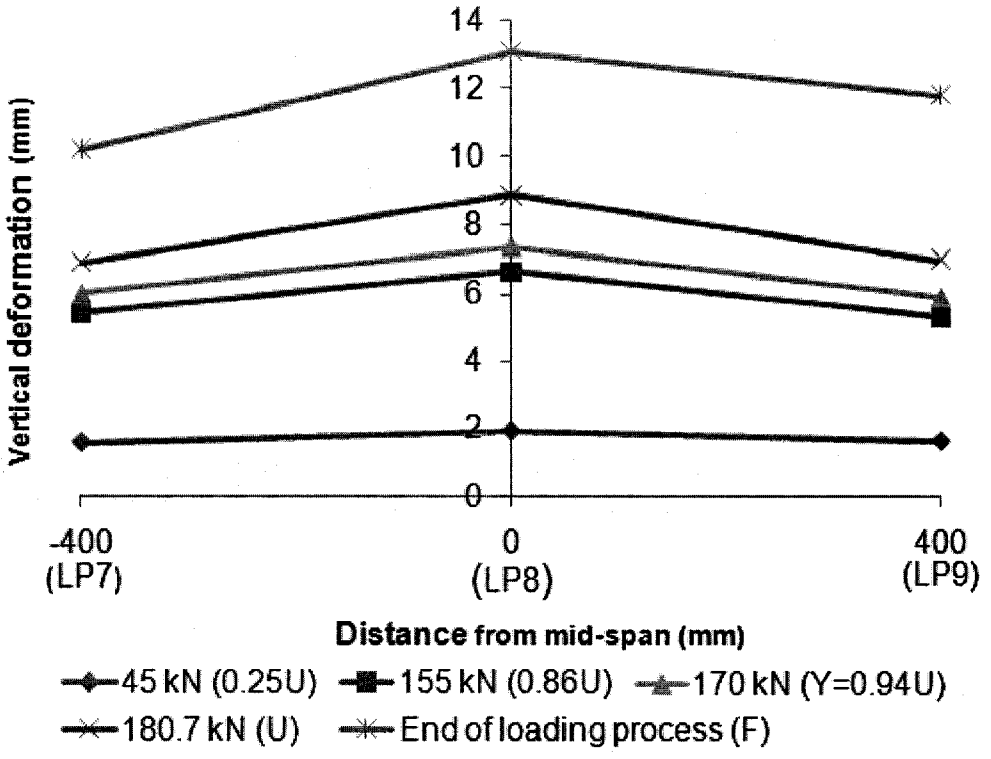

Figure 3.15: Vertical deformation response for TS

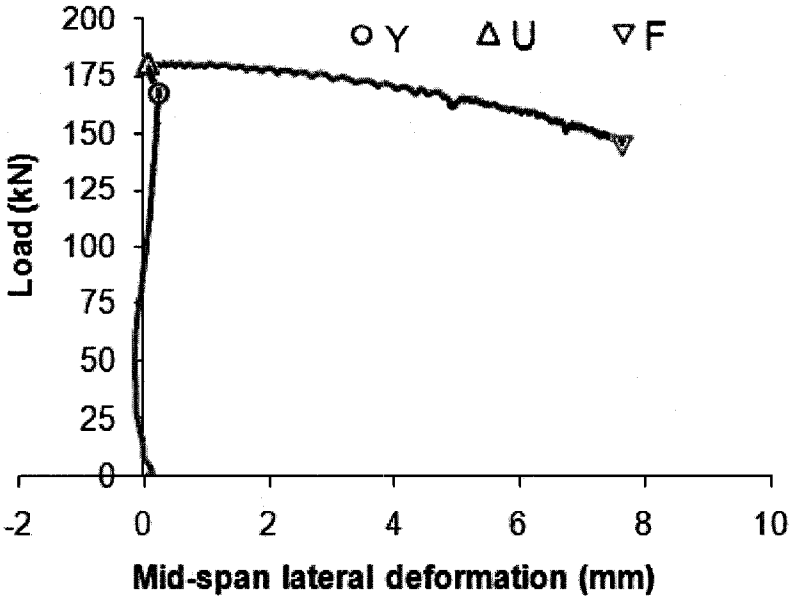

Figure 3.16: Load vs. mid span lateral deformation TS (P5)

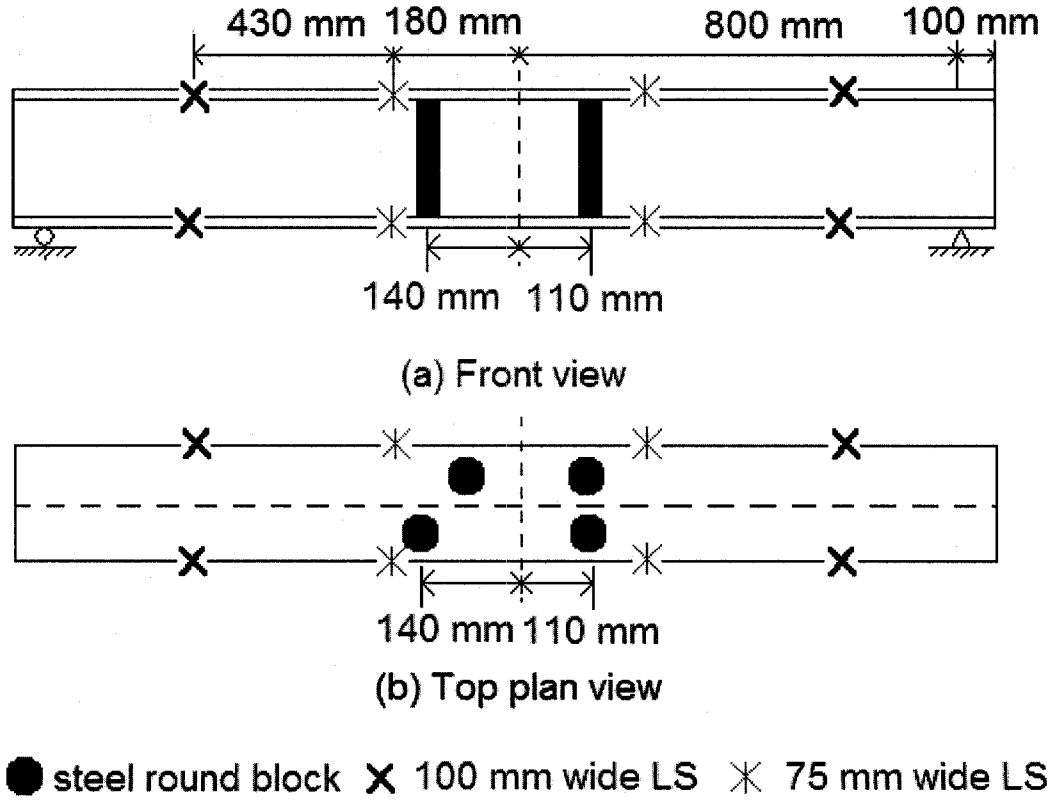

Figure 3.17: Locations of lateral supports and steel blocks
(a) Front view
(b) Top plan view

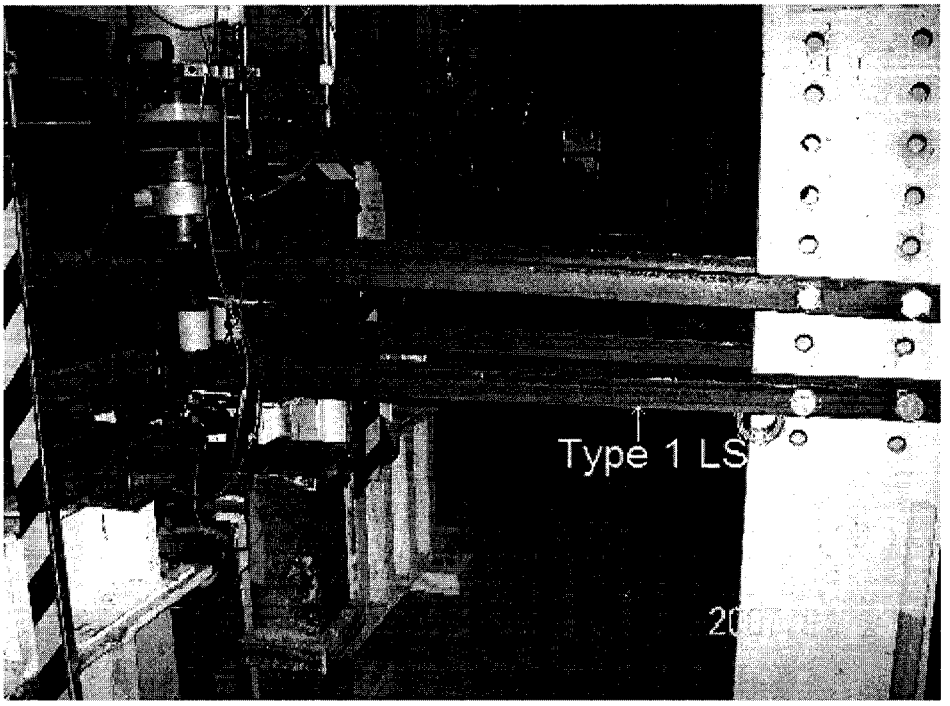

Figure 3.18: 75 mm wide later support

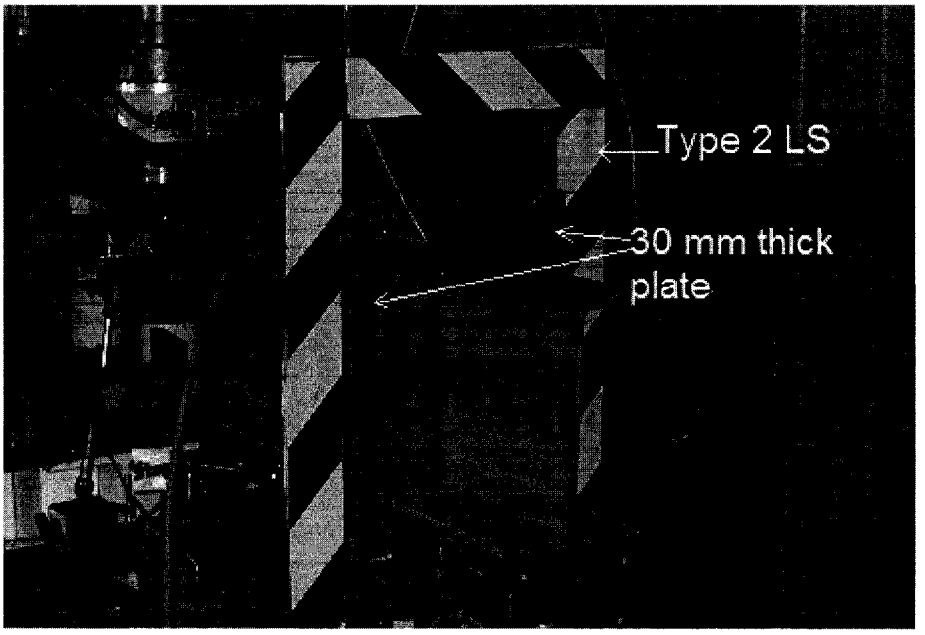

Figure 3.19: 100 mm wide later support

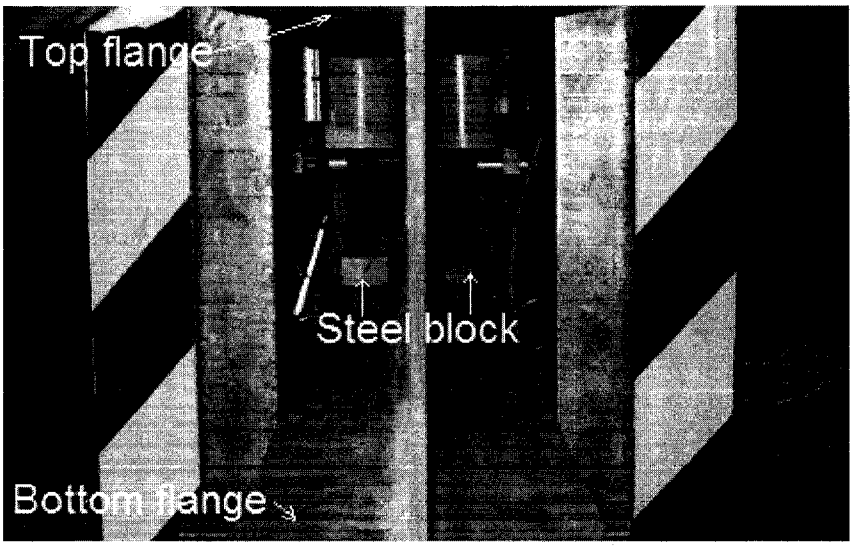

Figure 3.20: Steel blocks

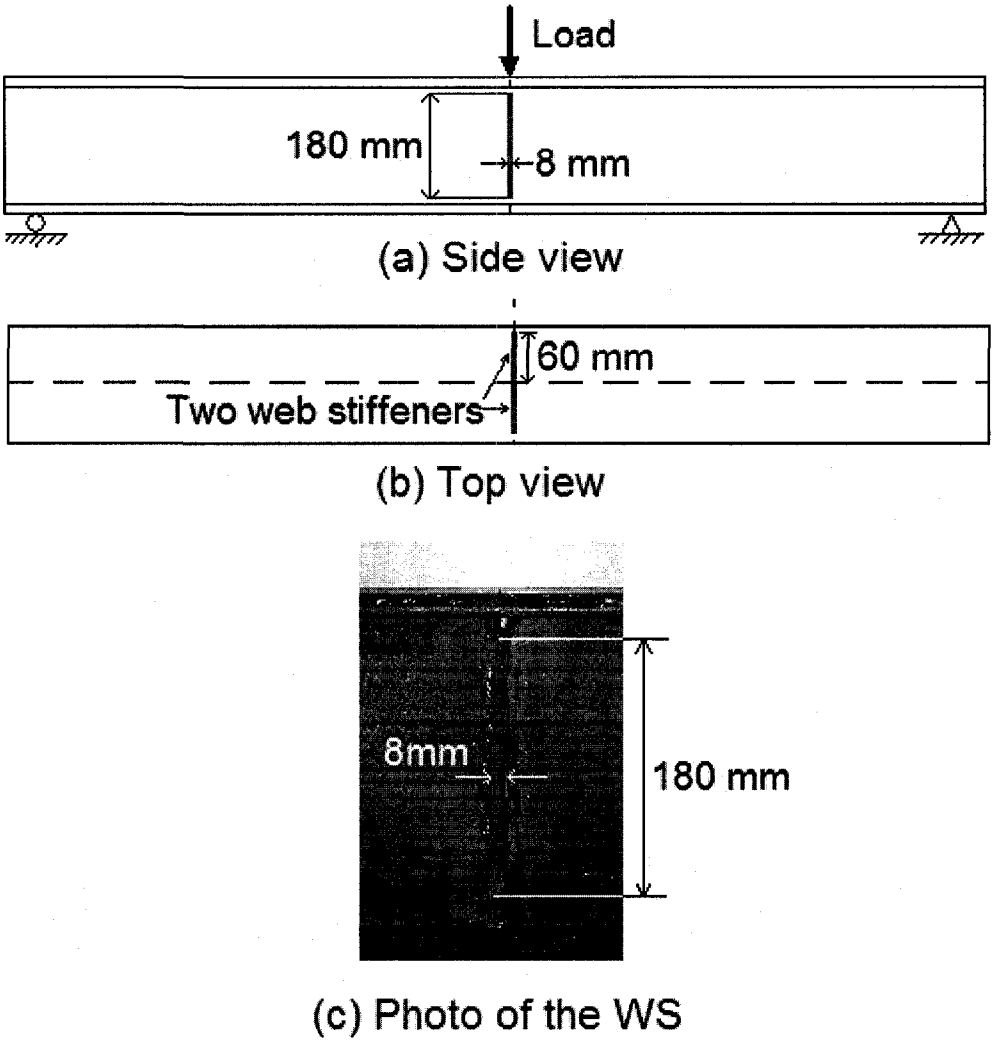

Figure 3.21: Web stiffness
(a) Side view
(b) Top view
(c) Photo of the WS

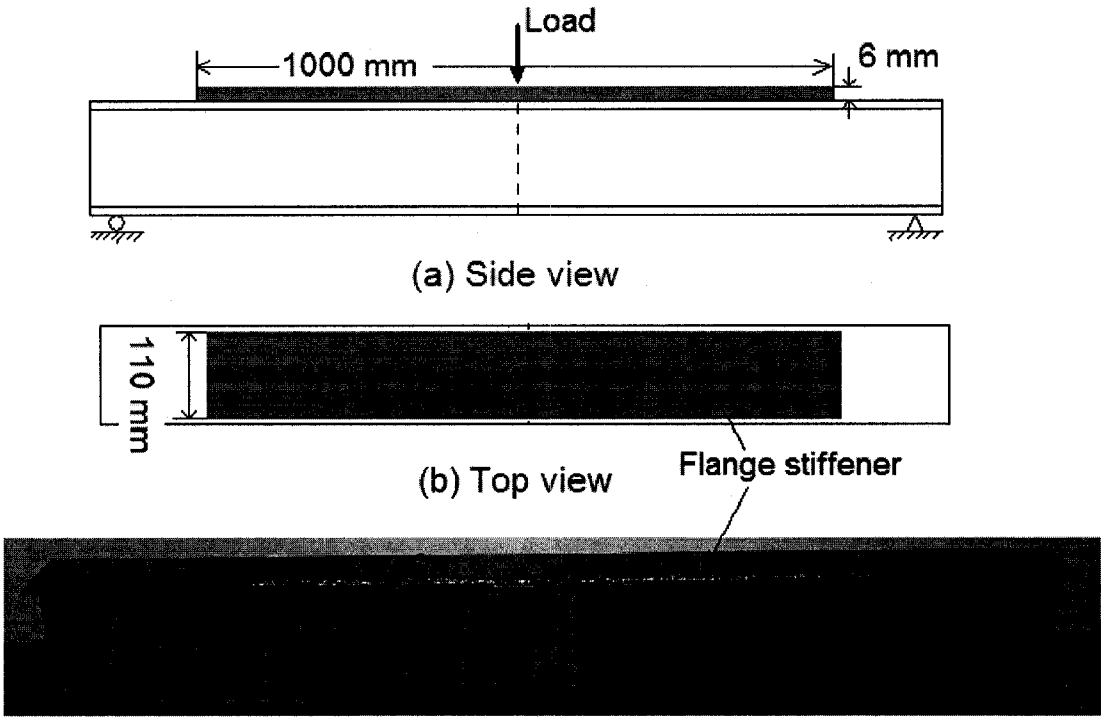

Figure 3.22: Flange stiffeners
(a) Side view
(b) Top view
(c) Photo of the plate

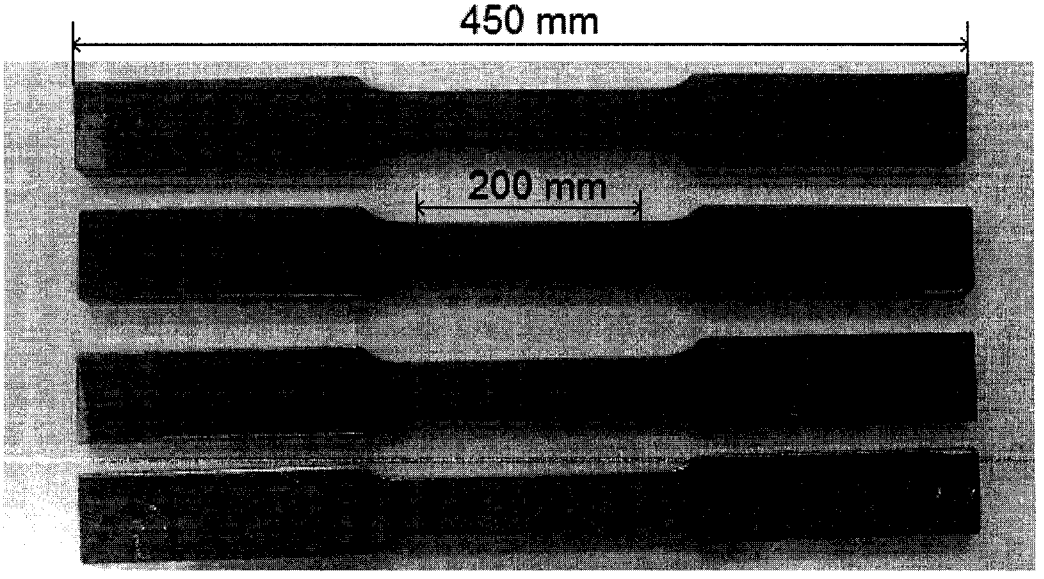

Figure 3.23: Steel coupon specimens

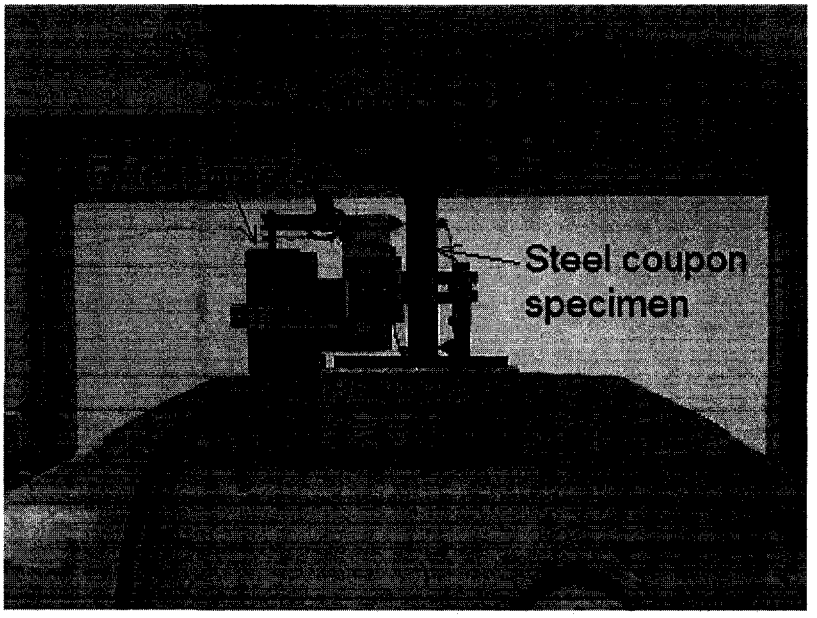

Figure 3.24: Tensile test setup for coupon tests

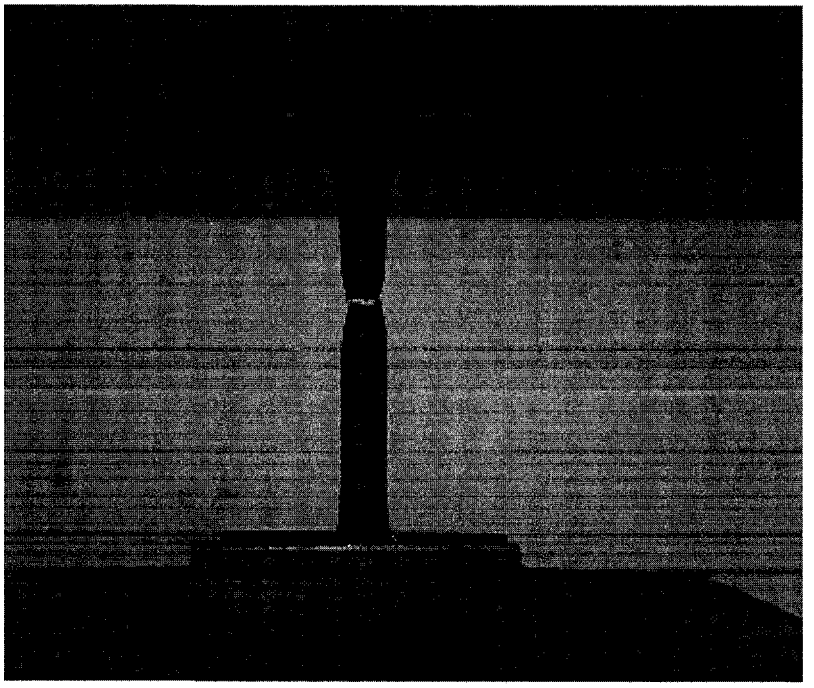

Figure 3.25: Failed steel coupon specimen

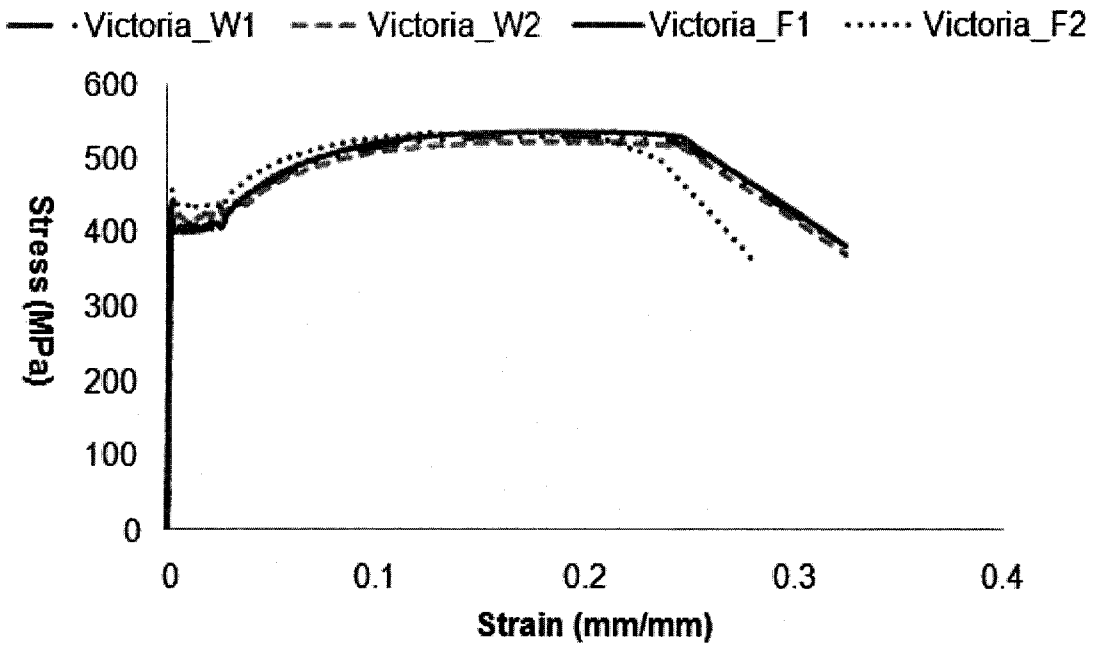

Figure 3.26: Stress vs. strain curve for steel tensile test (Victoria Steel Corporation)

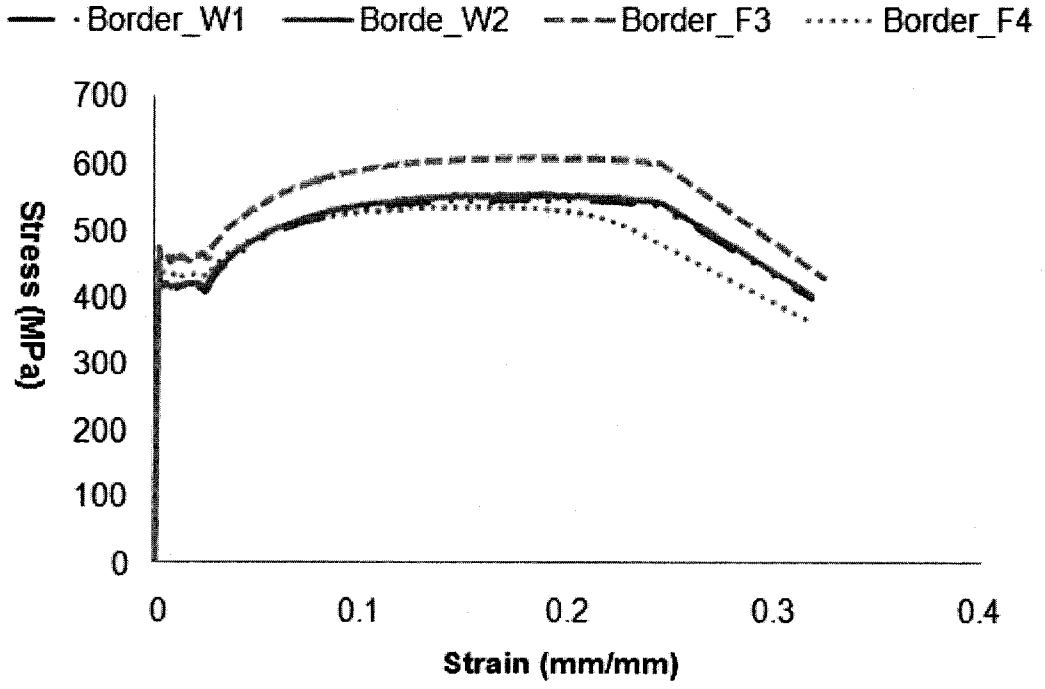

Figure 3.27: Stress vs. strain curve for steel tensile test (Border Steel Ltd.)

Figure 3.28: CFRP tensile test set-up

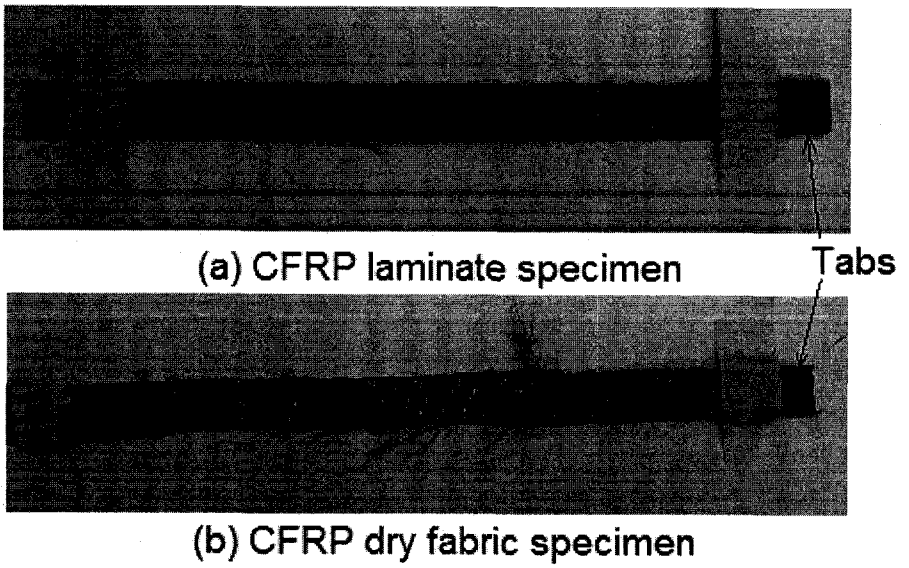

Figure 3.29: CFRP coupon specimens
(a) CFRP laminate specimen
(b) CFRP dry fabric specimen

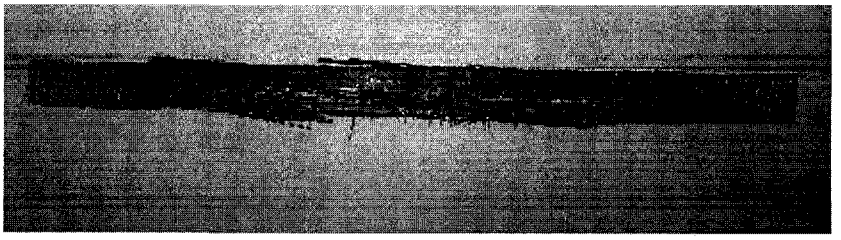

(a) CFRP laminate specimen

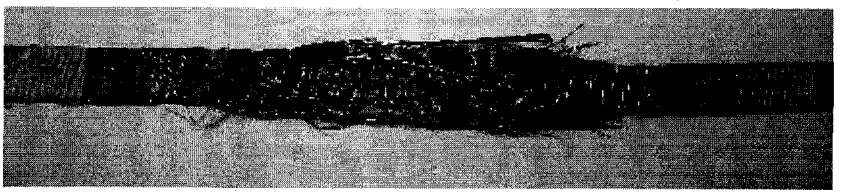

(b) CFRP dry fabric specimen

Figure 3.30: CFRP failed specimens
(a) CFRP laminate specimen
(b) CFRP dry fabric specimen

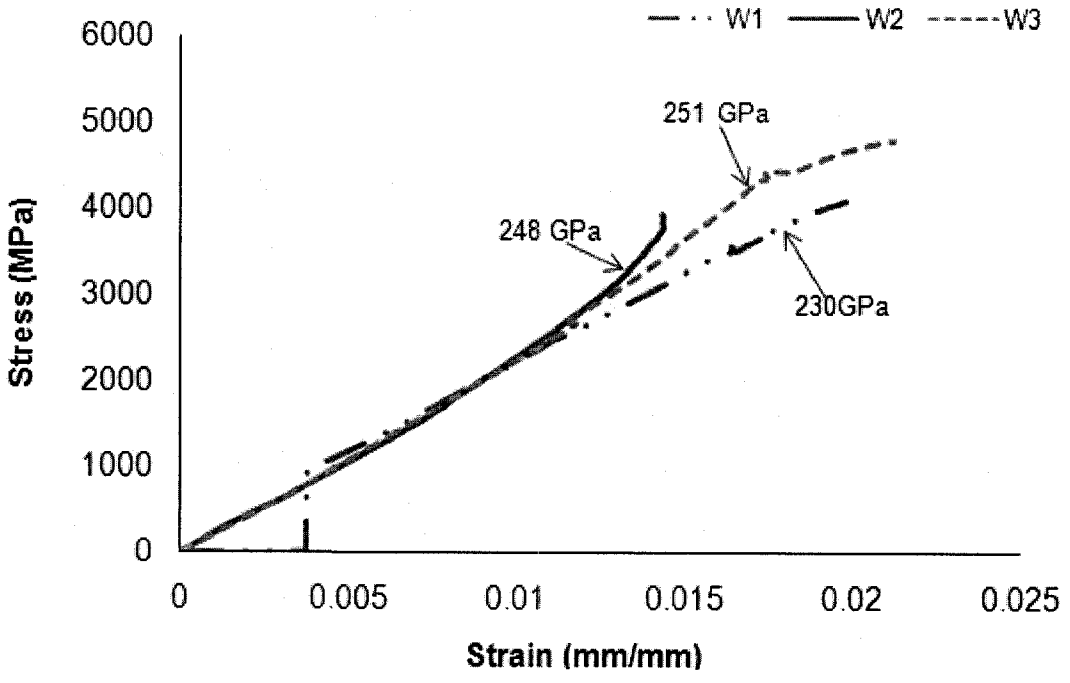

Figure 3.31: Stress-strain relationships obtained from CFRP laminate specimens

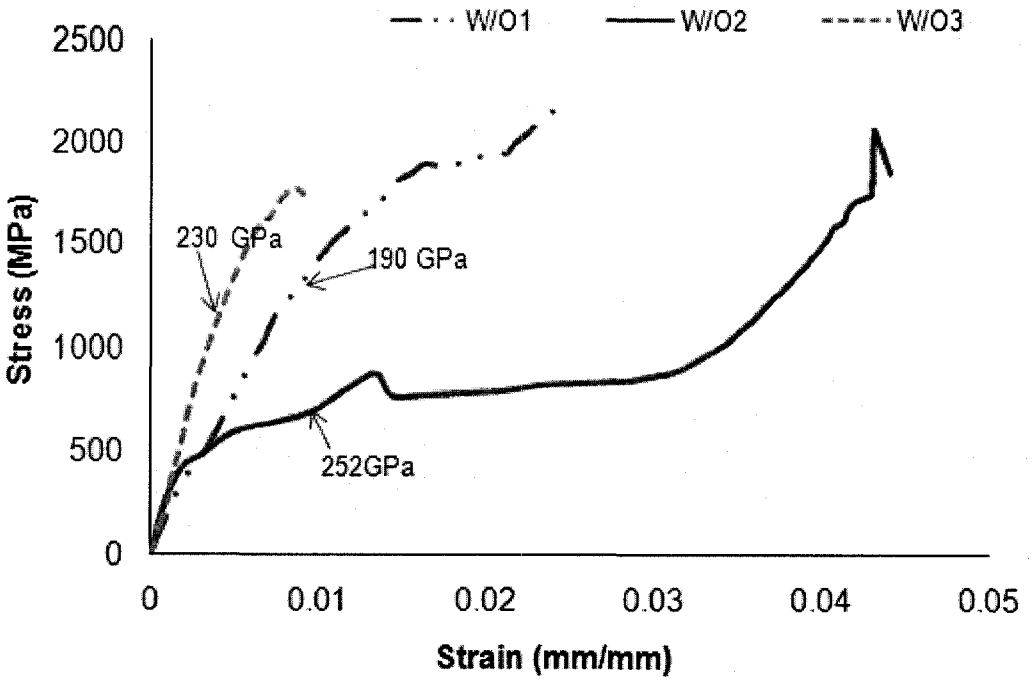

Figure 3.32: Stress-strain relationships obtained from CFRP dry fabric specimens

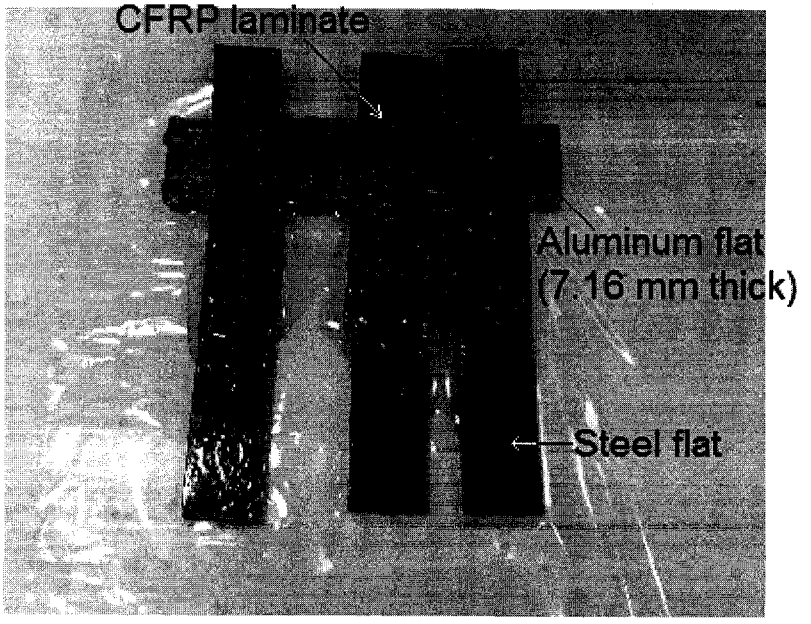

Figure 3.33: Epoxy shear coupon specimens (curing)

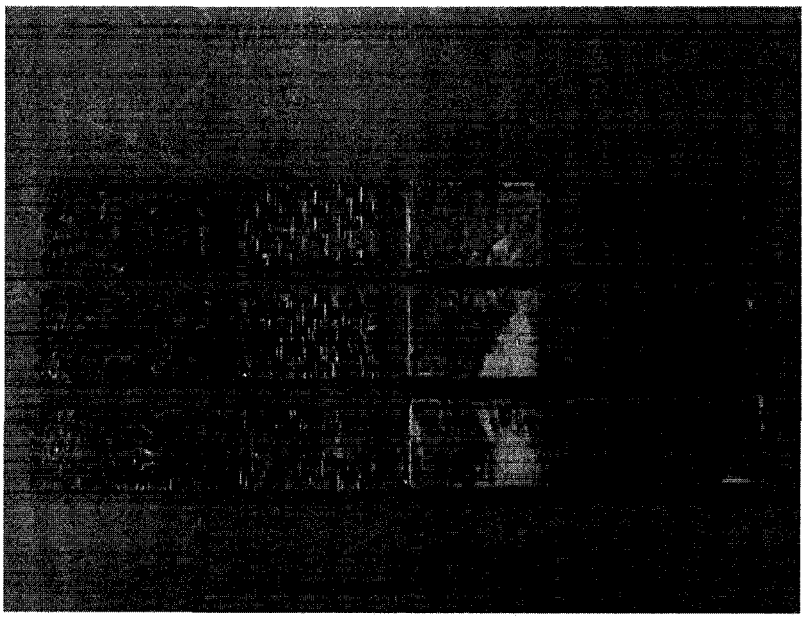

Figure 3.34: Failed epoxy shear coupon specimens

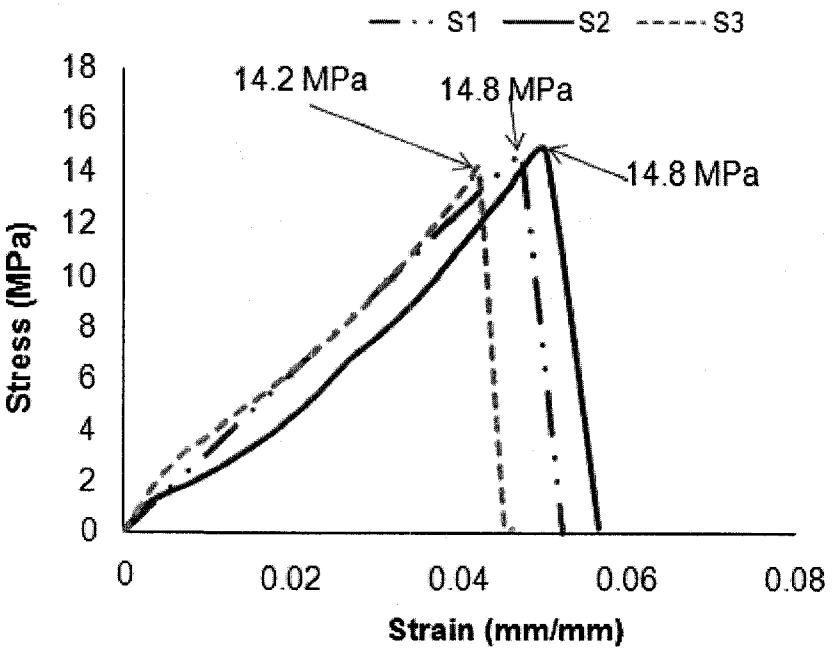

Figure 3.35: Shear stress-strain behaviors of epoxy (MBrace Saturant)

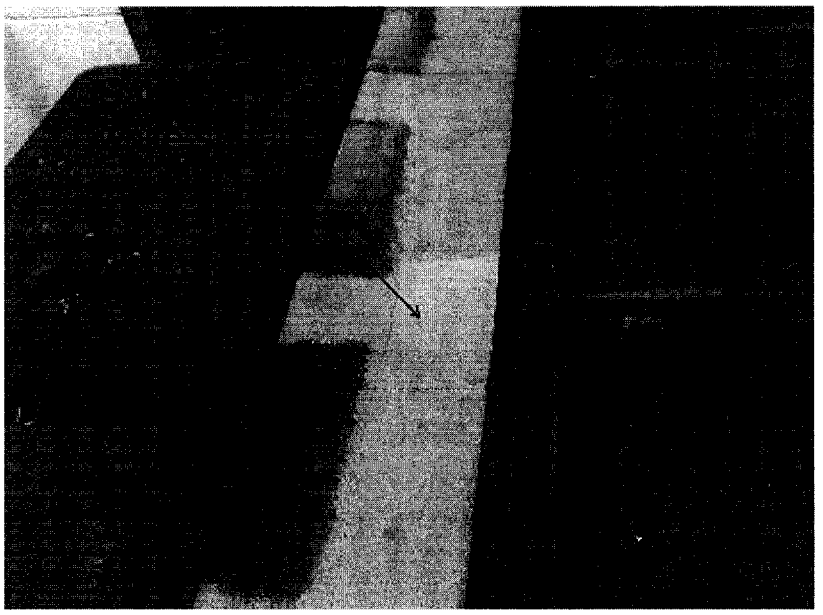

Figure 3.36: White metal finish after sand blasting

Figure 3.37: After applying MBrace Primer

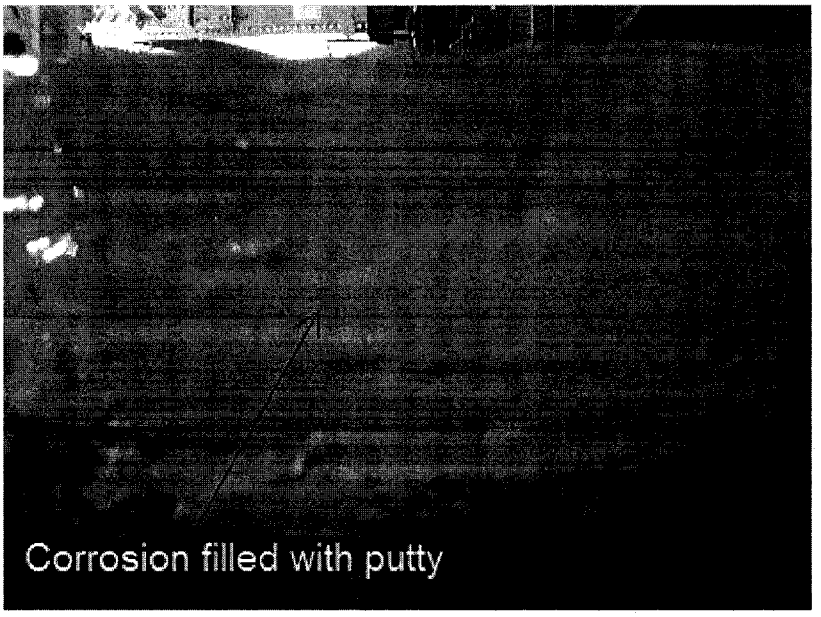

Figure 3.38: Corrosion filled with MBrace Putty

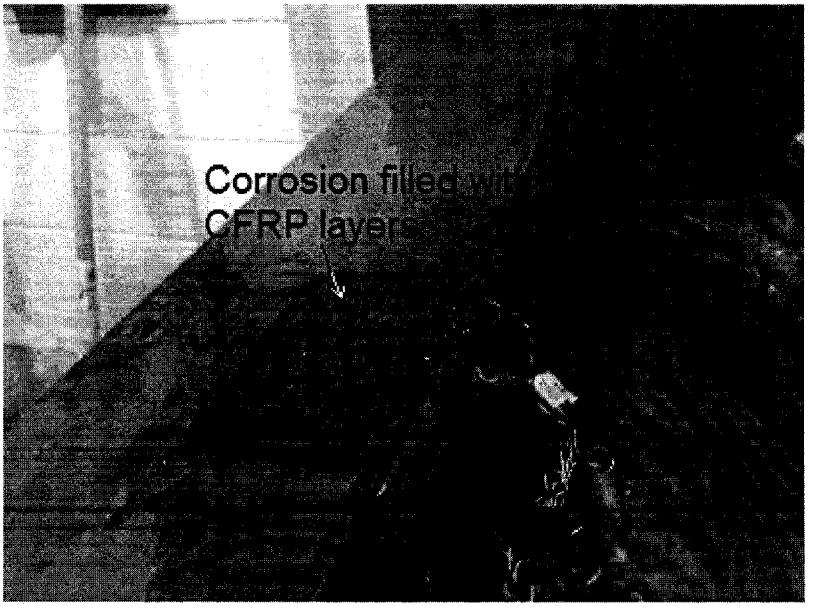

Figure 3.39: Corrosion filled with CFRP

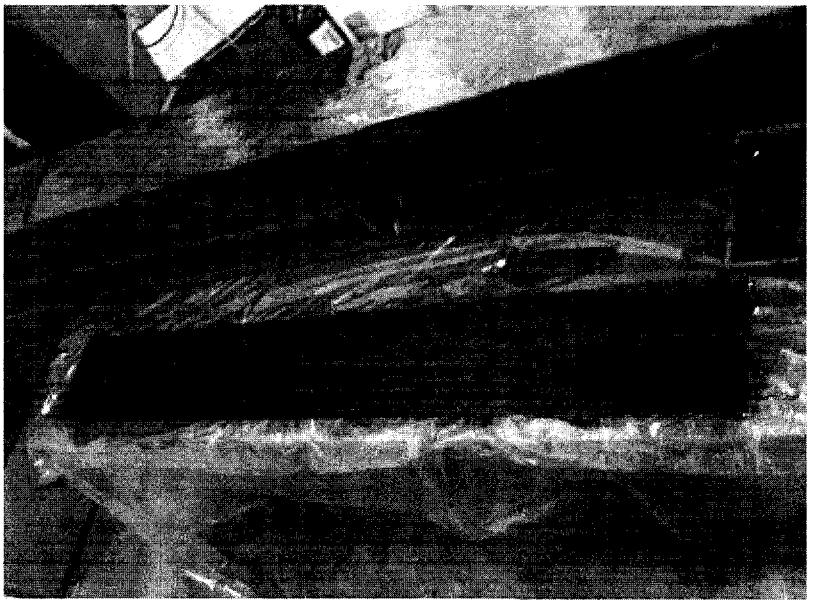

Figure 3.40: CFRP saturated in Saturant

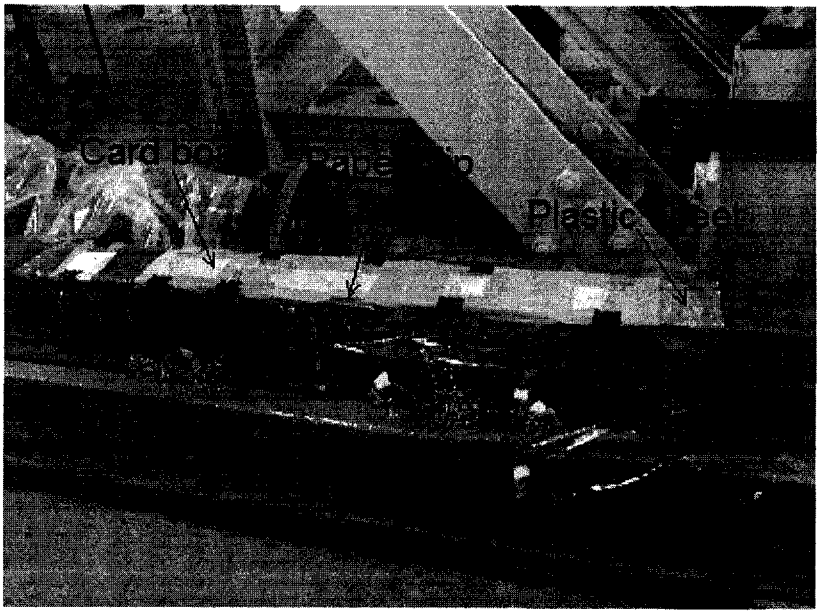

Figure 3.41: Curing of the CFRP

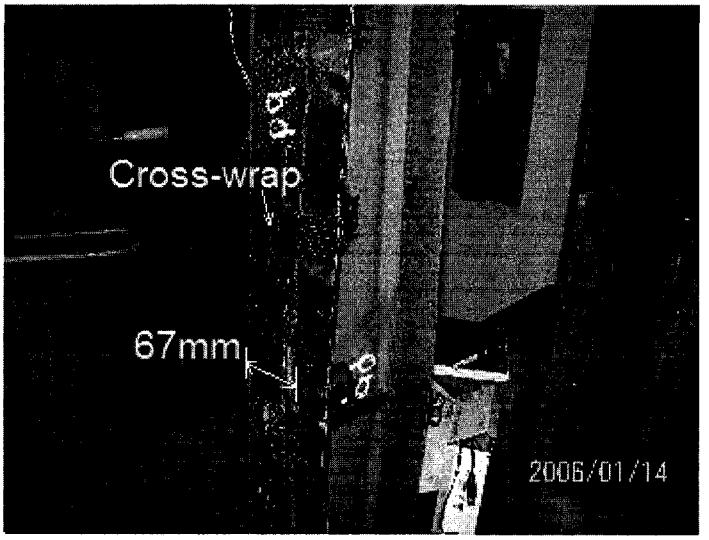

Figure 3.42: Specimen RC-W67-T2.4-G1 with 67 mm wide CFRP composite

Figure 3.43: Specimen with 133 mm wide CFRP composite

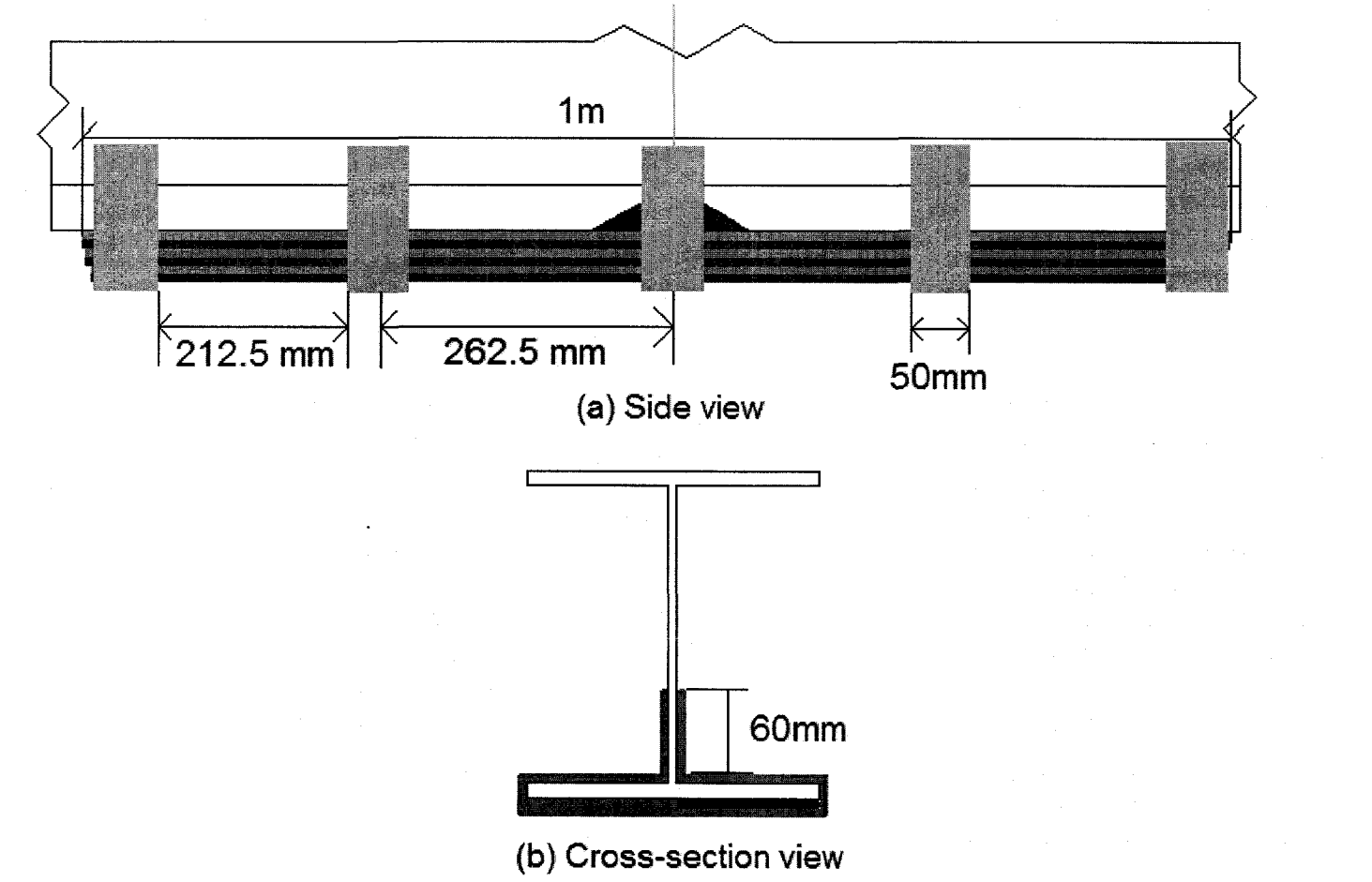

Figure 3.44: Cross wrap for RC-W67-T2.4-G1
(a) Side view
(b) Cross-section view

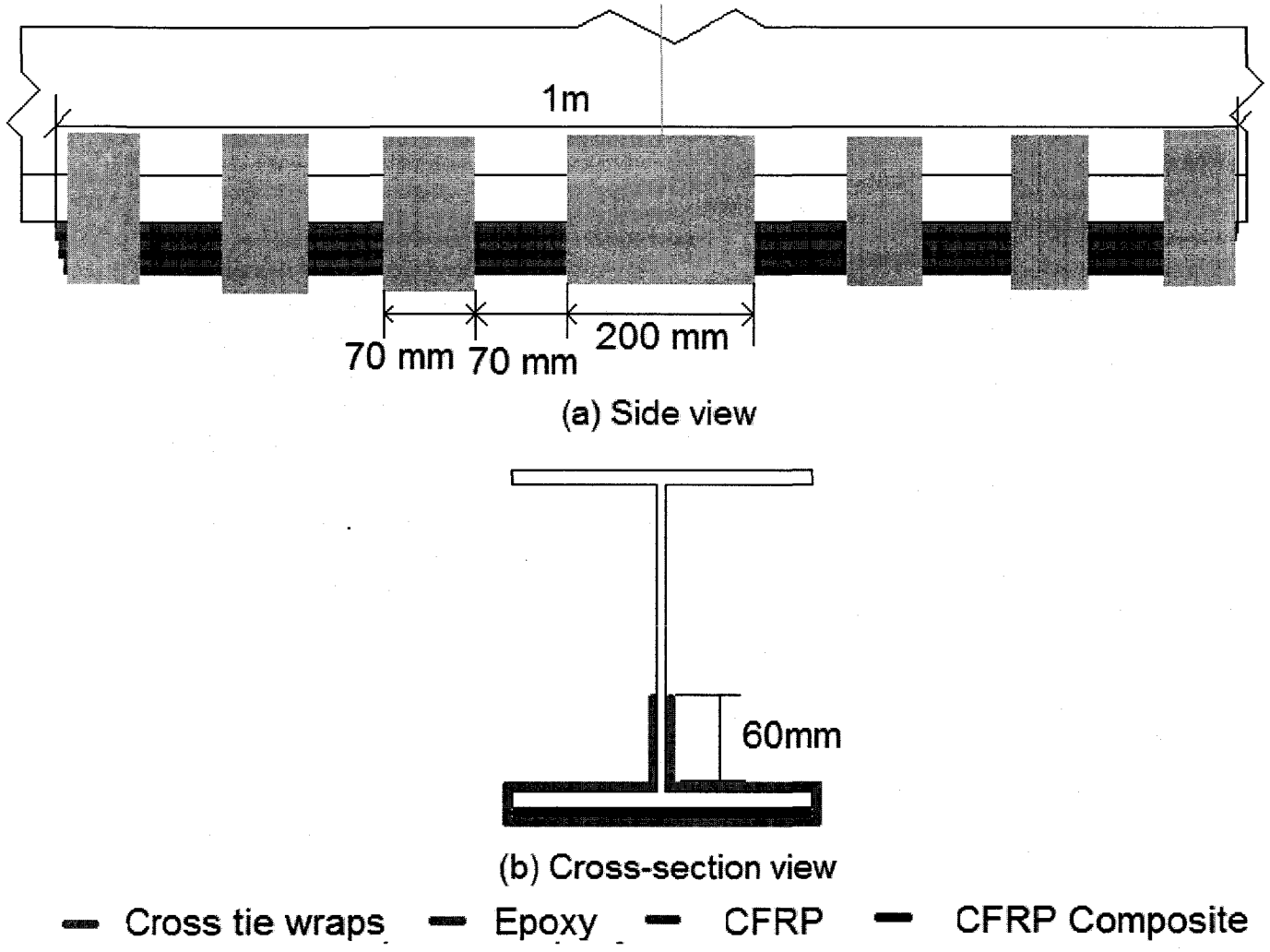

Figure 3.45: Cross wraps for RC specimens except RC-W67-T2.4-G1
(a) Side view
(b) Cross-section view

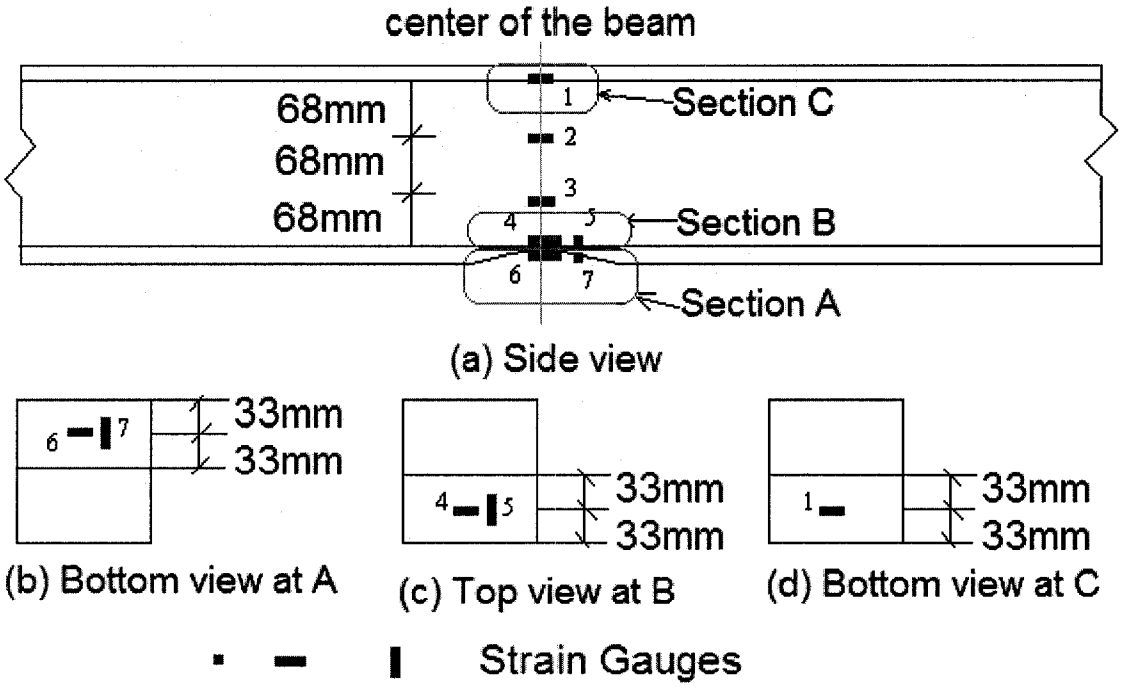

Figure 3.46: Strain gauge locations for CC-G1
(a) Side view
(b) Bottom view at A
(c) Top view at B
(d) Bottom view at C

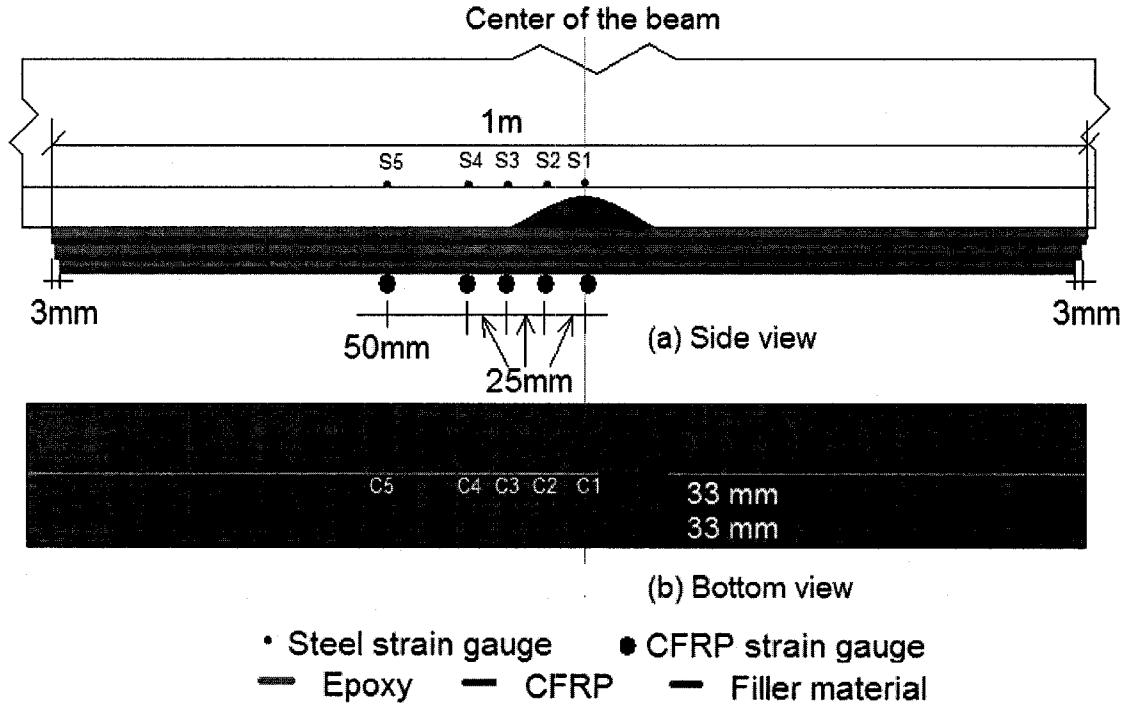

Figure 3.47: Strain gauge locations for all RC specimens of G1 and all specimens of G2
(a) Side view, and (b) Bottom view

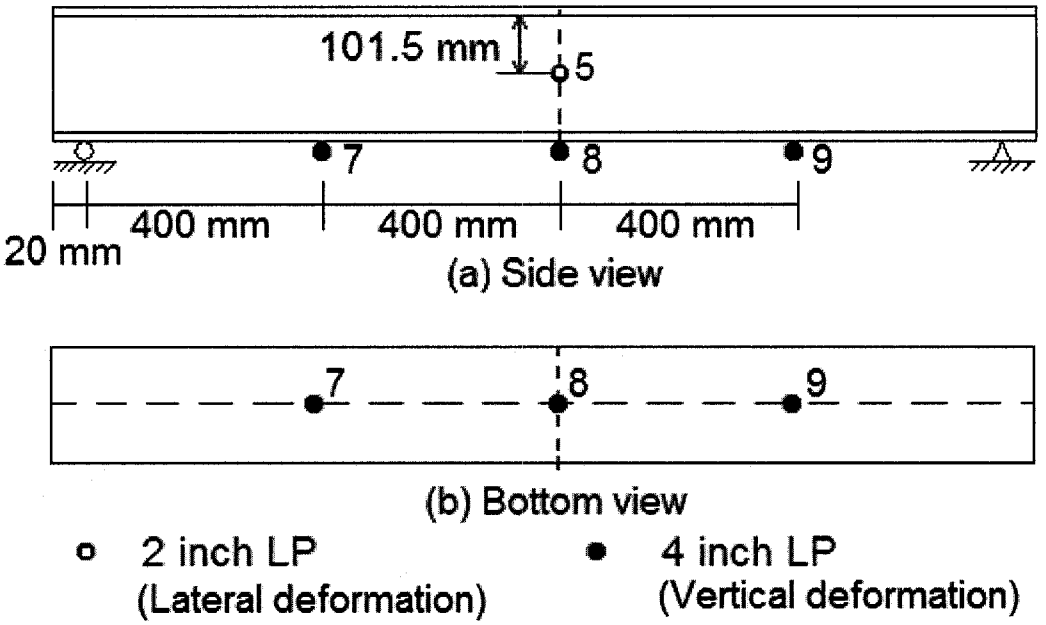

Figure 3.48: Locations for linear potentiometers
(a) Side view
(b) Bottom view

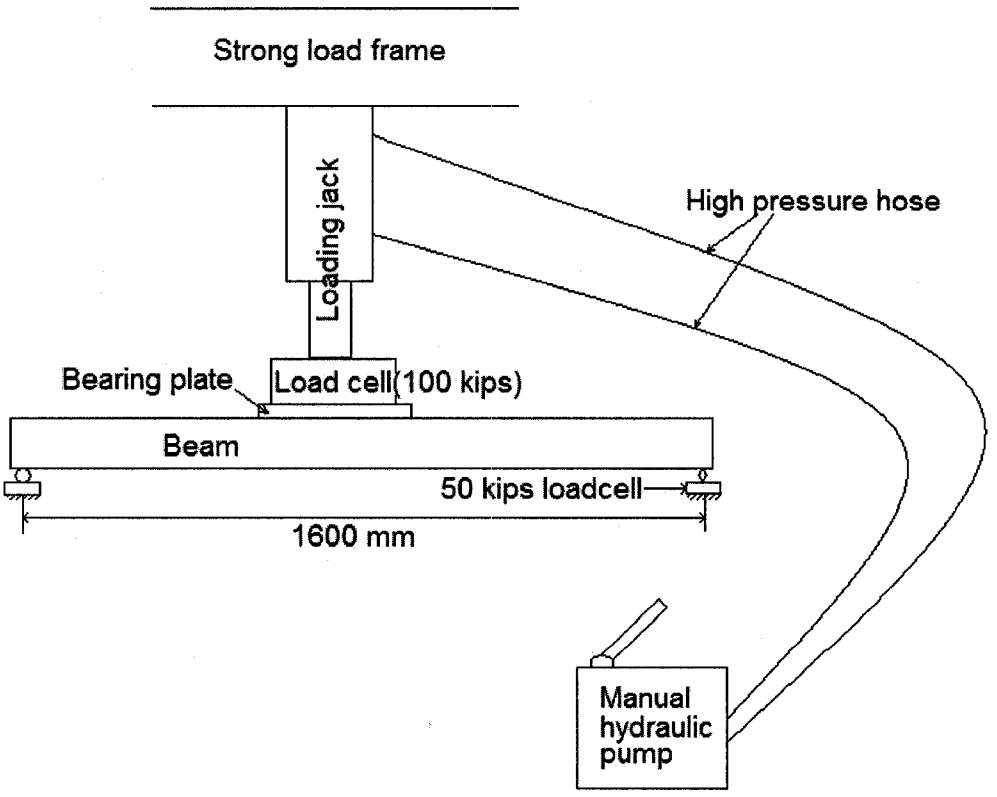

Figure 3.49: Sketch of test setup

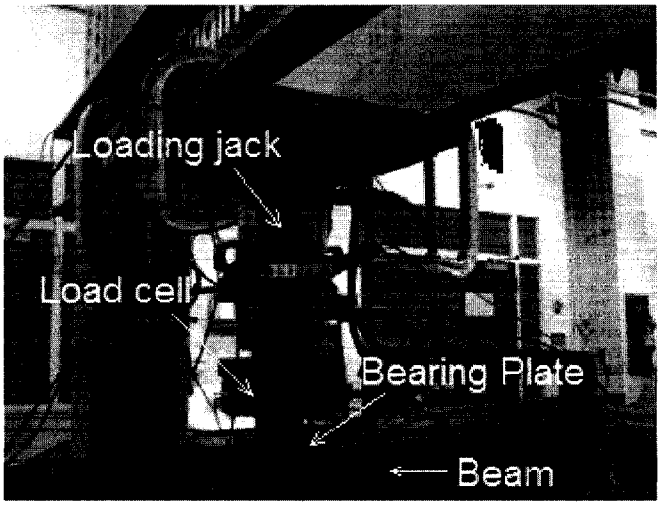

Figure 3.50: Photo of test set up: load cell and jack

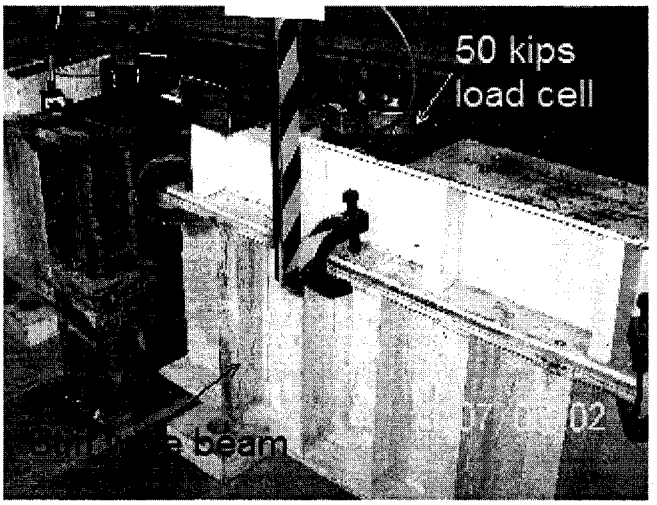

Figure 3.51: Stiff wide beam under the support

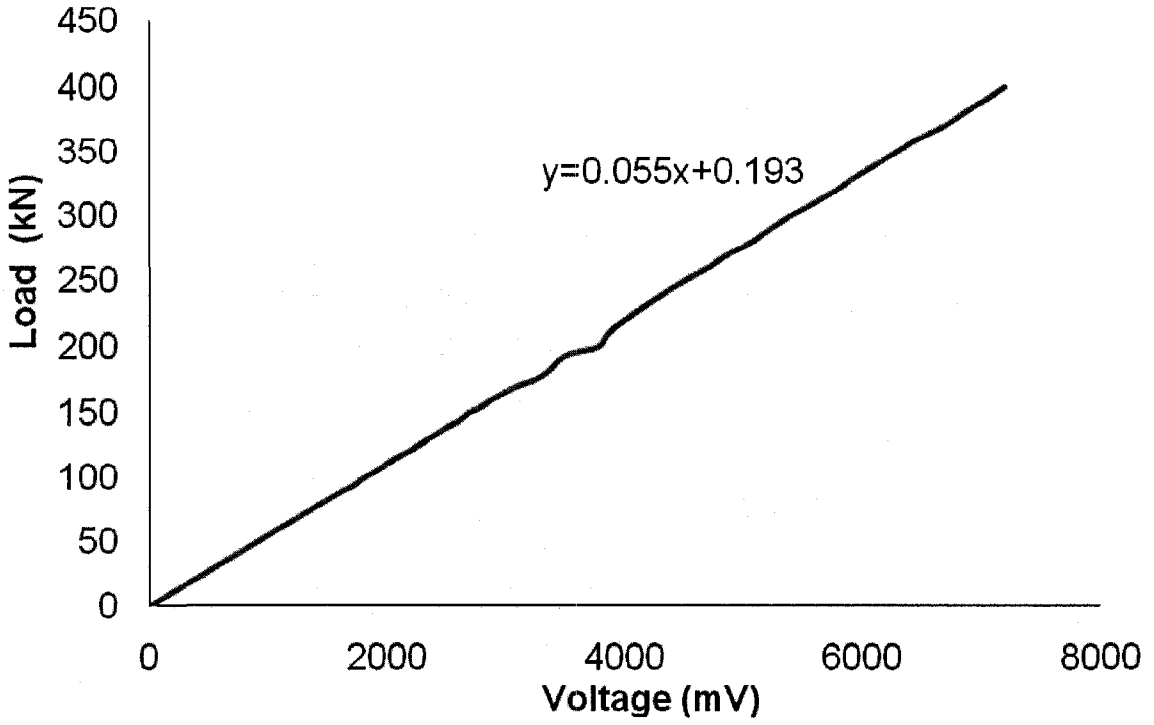

Figure 3.52: 445 kN (100kips) load cell calibration curve

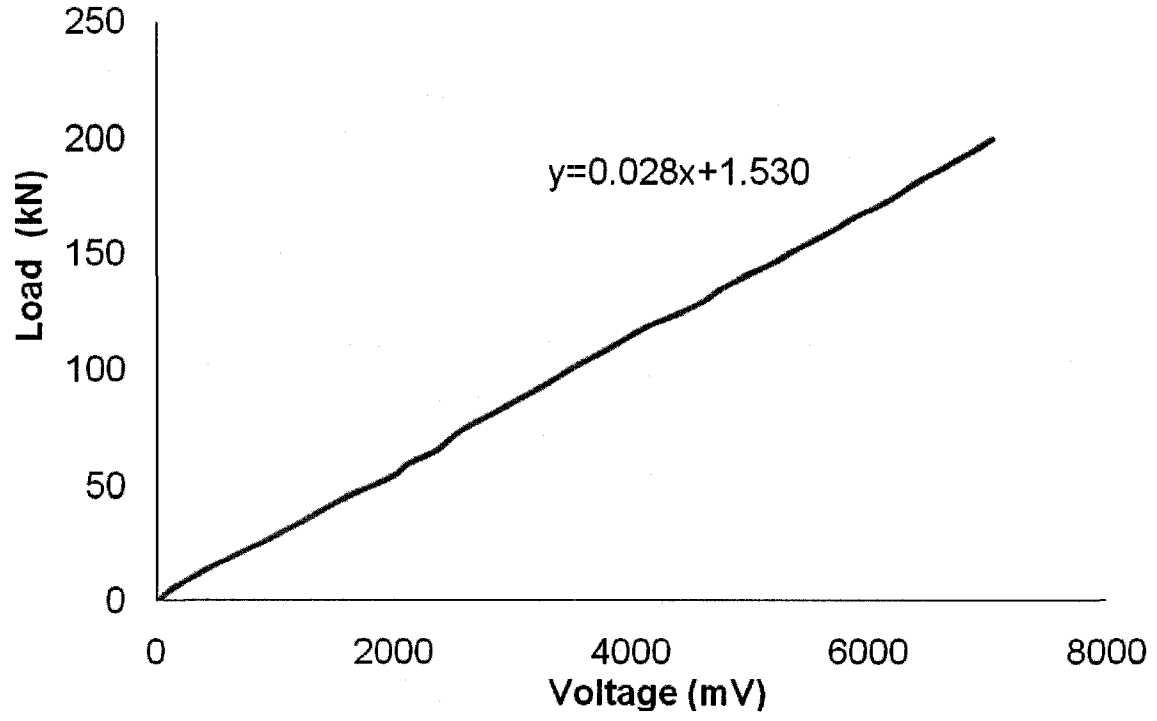

Figure 3.53: 223 kN (50kips) load cell (2) calibration curve

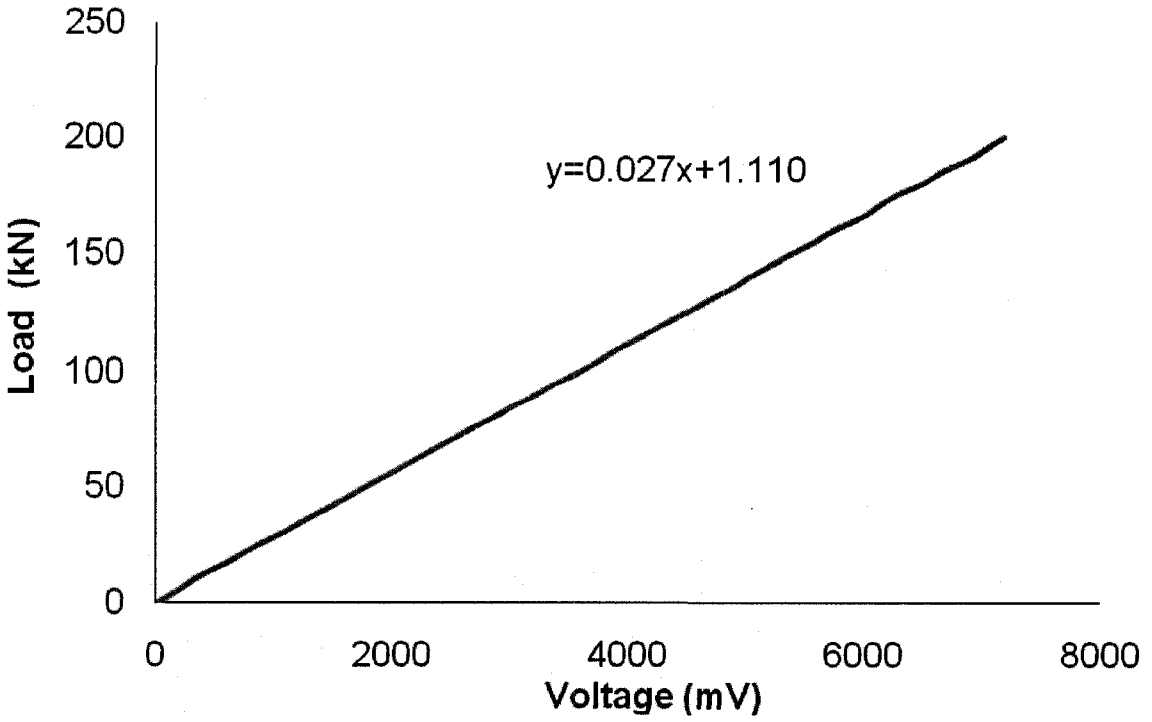

Figure 3.54: 222 kN (50kips) load cell (3) calibration curve

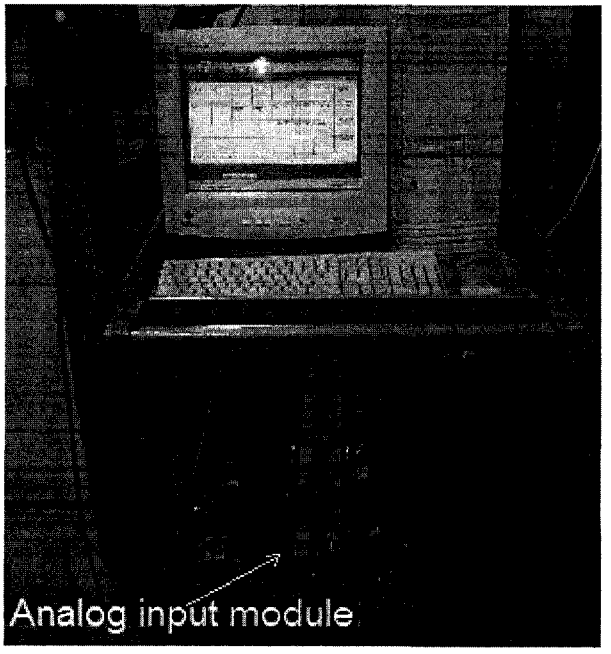

Figure 3.55: Data acquisition system

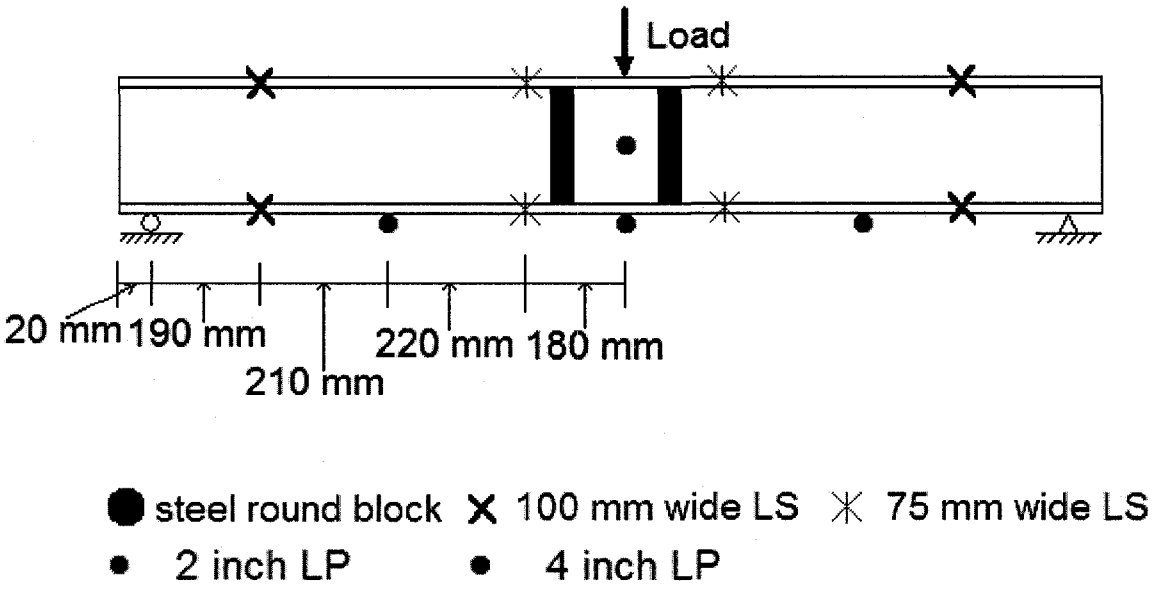

Figure 3.56: Test setup for specimens of Group1

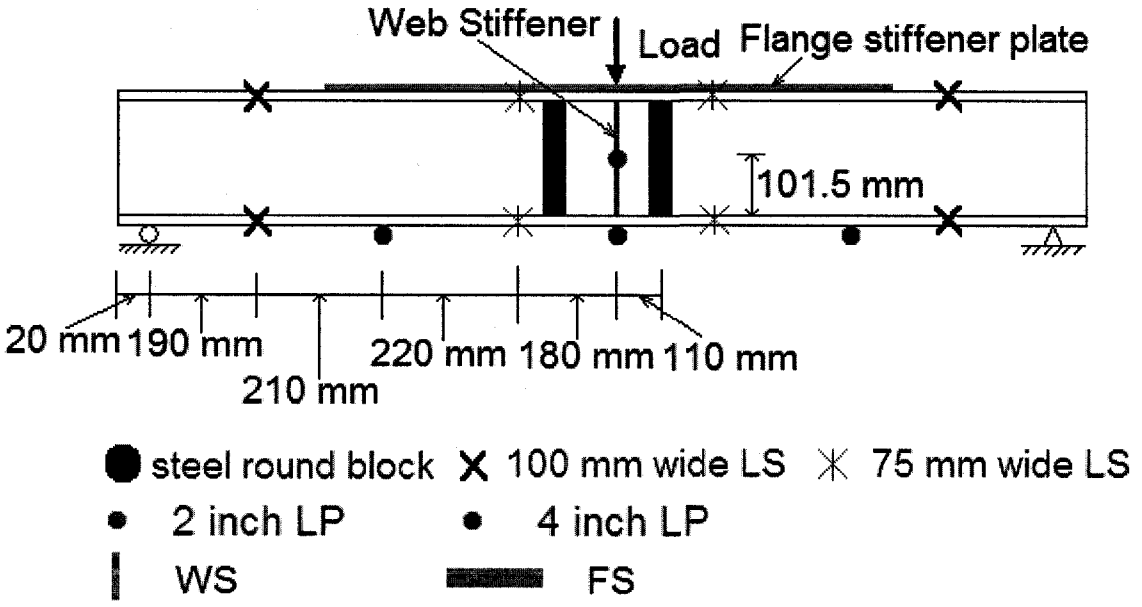

Figure 3.57: Test setup for specimens of Group2

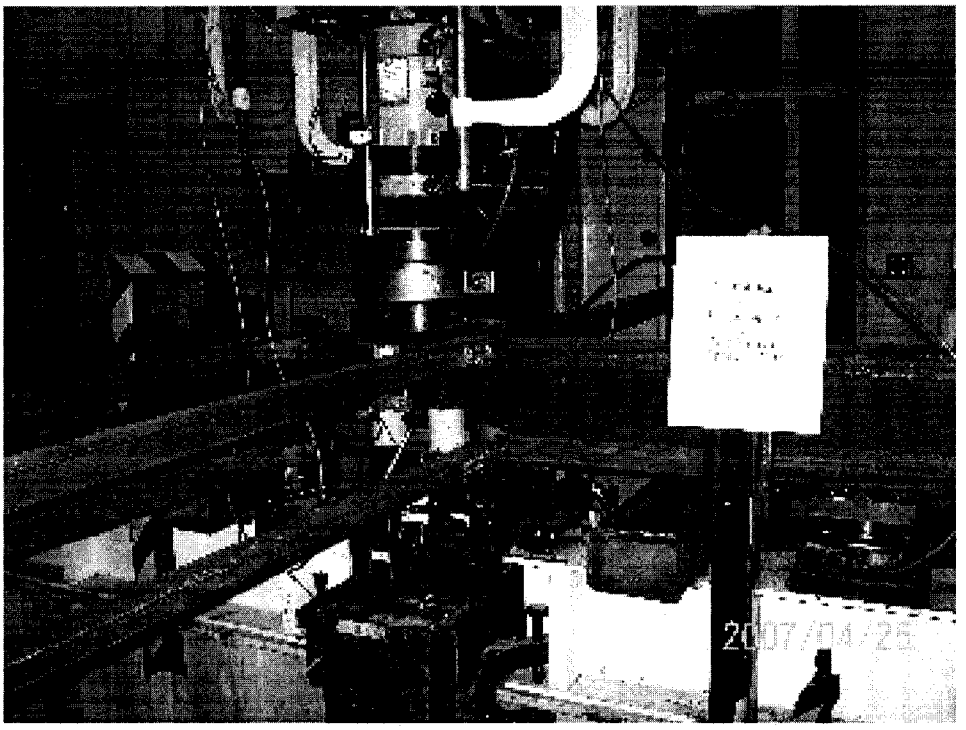

Figure 3.58: CV-G1 before test

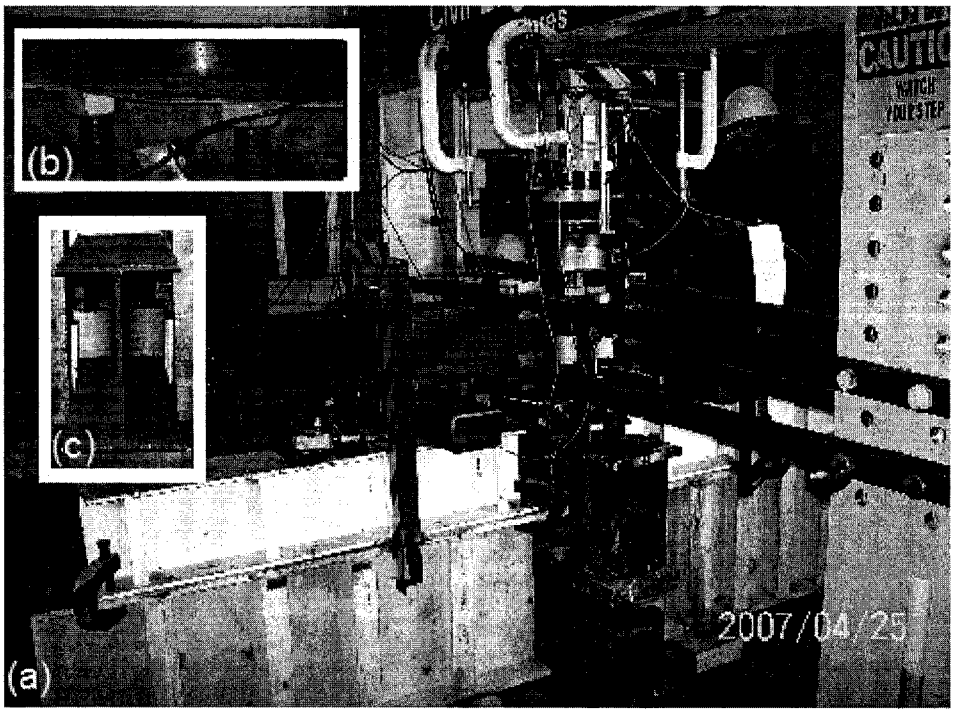

Figure 3.59: (a) CV-G1 after test
(b) Top flange buckled slightly
(c) No visible sign of torsion buckling

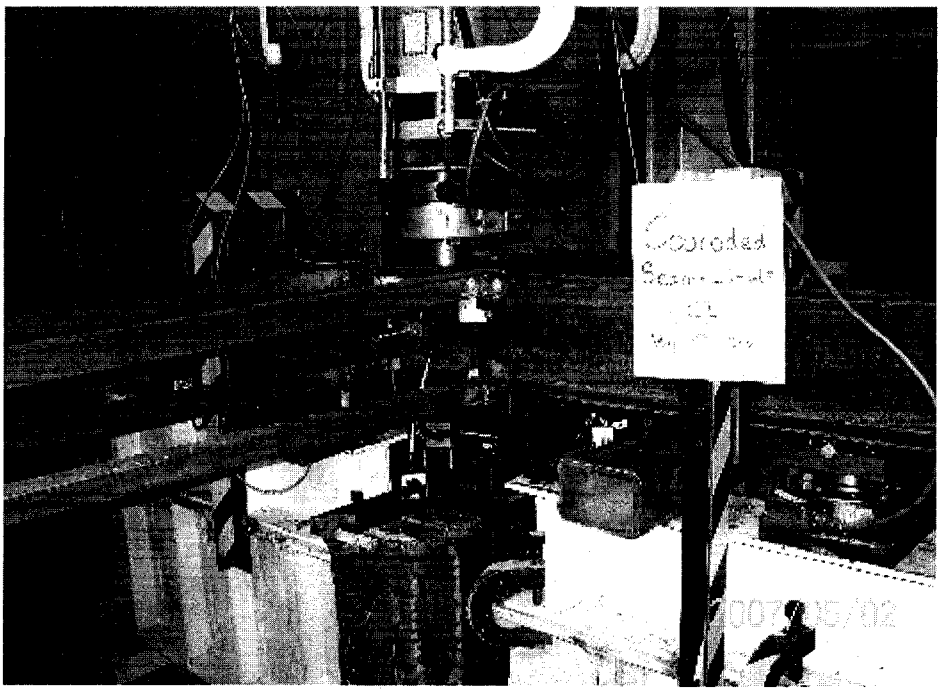

Figure 3.60: CC-G1 before test

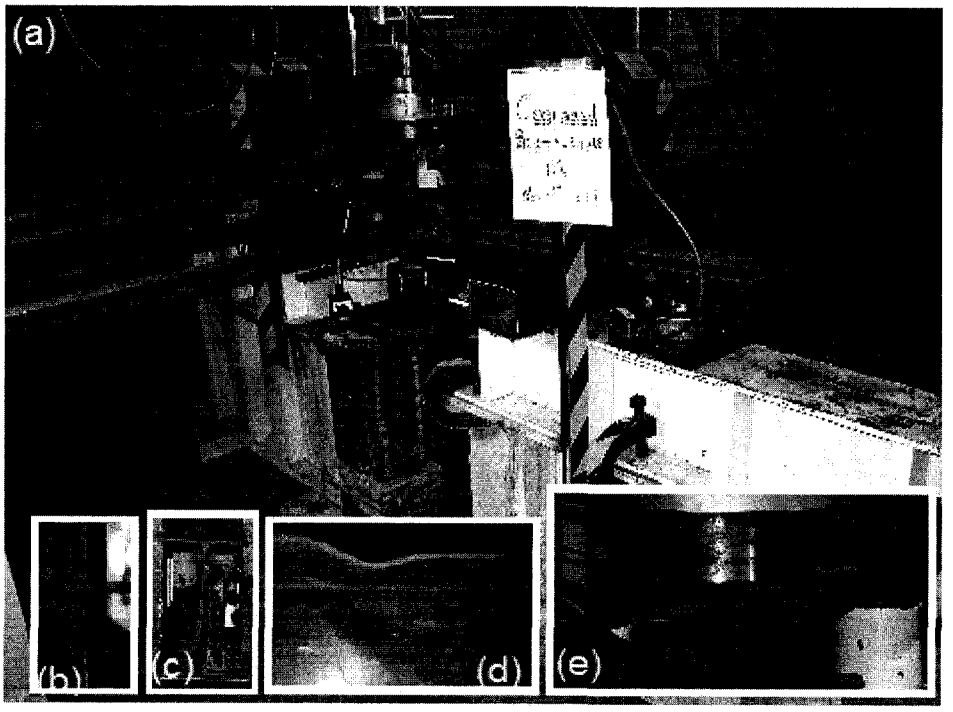

Figure 3.61: (a) CC-G1 after test
(b) Steel thinning at the corrosion area
(c) Slightly lateral torsion buckle
(d) Web buckled
(e) Flange buckled

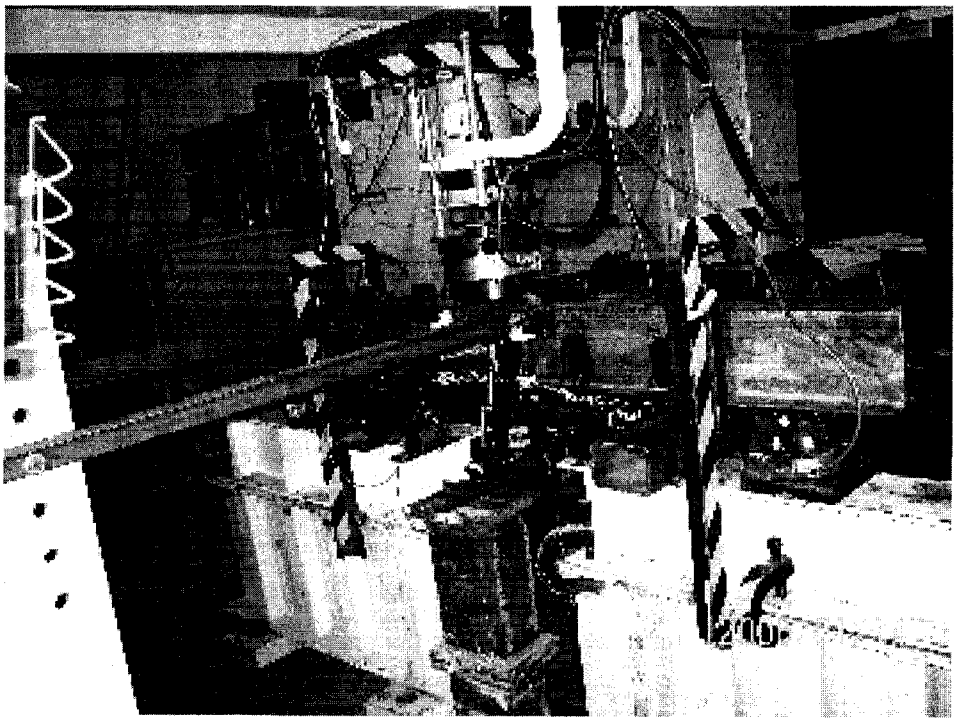

Figure 3.62: RC-W67-T2.4-G1 before test

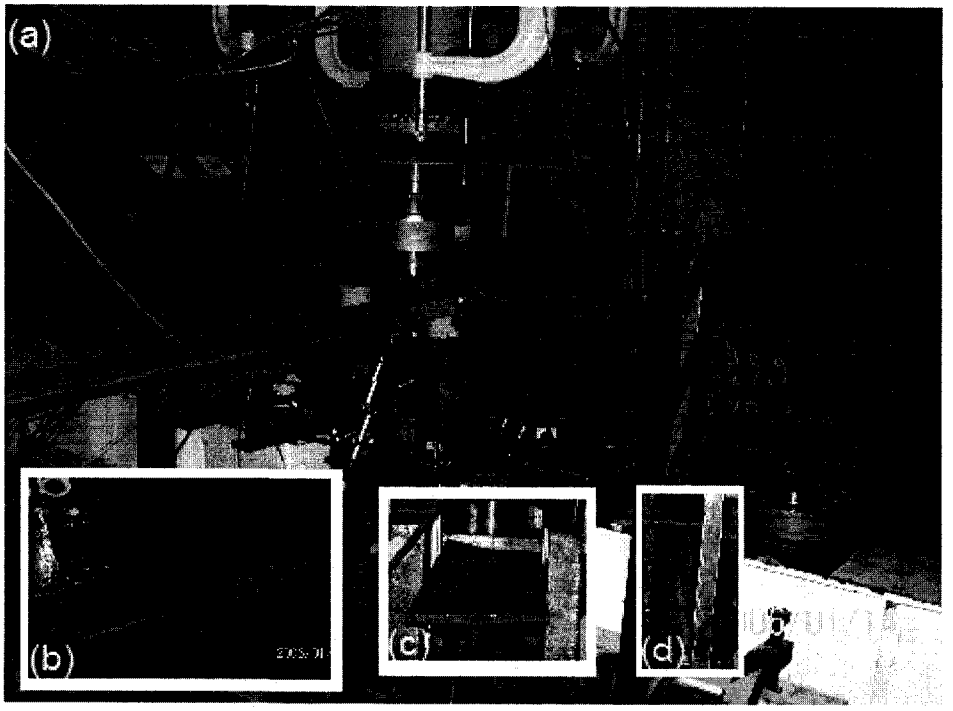

Figure 3.63: (a) RC-W67-T2.4-G1 after test
(b) CFRP debonding
(c) Flange buckling
(d) Lateral torsion buckling

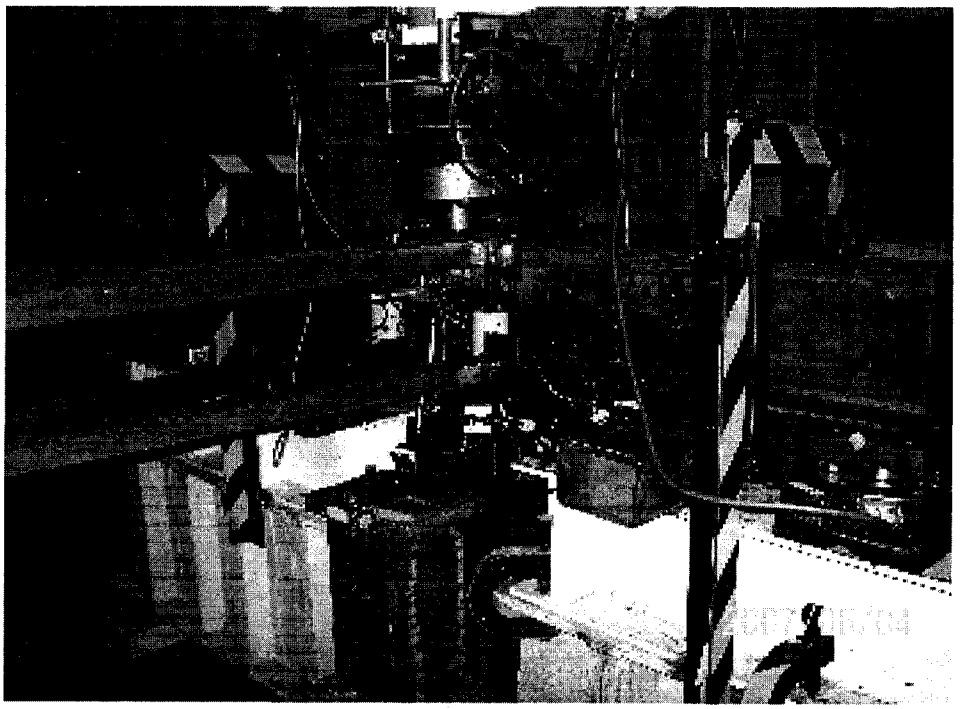

Figure 3.64: RC-W133-T2.4-G1 before test

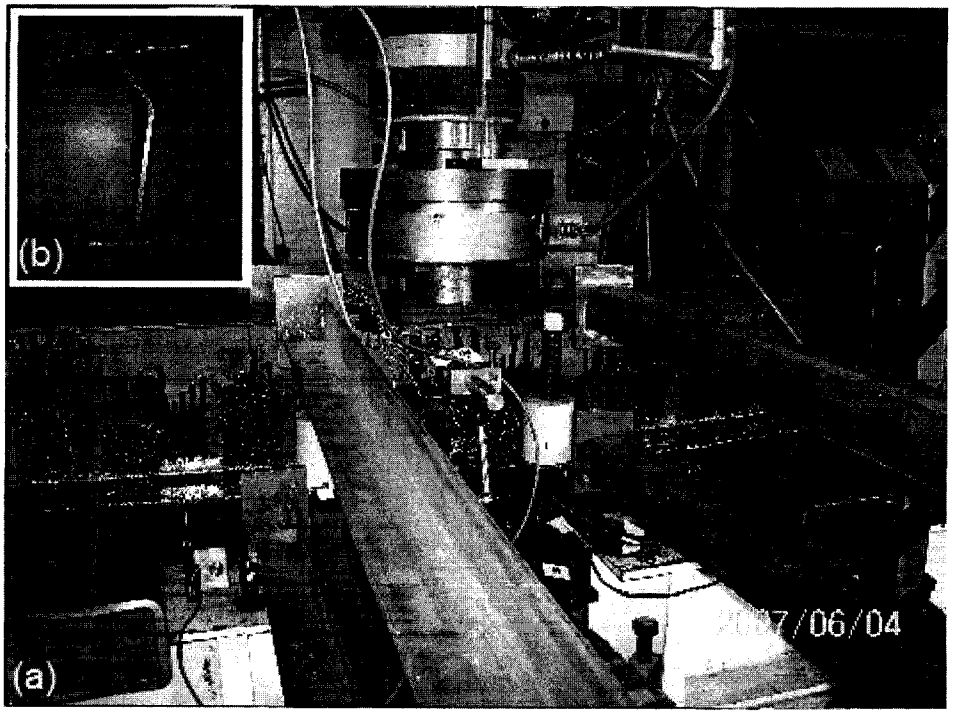

Figure 3.65: (a) RC-W133-T2.4-G1 after test
(b) Web buckling

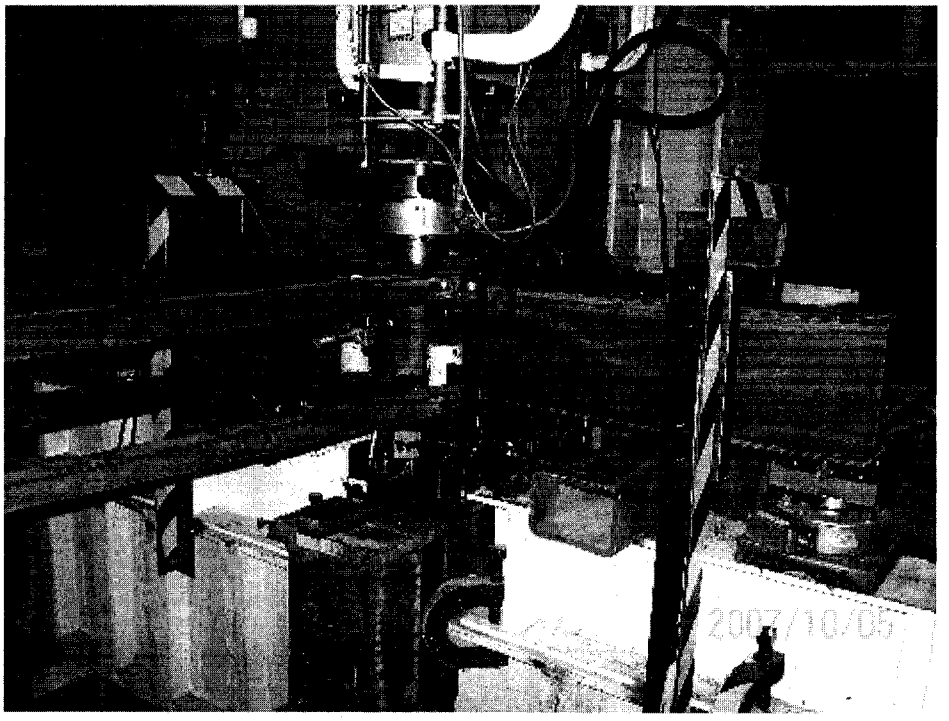

Figure 3.66: CV-G2 before test

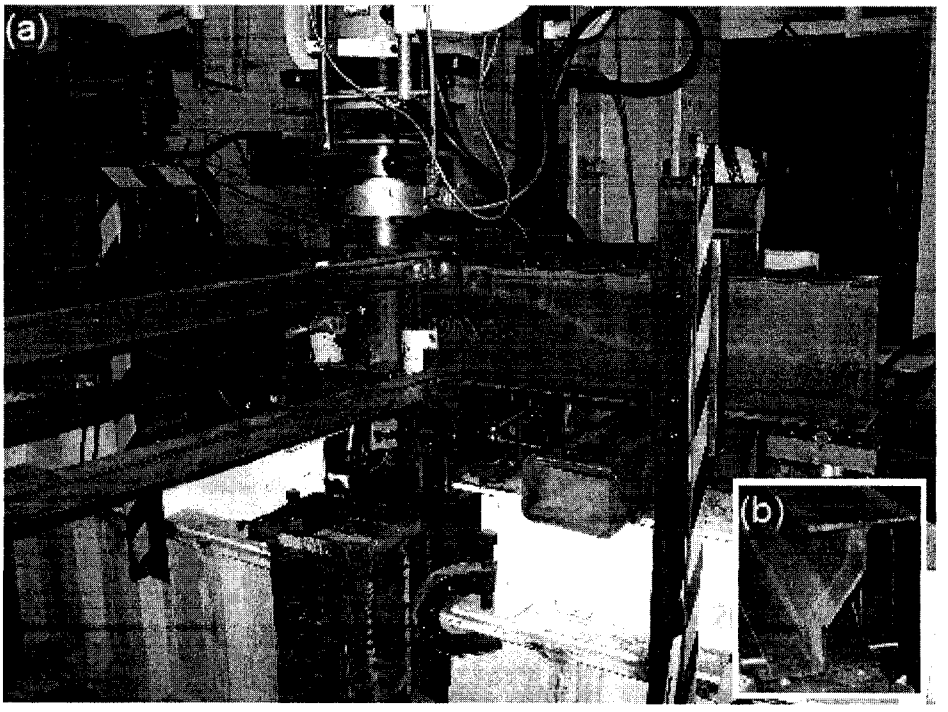

Figure 3.67: (a) CV-G2 after test
(b) Web buckled at roller support

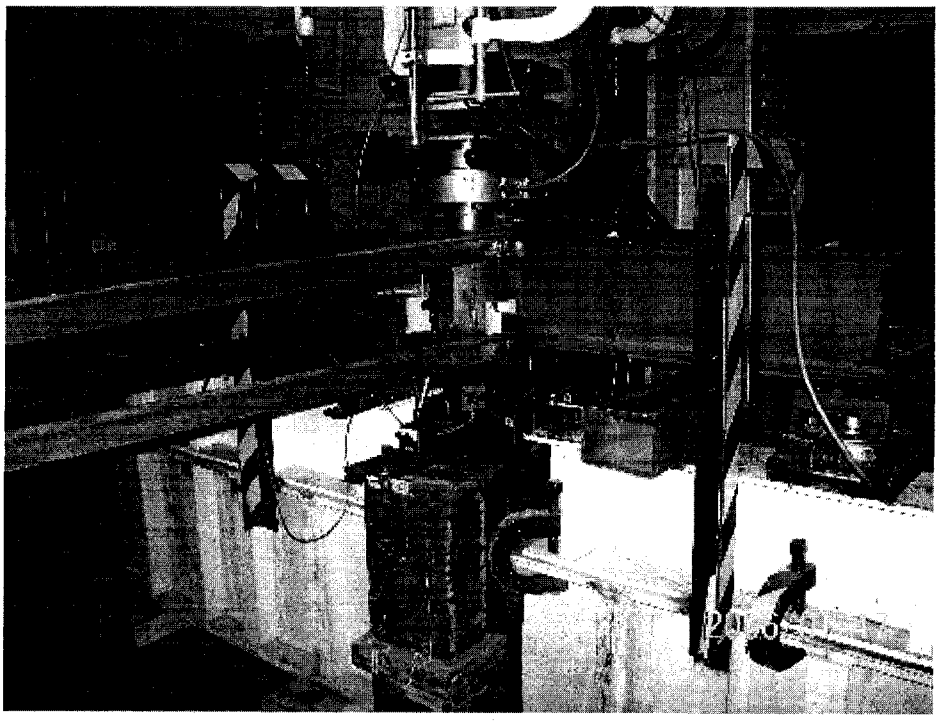

Figure 3.68: CC-G2 before test

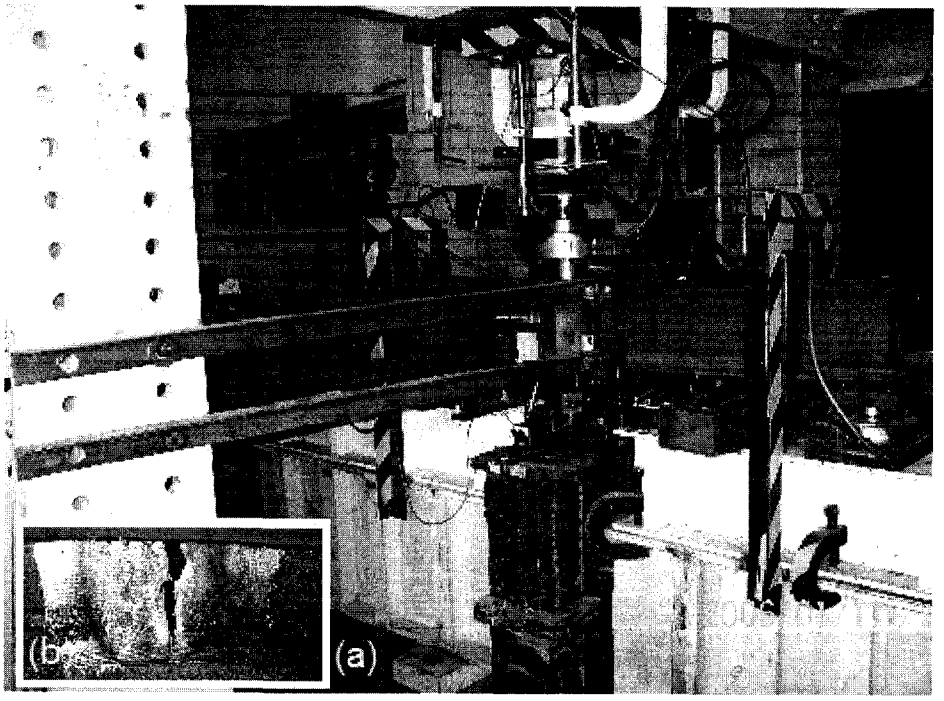

Figure 3.69: (a) CC-G2 after test
(b) Cracking at the center of the corrosion

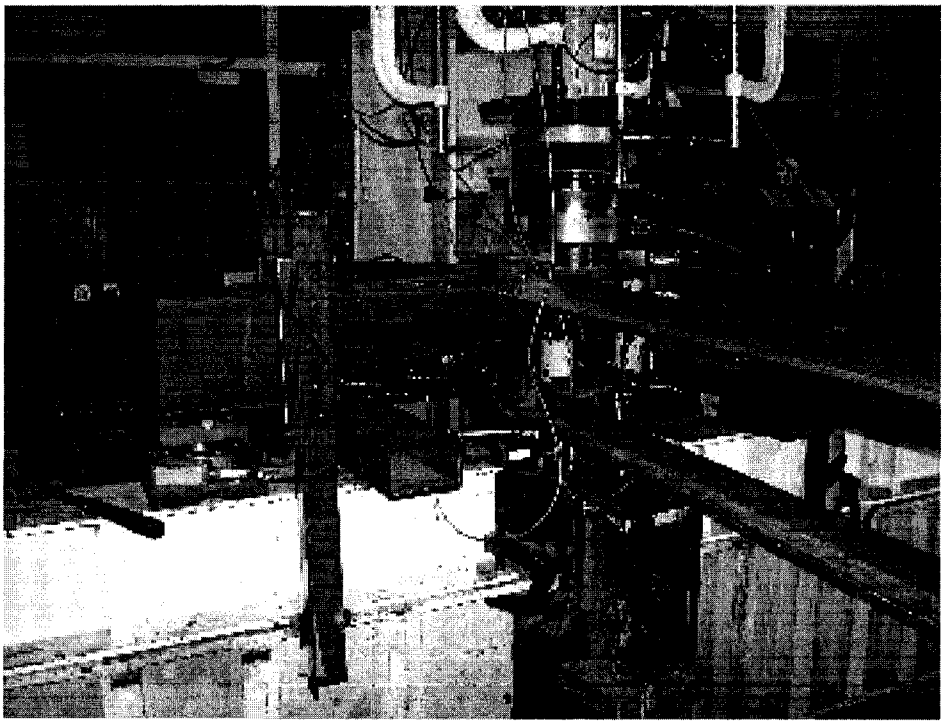

Figure 3.70: RC-W133-T2.4-G2 before test

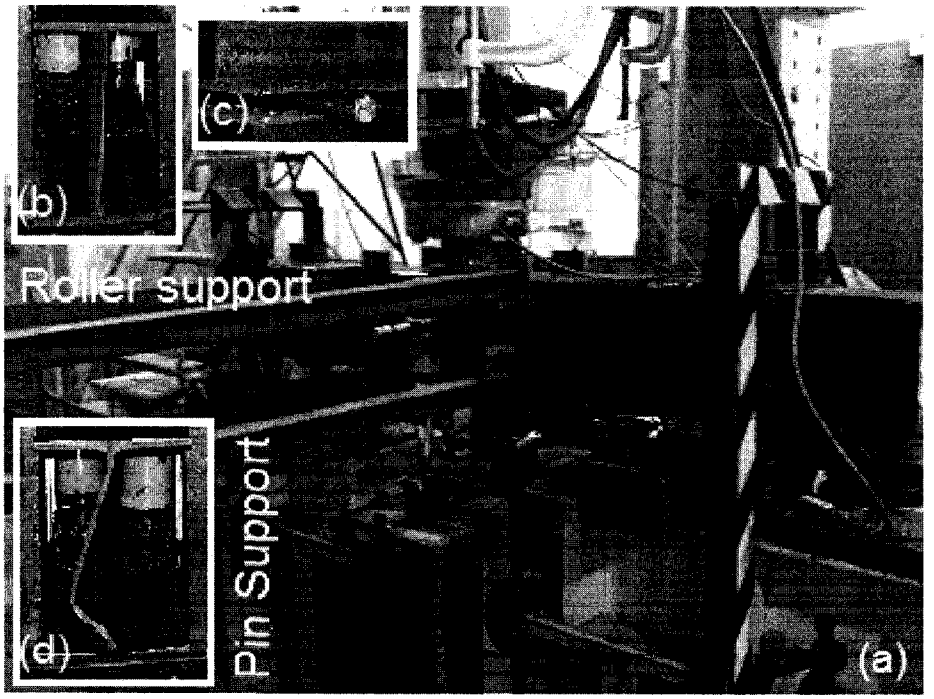

Figure 3.71: (a) RC-W133-T2.4-G2 after test
(b) No web buckling at roller support
(c) Flange buckled slightly at roller support
(d) Web buckled at pin support

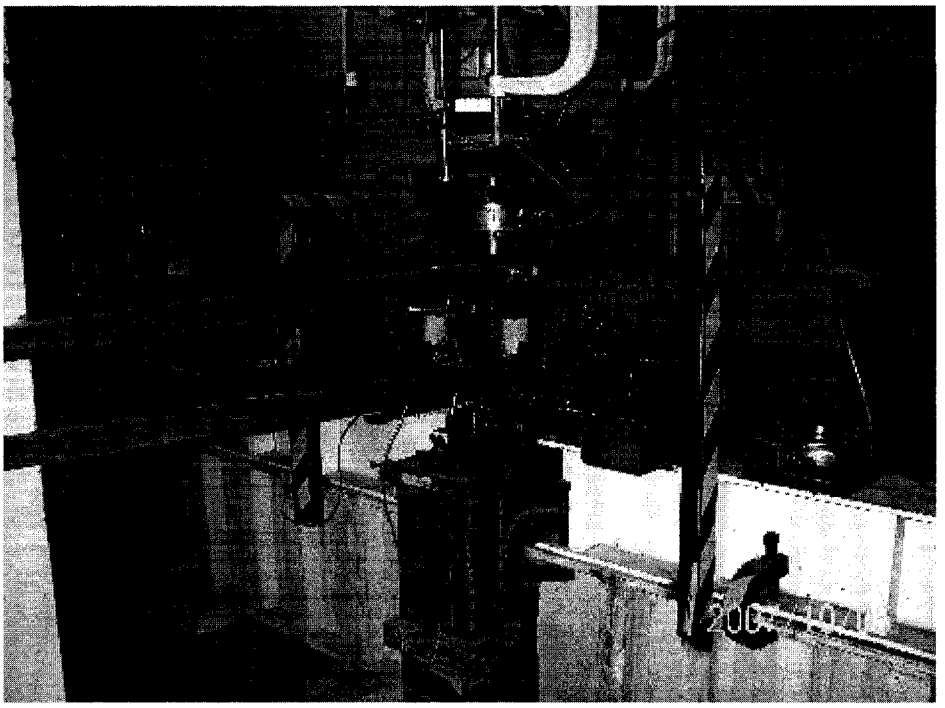

Figure 3.72: RC-W133-T1.2-G2 before test

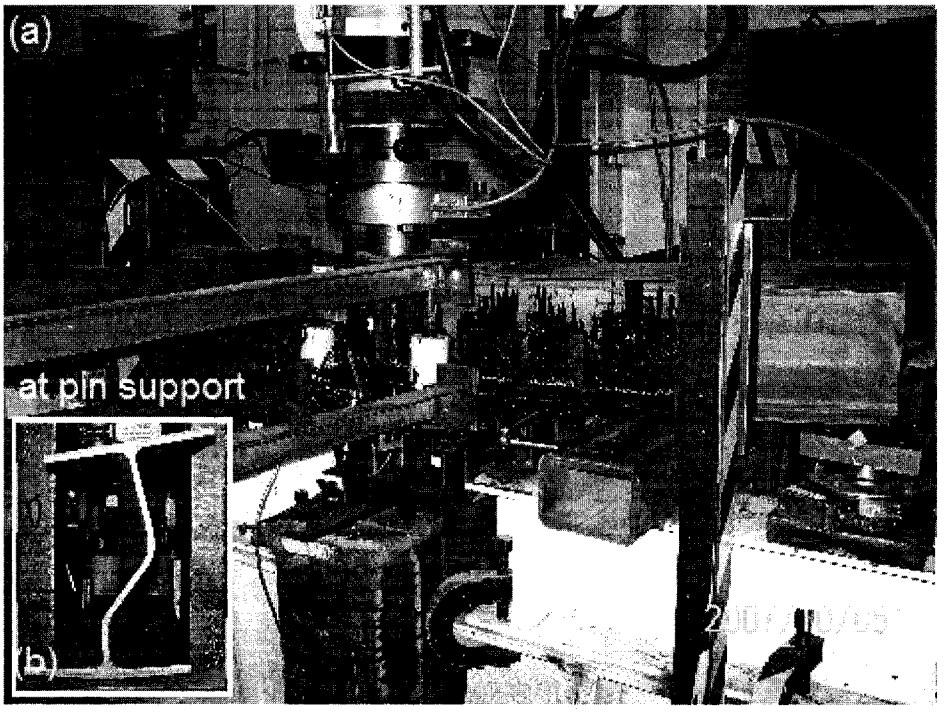

Figure 3.73: (a) RC-W133-T1.2-G2 after test
(b) Web buckled at pin support

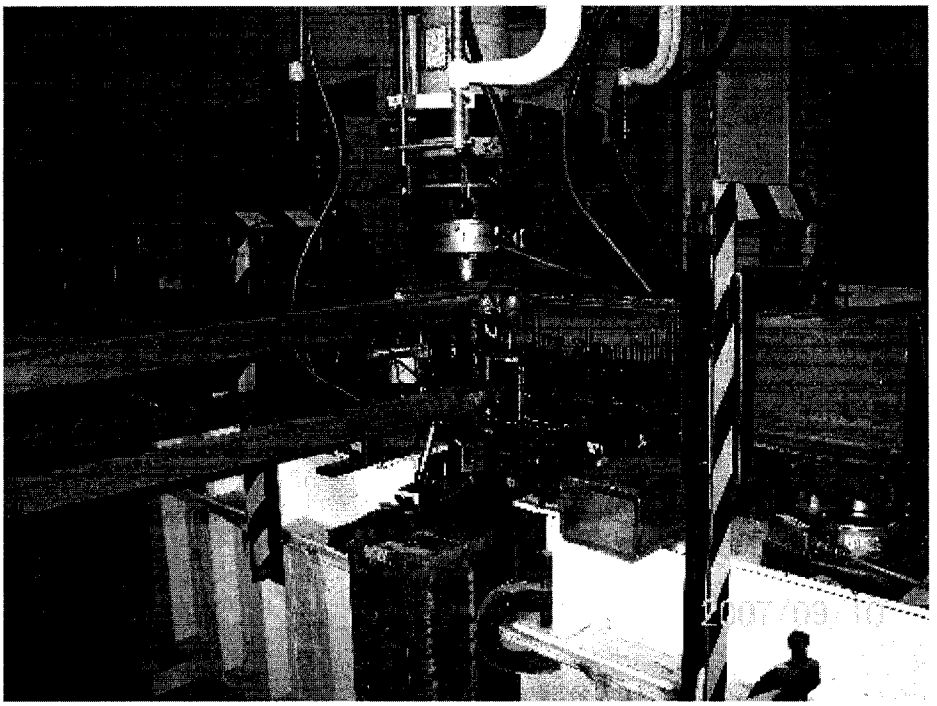

Figure 3.74: RC-W133-T0.6-G2 before test

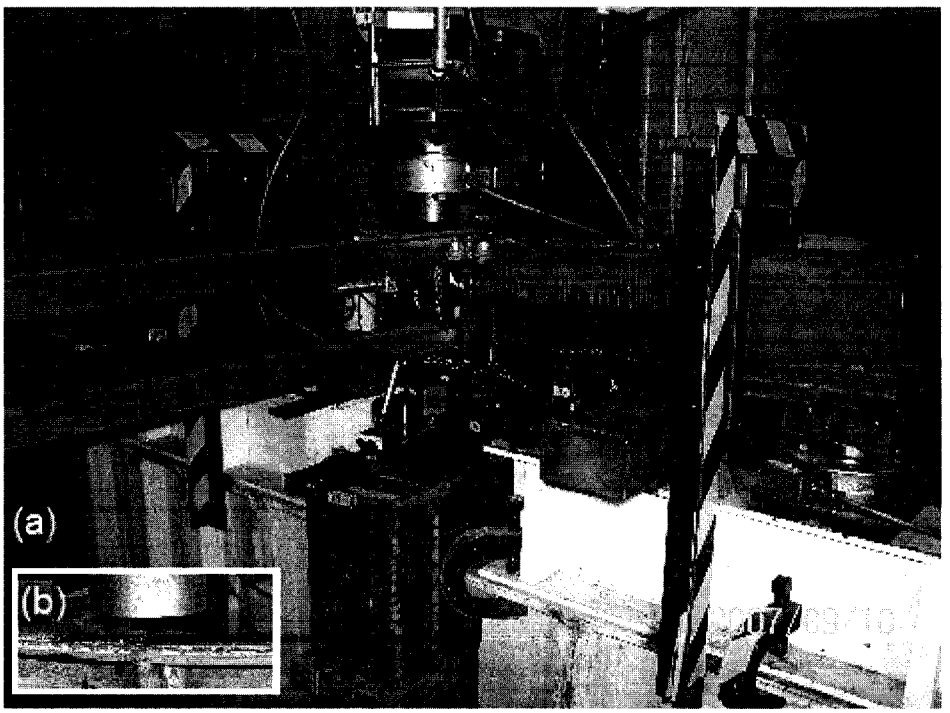

Figure 3.75: (a) RC-W133-T0.6-G2 after test
(b) No flange buckling under the load

4 EXPERIMENTAL RESULTS AND ANALYSIS

4.1 General

The objective of this study was to develop an alternative in-service repair method for corroded steel structure using Carbon Fiber Reinforced Polymer (CFRP). The viability and reliability of this repair system depends largely on the effectiveness of load transfer between CFRP composite and steel. A total of nine specimen were tested to study the effectiveness of this repair method. The test results are discussed in the following sections. The responses obtained from the specimens in terms of strain in steel, strain in CFRP, deflection, and ultimate load are described and presented in this chapter. Failure mechanisms obtained from these tests are also discussed in the chapter. The summary of the test results are presented in Table 4.1 to 4.4.

4.2 Behavior of Group1 Specimens

As mentioned in Chapter 3, group1 contained one control virgin specimen (CV-G1), one control corroded specimen (CC-G1), and two rehabilitated corroded specimens (RC-W67-T2.4-G1 and RC-W133-T2.4-G1). All four specimens were supported latterly using eight lateral supports as discussed in section 3.3.3. Four steel round blocks were also mounted between top and bottom flanges under the load application point to reduce the flange buckling (Figure 3.16). However, no web stiffeners were used in these specimens.

4.2.1 Specimen CV-G1

This is a control virgin (no corrosion) specimen. The load-deformation behavior for this specimen is shown in Figure 4.1. The deformation obtained from LP8 (Figure 3.48) is usually used for plotting the load-deformation behaviors for all the specimens unless otherwise specifically mentioned. This specimen yielded at 202 kN load (point Y) and 7.0 mm vertical deformation. The ultimate load was 243 kN (point U) and the vertical deformation was 31.5 mm. This beam specimen exhibited large elastic-plastic deformation. The test was discontinued at 247 kN (point F) and the vertical deformation at 34.0 mm, to avoid damages of the equipment. This specimen did not fail either due to

lateral torsion buckling, or due to web buckling. The location of the salient points identified by Y, U, and F in the figure depicts the global yield load point, ultimate load point, and failure load point, respectively.

Figure 4.2 shows the deformation response obtained from LP7, LP8, and LP9 (Figure 3.48) at 60 kN, 200 kN, 230 kN, 243 kN, and end of loading process. Like the trial specimen (TS), this specimen also deformed rapidly after it reached its yield load. The difference between deformations at "end of loading process" and at "unloaded condition" is the elastic deformation. The deformation which remained after unloading was the plastic deformation. Figure 4.3 is the load and mid-span lateral deformation (LP5) curve, which shows there was negligible lateral deformation for this specimen.

The failure mode of this specimen was ductile as shown in Figure 3.59a. There was no indication of lateral torsion or web buckling (Figure 3.56c). Figure 3.59b shows that the top flange buckled slightly under the load. Specimen CV-G1 showed a significant increase in ductility as compare to TS.

This specimen was tested to obtain strength and ductility of the undamaged (virgin) beam specimen and thus no strain gauges (SG) were used in this specimen. Therefore, no strain data is available.

4.2.2 Specimen CC-G1

4.2.2.1 Load-deformation behavior and failure mode

The load-deformation behavior for this specimen is shown in Figure 4.4. This specimen yielded at 165 kN load (point Y) and 5.7 mm mid-span vertical deformation. The ultimate load was 215 kN (point U) with a deformation of 13.4 mm. The test was stopped at 184 kN (point F) and at vertical deformation of 38.2 mm, to avoid damages of the equipment. The locations of the salient points identified by Y, U, and F, in the figure, indicate the global yield load point, ultimate load point, and failure load point, respectively.

This specimen first yielded at the corrosion followed by the severe web buckling at mid-span (Figure 3.61d). At that time, the top flange under the load buckled as well (Figure 3.61e). There was a slight lateral torsion buckling (Figure 3.61c) and it could be because of the non-symmetric in cross-section and loading. However, flange at corrosion did not tear or rupture.

Figure 4.5 shows the deformation response obtained from LP7, LP8, and LP9 (Figure 3.6) at 50 kN, 180 kN, 200 kN, 215 kN, end of loading, and at unloaded condition. Figure 4.6 shows the load and mid-span lateral deformation (LP5) curve. This curve shows that after the ultimate load was applied, the web buckled (Figure 3.61d).

4.2.2.2 Strain distribution

A few strain gauges (SG) were used in this specimen to study the strain distribution at the corrosion with respect to the beam's web (See Figure 3.46 for strain gauge locations). Strain-deformation behaviors obtained from this specimen are shown in Figure 4.7. Similar plot but for strain-load behaviors obtained from this specimen are shown in Appendix IV Figure A4.7. The locations and orientations of the strain gauges (SGs) are shown in Figure 3.46. In Figure 4.7, SG numbers are shown in parenthesis. The deformation was the vertical mid-span deformation obtained from the linear potentiometer (LP) 8 (See Figure 3.48).

The strain values obtained from longitudinal SG 3, 4, and 6 are positive (which means tension), and the strain obtained from longitudinal SG 1 and 2 are in negative (which means compression). It is because SG 3, 4, and 6 were oriented in the beam's longitude direction, and located below neutral axis, while SG 1 and 2 were located above the neutral axis and were oriented in the longitude direction of the beam. The values of strain obtained from SG 5 and 7 are also negative, because these gauges were oriented in the lateral direction of the beam and located on the top and bottom surfaces of the bottom flange, respectively (Figure 3.46). Figure 4.8a, b, and c shows the strain distribution of SG S1, S2, S3, S4, and S6 at 100 kN, 165 kN (yield load), and 215kN (ultimate load), respectively. The y-axis shows the distance from the bottom of the flange to the SG. The SG S6 failed before the yield load was applied, and SG S4 failed before the ultimate load

was applied. In Figure 4.48a, the plane section remained plane expect the bottom of the bottom flange (SG6) until 100 kN load was applied. Figure 4.48b shows the plane section remained plane expect the bottom flange (SG 4 and 6) until yield load (165 kN) was applied. SG 6 failed when the global vertical deformation reached three mm. Figure 4.48c shows the plane section did not remain plane for the entire cross-section of the beam when ultimate load (215 kN) was applied. SG4 failed when the global vertical deformation reached about 10 mm.

It can be seen from Figure 4.7 that the slopes of the strain increment for all strain gauges except SG 6 (located at center of corrosion and on corrosion face) are relatively small in between point O (start of loading) and point Y (yield). The strain of SG 6 started to increase relatively at higher rate at about global deformation of three mm. It could be because the strain gauge was located on the curved corroded surface (see Figure 3.46) and thus, the SG experienced high stress and strain concentration. The stain value for this SG dropped quickly soon after and it may be because of debonding of the gauge. The strain gauge did not probably bond well to the steel because of high curvature, thus resulting in early debonding.

Strain values for longitudinal SG 1, 2, and 3 (Figure 3.46), which were located on the top flange and web of the beam, increased slowly between point Y (yield load) and U (ultimate load), while strains for SG 4, 5, and 7, which were located on the inner (top) and outer (bottom) surface of the bottom flange, increased relatively faster. It should be noted that SG5 and 7 were transverse gauges. The SG 4 seems to started debonding when the deformation reached about 10 mm, and it eventually debonded completely.

In between points U (ultimate load) and F(end of test), strains for all strain gauges increased rapidly, especially at SG 4. The strain for SG 1 increased rapidly when the deformation reached 16 mm, this is due to top flange buckling. The strains for SG 2 and 3 also increased, and this is due to the web buckling.

4.2.3 Specimen RC-W67-T2.4-G1

4.2.3.1 Load-deformation behavior and failure mode

This was a corroded specimen rehabilitated with 67 mm wide CFRP, covering half width of the flange (Figure 3.42). Thickness of CFRP composite was 2.4 mm (three layers of BASF CF160 dry fabric). The load-deformation behavior for this specimen is shown in Figure 4.9. This specimen yielded at a load of about 200 kN (point Y) and 6.7 mm vertical deformation. The ultimate load was 236 kN (point U) and the vertical deformation was 11 mm. The specimen failed at 192 kN (point F) and at vertical deformation of 23.7 mm, due to CFRP debonded at its longitudinal termination line along lateral direction at the mid span area of the beam (Figure 4.10). The Figure 4.10 shows the cross-section of the specimen cut at its mid-span. The location of the salient points were identified by Y, U, F, 1 2, and 3 in the figure, indict the global yield point, ultimate load point, failure load point, first, second, and third debonding noises, respectively.

Figure 4.11 shows the deformation response obtained from LP7, LP8, and LP9 (Figure 3.48) at 60 kN, 200 kN, 225 kN, 236 kN, end of loading process, and at unload condition. Figure 4.12 is the load and mid-span lateral deformation (LP5) curve. This figure indicates that after reaching the ultimate load (U), the beam started to move laterally, because of the CFRP debonding.

It seems that the putty (corrosion filler) first debonded when the global deformation reached 4.38 mm (point 1 in Figure 4.9) and much before yield load (point Y) was applied. However, the debonding did not affect the global load vs. vertical deformation curve (Figure 4.9). The debonding of the CFRP occurred several times at different locations once the steel beam reached its yield. However, the major CFRP debondings are only identified in these figures (points 2 & 3). Because of each of these two debonding, the load capacity dropped and the beam started to twist in lateral torsion (LT) buckling mode. The type 2 (Figure 3.19) lateral supports at bottom flange were not provided in this specimen and this might be the primary reason for not being able to stop the torsion of the beam.

The failure of this specimen occurred due to the debonding of CFRP followed by LT buckling, as shown in Figures 3.63b and 4.10. Therefore, for the next specimen (RC-W133-T2.4-G1), CFRP covering full flange width (133 mm) and wider cross wraps were used. The flange of this specimen also buckled as shown in Figures 3.63c and 4.13. Figure 4.10 and 4.13 are pictures of a section of the beam cut off at the mid-span of the beam. Figure 3.63d shows there was torsional buckling which also occurred because of the CFRP debonding. Due to the CFRP debonding, this test (RC-W67-T2.4-G1) was discontinued and the specimen was unloaded when the global deformation was about 23 mm. The ultimate load capacity of this specimen could go up to the range what the vergin specimen (CV-G1 in Figure 4.1) exhibited. However, the ductility dropped significantly.

4.2.3.2 Strain distribution

Strain-deformation behaviors obtained from this specimen are shown in Figures 4.14 to 4.18. Similar plots but for strain-load behaviors obtained from this specimen are shown in Appendix IV Figures A4.14 to A4.18. The locations of the SGs are shown in Figure 3.47. The SGs used for measuring strain on steel surface and CFRP surface are denoted by S and C, respectively. The strain-deformation behaviors obtained from all steel strain gauges (S1 to S5) show a similar pattern. However, the strain magnitude increased from SG S5 to S4, SG S4 to S3, SG S3 to S2, and SG S2 to S1. The patterns of strain-deformation behavior of all CFRP strain gauges (C1 to C5) are also very similar. However, the strain magnitude increased from SG C5 to C4, SG C4 to C3, SG C3 to C2, and SG C2 to C1.

It can be seen from Figures 4.14 to 4.18 that the strain values obtained from all SGs increased linearly and slowly till point 1 when the filler putty debonded. The slopes of the strain increment for steel and CFRP are similar, indicating perfect bonding between CFRP composite and steel. The main reason for this seems to because of the strain compatibility between beam flange and bottom of CFRP (Figure 4.19). The minor differences in the could be because of the SGs used for CFRP (13 mm) are larger (longer and wider) than the SGs used for steel (3 mm) and the location of the steel SG could be slightly different from location of corresponding CFRP SG. Starting from point 1, the

putty debonded gradually from the steel, which in general caused the strain in the CFRP to increase much rapidly and the strain in the steel increased slightly, except for SG S1. This was because the load at the corrosion may not have fully transferred from the steel to the CFRP through the putty, indicating that the filling the corrosion with filler putty is not a good choice. Shortly after the putty debonded, the CFRP around the putty (corrosion) started debonding as well (See point Y of C2 at Figure 4.15), and the beam reached its yield load capacity. Shortly after the putty debonded, the SG S1 failed at about 8 mm vertical deformation.

Major debonding of the CFRP occurred twice in between point U and F at point 2 and 3. Strain in the CFRP decreased every time when CFRP debonding occurred, while strain in steel remained unchanged. Immediately after the CFRP debonding, the strain in CFRP started to increase until the next debonding in CFRP occurred. However, the strain in steel strain gauges remained nearly unchanged except for SG S2. After the debonding occurred at point 3, CFRP debonding was visible (Figure 4.12). The SG S2 shows the strain of the steel increased faster than other SGs on steel (S3, S4 and S5). It is because SG S2 is located at thinner steel flange at the corrosion area. After third debonding noise was heard, the strain value obtained from other SGs showed small increase in both steel and CFRP strain. The strain value in SG C1 became negative at about 17 mm vertical deformation, indicating that the CFRP locally became compressive.

4.2.4 Specimen RC-W133-T2.4-G1

4.2.4.1 Load-deformation behavior and failure mode

This was a corroded specimen rehabilitated with 133 mm wide CFRP. Thickness of the CFRP was 2.4 mm (three layers of BASF CF160 dry fabric). The load-deformation behavior for this specimen is shown in Figure 4.20. Specimen RC-W133-T2.4-G1 yielded at a load of 227 kN (point Y) (202 kN for CV-G1) and 6.9 mm vertical deformation. The ultimate load was 251 kN (point U) (243 kN for CV-G1) and the vertical deformation was 9.1 mm as shown in Figure 4.20. The specimen failed at 129 kN (point F) and the vertical deformation of 17.2 mm, due to severe web buckling (Figure 3.65b). Thus, this specimen

exhibited yield and ultimate load capacities higher than control virgin (CV-G1) specimen. However, because of severe web buckling, the ductility dropped significantly. The location of the salient points were identified by Y, U, F, 1, 2, and 3 in the figure, indicating the global yield point, ultimate load point, failure load point, first and second debonding noises, and severe web buckle, respectively.

Figure 4.21 shows the deformation response obtained from LP7, LP8, and LP9 (Figure 3.48) at 60 kN, 210 kN, 240 kN, 251 kN, end of loading process, and at unloading condition. Figure 4.22 is the load and mid-span lateral deformation (LP5) curve. This figure indicates after reaching the ultimate load (U), there was lateral movement because of the web buckled rapidly (Figure 3.65b).

Small cracking noises were heard when the load reached points 1 and 2. However, no visible debonding of the CFRP was noticed. After reaching its ultimate load (U), the beam started to buckle at the web, resulting rapid drop in the load capacity. This specimen failed due to web buckling as shown in Figure 3.65b. Therefore, web stiffeners were welded to all the Group 2 specimens to avoid web buckling.

4.2.4.2 Strain distribution

Strain-deformation histories obtained from this specimen are shown in Figures 4.23 to 4.27. Similar plots but for strain-load histories obtained from this specimen are shown in Appendix IV Figures A4.23 to A4.27. The locations of the SGs are identified in Figure 3.47. The strain-deformation behaviors obtained from all steel strain gauges (S1 to S5) show a similar pattern. However, the strain magnitude increased from SG S5 to S4, SG S4 to S3, SG S3 to S2, and SG S2 to S1. The patterns of strain-deformation behavior of all CFRP strain gauges (C1 to C5) are also very similar. However, the strain magnitude increased from SG C5 to C4, SG C4 to C3, SG C3 to C2, and SG C2 to C1. In general, strain magnitude reduced as SG location moved towards the corrosion. Strain gauges C2 and S3 did not work.

It can be seen from Figure 4.23 to Figure 4.27 that the strain increased linearly and slowly until point Y. Also the slopes of the strain increments for steel and CFRP are similar. In between points Y and U, two small cracking sounds were heard indicating the debonding

of the CFRP. After first debonding, the difference between the strains in steel and CFRP gradually increased. After debonding, the steel SGs above corrosion area (S1, S2, and S3) show higher strain than the corresponding CFRP SGs (C1, C2, and C3). This is due to thinner steel flange at the corrosion area. Here, interpolation for strain data of SG C2 and S3 are assumed. After the beam reached its ultimate load (U), the web started to buckle causing the load and the strains to drop.

4.2.5 Summary of group1 specimens

The steel for CV-G1 and CC-G1 specimens first yielded followed by large elastic-plastic deformation (high ductility). The test for undamaged or virgin (CV-G1) specimen was discontinued at about 34 mm (large) deformation to avoid damage in equipment. The corroded control specimen (CC-G1) also exhibited large elastic-plastic deformation until it failed due to sudden severe web buckling at mid-span. The rehabilitated specimens exhibited different behaviors than the CV-G1 and CC-G1 specimens, because of addition of CFRP composites. The rehabilitation technique was able to restore the load capacity to the level of undamaged or virgin beam (CV-G1). However, ductility of the rehab beams reduced significantly (64.8% for RC-W67-T2.4-G1 and 71.1% for RC-W133-T2.4-G1).

Restoring the ultimate load of corroded of steel beams can be achieved by bonding CFRP to the steel beam as shown in Figure 4.28. By using a 67mm wide CFRP, specimen RC-W67-T2.4-G1 was able to achieve the same ultimate load as the control beam. Specimen RC-W133-T2.4-G1 increased its ultimate load by 3.3 percent compared to the control beam. (See table 4.3 for details). However, specimen RC-W133-T2.4-G1 had the lowest ductility amongst all group 1 specimens. Thus, the addition of CFRP makes the beam stiffer and less ductile.

The rehabilitation technique resulted in decreased in stiffness by 4.3% for both RC-W67-T2.4-G1 and RC-W133-T2.4-G1 (Table 4.4 and Figure 4.28b). Stiffness is not associated with width of the CFRP composite in this project, as wider CFRP composite does not correspond to higher stiffness value.

For specimen RC-W67-T2.4-G1, putty was used to fill in the corrosion. The putty was completely debonded and crushed under the load. Thus, use of filler putty is not a good choice for this kind of repair. For specimen RC-W133-T2.4-G1, CFRP sheets were used to fill in the corrosion with only minor debonding. Therefore, the use of CFRP sheets to level the corrosion was utilized in all future tests.

All of the specimens in group 1 had web and flange buckling, some less severe than others. Thus, web stiffeners were used in tests of group2 to avoid web buckling at mid-span under the load application point. Furthermore, flange stiffener was also used to avoid flange buckling under the load point.

4.3 Behavior of Group2 Specimens

As mentioned in Chapter 3, group2 contained one control virgin specimen (CV-G2), one control corroded specimen (CC-G2), and three fixed specimens (RC-W133-T2.4-G2, RC-W133-T1.2-G2, and RC-W133-T0.6-G2). All specimens had web stiffeners to prevent web buckling at mid-span, and flange stiffener to prevent flange buckling at top flange as discussed in section 3.3.4. Also the specimens were supported laterally at both top and bottom flanges using four lateral supports at each side of the beam specimens. Four steel round blocks were also mounted between top and bottom flanges under the load application point to reduce the flange buckling.

4.3.1 Specimen CV-G2

The load-deformation behavior for this specimen is shown in Figure 4.29. This specimen yielded at a load of 233 kN (point Y) and 6.9 mm vertical deformation. The ultimate load was 322 kN (point U) and the vertical deformation was 32.8 mm. The specimen failed at 197 kN (point F) and the vertical deformation was 36.5 mm, due to web buckling at the roller support (Figure 3.67b). The location of the salient points identified by Y, U, and F in the figure, depict the global yield load point, ultimate load point, and final load application point. The test was then discontinued.

Figure 4.30 shows the deformation response obtained from LP7, LP8, and LP9 (Figure 3.48) at 80 kN, 275 kN, 305 kN, 322 kN, end of loading process, and at unloaded condition. Figure 4.31 is the load and mid-span lateral deformation (LP5) curve, which shows that there was about 2 mm of lateral deformation for this specimen.

After the ultimate load applied to the specimen, the web buckled at the roller support as shown in Figure 3.67b, resulting the load to drop rapidly as shown in Figure 4.29. The lateral support close to the roller support failed at point F, and the test was discounted. This specimen (CV-G2) exhibited high ductility and did not fail either due to LT buckling, or due to top flange buckling, or due to buckling of web at mid-span.

This specimen was tested to obtain strength and ductility of the undamaged (virgin) beam specimen and thus no strain gauges (SG) were used in this specimen. Therefore, no strain data is available.

4.3.2 Specimen CC-G2

4.3.2.1 Load-deformation behavior and failure mode

The load-deformation behavior for this specimen is shown in Figure 4.32. Specimen CC-G2 yielded at a load of 212 kN (point Y) and 7.1 mm vertical deformation. The ultimate load was 260 kN (point U) and the vertical deformation was 20.2 mm. The specimen failed at 251 kN (point F) and the vertical deformation of 28.3 mm, due to steel cracked and splitted at the center of the corrosion (See Figure 3.69b). The location of the salient points identified by Y, U, F, 1 and 2 in the figure, depicts the global yield load point, ultimate load point, failure load point, steel beginning to tear, and complete flange tearing, respectively.

Figure 4.33 shows the deformation response obtain from LP7, LP8, and LP9 (Figure 3.48) at 65 kN, 220 kN, 250 kN, 260 kN, end of loading process, and at unloaded condition. Figure 4.34 is the load and mid-span lateral deformation (LP5) curve. This specimen exhibited about 3 mm of total lateral deformation. This lateral deformation occurred due to steel at the center of the corrosion reached its yield and cracked.

This specimen failed by steel yield followed by tearing (splitting) of the bottom flange at the center of the corrosion as shown in Figure 3.69b. The test was discontinued when the deformation reached about 30 mm to avoid damages in the equipments. There was no web or flange buckling (see Figure 4.35 for details). Figure 4.35 shows a picture of a section of the beam cut of from its mid-span.

4.3.2.2 Strain distribution

A few strain gauges (SG) were used in this specimen to study the strain distribution at the corrosion with respect to the beam's web (See Figure 3.47 for strain gauge locations). Strain-deformation behaviors obtained from this specimen are shown in Figures 4.36 and 4.37. Similar plot but for strain-load behaviors obtained from this specimen are shown in Appendix IV Figures A4.36 and A4.37. Strain-deformation behavior for SG S1 is shown on a separate figure since the SG experienced much higher strain than others did. It could be because the strain is located at thinnest part of the steel flange of corrosion area.

It can be seen from Figure 4.36 and 4.37 that the strain increased linearly and slowly until point Y and the slopes for all the strain increments are similar. Right after the yield point, the steel started to yield and the strain obtained from SG S1 increased rapidly until point 1. At point 1, the steel at the center of the corrosion started to tear and as a result, the strain at each measured location dropped rapidly. However, strains in SG S1 dropped significantly (Figure 4.36) since the gauges was located very close to the separation line. At point 2, the bottom flange steel was completely torn and separated at the center of the corrosion. In between points 2 and U, the strains obtained from SG S2 and SG S3 began to increase, while the strains in SG S4 and SG S5 decreased slightly. After ultimate load was applied to the specimen, the strains obtained from SG S2, SG S3, SG S4 and SG S5 continuously increased even though the load remained almost unchanged. This may be because the bottom flange steel was separated (splitted) at mid-span.

4.3.3 Specimen RC-W133-T2.4-G2

4.3.3.1 Load-deformation behavior and failure mode

This was a corroded specimen rehabilitated with 133 mm wide covering full width of flange and 2.4 mm thick (eight layers of Sikawrap Hex 230c) CFRP composite. The load-deformation behavior for this specimen is shown in Figure 4.38. This specimen yielded at a load of 255 kN (point Y) (specimen CV-G2 yield at 212 kN) and 7.6 mm vertical deformation. The ultimate load was 354 kN (point U) (specimen CV-G2 was 260 kN) with a vertical deformation of 13.8 mm. The specimen failed at 160 kN (point F) and vertical deformation of 16.5 mm (specimen CV-G2 was 36.5 mm), due to web buckling at the pin support (Figure 4.39). The location of the salient points identified by Y, U, F, and 1 in the figure depicted the yield point, ultimate load point, failure load point, and the CFRP debonding noise, respectively.

Figure 4.40 shows the deformation response obtained from LP7, LP8, and LP9 (Figure 3.48) at 90 kN, 300 kN, 335 kN, 254 kN, end of loading process, and at unloaded condition. The vertical deformation became unsymmetrical after the ultimate load (point U) was applied. Deformation at 400 mm away on the right of the mid-span of the beam (LP9) was 6.9 mm larger than the deformation at 400 mm away on the left of the mid-span of the beam (LP7). After unloading, the deformation difference between LP9 and LP7 was 6.7 mm. The unsymmetry in vertical deformation could be due to the web buckling at the pin support as shown in Figure 4.39. This Figure shows the end part of the beam.

Figure 4.41 is the load and mid-span lateral deformation (LP5) curve, which shows that there was very small (0.46 mm maximum) lateral deformation in this specimen. This lateral deformation could be because of the unsymmetrical cross-section.

This specimen failed due to sever web buckling at the pin support, as shown in Figure 3.71d. The test was discontinued shortly after the web buckled at pin support. Ductility of this specimen reduced significantly (see Table 4.2). There was no web or flange buckling at the mid-span (under the load application point) as shown in Figure 4.42. Figure 3.71b

shows the web buckled at roller support, and Figure 3.71c shows the flange buckled slightly at roller support. Although CFRP debonding noise was heard at point 1, no visible sign of debonding could be found (See figure 4.43 for details). Figure 4.42 and 4.43 show a piece of specimen cut out from the mid-span of the beam specimen.

4.3.3.2 Strain distribution

Strain-deformation behavior obtained from this specimen are shown in Figures 4.44 to 4.48. Similar plot but for strain-load data obtained from this specimen are shown in Appendix IV Figures A4.44 to A4.48. The locations of the strain gauges are shown in Figure 3.47. The strain-deformation behaviors obtained from all steel strain gauges (S1 to S5) show a similar pattern. However, the strain magnitude increased from SG S5 to S4, SG S4 to S3, SG S3 to S2, and SG S2 to S1. The patterns of strain-deformation behavior of all CFRP strain gauges (C1 to C5) are also very similar. However, the strain magnitude increased from SG C5 to C4, SG C4 to C3, SG C3 to C2, and SG C2 to C1. In general, strain magnitude reduced as SG location moved towards the corrosion. Strain gauges C2 and S3 did not work.

It can be seen in Figures 4.44 to 4.48 that the strain increased almost linearly until point Y. Also the slopes of the strain increments for steel and CFRP are similar. Beyond yield point (Point Y), the differences between the strains in steel and the CFRP increased indicating that the load may not have fully transferred from the steel to CFRP beyond yield point (Point Y). However, as mentioned earlier, no visible sign of debonding was found on the specimen. After debonding occurred (point 1), the specimen resumed increasing its load, increasing the strains in steel and CFRP until point U (ultimate load). In between point Y and U, a small CFRP debonding sound was heard at point 1, indicating the CFRP started to debond, causing all the strains to drop slightly at all measuring points. At ultimate load (point U), the web at the pin support buckled and the load dropped suddenly. The strains for the CFRP under the corrosion (C1 to C3) dropped significantly. This may be due to sudden drop of load capacity at ultimate load (point U). After the sudden drop in strain, the strain in SG C1 to C3 increased slightly till the end of loading. This is because SG C1 to C3 were located at the corrosion area resulting higher

strain (tie action) in these gauges. The strains at all other locations (SG C4, C5, and SG S1 to S5) dropped at much lower rate from ultimate load (point U) to failure load point (point F).

4.3.4 Specimen RC-W133-T1.2-G2

4.3.4.1 Load-deformation behavior and failure mode

This was a corroded specimen rehabilitated with 133 mm wide covering full flange width and 1.2 mm thick (four layers of Sikawrap Hex 230c) CFRP composite. The load-deformation behavior for this specimen is shown in Figure 4.49. Specimen RC-W133-T1.2-G2 yielded at a load of 250 kN (point Y) (specimen CV-G2 yield at 212 kN) and 8.0 mm vertical deformation. The ultimate load was 330 kN (point U) (specimen CV-G2 was 260 kN) and the vertical deformation was 20.9 mm. The specimen failed at 189 kN (point F) and the vertical deformation was 27.8 mm (specimen CV-G2 was 36.5 mm), due to web buckled at pin support. The locations of the salient point identified by Y, U, F, 1 and 2 in the figure, indicates the specimens global yield load point, ultimate load point, failure load point, CFRP debonding noise and severe web buckle at pin support respectively.

Figure 4.50 shows the vertical deformation response obtained from LP7, LP8, and LP9 (Figure 3.48) at 80 kN, 280 kN, 315 kN, 330 kN, end of loading process, and at unloaded condition. The deformation became unsymmetrical after the ultimate load (point U) was applied. At the end of the loading process (point F), the vertical deformation at 400 mm away on the right side of mid-span of the beam specimen (LP9) was 7.7 mm larger than the vertical deformation at 400 mm away on the left side of mid-span of the beam specimen (LP7). At unloaded condition, the vertical deformation difference between LP9 and LP7 was 4.2 mm. This seems to be due to the web buckling at the pin support (See Figure 4.51 and Figure 3.73b). Figure 4.51 shows a small section of beam cut out from the pin support end of the beam specimen. Figure 4.52 depicts the load and mid-span lateral deformation (LP5) curve, which shows there was about 2 mm of lateral deformation of the beam specimen.

Small debonding noise was heard when the load reached point 1. The CFRP debonding were later found after taking a small section of the specimen at mid-span of the beam (see Figure 4.53). After reaching the ultimate load, the load started to drop slowly, and the web at the pin support started to buckle. When the deformation reached point 2, the buckling became significant, resulting in the rapid drop in the load capacity (Figure 4.49). This test was then discontinued. No web or flange buckling at the mid span of the specimen occurred (Figure 4.54). This specimen exhibited more ductility than specimen RC-W133-T2.4-G2, but little lesser ductility than CV-G2.

4.3.4.2 Strain distribution

Strain-deformation behavior obtained from this specimen are shown in Figures 4.55 to 4.59. Similar plot but for strain-load behavior for this specimen are shown in Appendix Figures IV A4.55 to A4.59. The locations of the strain gauges are shown in Figure 3.47. The strain-deformation behaviors obtained from all steel strain gauges (S1 to S5) show a similar pattern. However, the strain magnitude increased from SG S5 to S4, SG S4 to S3, SG S3 to S2, and SG S2 to S1. The patterns of strain-deformation behavior of all CFRP strain gauges (C1 to C5) are also very similar. However, the strain magnitude increased from SG C5 to C4, SG C4 to C3, SG C3 to C2, and SG C2 to C1. In general, strain magnitude reduced as SG location moved towards the corrosion. Strain gauges C2 and S3 did not work.

It can be seen in Figures 4.55 to 4.59 that the strain increased linearly and slowly until point Y. Also, the slopes of the strain increment for steel and CFRP are similar. Between points Y and U, one cracking sound was heard at point 1 and the load dropped slightly (Figure 4.49). SG C1 and SG C3 failed soon after this debonding (point 1). Figure 4.58 shows that the strain in SG C4 dropped rapidly at point 1, indicating debonding occurred around location C4. The strain in all other steel SGs (SG S2, SG S3, and SG S5) dropped slightly. The strain for the CFRP SG C2, C4, and C5 increased rapidly. This could be because the steel was already yielded, and CFRP was carrying the additional load. Because of this debonding, the differences between strains in the steel and the CFRP increased. This indicates that the load did not fully transfer from the steel to the CFRP.

However, as mentioned before, during the test, no visible sign of debonding was found on the specimen. After debonding occurred, the specimen resumed increasing loads (Figure 4.49) and the strains for the CFRP continued to increase while the strain for steel remained nearly unchanged. The steel SG at the center of the corrosion (SG S1) failed when the global deformation reached 19 mm. The specimen reached its ultimate load point at 330 kN and 20.9 mm vertical deformation (Figure 4.49). Between points U (ultimate load) and 2 (large buckling in the web at pin end), the strains in all SGs (Steel and CFRP SGs) expect SG C2 remained unchanged while the load decreased rapidly and deformation increased very little. The incense in strain at location C2 is because SG C2 is located at thinner steel flange at the corrosion area. The strains for the CFRP SG C2 failed at point U. However, the strains in SG S4, and SG S5 dropped slightly and strains in remaining SGs at all other locations increased slightly.

4.3.5 Specimen RC-W133-T0.6-G2

4.3.5.1 Load-deformation behavior and failure mode

This is a corroded specimen rehabilitated with 133 mm wide covering the full flange width and 0.6 mm thick (two layers of Sikawrap Hex 230c) CFRP composite. The load-deformation behavior for this specimen is shown in Figure 4.60. This specimen had a yield load of 215 kN (point Y) (specimen CV-G2 yield at 212 kN) and 6.5 mm vertical deformation. The ultimate load was 276 kN (point U) (specimen CV-G2 was 260 kN) and the vertical deformation was 11.6 mm. The specimen failed at 247 kN (point F) and the vertical deformation was 31.4 mm (specimen CV-G2 was 36.5 mm), due to CFRP and steel splitted at mid-span of the beam (at the corrosion). The locations of the salient points identified by Y, U, F, 1 2, and 3 in the figure, depict the yield point, ultimate load point, failure load point, CFRP first, second, and third debonding noise, respectively.

Figure 4.61 shows the deformation response obtained from LP7, LP8, and LP9 (Figure 3.48) at 70 kN, 235 kN, 260 kN, 276 kN, end of loading process, and at unloaded condition. Figure 4.62 is the load and mid-span lateral deformation (LP5) curve, which

shows that the steel at the corrosion starts to rip (point 1) until the failure load point (shown by point F). There was about 3 mm of total lateral deformation.

Small debonding noise was heard when the load reached point 1, indicating CFRP debonding, due to the deformation at the corroded area of the steel. The CFRP cross-wraps adjacent to corrosion also ruptured and debonded at this point. After reaching the ultimate load, two more loud cracking sounds (point 2 and 3) were heard. At point 3, both CFRP splitted and fibers broken, and steel fractured at the corroded area as shown in Figure 4.63 to 4.65. These figures show a section of the beam cut from mid-span of the beam specimen.

The failure mode of this specimen was the steel yield, followed by the CFRP splitting and steel rupture at the corrosion area. After point 3 (third debonding of CFRP), the loading capacity dropped to CC-G2 level, indicating that rehabilitation method at this point became totally ineffective. Since the specimen could no longer increase its load, the test was discounted when the deformation reached 30 mm. Figure 3.75b shows there was no flange buckling under the load application point. This specimen did not experience web buckling.

4.3.5.2 Strain distribution

Strain-deformation data obtained from this specimen are shown in Figures 4.66 to 4.70. Similar plot but for strain-load data obtained from this specimen are shown in Appendix IV Figures A4.66 to A4.70. The locations of the SGs are shown in Figure 3.47. The strain-deformation behaviors obtained from all steel strain gauges (S1 to S5) show a similar pattern. The patterns of strain-displacement behaviors of all CFRP strain gauges (C1 to C5) are also very similar.

It can be seen from Figures 4.66 to 4.70 that the strain increased linearly and slowly until point Y. In addition, the slopes of the strain increment for steel and CFRP are similar. Between points Y and U, one cracking sound was heard. At this point, slightly drop in strain occurred at SG S1, S3, S4, S5, C4, and C5. The strain at all other locations dropped significantly. This is because the CFRP debonded under the corrosion. Immediately after

this debonding, the strain in the steel gauges SG S1 and SG S2 increased rapidly, and strain of CFRP obtained from SG C1 and SG C2 were relatively low, as a result of the CFRP debonding. Strain in SG S1 dropped shortly to a lower value, this is because the steel under the corrosion was starting to rupture. Since the CFRP debonded under the corrosion, the load was carried by CFRP beyond location C3. Due to the large amount load was carried by CFRP beyond location C3, CFRP ruptured at location C3 and C4. As a result, SG C 3 and SG C4 failed shortly after debonding (point 1).

In between point U (ultimate load) and point 2 (second cracking sound), the strain in SG S1 and C1 dropped, while the strain in other SG increased. This is because the steel was rupturing. After the beam reached the ultimate load, two more cracking sounds were heard (points 2 and 3). When the second cracking sound (point 2) were heard, strains in SG C1, C2, C5, S2, and S5 drop significantly, strains in SG S1, S4 and S5 drop slightly. This is because more CFRP debonding happed and steel is continue to rupture under the corroded area. The strains in SG S3 increased significantly at the same time, this is because SG S3 is located at the edge of the corrosion, where the steel bottom flange is thinner. After point 3 (third cracking sound), all the strain obtained from all locations except SG S1 and SG S5 dropped to less than 1000 micro-strain. This means the load was no longer carried by the steel or CFRP at locations 1, 2, 3 and 4. At this point, the CFRP splitted and fibers broken, and steel fractured.

4.3.6 Conclusion on group2 specimens

The control virgin (undamaged) and control corroded specimens failed primarily due to the steel yield (Table 4.3). The rehabilitated specimens exhibited different behavior than the control specimen, because of the addition of CFRP matrix. The results of the rehabilitation technique was successful in restoring the ultimate load to the level of control virgin beam as shown in Figure 4.71.

4.3.6.1 Yield load

Yielding load is associated with tension steel strain. Table 4.1 illustrates the summary of the maximum strains in steel and CFRP at different loading stages for steel and CFRP in

the tension zone. As mentioned before, the CFRP composites were applied on the outside surface of the bottom flange which sustained more strain than the inner surface of the bottom flange. The yielding load was affected due to use of CFRP matrix. Table 4.3 illustrates the measured yield and ultimate loads for all specimens, a percentage increase of 9.4%, 7.3% and -7.7% between specimens CV-G2 and RC-W133-T2.4-G2, RC-W133-T1.2-G2, and RC-W133-T0.6-G2 respectively. A negative sign indicates decrease in load capacity. Thus, RC-W133-T2.4-G2 and RC-W133-T1.2-G2 showed increase in yield load capacity, but RC-W133-T0.6-G2 failed to go to the level of control virgin specimen.

4.3.6.2 Ultimate load

Table 4.3 summarizes the ultimate load carrying capacity for each group. The rehabilitation technique resulted in increase in load carrying capacity by 9.9%, 2.5%, and -14.3% for RC-W133-T2.4-G2, RC-W133-T1.2-G2 and RC-W133-T0.6-G2, respectively. when compared to CV-G2. A negative sign indicates decrease in load capacity. Thus, RC-W133-T2.4-G2 and RC-W133-T1.2-G2 showed increase in ultimate load capacity, but RC-W133-T0.6-G2 failed to go to the level of control virgin specimen. It should be noted from these results that the thickness of the CFRP is important in the rehabilitation method. The maximum depth of corrosion in this project was 4 mm (Figure 3.8), and the optimum thickness of the CFRP matrix required in this project was 1.2mm (four layers of Sikawrap Hex 230c).

4.3.6.3 Stiffness

Table 4.4 summarizes the stiffness for each group. The rehabilitation technique resulted in increase in stiffness by 8.4%, 5.7%, and 2.3% for RC-W133-T2.4-G2, RC-W133-T1.2-G2 and RC-W133-T0.6-G2, respectively (Table 4.4 and Figure 4.71b). Stiffness is associated with thickness of the CFRP composite in this project, as thicker CFRP composite correspond to higher stiffness value.

4.3.6.4 Ductility

Ductility is the ability of a structure to undergo large deformation before its failure. It is an important requirement in the design of any structural element. Ductile structure can

exhibit large plastic deformation before failure; therefore, it provides visual indications to provide the opportunity for remedial actions prior to complete collapse.

Ductility is defined as the global deformation at the first sign of failure, which is presented in Table 4.2 for all specimens. As expected, control virgin specimens exhibited the most ductile behavior. Since the retrofit applications result in an extra reinforcement, the bending stiffness of the specimen (EI) increases as the thickness of the CFRP increases. The bending stiffness increased by 10%, 5.4% and 3% for RC-W133-T2.4-G2, RC-W133-T1.2-G2 and RC-W133-T0.6-G2 respectively, when compared to CV-G2 (See Appendix II for details). Ductility is associated with bending stiffness in this project, as higher values of bending stiffness correspond to lower ductility. The ductility changed from 35.1 to 13.8 mm (61% reduction) for RC-W133-T2.4-G2 (eight layers of Sikawrap Hex 230c) compared to CV-G2. This changed from 35.1mm to 25.9 mm (26% reduction) for RC-W133-T1.2-G2 (four layers of Sikawrap Hex 230c); and from 35.1 mm to 31 mm (12% reduction) for RC-W133-T0.6-G2 (two layers of Sikawrap Hex 230c) (Table 4.2).

4.3.6.5 Strain

Table 4.1 illustrates a sample of the strains during different loading stages for the steel and CFRP. The highest strain for both the steel and CFRP were found at the center of the corrosion (locations C1 and S1). Strains measured at locations C5 and S5, the strain measure location furthest from the center of the corrosion, have the lowest values. The strain in the steel is similar to that of the CFRP until debonding occurred. Once debonding occurred, the load could not fully transfer to the CFRP through the bonding, and the different strains between CFRP and steel increased.

4.4 Summary

This chapter discussed all the test results, which include vertical deformation, ultimate load, lateral deformation, strain in steel, and strain in CFRP.

Table 4.1: Summary of the test results (Steel and CFRP strain)*

ε	Steel strain ε (micro strain)[1]			CFRP strain ε (micro strain)[1]		
Specimen	ε P_y	ε P_{ult}	ε_{max}	ε P_y	ε P_{ult}	ε_{max}
Group 1						
CV-G1	--	--	--	--	--	--
CC-G1[2]	18541	68821	953444[3]	--	--	--
RC-W67-T2.4-G1	23886	994203[3]	994203[3]	1760	3257	3943
RC-W133-T2.4-G1	2506	11347	14048	2363	3521	3636
Group 2						
CV-G2	--	--	--	--	--	--
CC-G2	6692	13727	36378	--	--	--
RC-W133-T2.4-G2	2837	15267	15897	2890	7436	7501
RC-W133-T1.2-G2	1867	69803	1003024[3]	3921	1004309[3]	1004309[3]
RC-W133-T0.6-G2	1934	2089	17738	2026	1004638[3]	1004638[3]

[1]The reading expects CC-G1 represent:
Strain gauge S5 (longitudinal tension steel strain at center of the top side of the bottom flange, Figure 3.47)
Strain gauge C5 (longitudinal tension CFRP strain at center of the CFRP wraps, Figure 3.47)

[2] The reading represent Strain gauge 4 (longitudinal tension steel strain at center of the top side of the bottom flange, Figure 3.46)

[3] Strain gauge failed

Strain at P_y is the strain when yield load applied.

Strain at P_{ult} is the strain when ultimate load applied.

Strain at P_{max} is the maximum strain recorded in the test

Table 4.2: Summary of the test results (mid-span vertical deformation and ductility change)

Specimen	Δ_y mm	Δ_{ult} mm	$\Delta_{failure}$ mm	$\%\Delta_y$ Decreasing	$\%\Delta_{ult}$ Decreasing	$\%\Delta_{failure}$ Decreasing
Group 1						
CV-G1	7.0	31.5	31.5	--	--	--
CORRODED	5.7	13.4	20.3	18.6%	57.5%	35.6%
RC-W67-T2.4-G1	6.7	11	11.1	4.3%	65.1%	64.8%
RC-W133-T2.4-G1	6.9	9.1	9.1	1.4%	71.1%	71.1%
Group 2						
CV-G2	6.9	33.9	35.1	--	--	--
CC-G2	7.1	20.2	28.0	-3%	40.4%	20.2%
RC-W133-T2.4-G2	7.6	13.8	13.8	-10.1%	59.3%	60.7%
RC-W133-T1.2-G2	7.9	20.8	25.9	-14.5%	38.6%	26.2%
RC-W133-T0.6-G2	6.5	8.1	31	5.8%	76.1%	11.7%

Δ_y is the mid-span vertical deformation when the yield load applied.
Δ_{ult} is the mid-span vertical deformation when the ultimate load applied.
$\Delta_{failure}$ is the mid-span vertical deformation at first sign of failure.

Table 4.3: Summary of the test results (load values and failure mode)

Specimen	P_y kN	P_{ult} kN	$\%P_y$ Increasing	$\%P_{ult}$ Increasing	Type of failure
Group 1					
CV-G1	202	243	--	--	Steel yield, was stopped for safety of the equipments
CORRODED	165	215	-18.3%	-11.5%	Steel yield follow by web buckled at mid-span
RC-W67-T2.4-G1	200	236	1%	-2.9%	CFRP debonded
RC-W133-T2.4-G1	227	251	12.4%	3.3%	Web buckled at mid-span
Group 2					
CV-G2	233	314	--	--	Steel yield followed by web buckled at roller support
CC-G2	212	260	-9.0%	-17.2%	Steel yield and ruptured at corrosion
RC-W133-T2.4-G2	255	354	9.4%	12.7%	Web buckled at pin support
RC-W133-T1.2-G2	250	330	7.3%	5.1%	Web buckled at pin support
RC-W133-T0.6-G2	215	276	-7.7%	-12.1%	Steel yield follow by CFRP and steel rupture

Table 4.4: Summary of the test results (stiffness)

Specimen	Stiffness kN/mm	% stiffness increase
Group 1		
CV-G1	32.4	--
CORRODED	28.2	-13.0%
RC-W67-T2.4-G1	31.0	-4.3%
RC-W133-T2.4-G1	31.0	-4.3%
Group 2		
CV-G2	34.8	--
CC-G2	32.3	-7.2%
RC-W133-T2.4-G2	38.0	8.4%
RC-W133-T1.2-G2	36.8	5.7%
RC-W133-T0.6-G2	35.6	2.3%

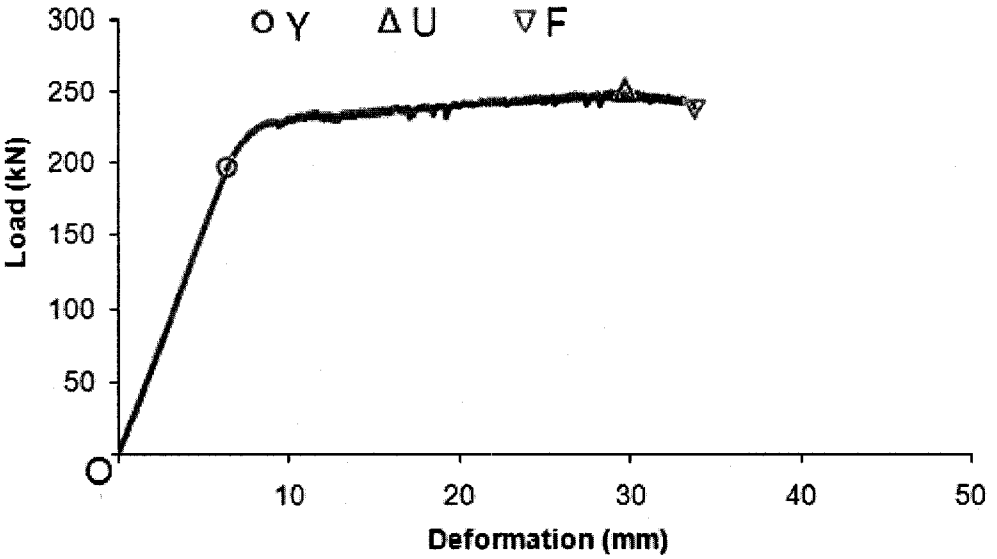

Figure 4.1: Load vs. mid span (LP8) vertical deformation behavior of CV-G1

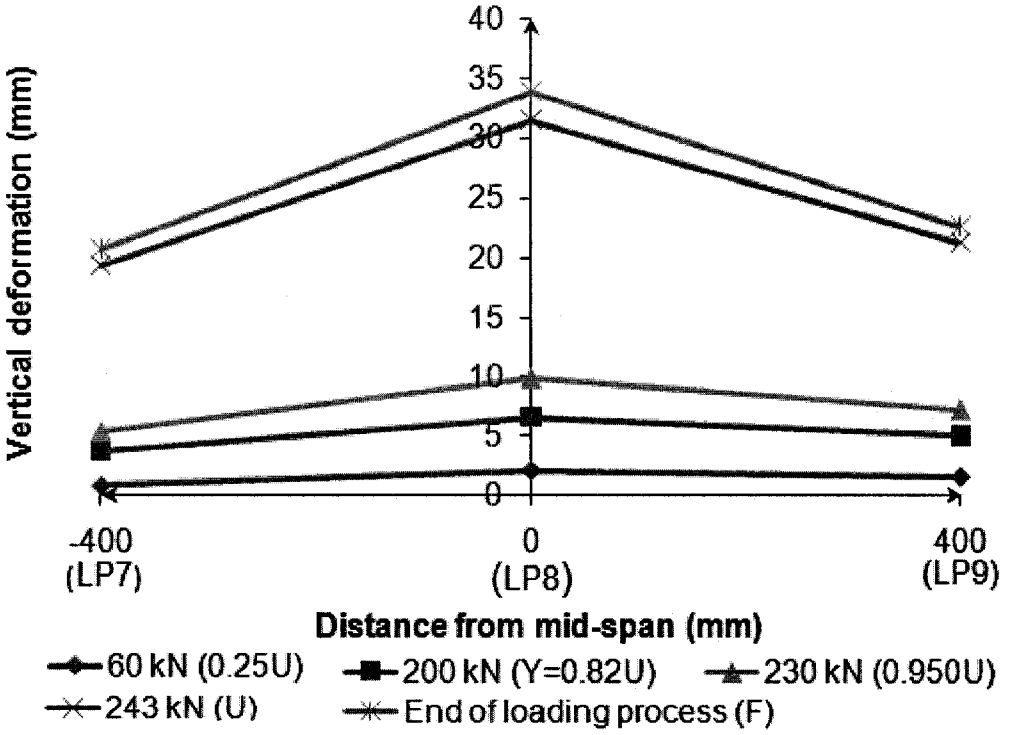

Figure 4.2: Vertical deformation response for CV-G1

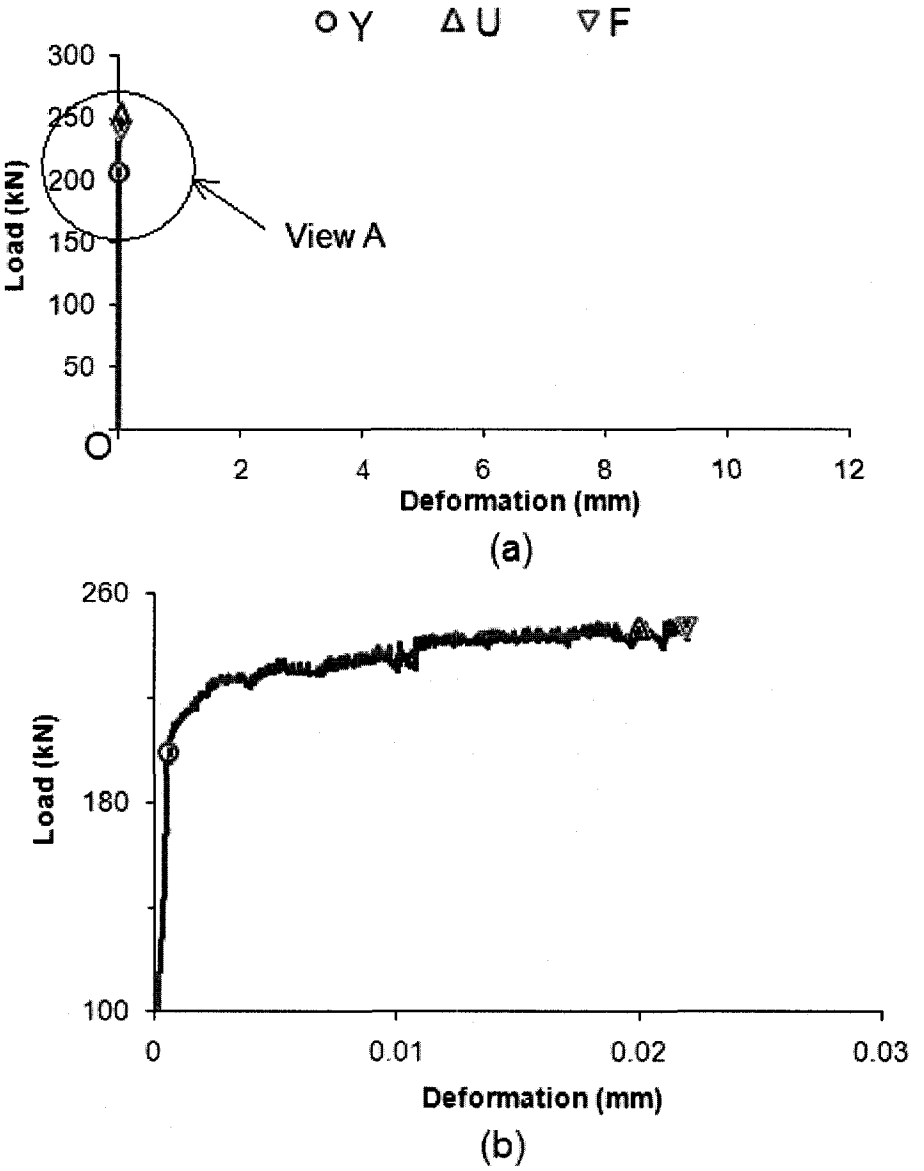

Figure 4.3: (a) Load vs. mid span (LP5) lateral deformation behavior of CV-G1 and (b) Details of view "A"

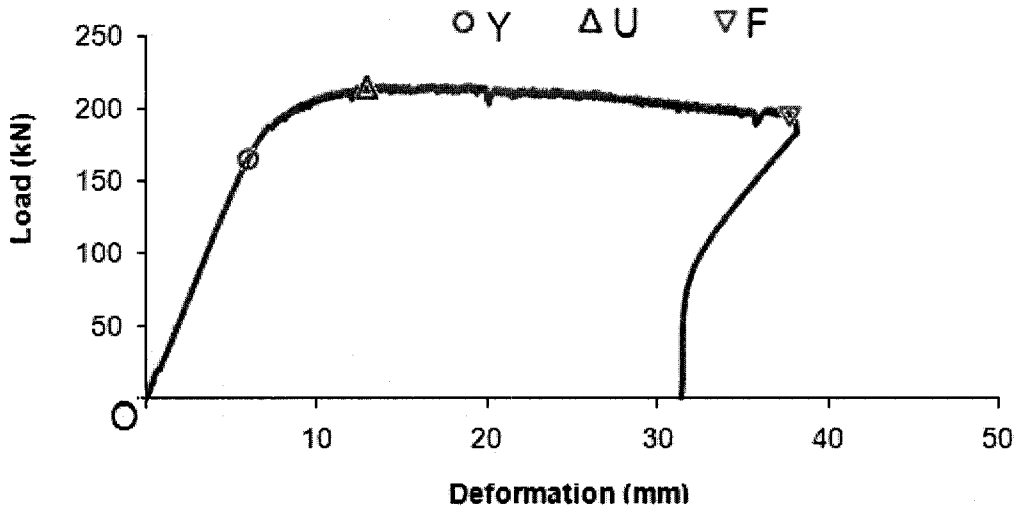

Figure 4.4: Load vs. mid span (LP8) vertical deformation behavior of CC-G1

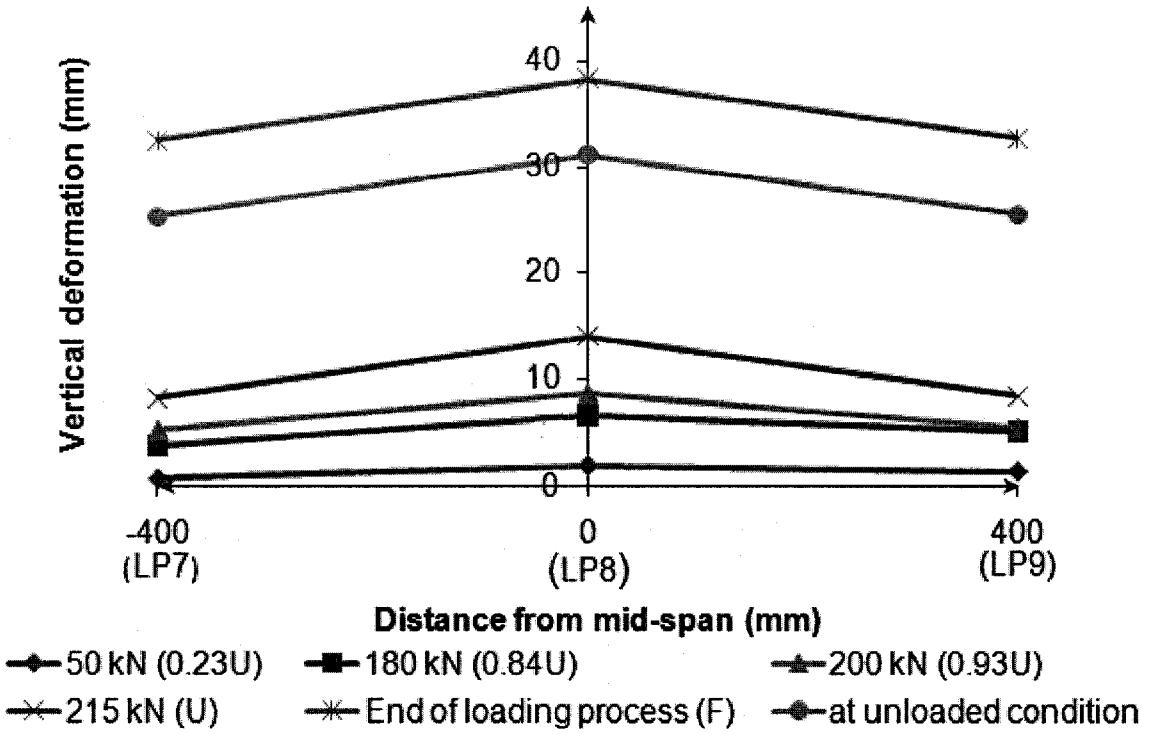

Figure 4.5: Vertical deformation response for CC-G1

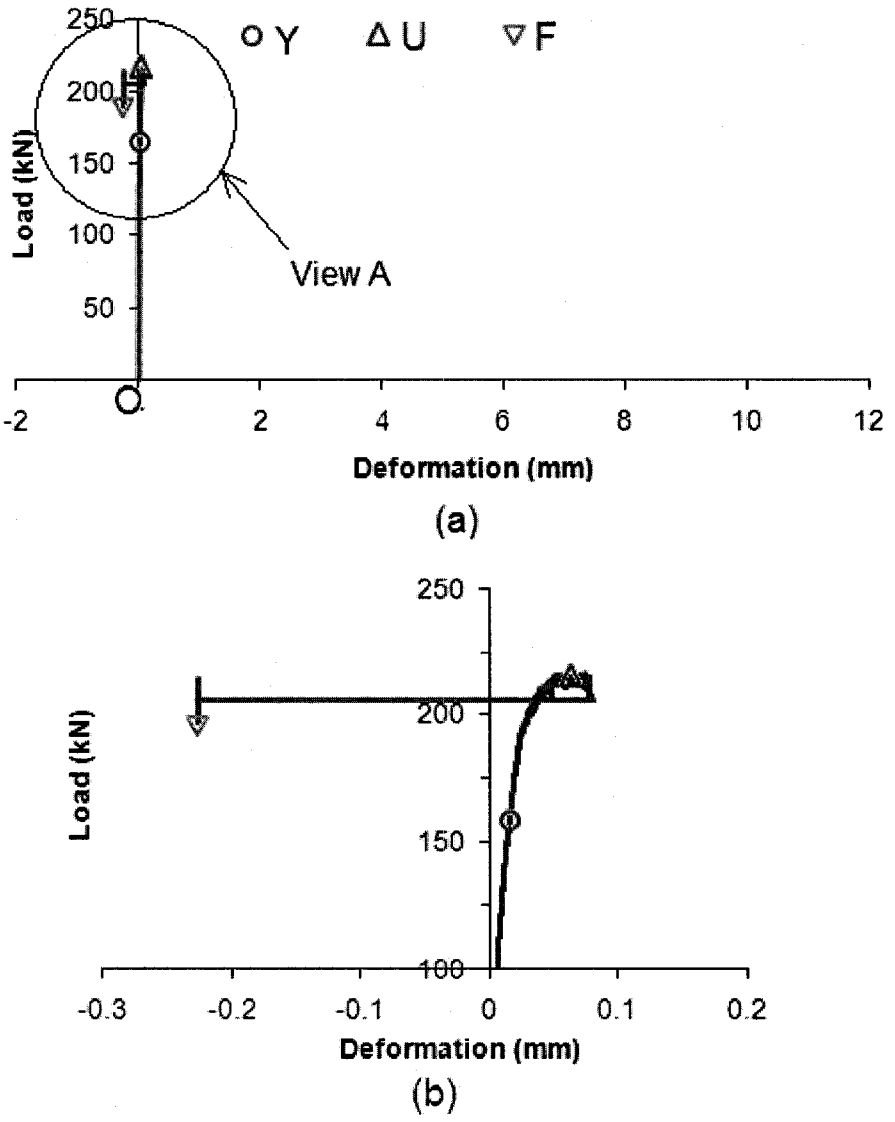

Figure 4.6: (a) Load vs. mid span (LP5) lateral deformation behavior of CC-G1 and (b) Details of view "A"

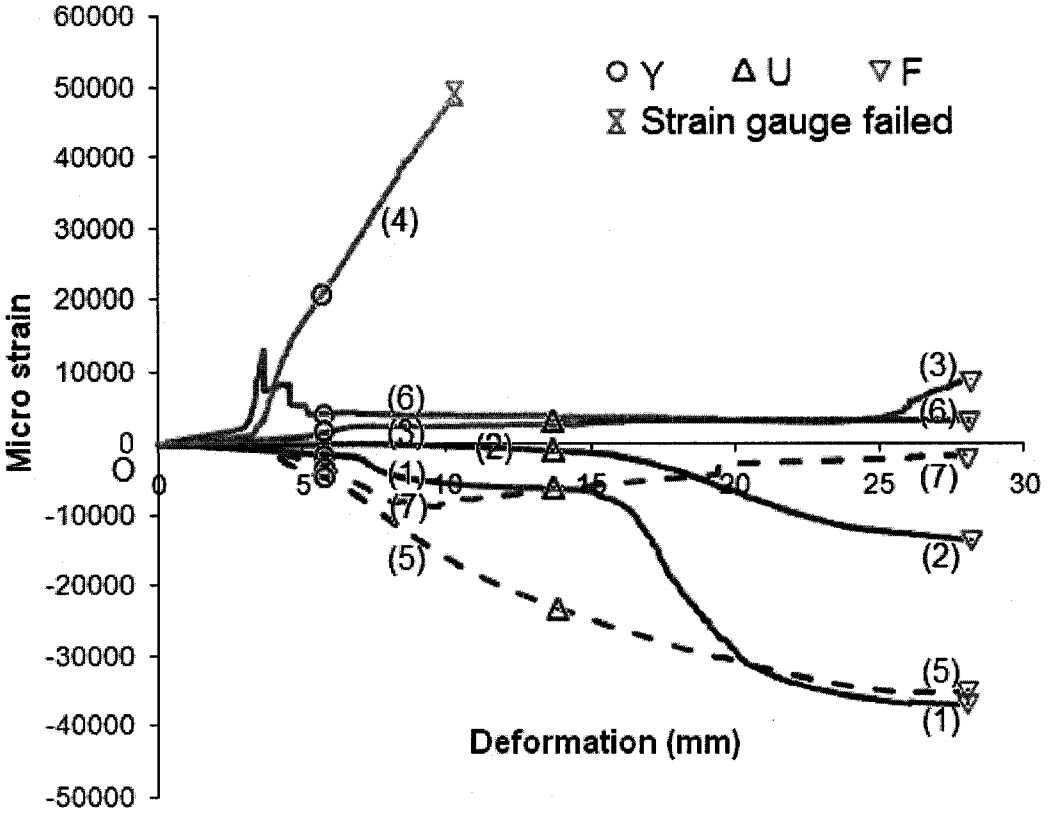

Figure 4.7: Local strain vs. deformation CC-G1 (Strain Gauge 1-7)

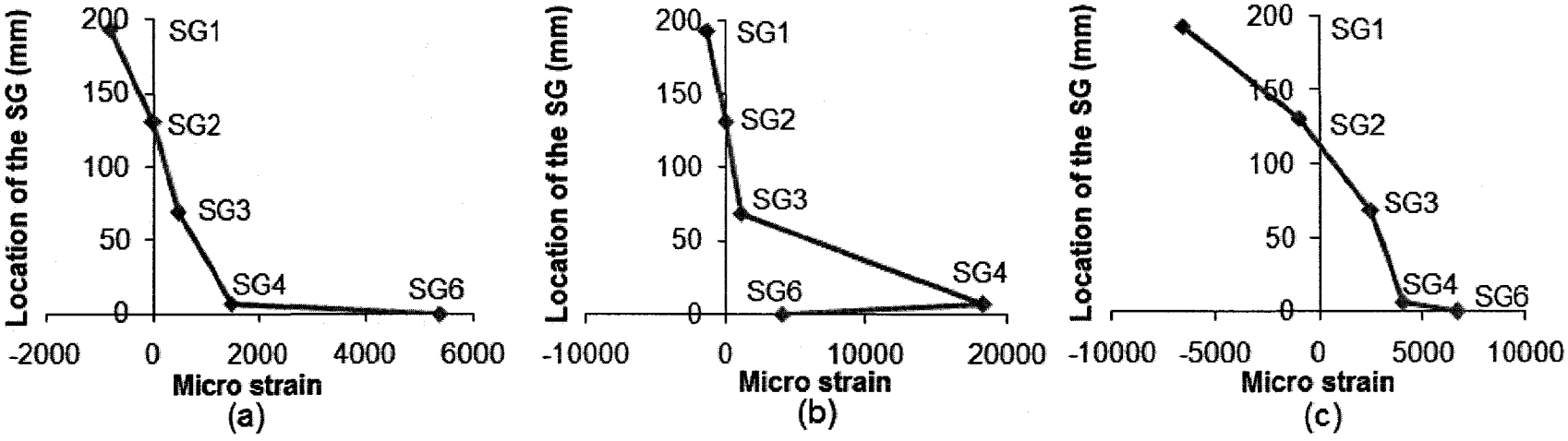

Figure 4.8: Strain distribution CC-G1 (Strain Gauge 1, 2, 3, 4, and 6)
(a) at 100 kN, (b) at 165 kN (yield load), and (c) at 215 kN (ultimate load)

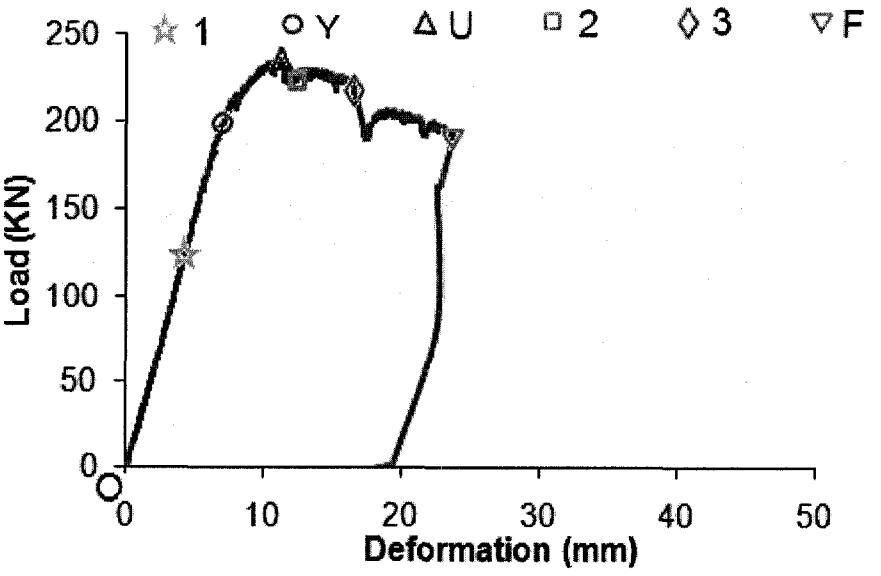

Figure 4.9: Load vs. mid span (LP8) vertical deformation behavior of RC-W67-T2.4-G1

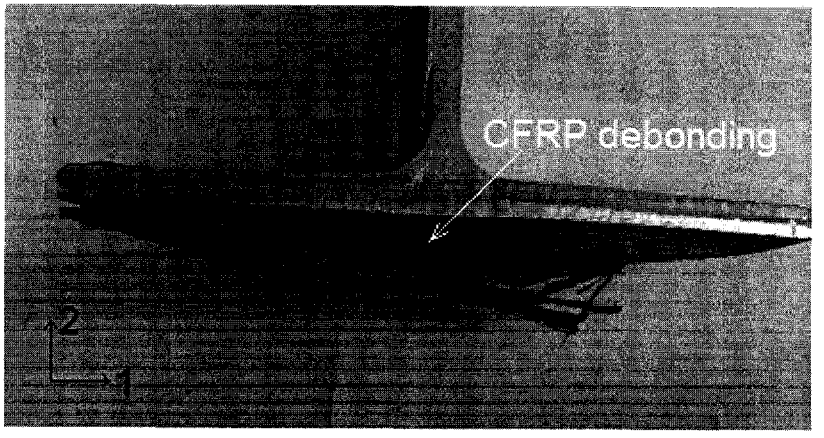

Figure 4.10: RC-W67-T2.4-G1: CFRP debonding

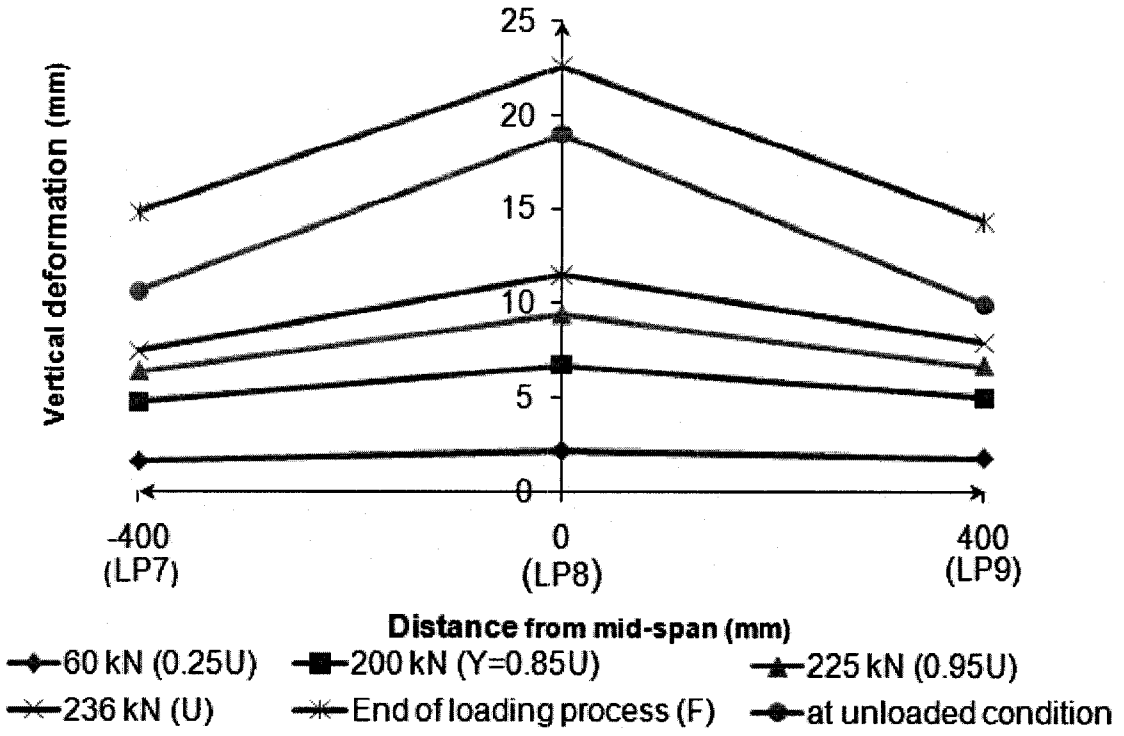

Figure 4.11: Vertical deformation response for RC-W67-T2.4-G1

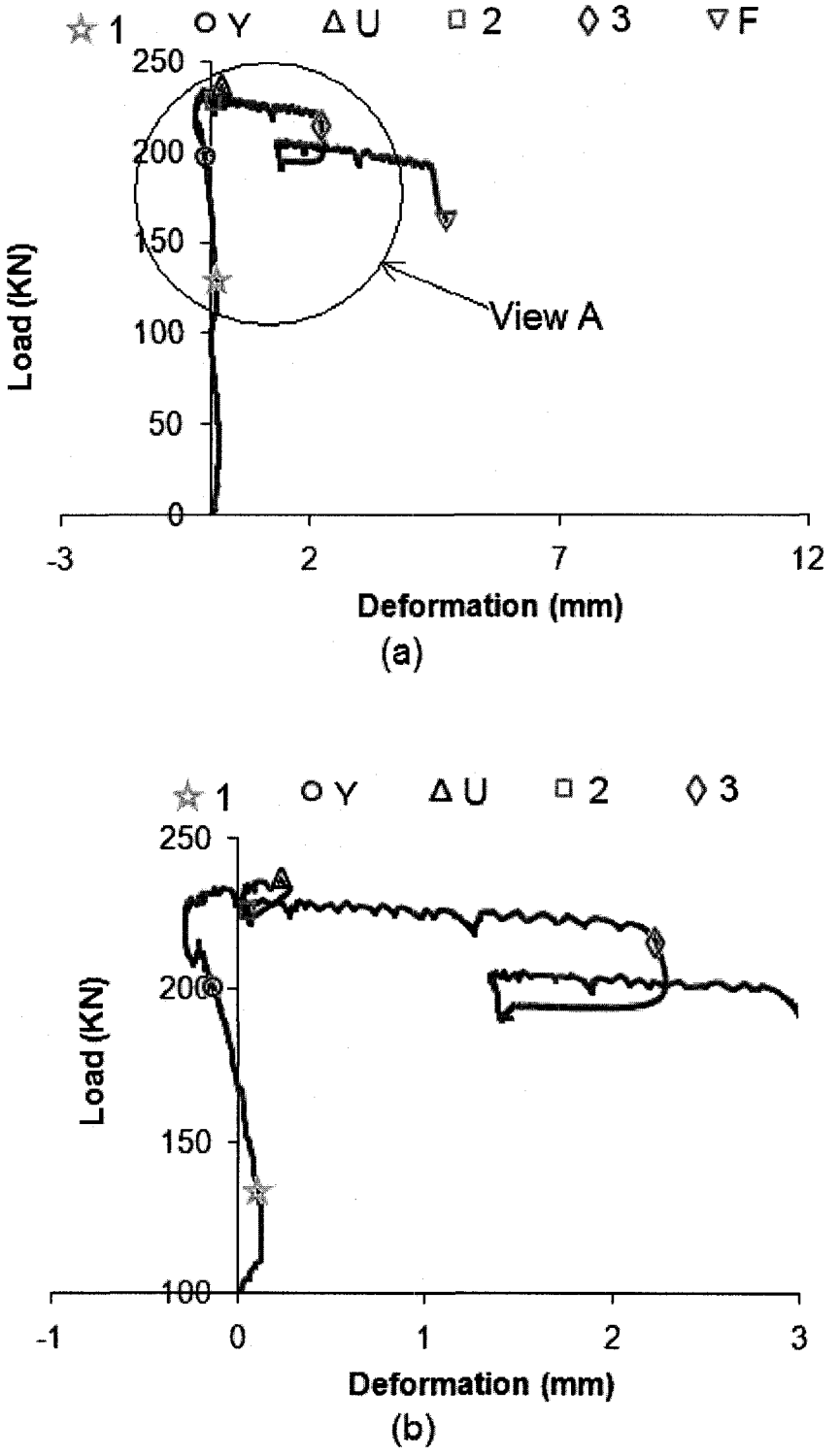

Figure 4.12: (a) Load vs. mid span (LP5) lateral deformation behavior of RC-W67-T2.4-G1 and (b) Details of view "A"

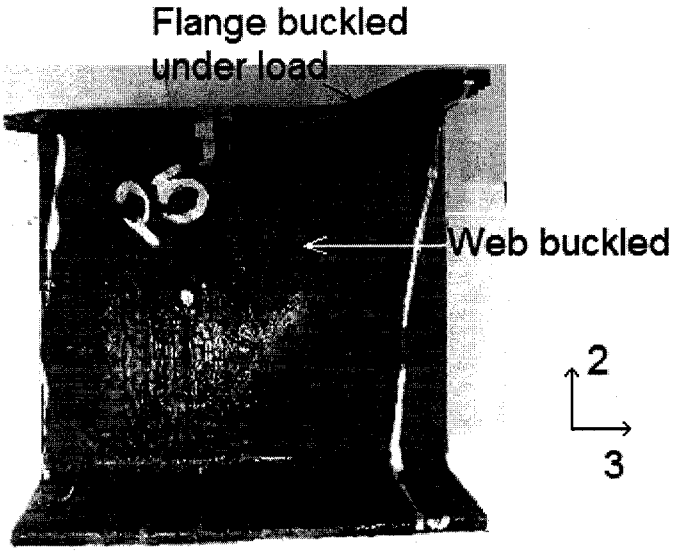

Figure 4.13: RC-W67-T2.4-G1: Flange and web buckled under the load

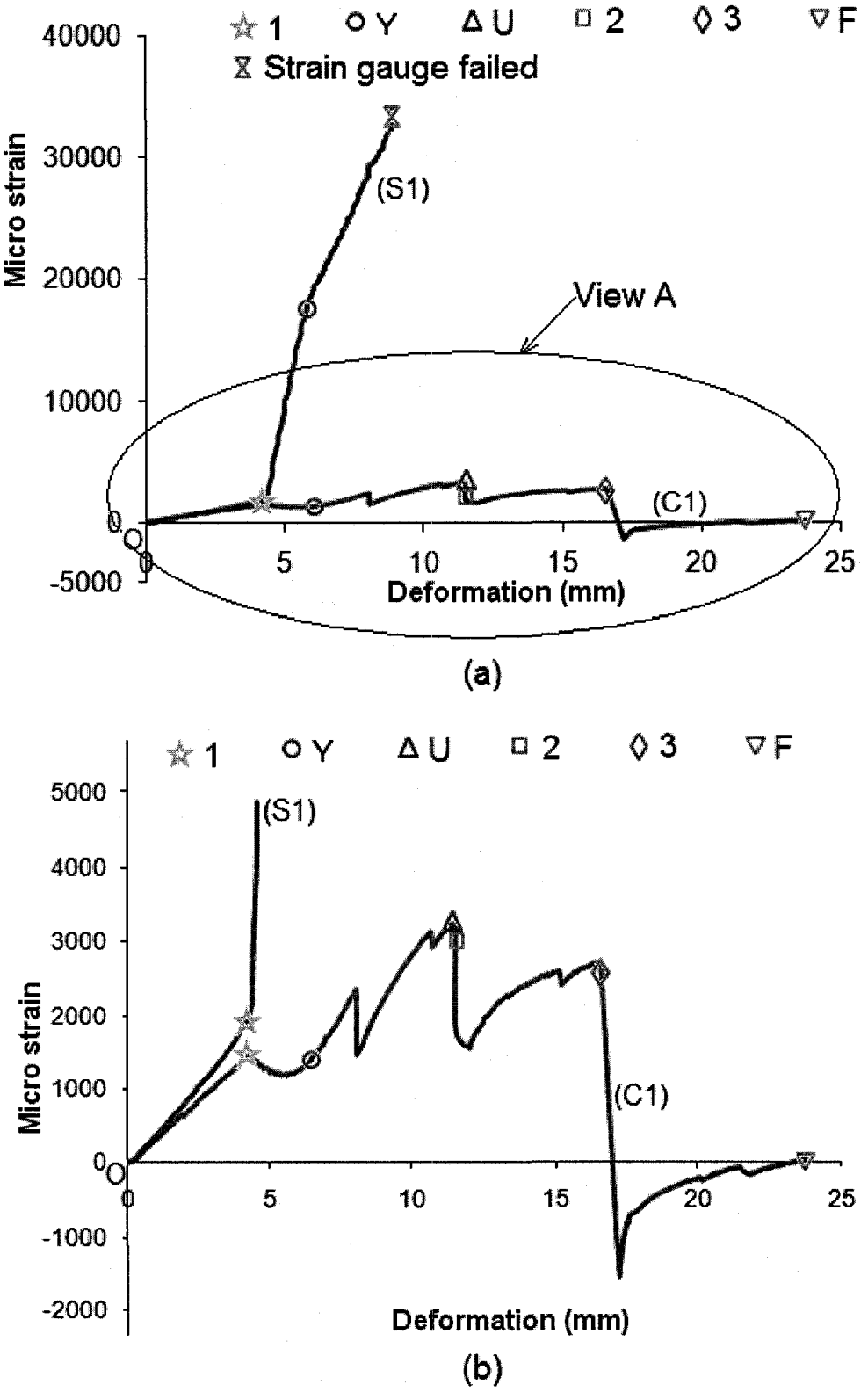

Figure 4.14: (a) Local strain from SG C1 & S1 vs. deformation for RC-W67-T2.4-G1 and (b) Details of View "A"

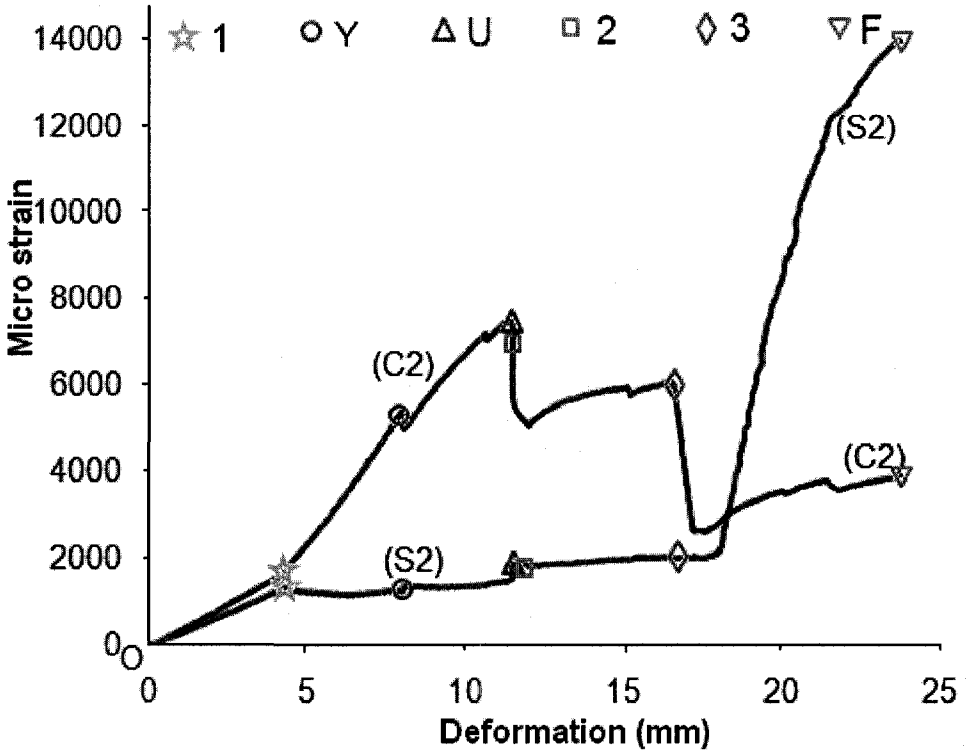

Figure 4.15: Local strain from SG C2 & S2 vs. deformation for RC-W67-T2.4-G1

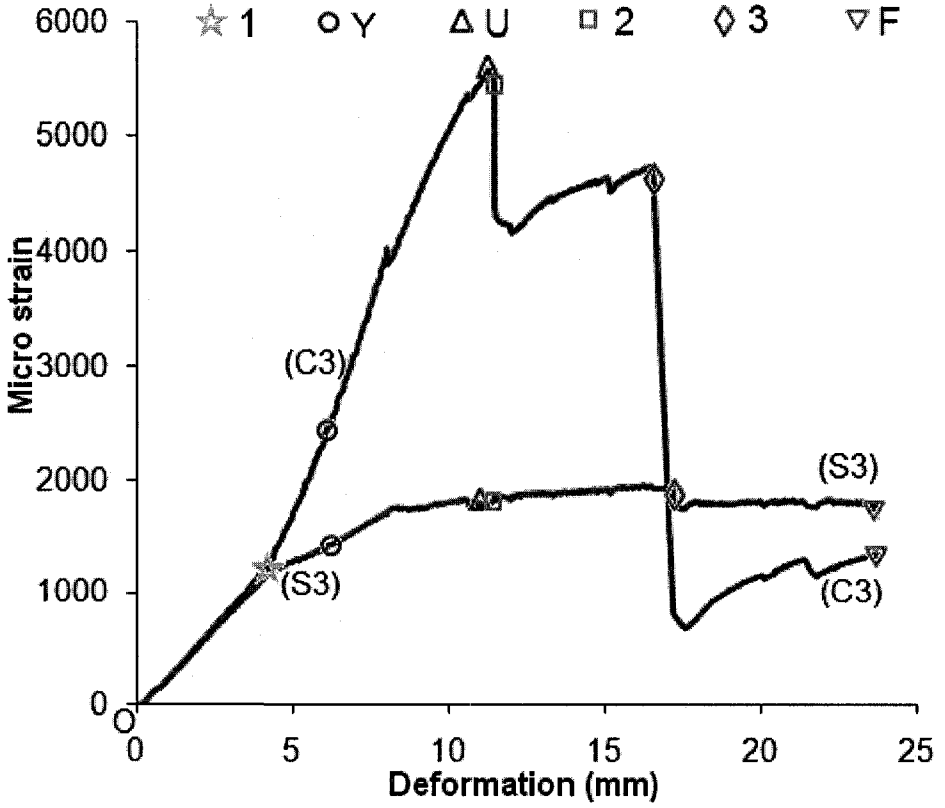

Figure 4.16: Local strain from SG C3 & S3 vs. deformation for RC-W67-T2.4-G1

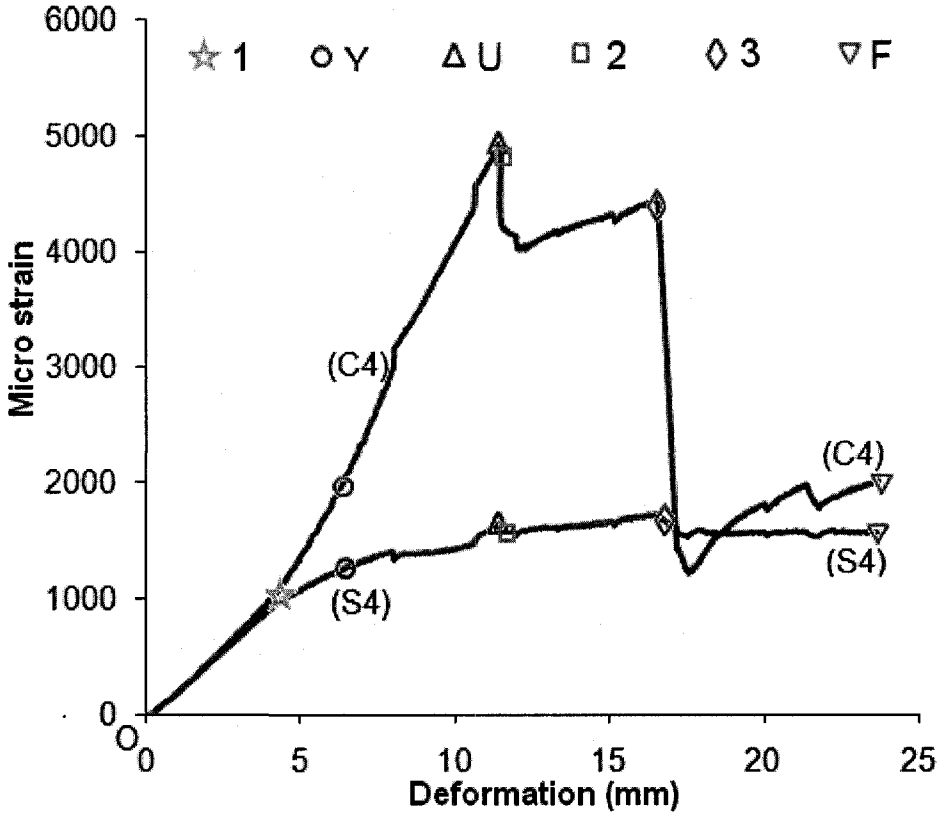

Figure 4.17: Local strain from SG C4 & S4 vs. deformation for RC-W67-T2.4-G1

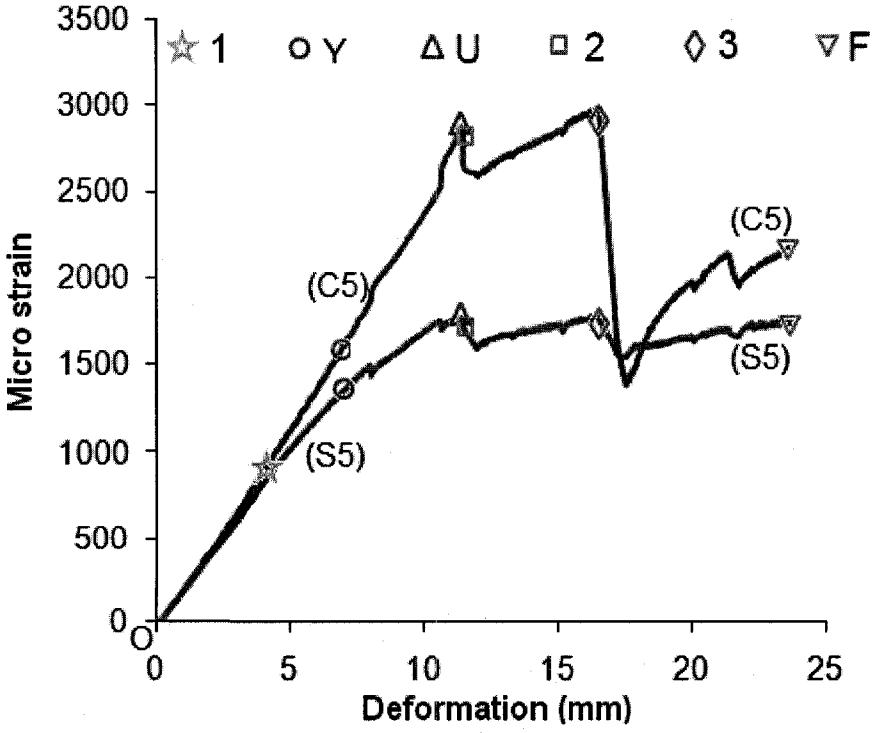

Figure 4.18: Local strain from SG C5 & S5 vs. deformation for RC-W67-T2.4-G1

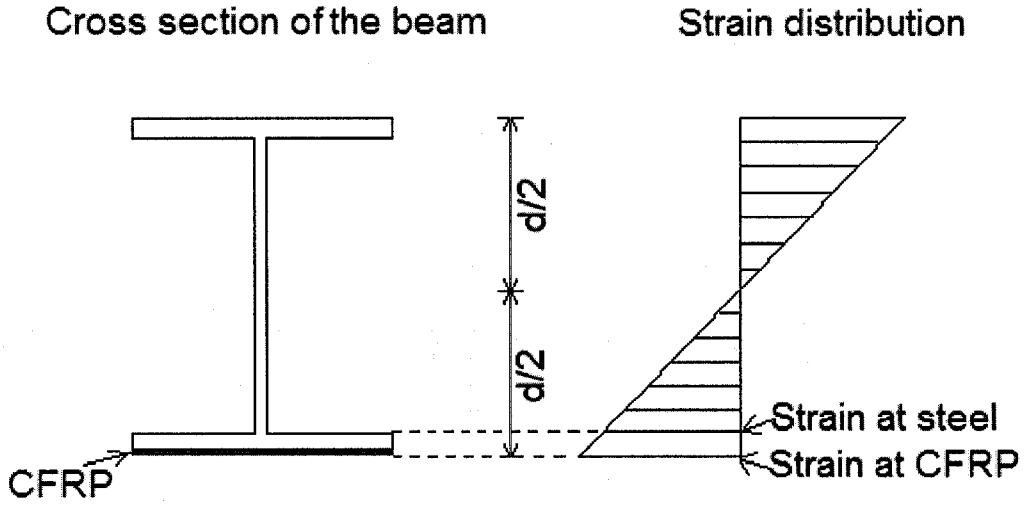

Figure 4.19: Strain distribution (assuming plane section remains plane)

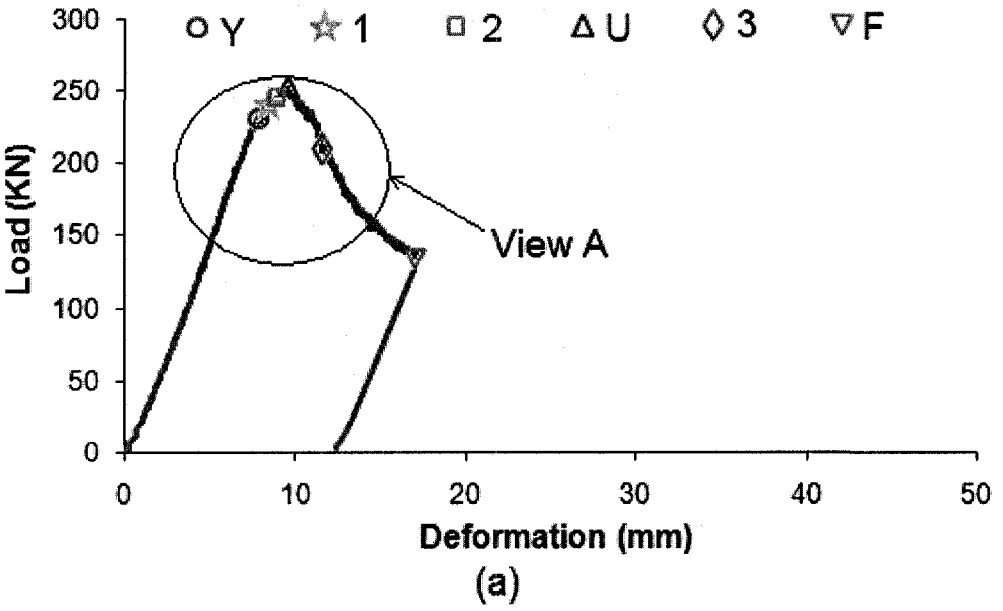

(a)

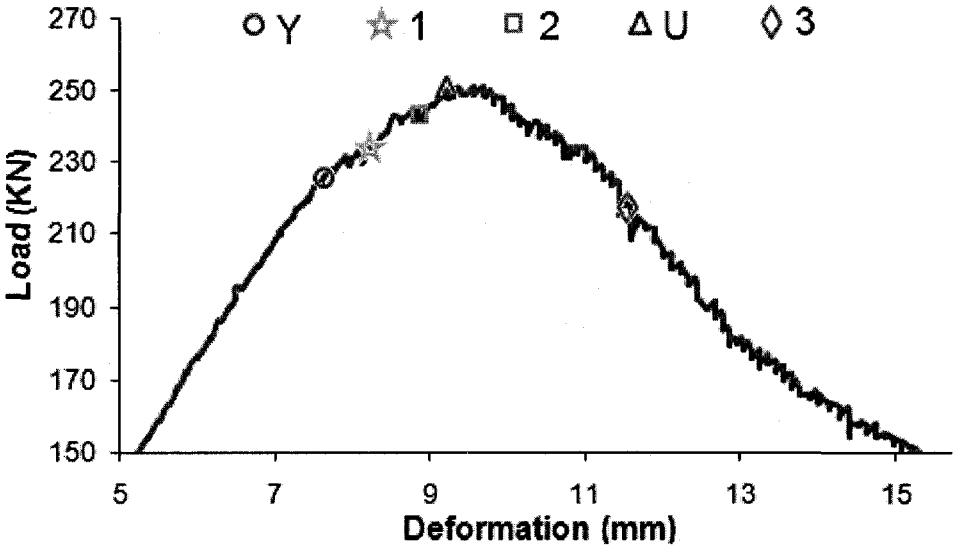

(b)

Figure 4.20: (a) Load vs. mid span (LP8) vertical deformation behavior of RC-W133-T2.4-G1 and (b) Details of View "A"

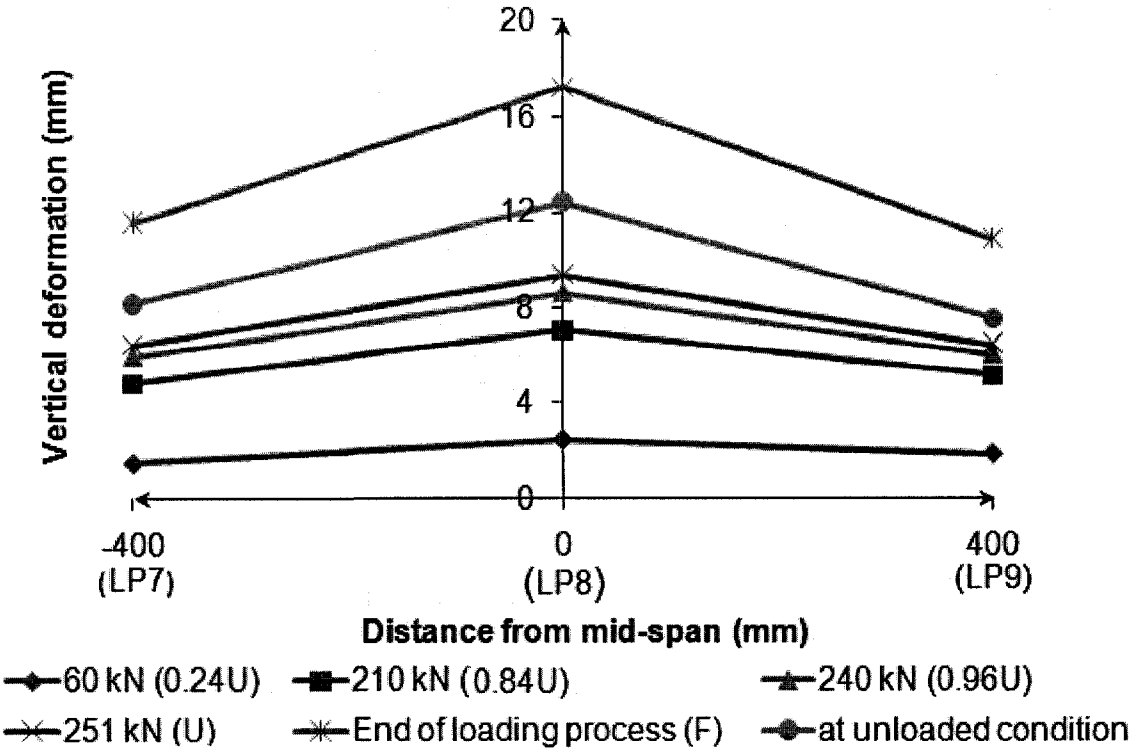

Figure 4.21: Vertical deformation response for RC-W133-T2.4-G1

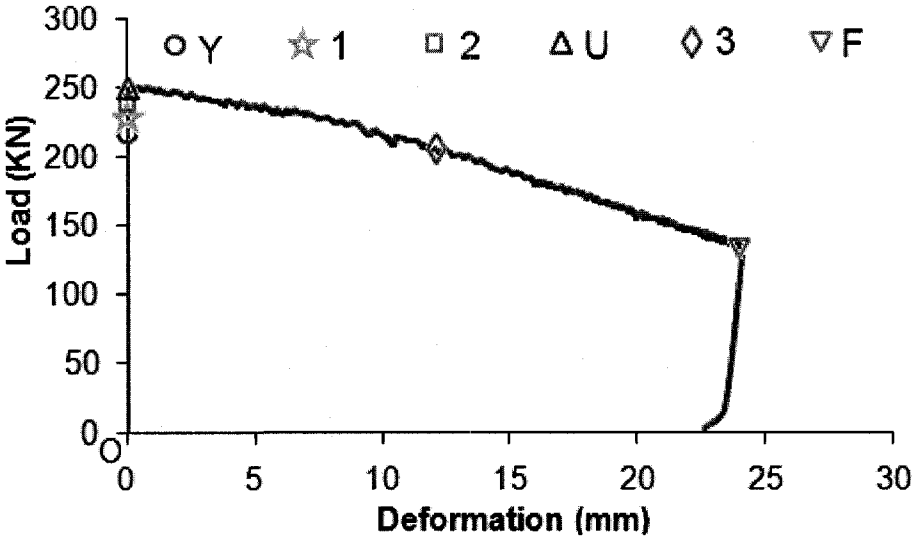

Figure 4.22: Load vs. mid span (LP5) lateral deformation behavior of RC-W133-T2.4-G1

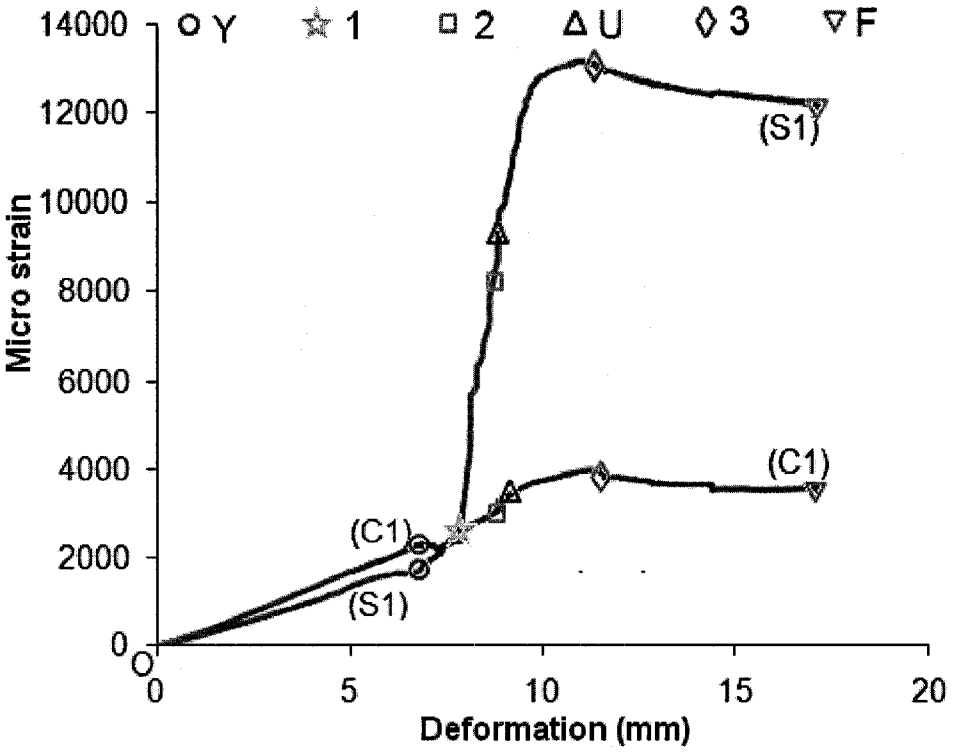

Figure 4.23: Local strain from SG C1 & S1 vs. deformation for RC-W133-T2.4-G1

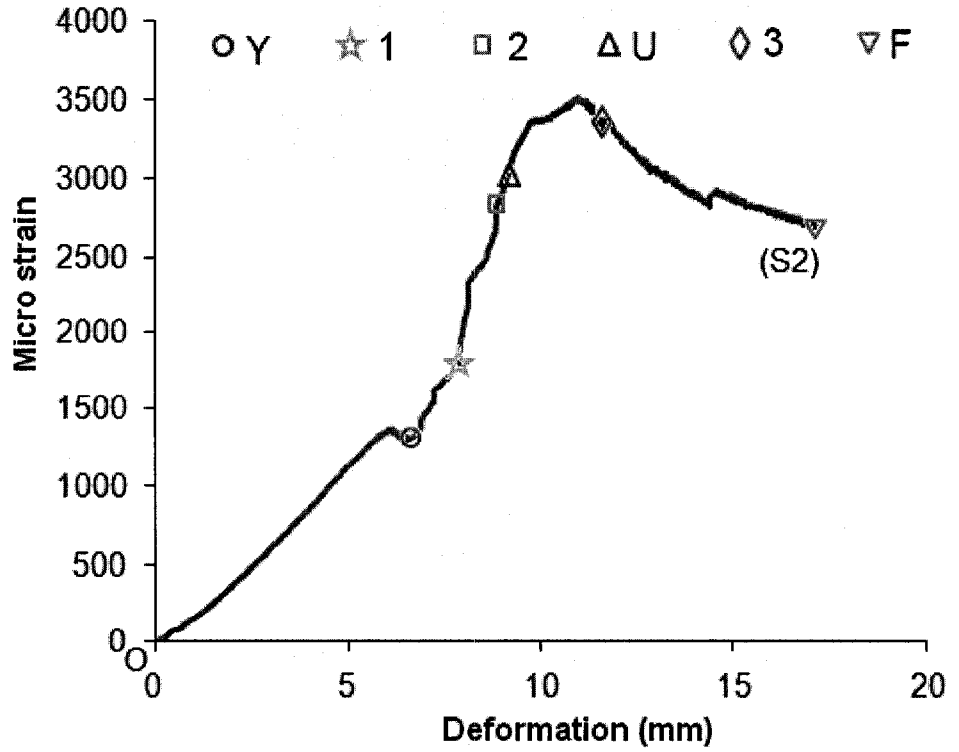

Figure 4.24: Local strain from SG S2 vs. deformation for RC-W133-T2.4-G1

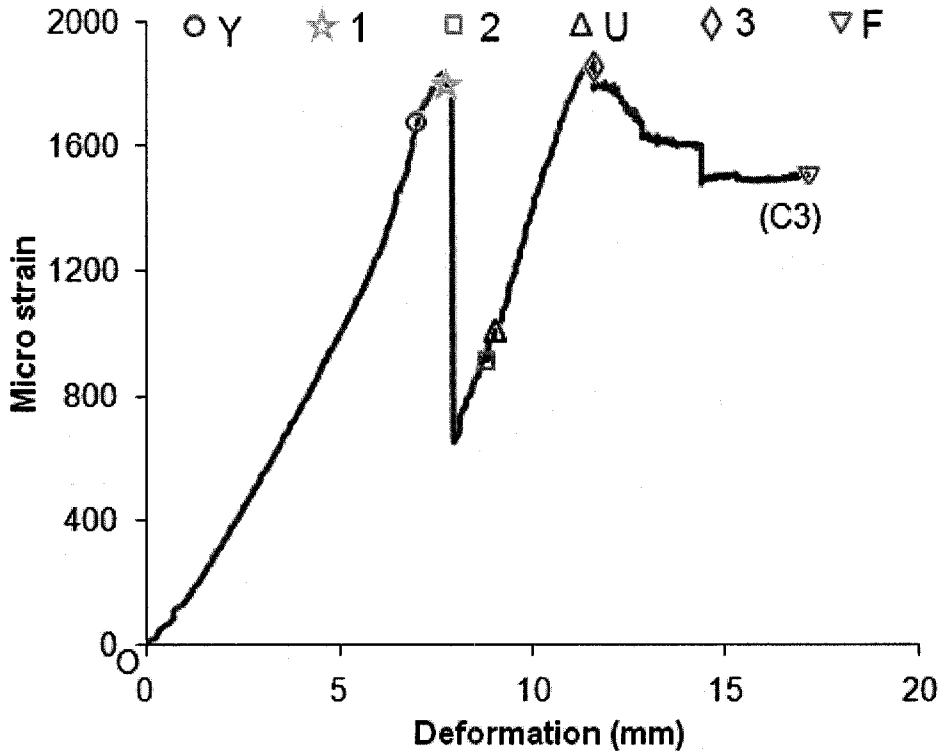

Figure 4.25: Local strain from SG C3 vs. deformation for RC-W133-T2.4-G1

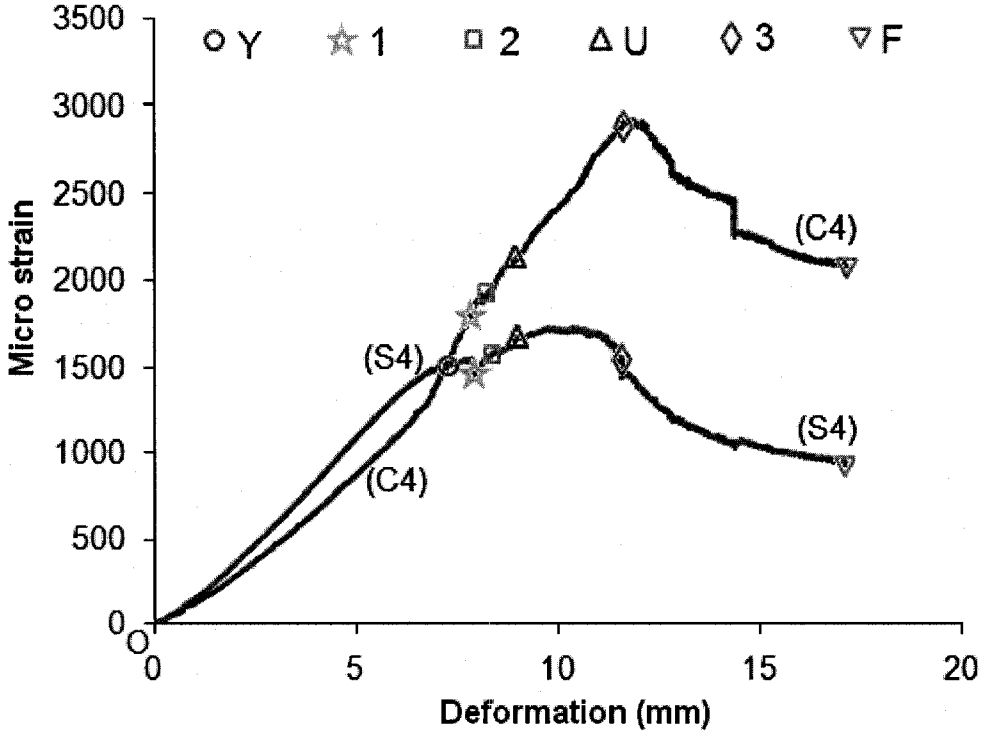

Figure 4.26: Local strain from SG C4 & S4 vs. deformation for RC-W133-T2.4-G1

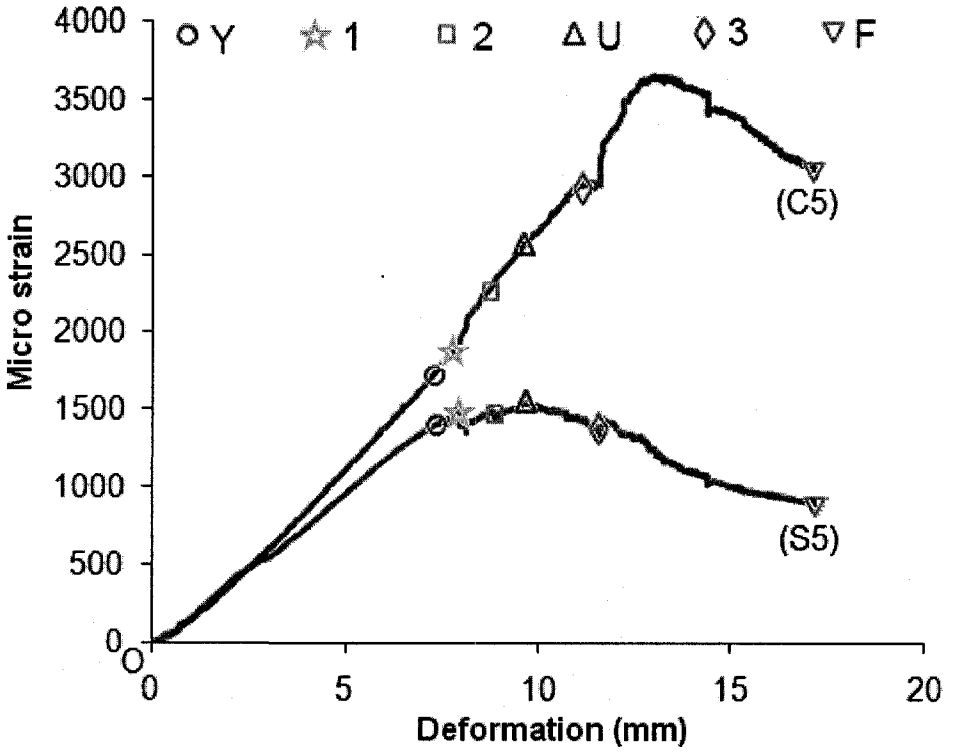

Figure 4.27: Local strain from SG C5 & S5 vs. deformation for RC-W133-T2.4-G1

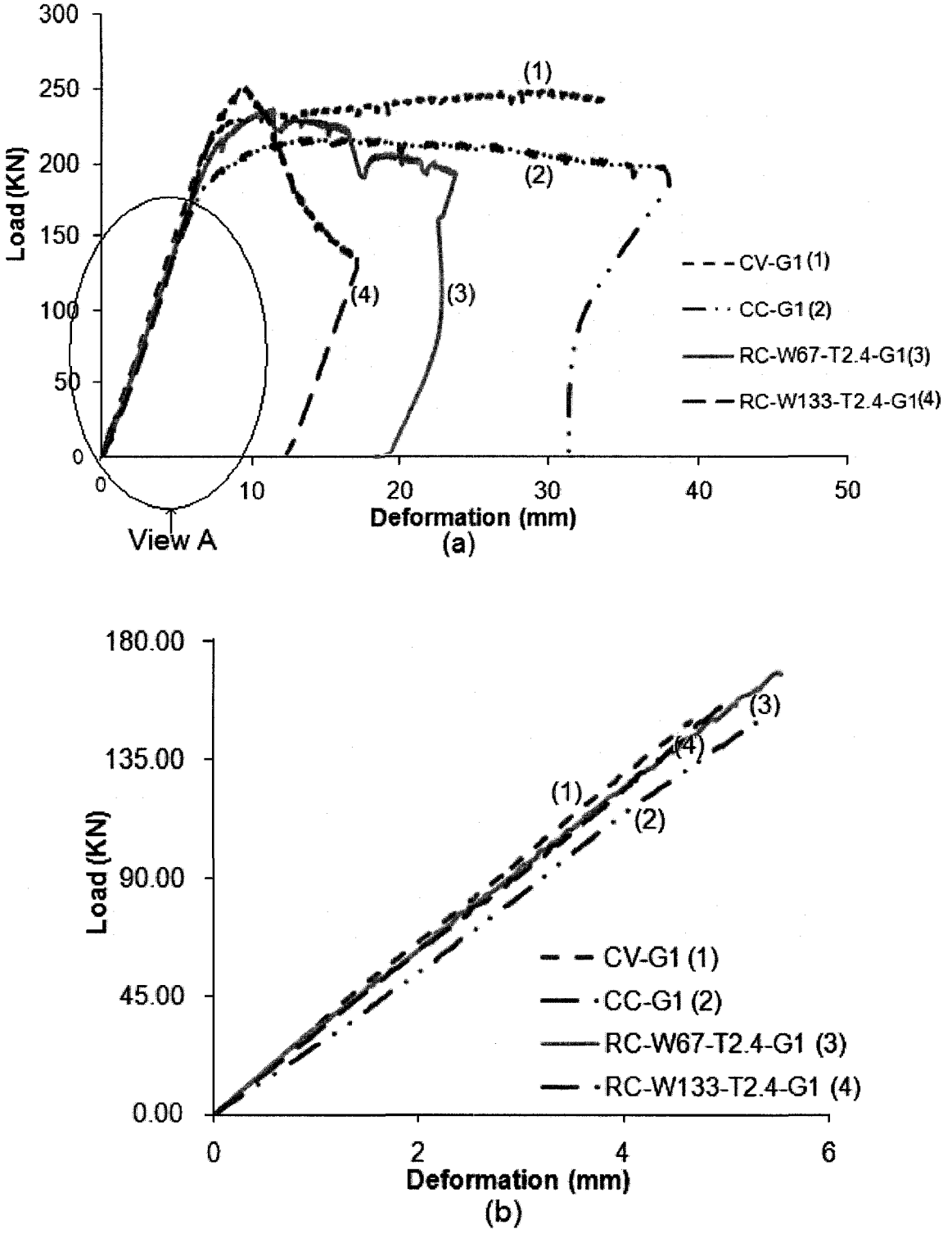

Figure 4.28: (a) load vs. vertical deformation behavior of group 1 specimens and (b) detail of view "A"

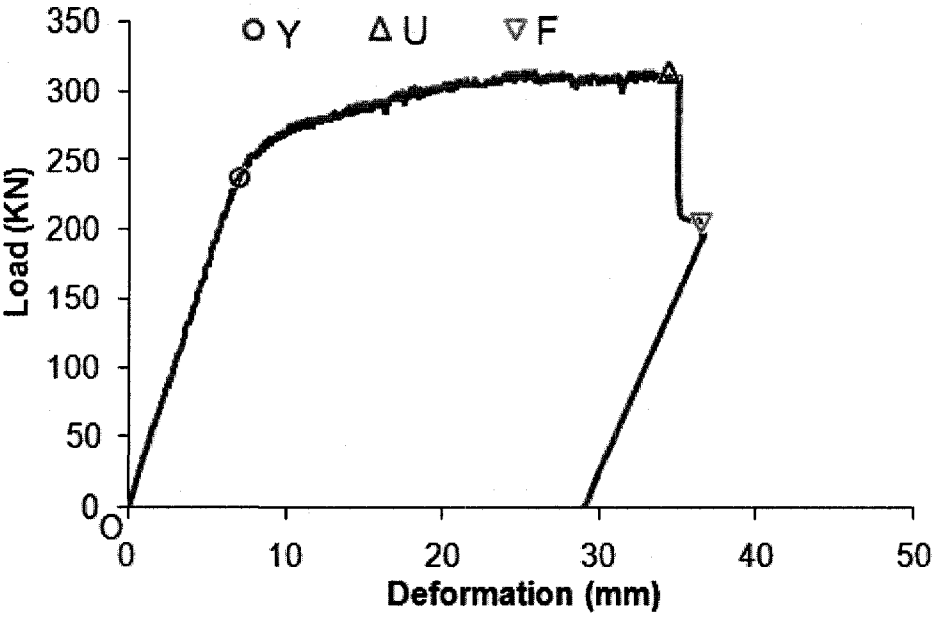

Figure 4.29: Load vs. mid span (LP8) vertical deformation behavior of CV-G2

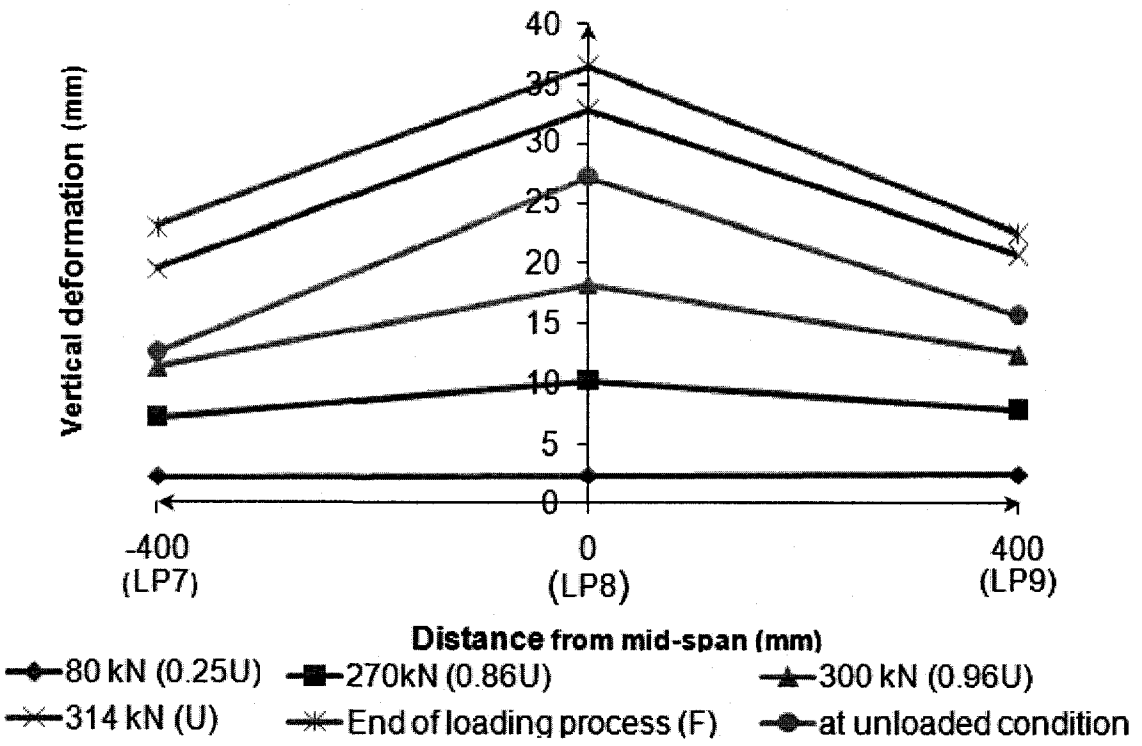

Figure 4.30: Vertical deformation response for CV-G2

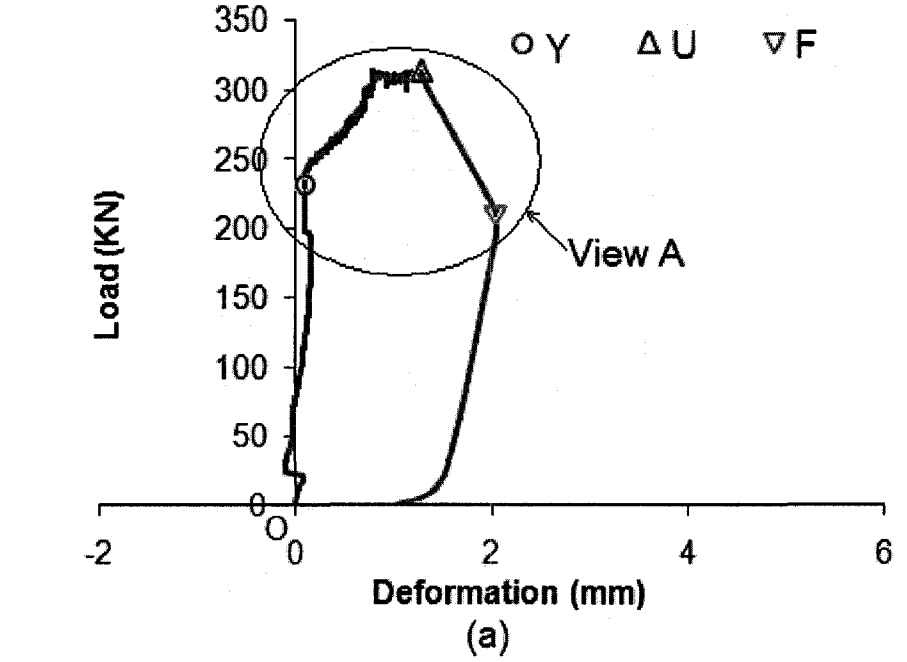

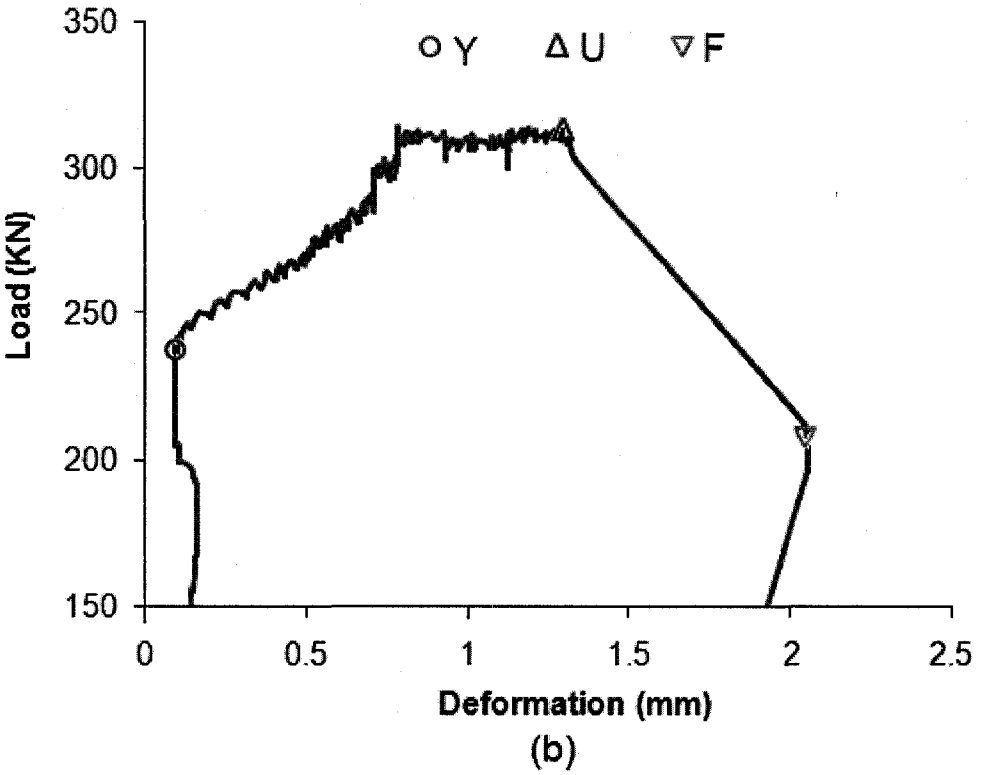

Figure 4.31: (a) Load vs. mid span (LP5) lateral deformation behavior of CV-G2 and (b) Details of view "A"

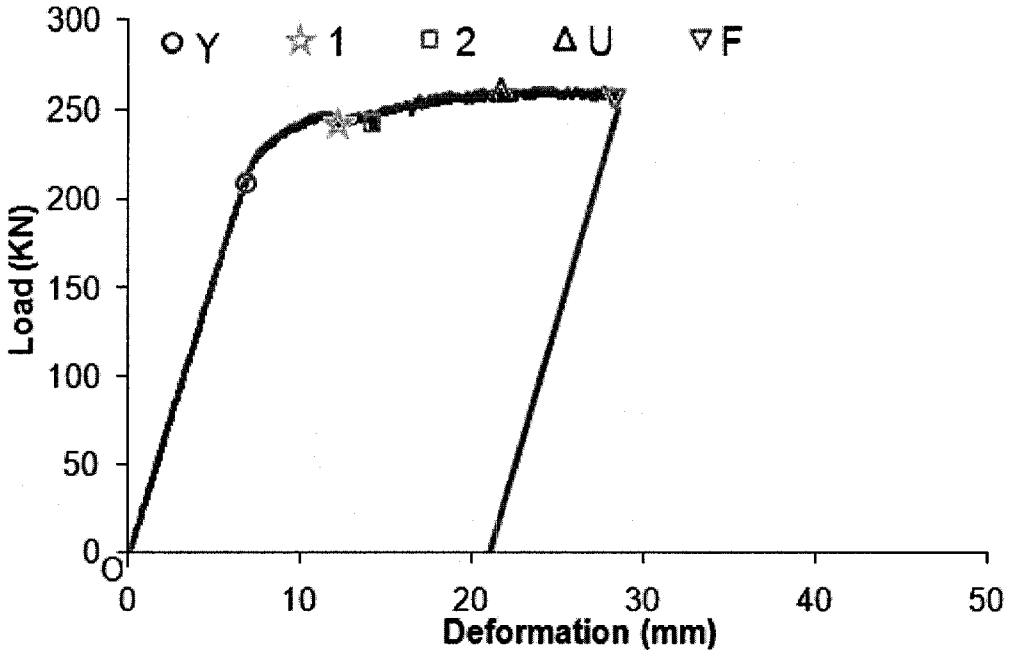

Figure 4.32: Load vs. mid span (LP8) vertical deformation behavior of CC-G2

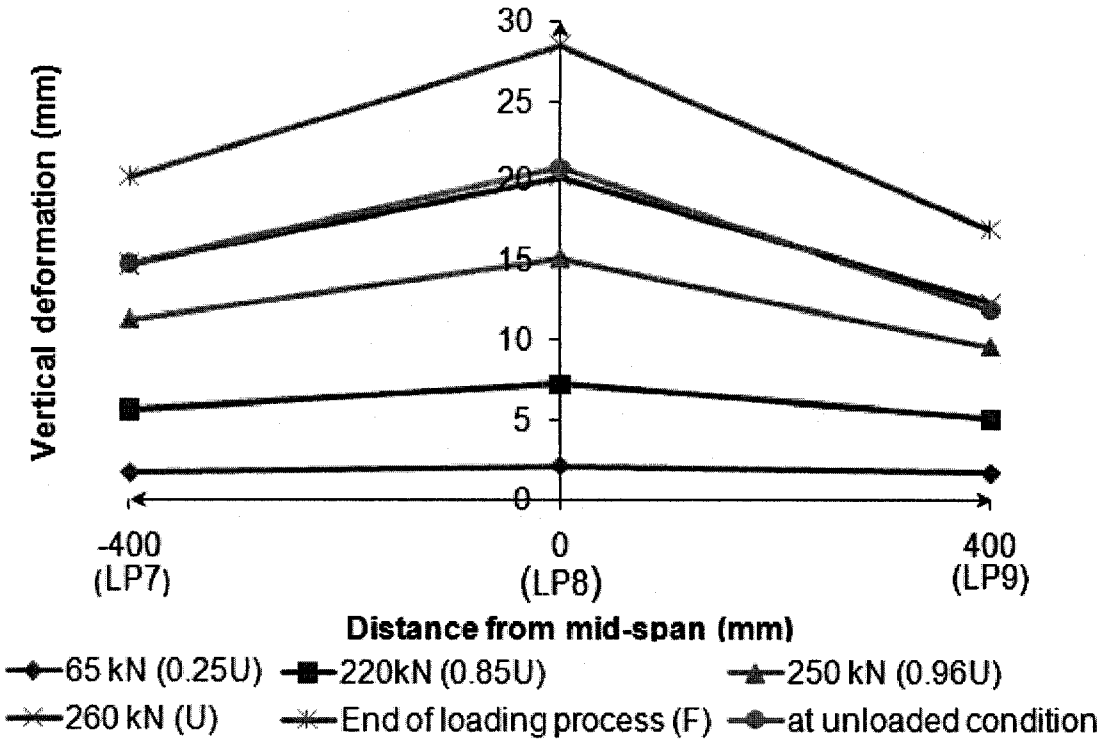

Figure 4.33: Vertical deformation response for CC-G2

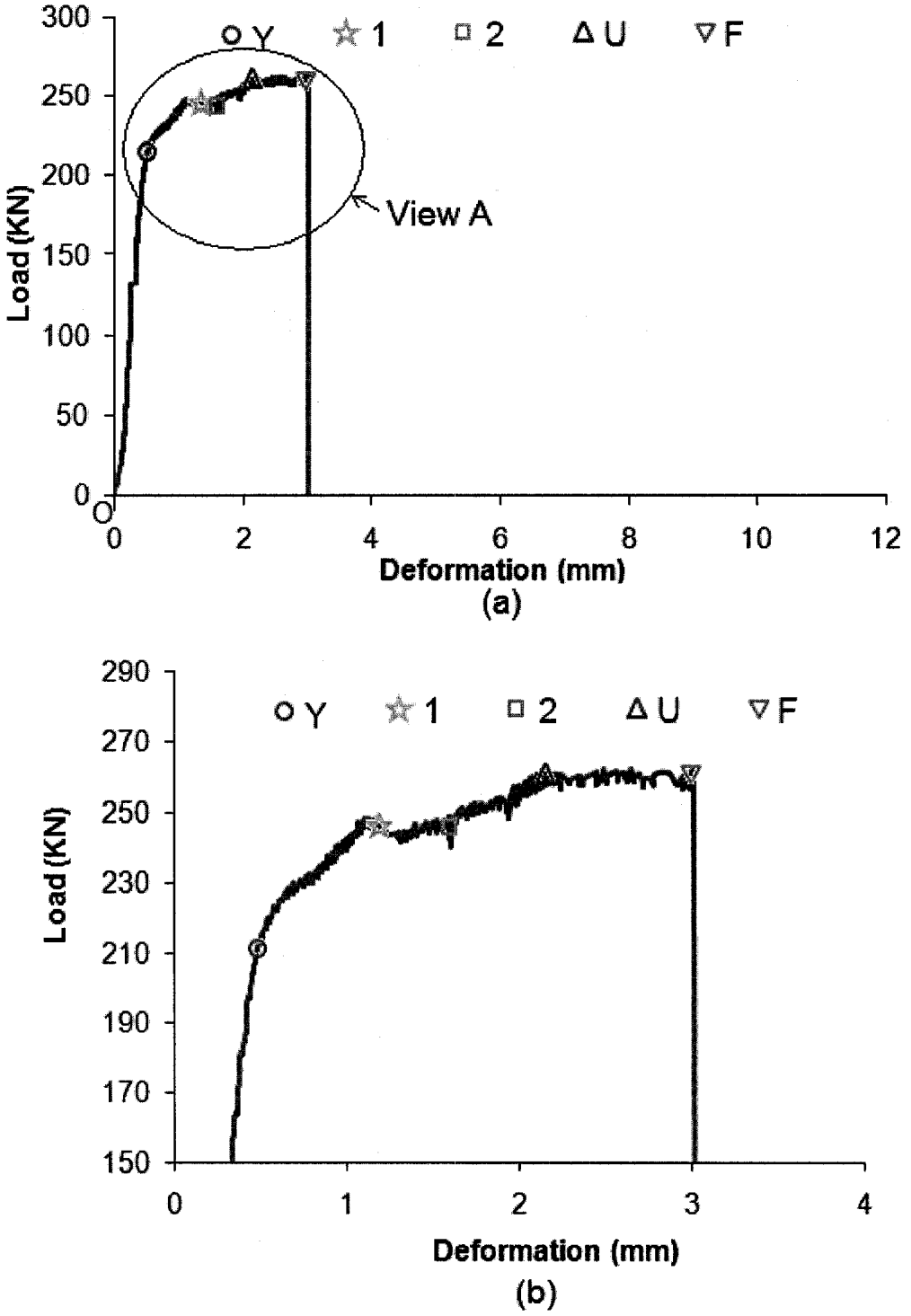

Figure 4.34: (a) Load vs. mid span (LP5) lateral deformation behavior of CC-G2 and (b) Detail of view "A"

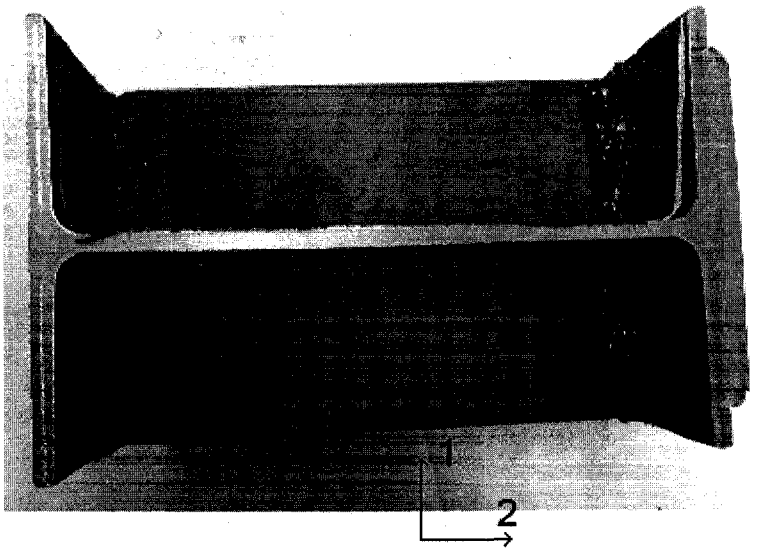

Figure 4.35: CC-G2, no web or flange buckled

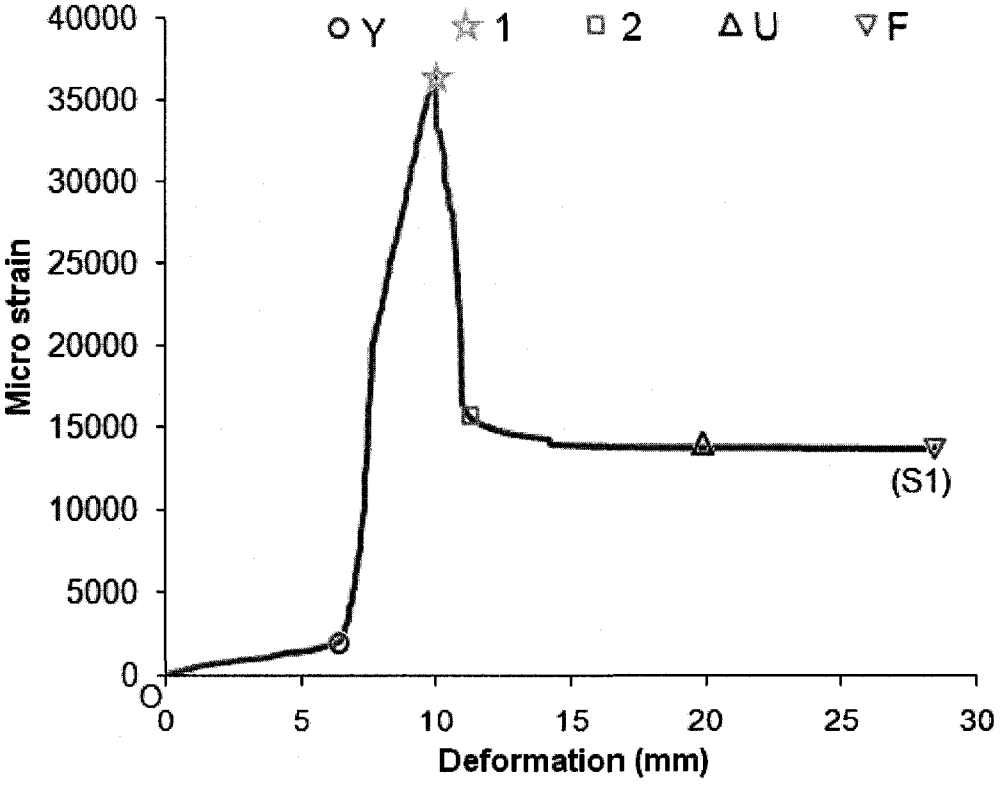

Figure 4.36: Local strain from SG S1 vs. deformation for CC-G2

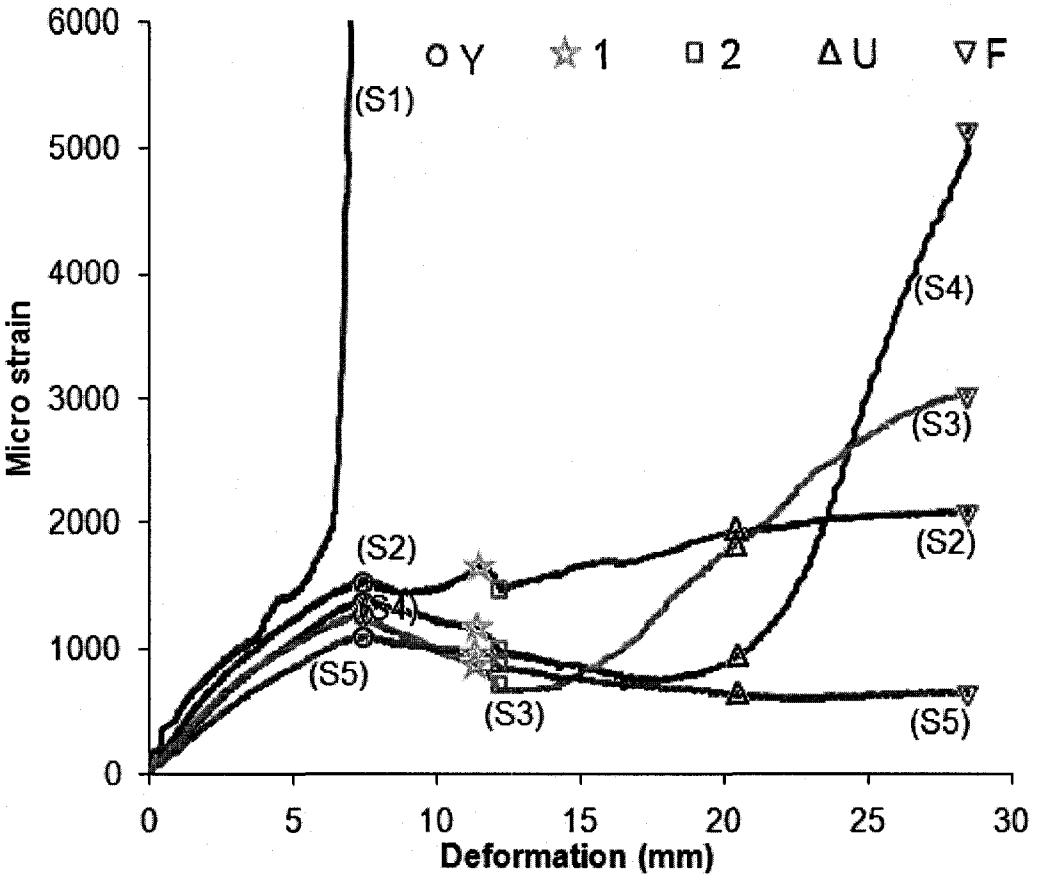

Figure 4.37: Local strain from SG S2 to S5 vs. deformation for CC-G2

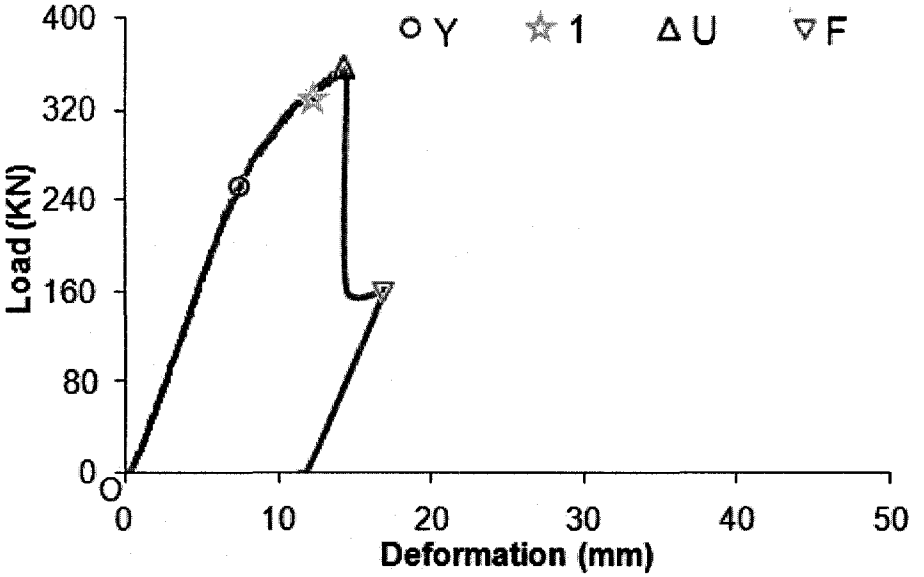

Figure 4.38: Load vs. mid span (LP8) vertical deformation behavior of RC-W133-T2.4-G2

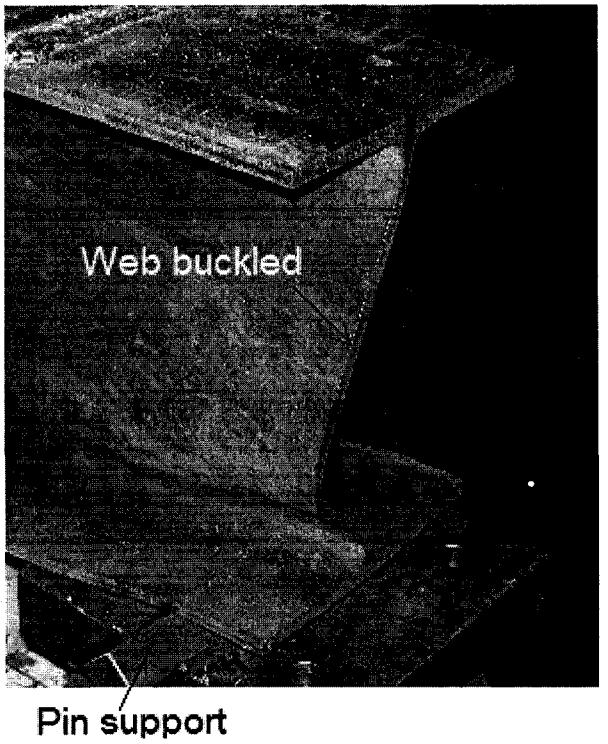

Figure 4.39: RC-W133-T2.4-G2, web buckled at pin support

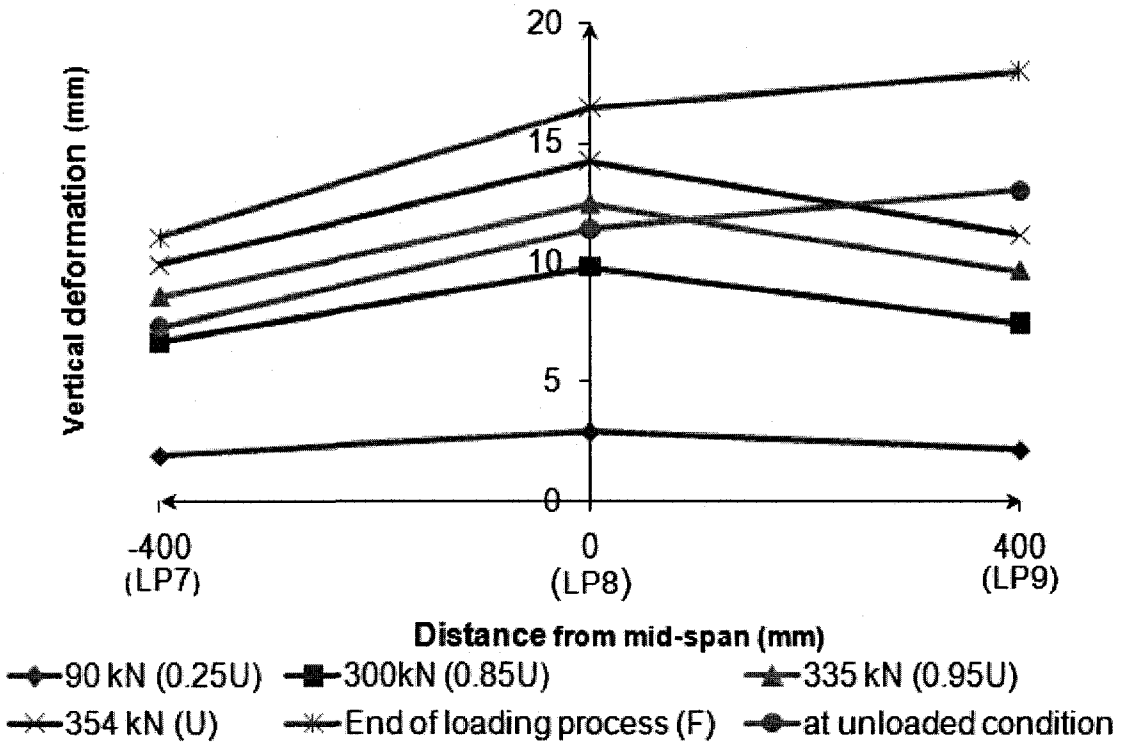

Figure 4.40: Vertical deformation response for RC-W133-T2.4-G2

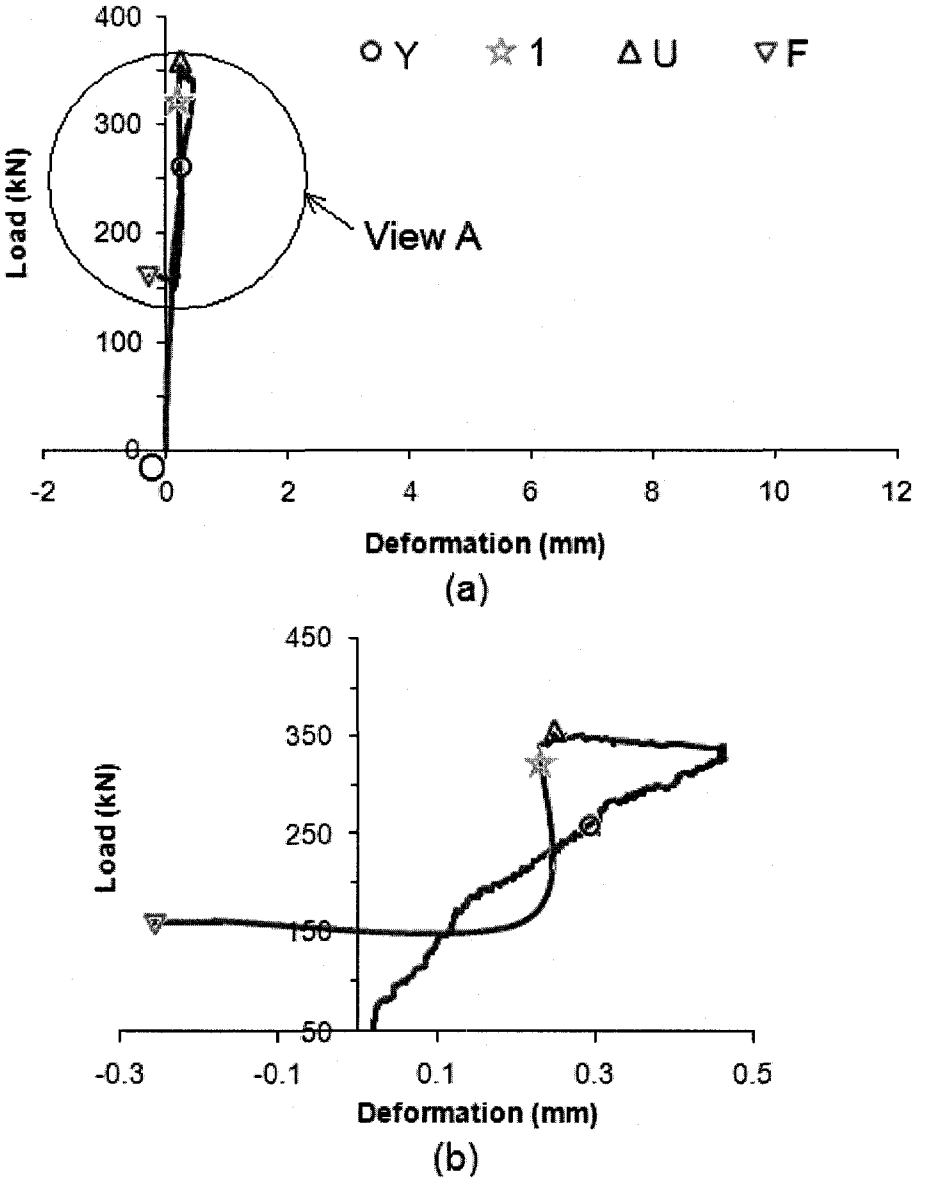

Figure 4.41: (a) Load vs. mid span (LP5) lateral deformation behavior of RC-W133-T2.4-G2 and (b) Details of view "A"

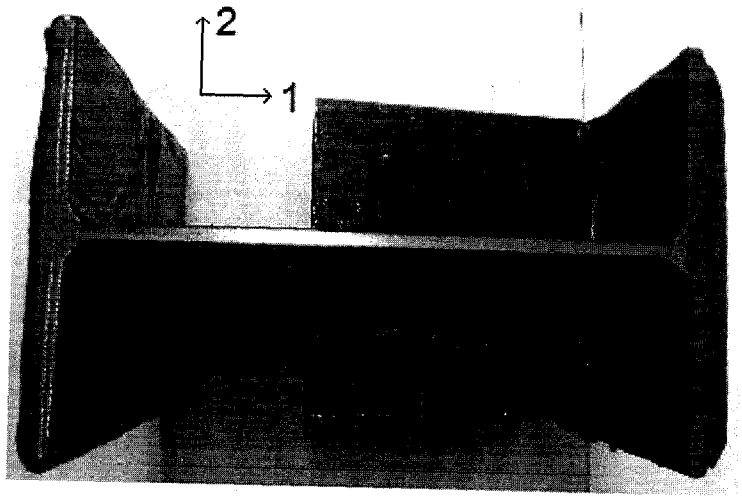

Figure 4.42: RC-W133-T2.4-G2, no web or flange buckle

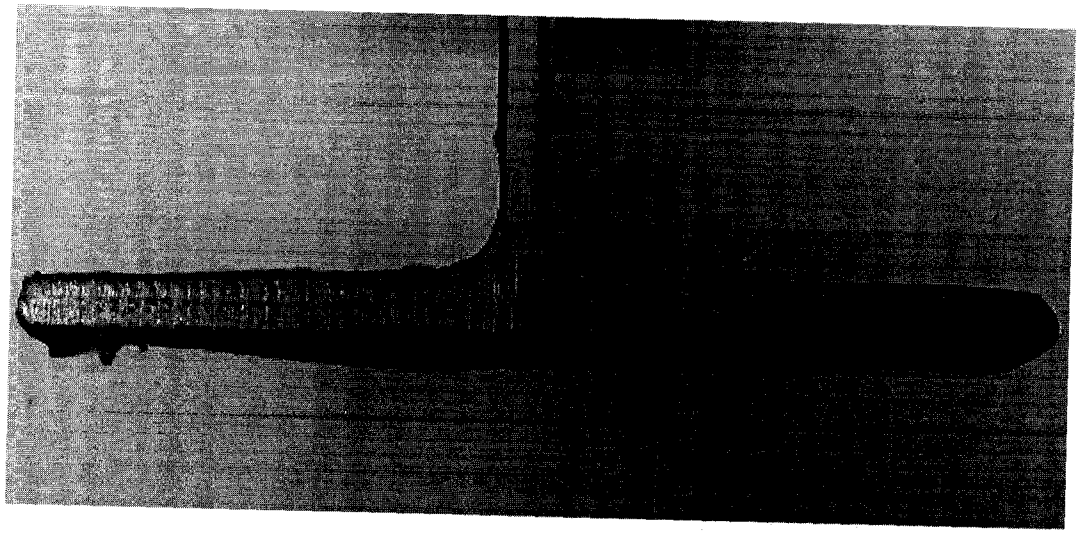

Figure 4.43: RC-W133-T2.4-G2, no visible sign of debonding at mid-span

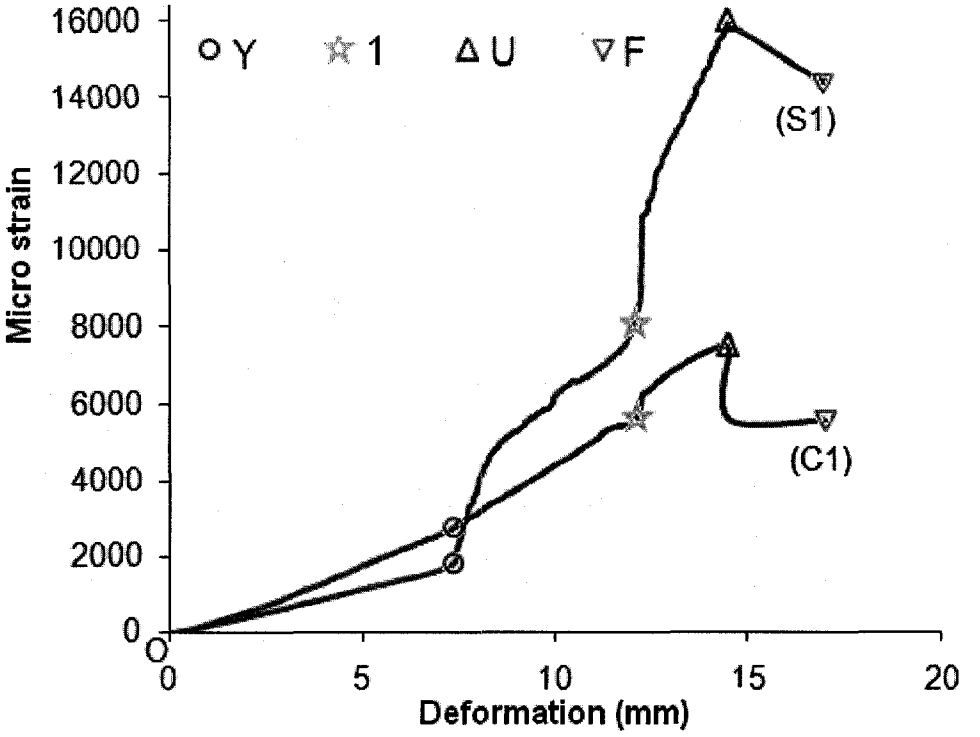

Figure 4.44: Local strain from SG C1 & S1 vs. deformation for RC-W133-T2.4-G2

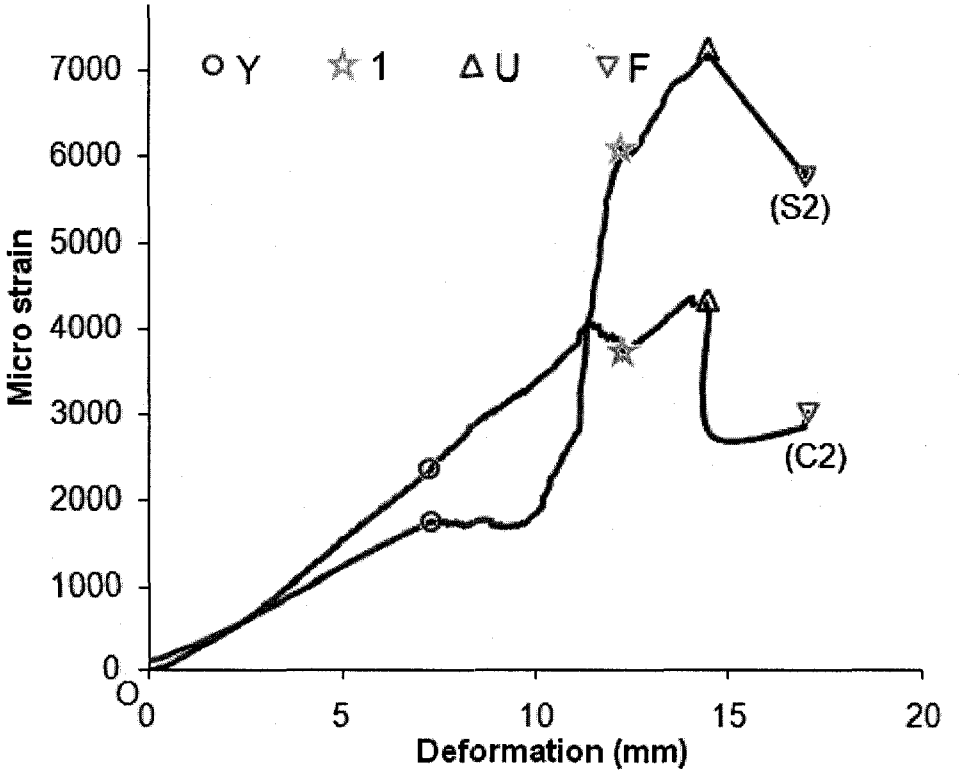

Figure 4.45: Local strain from SG C2 & S2 vs. deformation for RC-W133-T2.4-G2

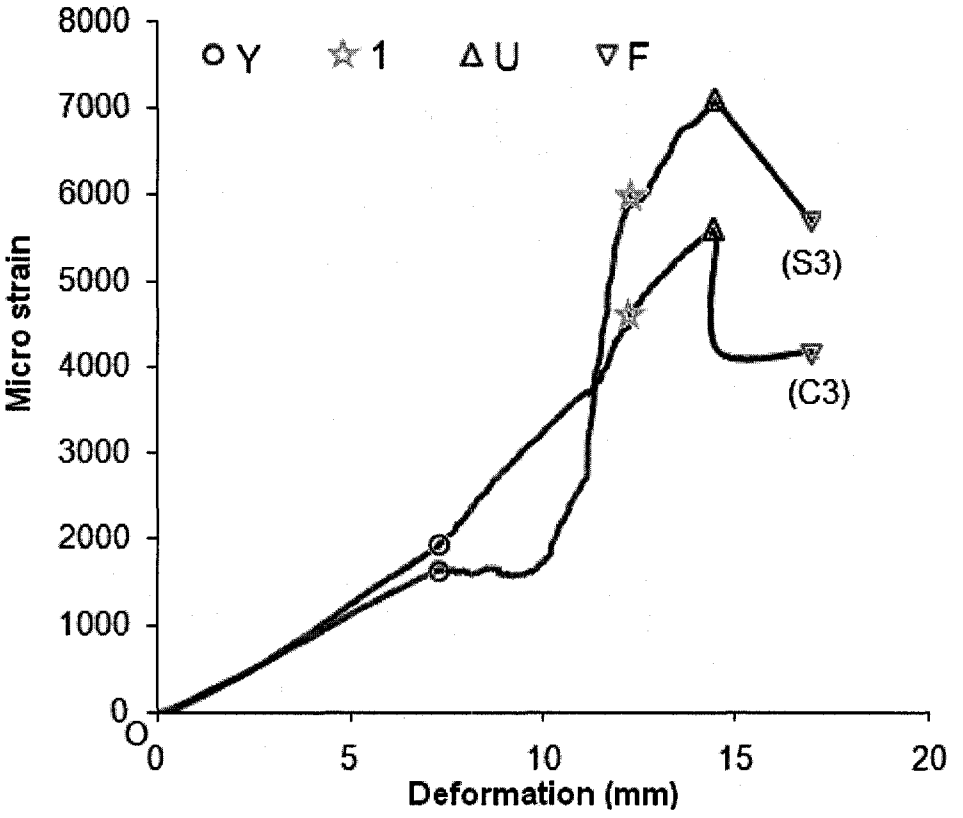

Figure 4.46: Local strain from SG C3 & S3 vs. deformation for RC-W133-T2.4-G2

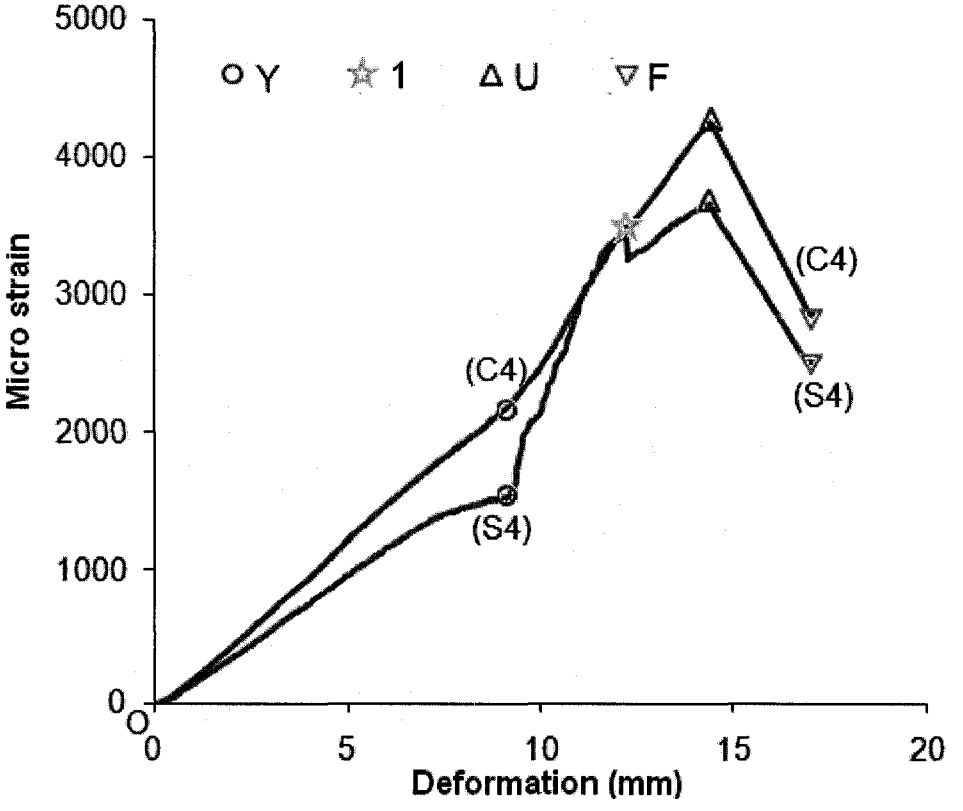

Figure 4.47: Local strain from SG C4 & S4 vs. deformation for RC-W133-T2.4-G2

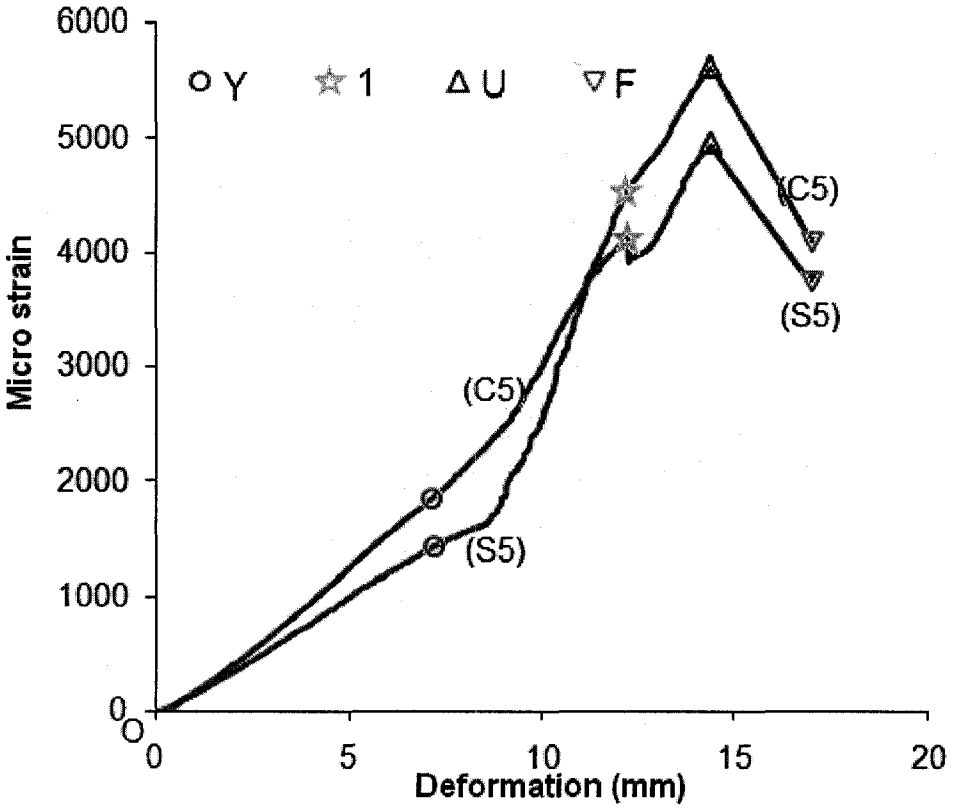

Figure 4.48: Local strain from SG C5 & S5 vs. deformation for RC-W133-T2.4-G2

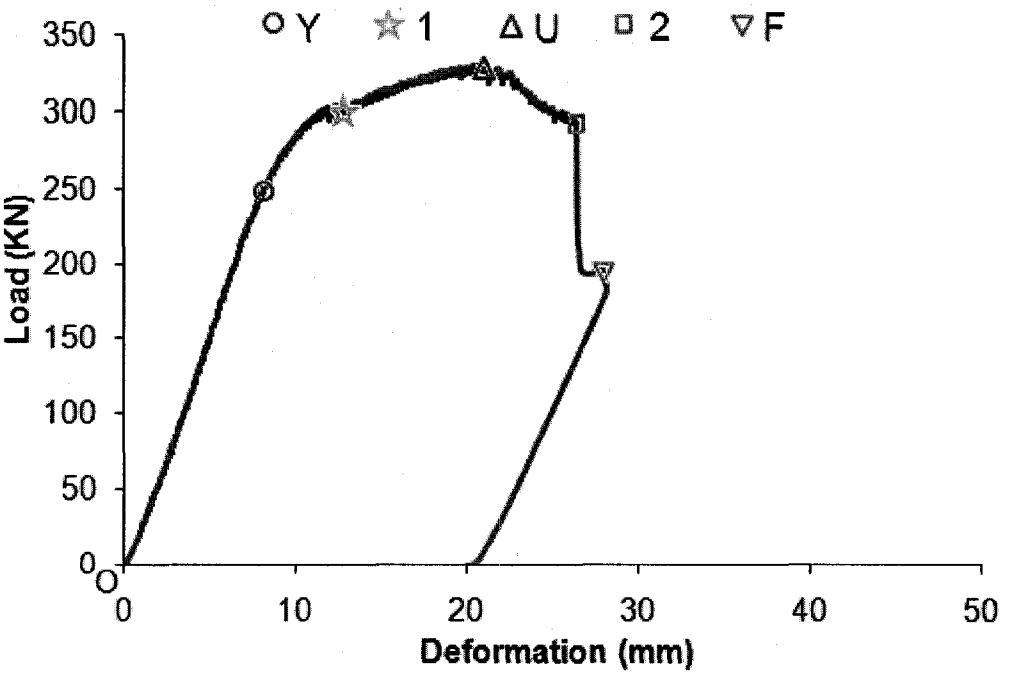

Figure 4.49: Load vs. mid span (LP8) vertical deformation behavior of RC-W133-T1.2-G2

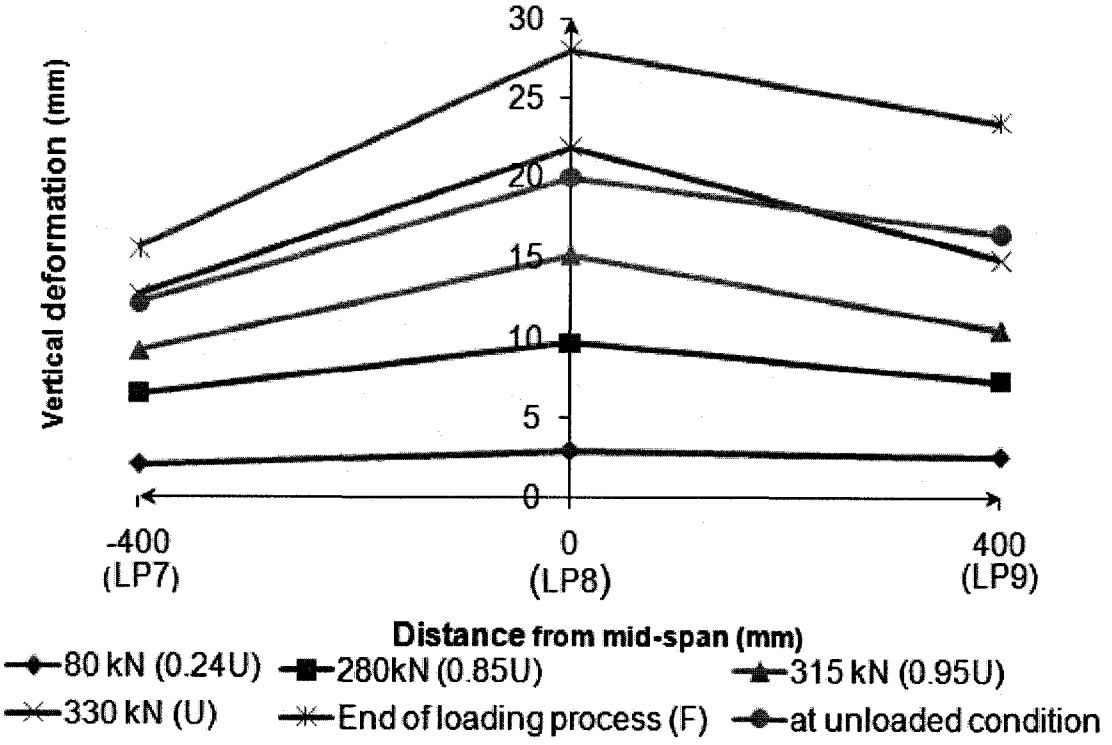

Figure 4.50: Vertical deformation response for RC-W133-T1.2-G2

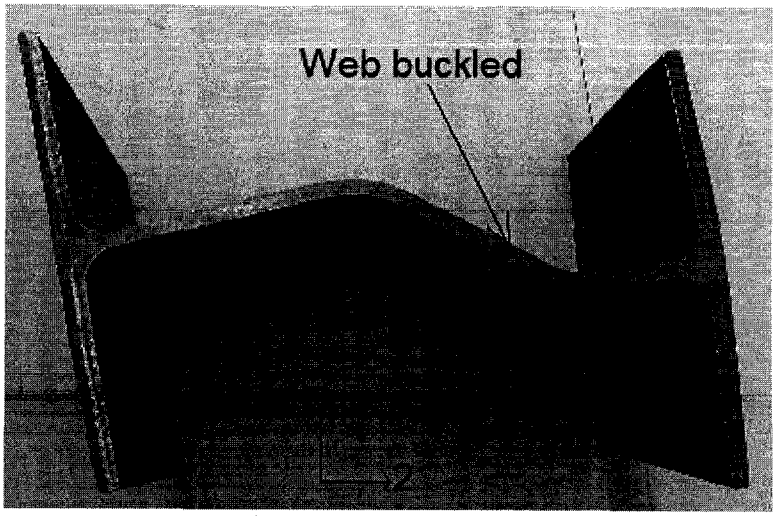

Figure 4.51: RC-W133-T1.2-G2, web buckled at pin support

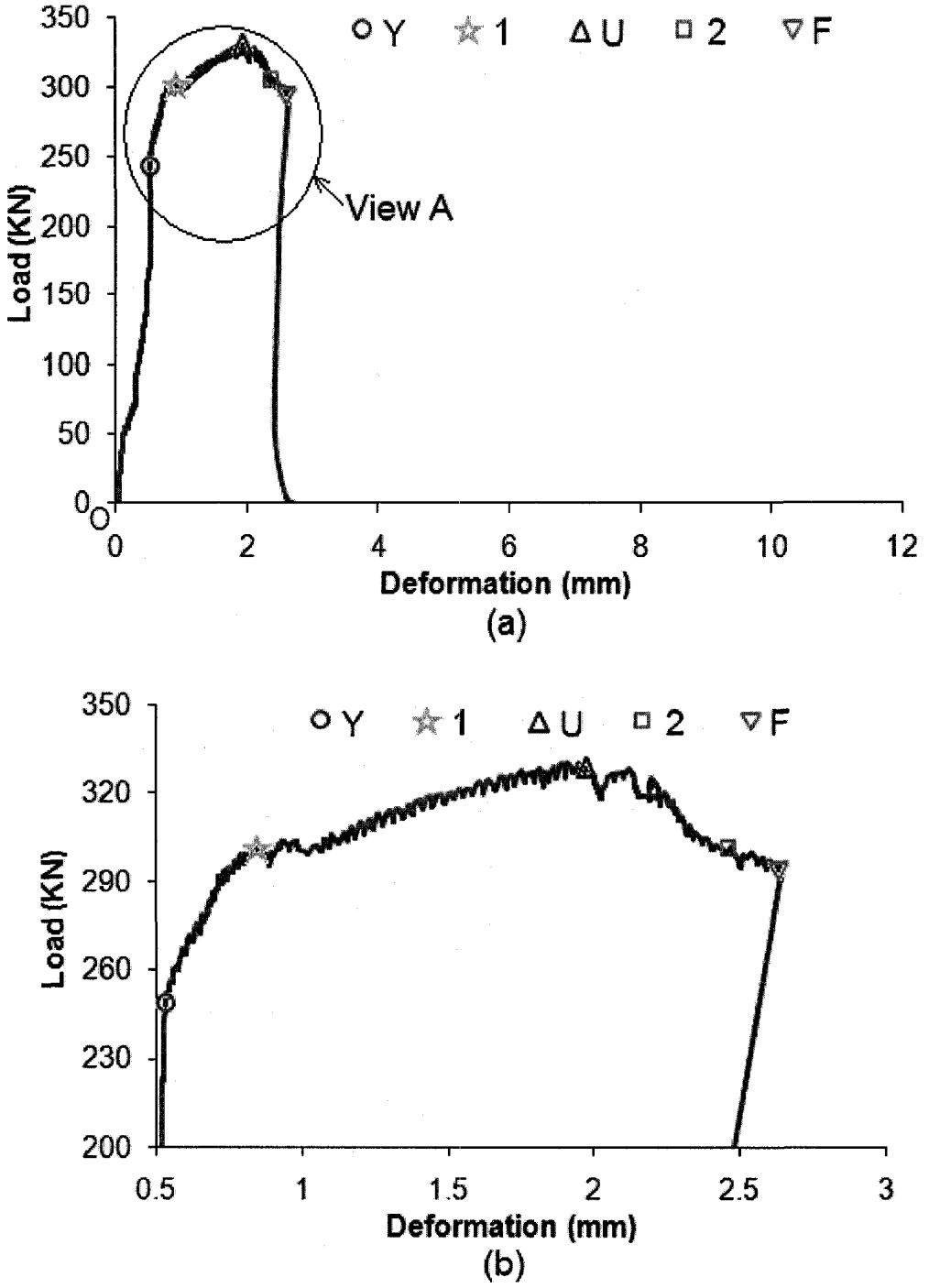

Figure 4.52: (a) Load vs. mid span (LP5) lateral deformation behavior of RC-W133-T1.2-G2 and (b) Details of view "A"

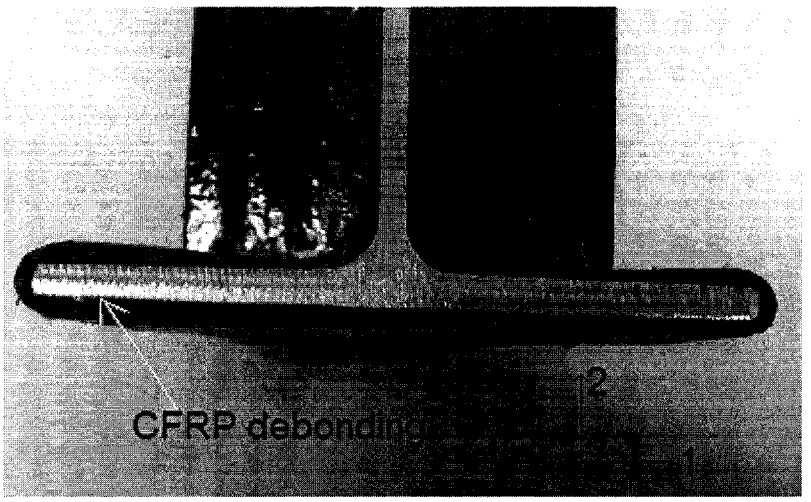

Figure 4.53: RC-W133-T1.2-G2, CFRP debonding

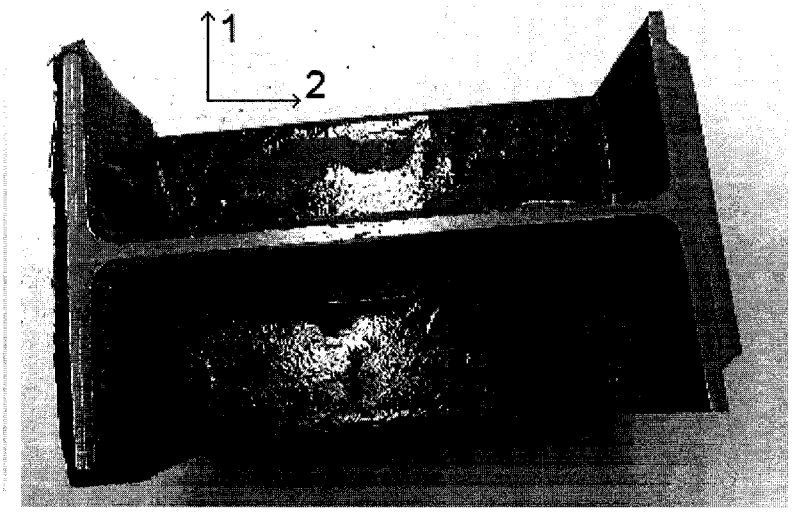

Figure 4.54: RC-W133-T1.2-G2, no web or flange buckled at the central of the beam

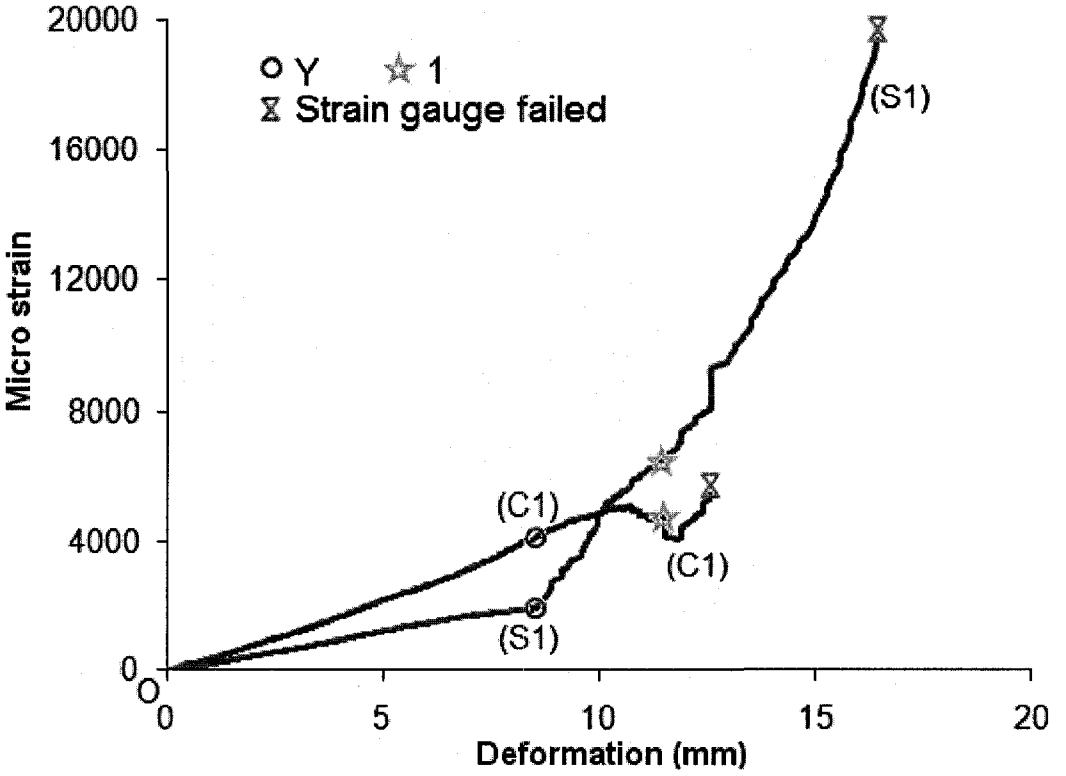

Figure 4.55: Local strains from SG C1 & S1 vs. deformation for RC-W133-T1.2-G2

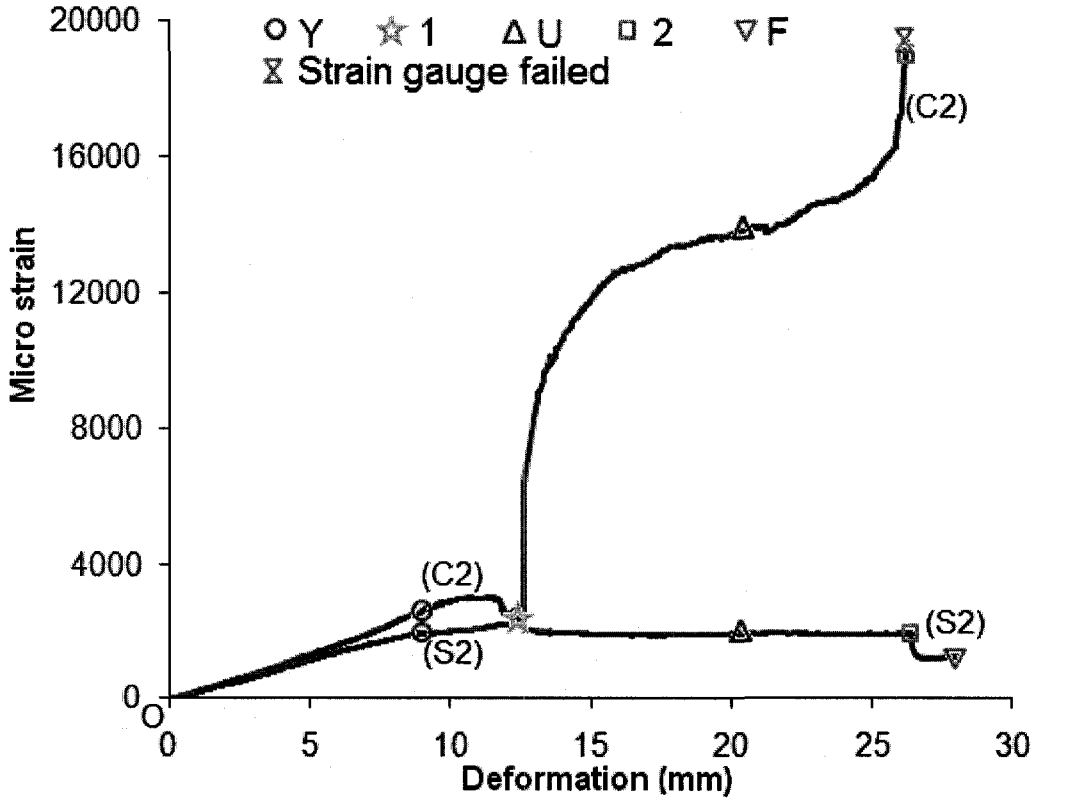

Figure 4.56: Local strain from SG C2 & S2 vs. deformation for RC-W133-T1.2-G2

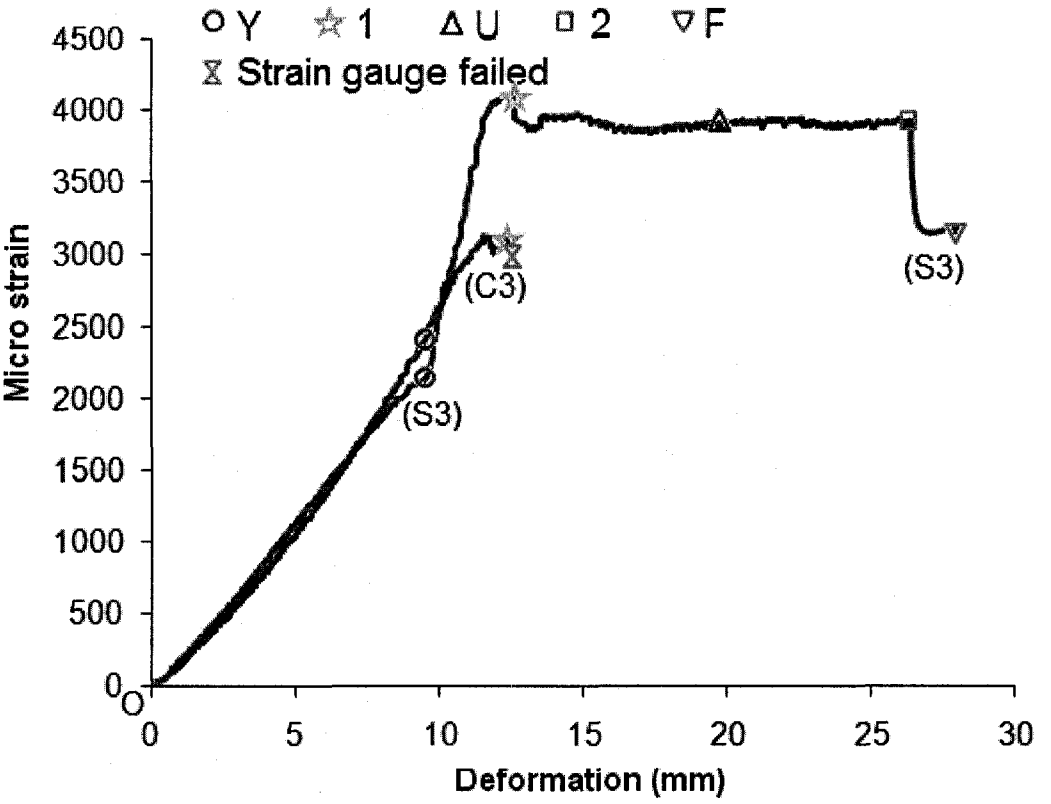

Figure 4.57: Local strain from SG C3 & S3 vs. deformation for RC-W133-T1.2-G2

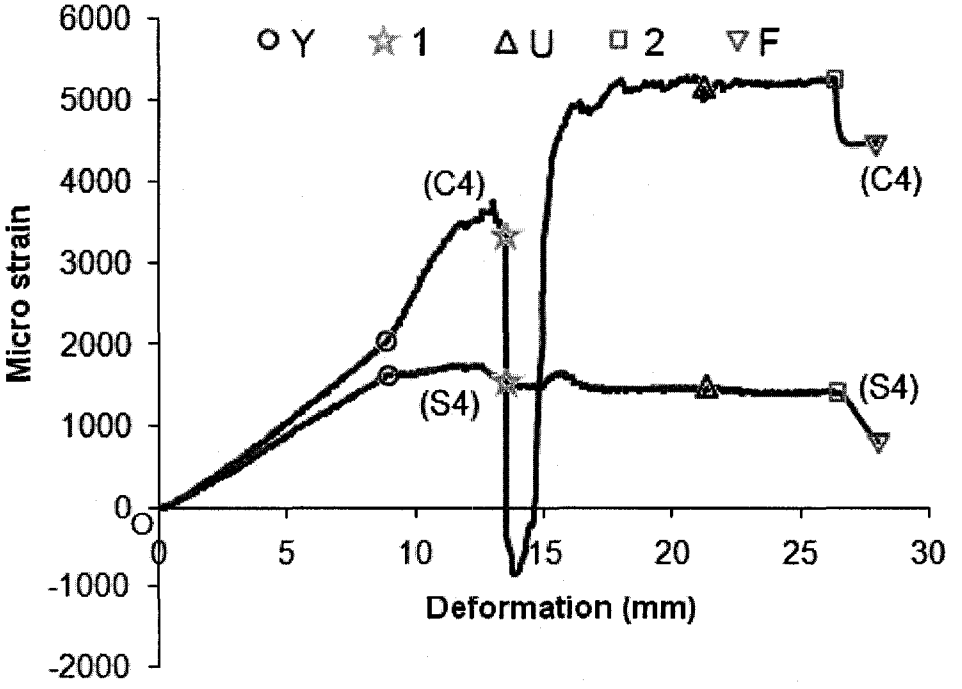

Figure 4.58: Local strain from SG C4 & S4 vs. deformation for RC-W133-T1.2-G2

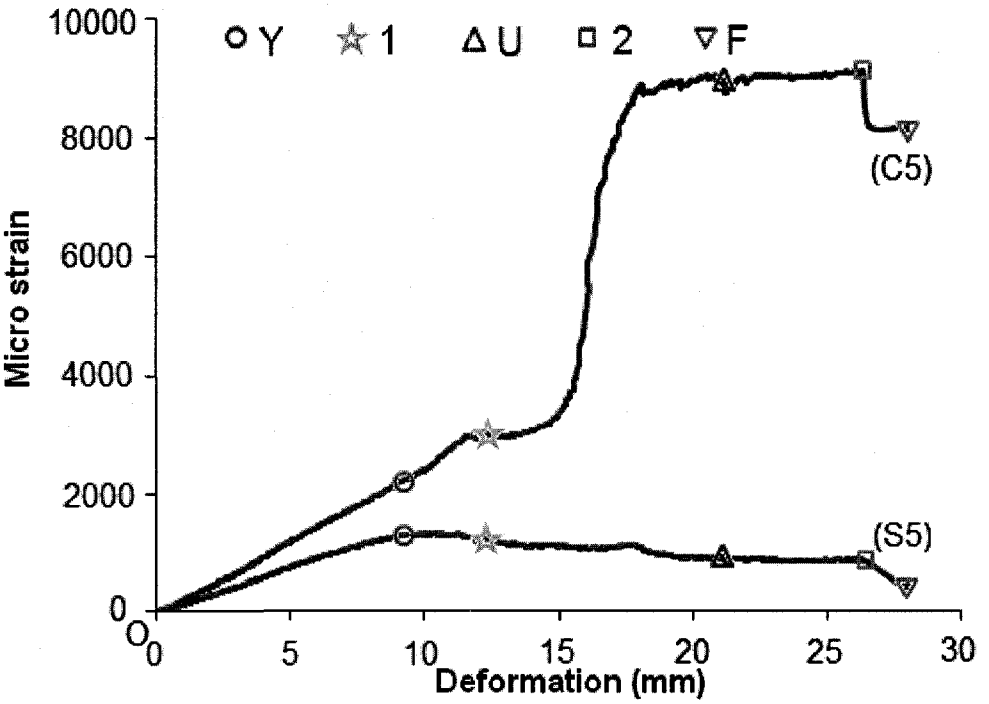

Figure 4.59: Local strain from SG C5 & S5 vs. deformation for RC-W133-T1.2-G2

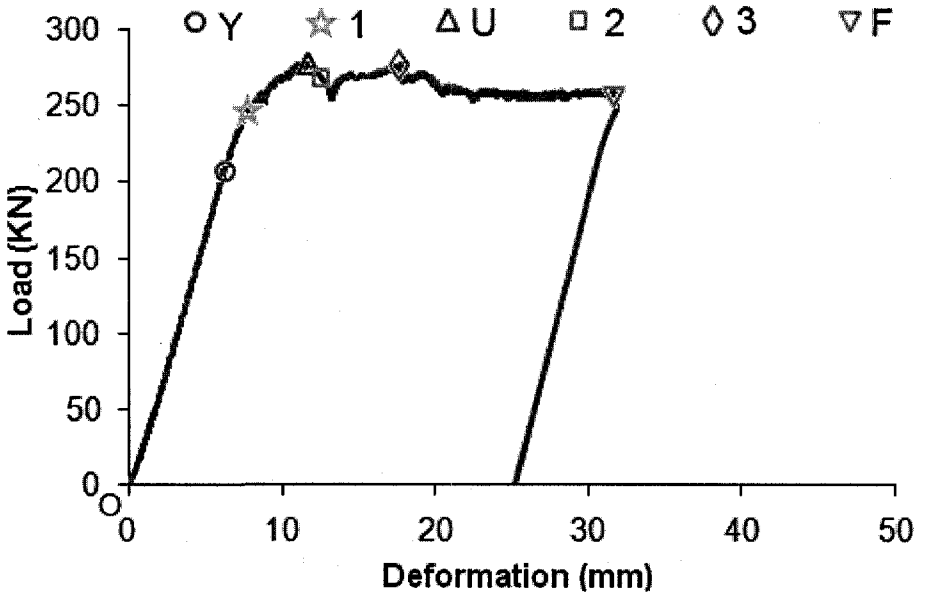

Figure 4.60: Load vs. mid span (LP8) vertical deformation behavior of RC-W133-T0.6-G2

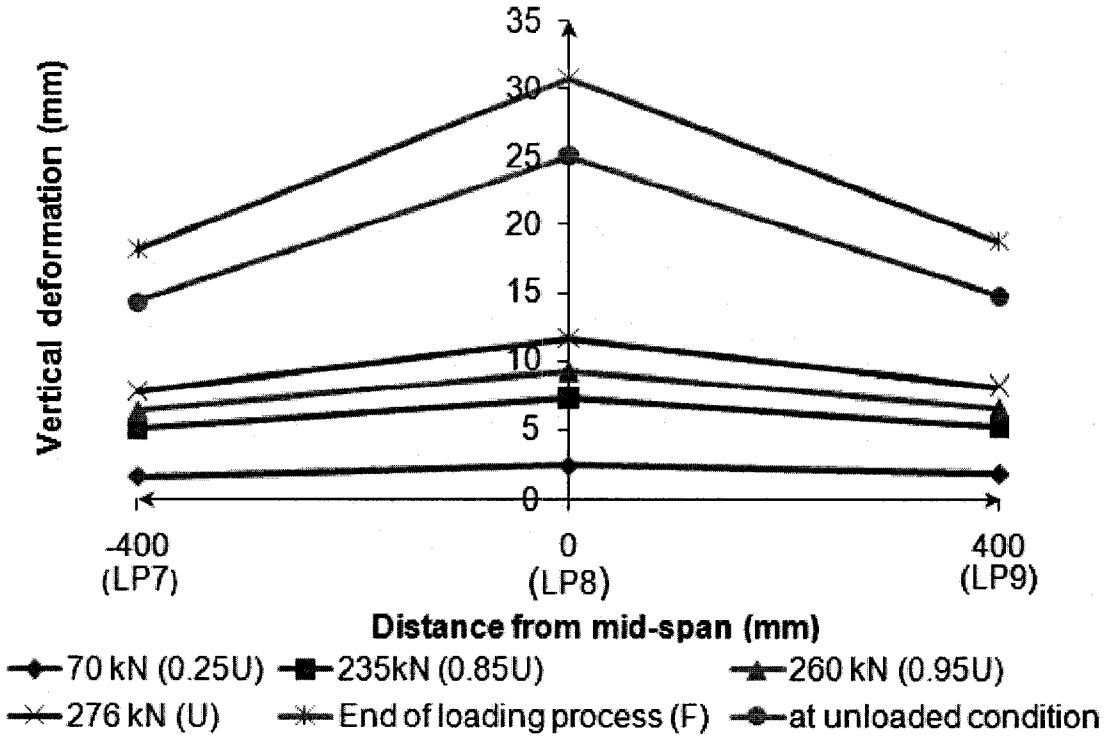

Figure 4.61: Vertical deformation response for RC-W133-T0.6-G2

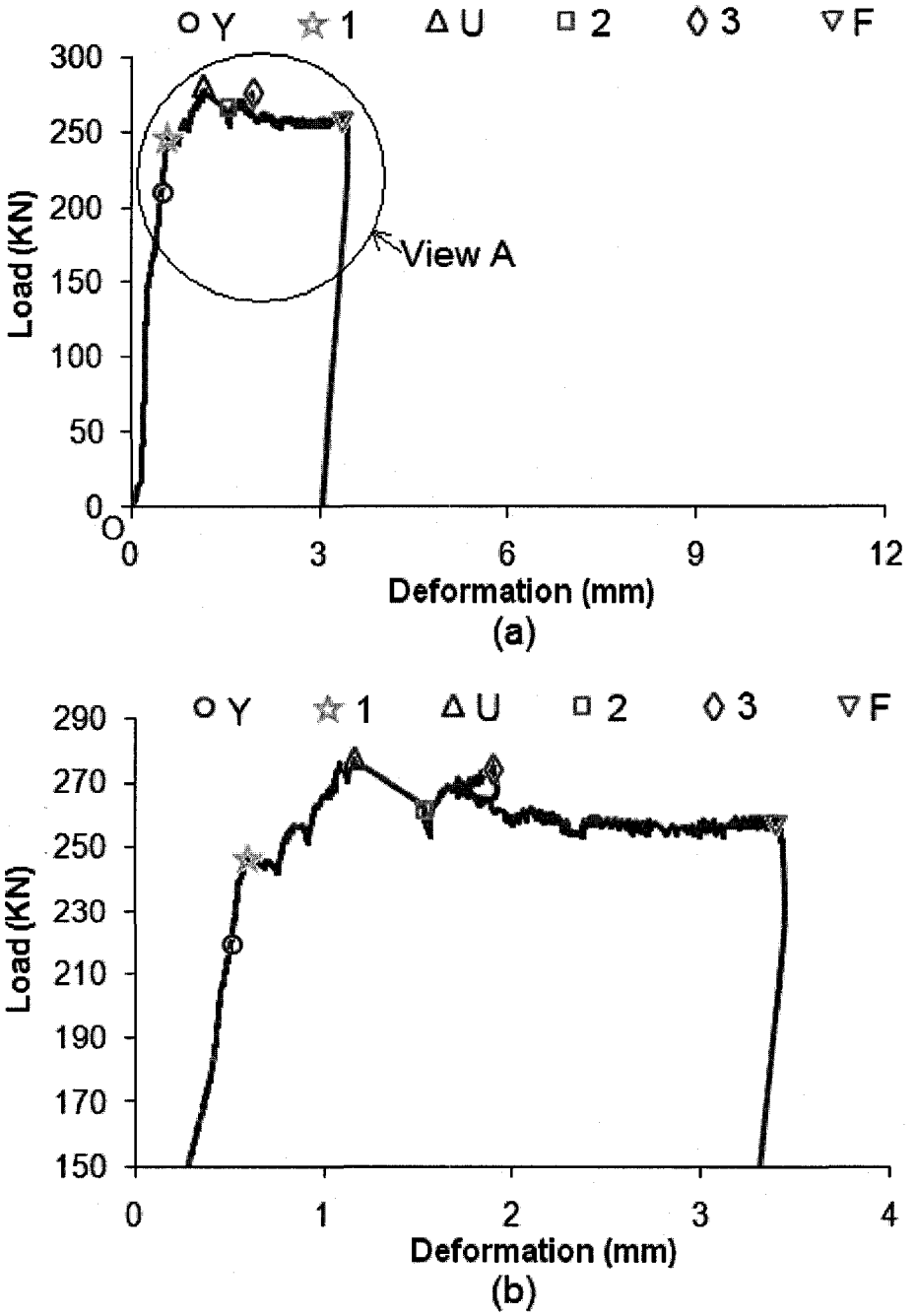

Figure 4.62: (a) Load vs. mid span (LP5) lateral deformation behavior of RC-W133-T0.6-G2 and (b) Detail of view "A"

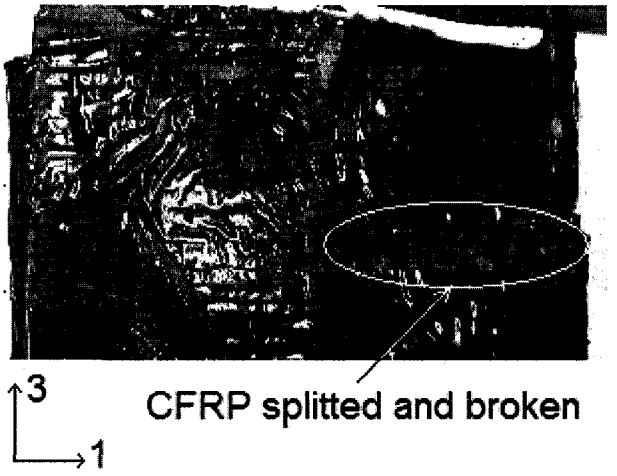

Figure 4.63: RC-W133-T0.6-G2, CFRP wrap and cross-wrap splitting

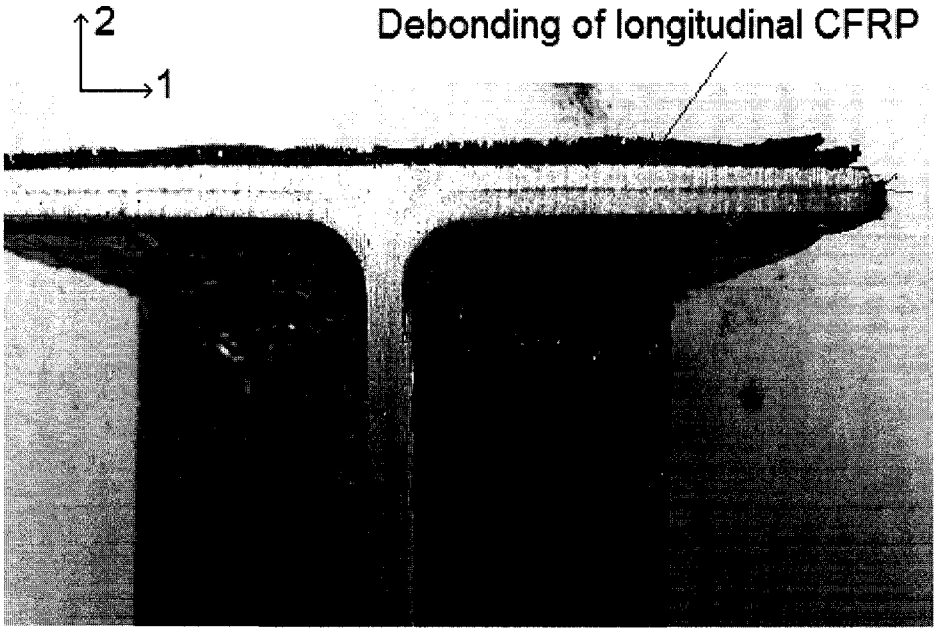

Figure 4.64: RC-W133-T0.6-G2, CFRP debonded

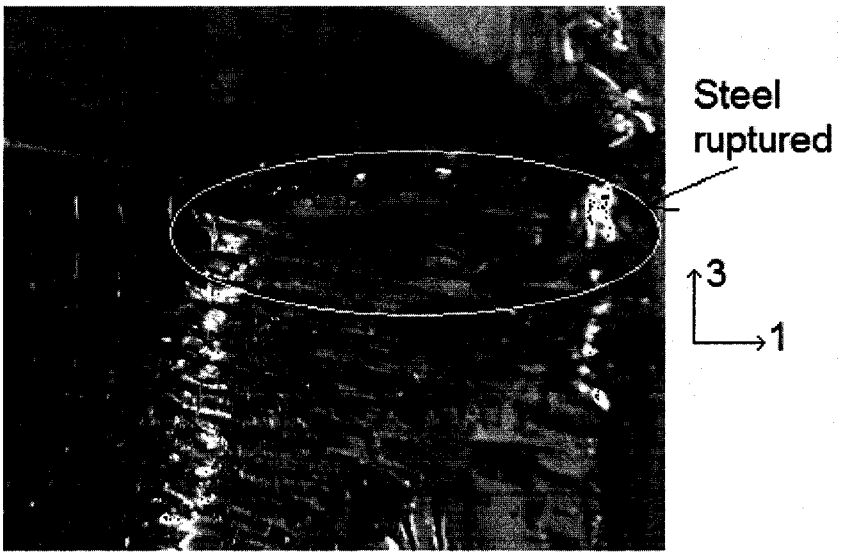

Figure 4.65: RC-W133-T0.6-G2, steel ruptured

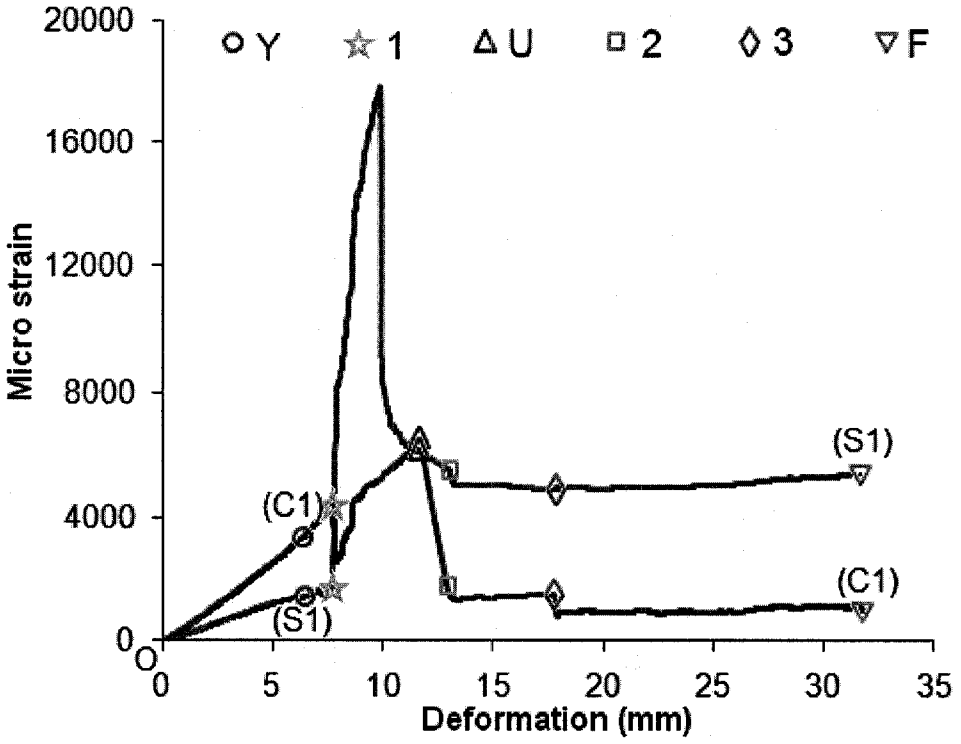

Figure 4.66: Local strain from SG C1 & S1 vs. deformation for RC-W133-T0.6-G2

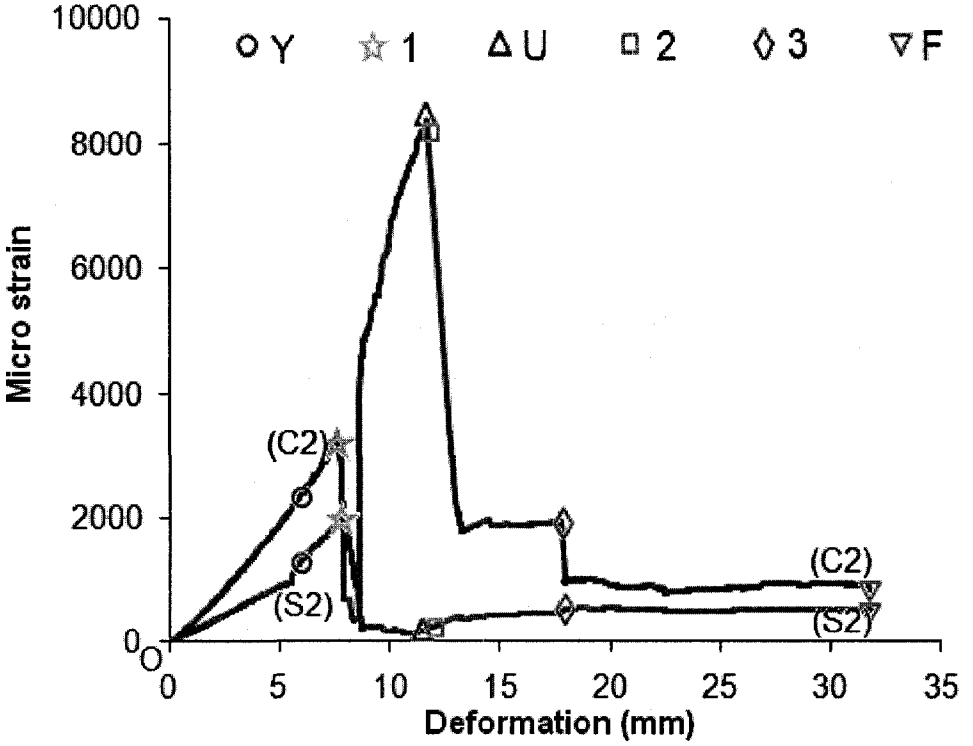

Figure 4.67: Local strain from SG C2 & S2 vs. deformation for RC-W133-T0.6-G2

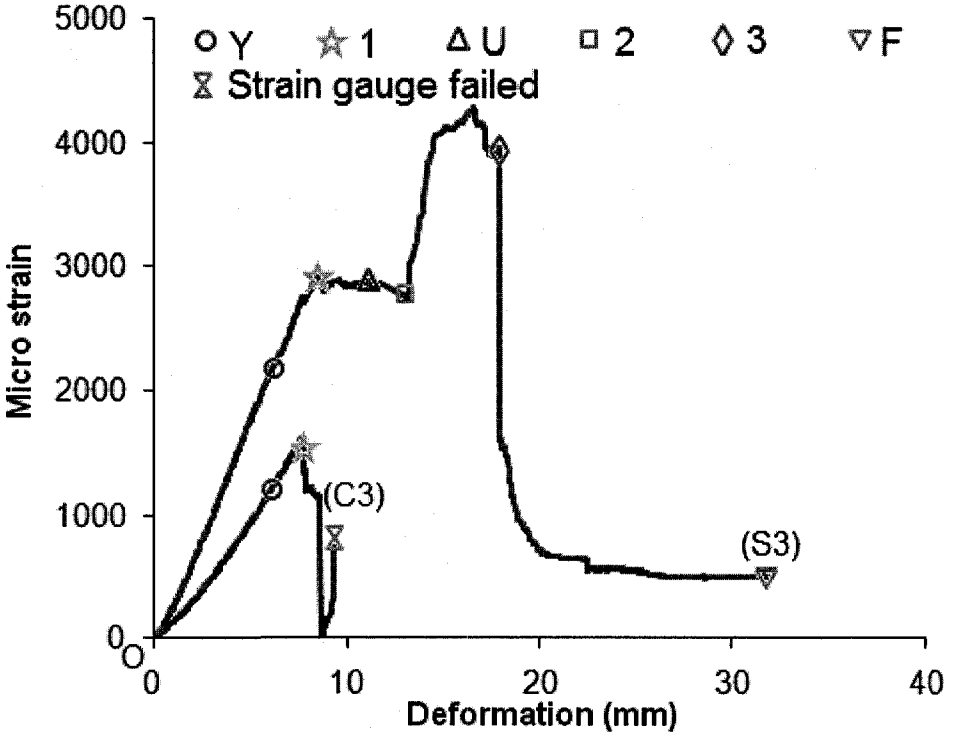

Figure 4.68: Local strain from SG C3 & S3 vs. deformation for RC-W133-T0.6-G2

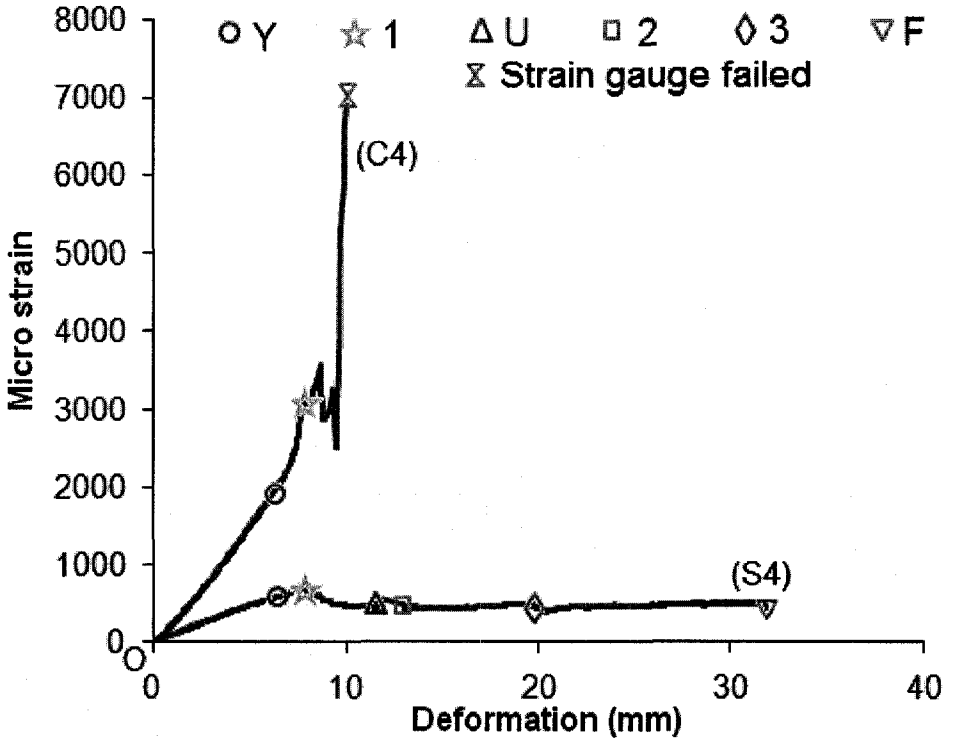

Figure 4.69: Local strain from SG C4 & S4 vs. deformation for RC-W133-T0.6-G2

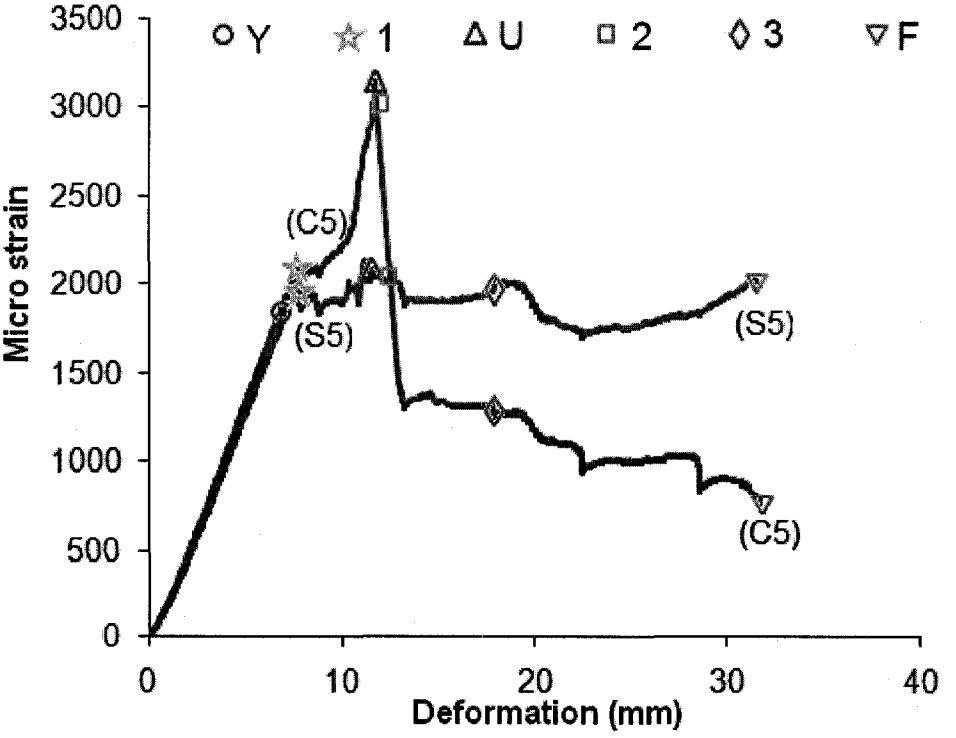

Figure 4.70: Local strain from SG C5 & S5 vs. deformation for RC-W133-T0.6-G2

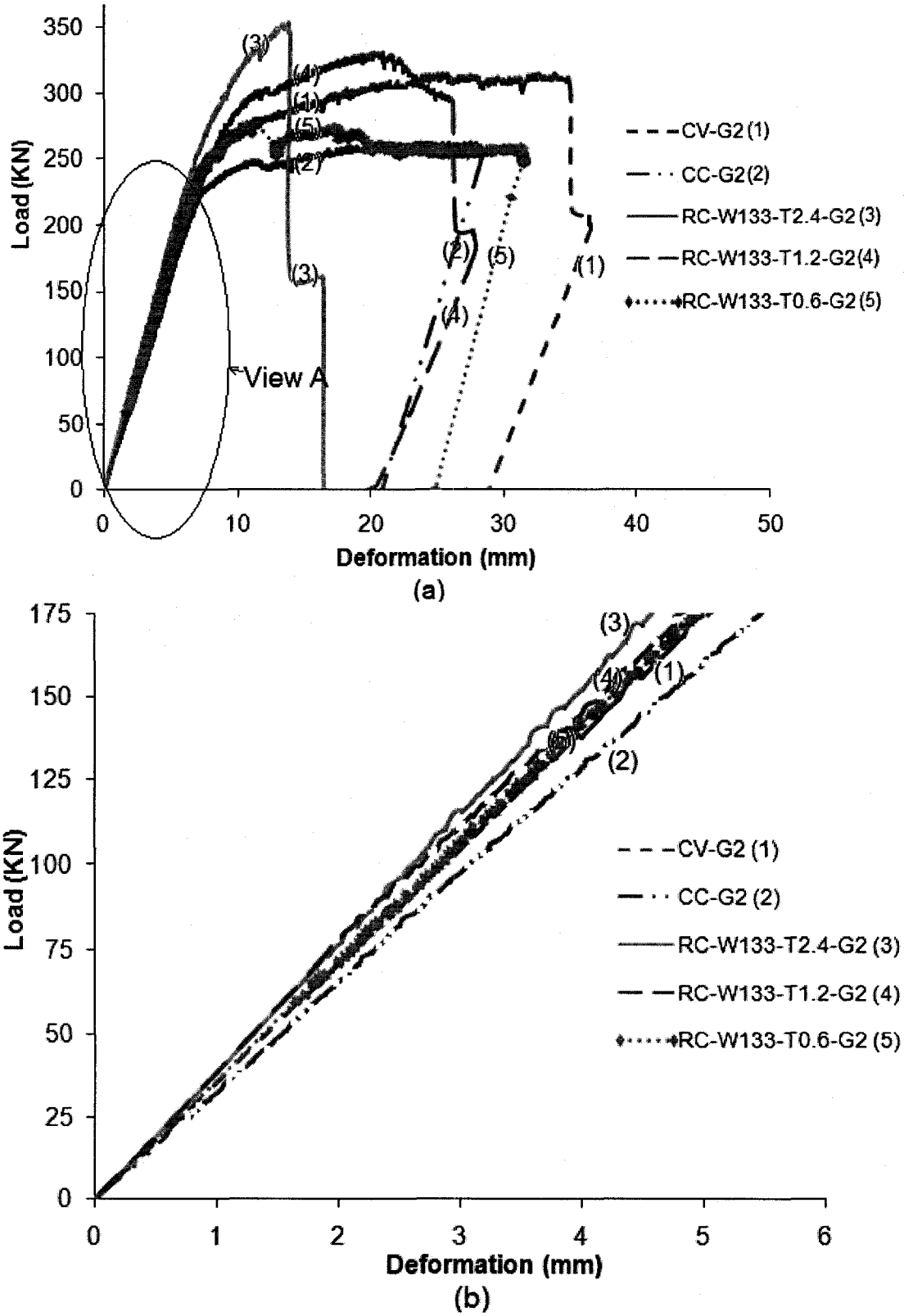

Figure 4.71: (a) Load vs. deformation behavior of group 2 specimens and (b) detail of view "A"

5 FINITE ELEMENT ANALYSIS

5.1 General

All the five specimens and the parameter study were modeled using ABAQUS Standard Version 6.6-1 (which will be referred to as ABAQUS in future discussion), a commercially available general purpose finite element (FE) package developed by Hibbitt, Karlsson & Sorensen, Inc [HKS 2006]. This software package was selected for several reasons. It allows the beams to undergo large deformation using finite (large) strain formulations. This software also offers different efficient shell elements for both thin and thick shells, and non-linear constitutive models with various material hardening rules, such as isotropic, kinematic, and mixed hardening rules.

Another advantage is that ABAQUS offers both load and displacement controlled solution schemes. A load-controlled scheme is necessary to model the initial elastic loads applied to the beams, while displacement-controlled schemes are necessary to pass the elastic yielding load point and carry out elastic-plastic analysis. In addition, ABAQUS allows partial control on the solution process and convergence criteria. Consequently, faster or slower solution processes can be chosen and convergence criteria can either be relaxed or tightened by the user.

Full-scale tests on five beam specimens and the parameter study made a significant contribution in understanding the effect of surface corrosion and repair of corroded beam with CFRP composite. However, the experimental test is time consuming and expensive, and cannot provide all the information that might be required for thorough research. As a result, mathematical or numerical model analysis is an alternative solution for predicting the behavior of a corroded beam and the effects of CFRP repair.

The primary objective in developing a numerical tool is to be able to predict behaviors similar to that observed from group 2's five beam tests. A secondary objective is to develop a parameter study included thirty-six rehabilitated beam specimens to study the influence of the thickness and length of corrosion on the minimum thickness of CFRP

required to repair the corroded beam. The finite element (FE) models of beam specimens were calibrated using the test data obtained from this study.

5.2 Finite Element Method

Classical mathematical solution techniques like those using partial differential equations are generally not useful for most practical structural engineering problems because the geometry and load history are too complicated. In these cases, numerical methods such as finite element method (FEM) need to be adopted. The FEM has advantages over most other numerical analysis methods. For example, FEM is applicable to any field problem and there is no restriction on geometric, boundary conditions, loadings, and material properties.

In the first step of finite element analysis (FEA), the whole structure is divided into sets of small (finite) pieces (elements), each set with the same geometric pattern and physical assumption, and the stiffness of each element is formulated. Each finite element is interconnected with the adjacent element through their nodal points, where there is nodal force acting at each node and the node is subjected to displacement. For each element, a standard set of equilibrium equations can be developed as:

$$[\ K\ ] \times \{\ U\ \} = \{\ P\ \} \qquad (5.1)$$

Where $[K]$ is the structure stiffness matrix, $\{U\}$ is the nodal displacement matrix, and $\{P\}$ is applied load matrix. Superimposing these element equations mathematically into a matrix format assembles these elements to form the whole structure. After applying the boundary conditions, required loads, and displacement, the matrix equation is solved to find the unknown parameters. Substituting these values into the matrix, displacement and stress distribution everywhere within the element are calculated. A detailed discussion of FEM and solution process can be found elsewhere (for example, Bhatti, 2005).

5.3 Details of Finite Element Models

Different considerations that were made during numerical modeling are discussed in the following subsections, which also discuss the types of solution techniques that were used and the options available in ABAQUS.

5.3.1 Element

The specimens were divided into a mesh of finite elements. Four-node shell element (S4R) was used for the models and analyses. The S4R is a general-purpose 4-node quadrilateral stress/displacement shell element with reduced integration (one intergration point) and a large-strain formulation. Each of the four nodes has six degrees of freedom, namely three translations (u_1, u_2, and u_3) in the direction of three axes (x, y, and z), and three rotations (θ_1, θ_2, and θ_3) about these three local axes. Element formulation of this element does not suffer from unconstrained hourglass modes and transverse shear locking (HKS, 2006).

The S4R, being a general-purpose shell element, can be used to model the behavior for both thick and thin shells. This element has the capability of modeling transverse shear deformation. It uses thick shell theory as the shell thickness increases and becomes discrete Kirchhoff thin shell element as the thickness decreases. The transverse shear deformation becomes very small as the shell thickness decreases (HKS 2006). Thick shells are needed in cases where transverse shear flexibility is important. They are not required if the shell is thin because, for thin shells, the shear deformation is negligible. For the current study, thin shell formulation was required.

Default values of shear stiffness in ABAQUS are based on the ratio of area of the element to thickness of the element, discussed in the ABAQUS manual (HKS, 2006). The default values are adjusted automatically by ABAQUS if necessary to avoid shear locking in the elements. However, the default values can be changed if the default shear stiffness becomes too large and a shear locking occurs during the analysis. Only the default values were used in the current analysis and no problems were noticed.

This element accounts for finite membrane strains and allows for change in thickness. Membrane strains are those strains that exist in the shell, especially in a thin shell, but are not due to bending. They are suitable for large deformation and finite strain analysis and found effective in modeling the severe local buckling in flange and web under the load conditions of the experimental tests. The derivatives of the position vector of a point on the deformed reference surface with respect to the same point on the undeformed reference surface gives the membrane strains on the surface. This allows for a variation in the thickness of the shell element at different load increments, as occurred in the actual pipe test specimens. The strains that result from bending are assumed to be small and derived from the derivatives of the normal to the reference surface.

This S4R element uses has an isoparametric formulation, which means that the element displacements are interpolated in the same way as the geometry interpolation. Therefore, it is assumed that each nodal point coordinate necessary to describe the geometry of the element, there corresponds one nodal point displacement.

The default number of integration points through the thickness of the shell is five and the default value was used for the modeling. However, it is possible to change the number of default integration points. Simpson's rule is used to approximate the integration. The section points through the thickness of the shell are numbered consecutively, starting with point 1 at the "bottom" surface of the shell. The S4R has only one integration point on its mid-surface and it is a reduced integration element. Reduced integration uses a lower-order integration to form the element stiffness. Reduced integration usually provides more accurate results (provided the elements are not distorted), and significantly reduces running time, especially in three dimensions. Reduced integration does not cause any change in the convergence rate and often improves the displacements and stress predictions significantly.

Reduced integration may however, introduce some "hourglass" deformation modes. This S4R element has hourglass control to prevent it to from an hourglass mode. An hourglass mode is a mode of deformation, other than conventional rigid body motion, that does not develop any strain energy. Consequently, like rigid body motion, this mode of

deformation poses similar numerical instability in the solution process. The hourglass mode can be associated with in-plane (membrane deformation modes) displacements or it may be due to rotational (bending modes) modes (HKS, 2006a). Element S4R formulation in ABAQUS provides control on both of these modes. ABAQUS uses a small artificial stiffness associated with rotation about the shell normal to prevent hourglass modes. The default stiffness values are given in HKS (2006b). The default stiffness values used are sufficiently small such that the artificial energy content is negligible. However, this default value can be changed if found that default values are not enough to stop the hourglass modes from happening. Only the default values were used in the current analyses and no difficulties were noticed.

5.3.2 Geometry and Boundary Conditions

A typical geometry that was used in the numerical analysis for this project is shown in Figure 5.1. The displacements u_1, u_2, and u_3 and the rotations θ_2 and θ_3 were restrained to simulate a pin support (point C). For the left support (roller) (point B), only displacement u_2 and rotation θ_2 were restrained to simulate a roller support as used in the test. These two points (point B and point C) in the test setup were 100mm away from the right/left bottom ends of the beam. For beam specimens, this distance (100 mm) does not have any significance because these points were connected to the bottom ends of the beam in such a way that the portion of the model between pivot point and adjacent bottom ends of the beam behaved like a rigid body.

Multi-point constraints (MPC) algorithm were used between the nodes on the bottom ends of the beam and the adjacent pivot point (Point B and Point C in Figure 5.1) to simulate physical connectivity of the beam ends to the nearest support. The MPC-BEAM was used to constrain the degree of freedoms of the nodes (slave nodes) on the bottom flange at the ends of the beam to the degree of freedoms of the points (B and C) and thus, allowing the portions of the structure in between the beam specimen and the nearest pivot node to behave like a rigid body. The MPC-BEAM acts very similar to a rigid beam element except no element exists in the earlier case, and thus, reducing significant processing efforts and time. Consequently, the ends of the beam bottom flange were

subjected to the same boundary conditions that were applied to the nearest pivot point (master node).

A flange stiffener, 1000 mm long x 110 mm wide x 6 mm thick steel plate, was welded to the center top flange of the beams to avoid flange buckle under the load application point as shown in Figure 3.22. For simplicity in numerical modeling and analysis, this plate was simulated by moving the nodes in that area up by 3 mm and increasing the thickness by 6 mm (see Figure 5.2 for details). A point load was applied in the negative y direction on the load point (master node, Point A in Figure 5.1) same way as it was applied on the test specimen. MPC-BEAM algorithm was used between the nodes, which are located at the top flange of the beam and located within 100 mm to the mid-span, and the load point (point A) to simulate the jack acting on the loading plate.

The corrosion was modeled by moving the nodes in corrosion zone up by maximum 2 mm at the center of the corrosion, and reducing the thickness of the bottom of the beam flange gradually (see Figure 5.3 for details).

Layers of MBrace CFRP and epoxy were simulated together as one thick layer of MBrace composite system assuming no separation between two CFRP composite layers. Thus, the number of nodes and elements reduced significantly. Therefore, a smaller stiffness matrix was required, leading to save in solution processing time drastically. The nodes of the CFRP composite were constrained to the bottom of the beam flange by using MPC algorithm. Thus, a perfect bonding between CFRP composite and bottom flange of the beam was modeled. As a result, the cross wraps (ties) used in experiments were not required for the FE model.

Lateral support systems were modeled by constraining displacement u_1 at required nodes, while the steel blocks were modeled by constraining displacement u_2 between necessary nodes on the top flanges of the beam (master) and the adjacent nodes on the bottom flange (slave) (See Figure 3.17 and 3.20 for locations). The web stiffeners were model by constrained displacement u_1, and rotation θ_2 and θ_3 of the web at the mid span of the beam (See Figure 3.21 for location).

The filler material, MBrace putty or CFRP, was filled into the corroded hole in order to have a leveled surface for CFRP bonding in the experimental. The filler material alone does not affect structure's behavior, because of its short bonding length. Therefore, the filler material was not simulated in the program.

The installed thickness for MBrace primer is 0.075mm approximately. The primer was applied on the corroded surface to enhance the bonding. The effect of MBrace primer was not required in the numerical models.

5.3.3 Material Properties

Two different materials were used in the numerical modeling and analysis. They are steel and CFRP composite. The following subsections discuss material properties for these two materials.

5.3.3.1 Steel

A total of eight tension coupon specimens from the steel beam were tested to obtain the uniaxial stress-strain behavior of the beam material. Test procedures and test results are discussed in Sections 2.6.7 and 3.4.1, respectively. All eight steel tension coupon tests indicated almost identical behaviors. Table 5.1 presents the average material property in nominal sense. Figure 5.4 shows the graphical representation of the same "average" behavior for all five tension coupons.

The Point U is the ultimate load point and its coordinates are shown in the parenthesis. The nominal values of fracture stress and fracture strain were determined after the completion of the material tests. Subsequently, the Point F corresponding to the fracture nominal stress and fracture nominal strains as shown in Figure 5.4. No data could be recorded in between ultimate load point (U) and the fracture (F) and consequently, the material behavior was assumed to be linear in between these two points as shown in Figure 5.4.

The material properties obtained from the axial tensile coupon tests were expressed in "engineering stress" and "engineering strain" (nominal) values (Figure 5.4). These

engineering (nominal) values were computed based on classical strength of material definitions for the undeformed original cross sectional dimensions. They are reasonably good for linear elastic and small strain analyses. The current finite element models were required to run up to very large deformations and strains. Therefore, "true stress-true strain" behavior as presented in Figure 5.5 was required. The ultimate load and fracture points are indicated in this figure by the same notations *U* and *F,* respectively. ABAQUS however, requires "true stress" and "true plastic strain" behavior irrespective of type of analysis. The true stress (σ_{true}) and true *plastic* strain ($\varepsilon_{\ln}^{pl}$) are calculated using the following expressions (HKS, 2006b).

$$\sigma_{true} = \sigma_{nom}(1+\varepsilon_{nom}) \tag{5.2}$$

and

$$\varepsilon_{\ln}^{pl} = \ln(1+\varepsilon_{nom}) - \frac{\sigma_{true}}{E} \tag{5.3}$$

where σ_{nom} is the nominal or engineering stress, ε_{nom} is the nominal or engineering strain recorded from the material tests, and E is the modulus of elasticity. The true stress and true plastic strain behavior obtained based on the nominal values in Table 5.1 and using Equations (5.2) and (5.3) is shown in Figure 5.6.

A yield criterion specifies the state of multi-axial stress corresponding to the start of plastic flow. The default in ABAQUS is the classical Mises yield criterion. This is good enough for initially isotropic metals like the one used in the test beam specimens. This criterion was used for the current finite element models. The yield criterion assumes that the yield of the metal is independent of the equivalent pressure stress.

The associated plastic flow rule was used to relate the plastic strain increments to the current stresses and stress increments subsequent to yielding. Associated plastic flow means that, as the material yields, the inelastic (plastic) deformation rate is in the direction of the normal to the yield surface. This assumption is generally acceptable for most metals including the beam material in the current model.

A hardening rule describes how the yield surface or yield condition changes with progressive yielding, so that the conditions (i.e. stress states) for subsequent yielding can be established. ABAQUS/Standard 6.6-1 (HKS, 2006b) provides options of various work hardening rules for metals: a perfect plasticity (no strain hardening) model, a nonlinear isotropic hardening model (called isotropic hardening model), a kinematic hardening (called as linear kinematic hardening) model, and mixed hardening model (called as nonlinear isotropic/kinematic hardening model).

A perfect plasticity model assumes that the yield surface does not change with the plastic deformation. It does not represent the true behavior of the beam materials that experience significant hardening after yielding. Therefore, it was not used for the current numerical modeling and analysis.

The isotropic hardening material model assumes that the center of yield surface remains at the same location while expanding or shrinking in size as the plastic strains develop as shown in Figure 5.7(a). The isotropic hardening material model in ABAQUS is nonlinear and a full range of stress-strain behavior can be defined. Both strain hardening and strain softening can be defined. Since no reversals in elastic-plastic strain occurred in the test specimens, isotropic material hardening model was used in this study.

In the kinematic hardening model, it is assumed that the size and shape of the yield surface remains constant but the yield surface translates in stress space (like a rigid body) with progressive yielding as shown in Figure 5.7(b). Bauschinger effect associated with stress reversals are considered in this hardening model. The Bauschinger effect means, when applying a tensile or compressive load beyond its elastic limit, the elastic limit for the compression or tension, respectively will reduce considerably, see Figure 5.8 for detail. In other words, the Bauschinger effect demonstrates that the material in the other direction becomes weaker due to stress reversal. Bauschinger effects are important when elastic-plastic strain reversals take place, such as one due to cyclic loads. Since no cyclic load was applied in the specimens, the kinematic hardening model was abandoned from use in this study. Uses of isotropic material hardening models provided global behaviors similar to the actual behaviors observed from the laboratory tests.

A combination of isotropic and kinematic hardening rules that are used in the mixed hardening model leads to a more general hardening rule. It provides more flexibility in describing the hardening behavior of the material. This hardening rule will give better predictions, but requires calibration that is more detailed and difficult. Since no reversals of elastic-plastic strain occurred in the test specimens, mixed hardening model was not necessary.

The hardening rule used in this project is the isotropic hardening model (Figure 5.6).

5.3.3.2 MBrace Strengthening system

Coupon tests were conducted for MBrace epoxy, MBrace CFRP dry fabric and MBrace CFRP composite. Test procedures and test results are discussed in Sections 2.6 and 3.4.2. The test result indicated that MBrace CFRP fabric and composites system exhibit linear elastic behavior. Only the MBrace CFRP composite was used in ABAQUS model. The values used in ABAQUS for modeling material behavior of CFRP composite are tensile modulus, poisson ratio, and rupture ratio are 243 GPa, 0.4 and 1.67%, respectively.

5.3.4 Mesh Selection

5mm long element were used throughout the whole specimen to avoid the influence of non-uniform mesh size on the behavior of the specimens. However, the specimen width is not uniform in the test, because of the dimension of the specimen. The specimens were categorized into two groups in accordance to their lengths, these are: (1) horizontal or 6 mm width elements, (2) vertical or 5 mm width elements. These numbers were chosen due to the geometric size of the I-beam. The horizontal (6 mm width) elements formed the flange of the beam, the aspect ratio for this kind element is 5:6 (length: width = 5 mm: 6 mm). The vertical (5 mm width) elements formed the web of the beam, the aspect ratio for this kind element is 1:1 (length: width = 5 mm: 5 mm).

5.3.5 Load Histories

The load that was applied to the test specimens was also applied to the numerical models. The axial point load P as was applied in several increments. Only the maximum numbers of increments, minimum increment size, and maximum increment size need to be defined in the ABAQUS input file. The ABAQUS solution scheme then finds out the optimum increment size and consequently the total number of increments required.

The load was applied in two steps. In the first step, load control was used until the specimen reached its ultimate load. In the second step, displacement control was used until the specimen failed.

5.3.6 Solution Strategy

Various nonlinear solution techniques are available these days. ABAQUS offers three nonlinear solution methods: Newton's methods (full Newton's method and modified Newton's method), Quasi-Newton's method, and Modified Riks method.

In the full Newton's method, the stiffness matrix [K] must be formed and solved in every iteration at each nodes and every direction as shown in Figure 5.9. Consequently, total solution time is high. Therefore, this method is usually avoided in large finite element codes. The most commonly used alternative to Newton is the modified Newton method, in which the [K] is recalculated only occasionally. This method is suitable for moderate nonlinear problems involving softening behavior; however, it should not be used in severely nonlinear analysis.

In quasi-Newton method, a series of approximate [K] is used rather than exact [K], the trade-off is that more iterations are required to converge, compared to Newton as shown in Figure 5.10. Thus, for some practical cases, quasi-Newton methods are more economic than full Newton, but in other cases, they are more expensive.

Riks method is a linearized arc-length solution method. It is capable of tracing the complicated stable and unstable equilibrium paths. In the Riks method, the basic algorithm remains the Newton's method. The only difference here is that the increment

size is limited by moving a given distance along the tangent line to the current solution position and searching for equilibrium in the plane that passes through the point and orthogonal to the tangent line, rather than to the tangent line that represents elastic material stiffness. A graphical representation is shown in Figure 5.11. This method however, fails to trace the equilibrium path if snap-through or snap-back behavior exists as presented in Figure 5.12. In that case, a cylindrical arc-length method is required and ABAQUS/Standard does not have this option in it.

The default solution technique in ABAQUS is Newton's method. ABAQUS automatically moves between full Newton's method and modified Newton's method (HKS, 2006a) based on the difficulties in updating [*K*] and the convergence rate. All the discussions made in earlier paragraphs are based on a load-controlled method. However, both load and displacement controls are available with Newton's method in ABAQUS. Two different control methods are discussed in the subsequent sections.

There are two ways to control the solution process: load control and displacement control. In a load-controlled method, an exact load level is specified for each loading step. Displacements *{u}* are found by solving the elastic load deformation relationship (Equation 5.1). This method works well until the solution process reaches the limit point (point 3 in Figure 5.9, 5.10,5.11, 5.13, and 5.14). At the limit point (Point 3 in Figures 5.9 and 5.10), the stiffness matrix becomes singular and the solution path diverges. This is shown in Figure 5.13. In the displacement-controlled method, increments of one or more displacements are specified and the remaining unknown displacements *{u}* are found by solving the same equation (5.1). The advantage with this method is that the stiffness matrix is better conditioned. Here, one or more displacements are known in the *{u}* vector and consequently only the reduced stiffness matrix, obtained from *[K]* needs to be inverted, thus the whole stiffness matrix *[K]* never turns out to be singular. The graphical representation of the displacement control method is shown in Figure 5.14. The advantage with this control is obvious from this figure. An intersection between a vertical line (line drawn at a desired increment in the displacement) and equilibrium path (load-deformation curve) can always be found.

Newton's methods are suitable for the current beam problems. Consequently, Newton's method with displacement control was adopted for the analysis of the models. Not much difficulty was noticed in passing the limit points.

5.3.7 Iteration and Convergence

ABAQUS incorporates an empirical algorithm designed to provide an accurate, and at the same time economical solution of the equilibrium equations of nonlinear systems. For structural stress analysis, ABAQUS uses four parameters: displacement, rotations, force, and moment to check the convergence at each increment. Default tolerance values are assigned with these parameters and they need not be adjusted for most cases. In difficult cases, however, the solution procedure may not converge with the default controls or may use an excessive number of increments and iterations. It may be useful to change certain control parameters. The default value of tolerance for force and moment is 0.005, and displacement and rotation is 0.01. Only default values were used for the current analyses.

ABAQUS uses a scheme based predominantly on the maximum force residuals (force and moment), following each iteration. By comparing consecutive values of these quantities, it determines whether convergence is likely in a reasonable number of iterations. If convergence is deemed unlikely, ABAQUS adjusts the load increment; if convergence is deemed likely, it continues with the iteration process. A minimum increment size is specified (either ABAQUS default or user's defined) to prevent excessive computation in case of limit load or modeling error and consequently the process stops.

5.4 Summary

Finite element models for the test specimens were made and analyzed using the ABAQUS software package. The major difficulty faced during the current modeling was simulating the boundary conditions similar to the actual test, which was overcome successfully by using a modified pin-roller support, only constraining displacement u_2 as described in Section 5.3.2. Results of current finite element analyses are discussed and compared with the test results in Chapter 6.

Table 5.1: Nominal stress and strain values

Nominal Strain (%)	*Nominal Stress (MPa)*
0	0
0.05	91.23
0.10	202.72
0.19	430.79
0.96	414.10
2.02	427.56
4.04	452.00
6.01	479.59
8.03	499.79
10.02	510.22
12.02	517.38
14.01	521.94
16.05	523.90
18.02	524.54
20.09	524.54
22.06	524.55
24.58	525.01
34.00	390.62

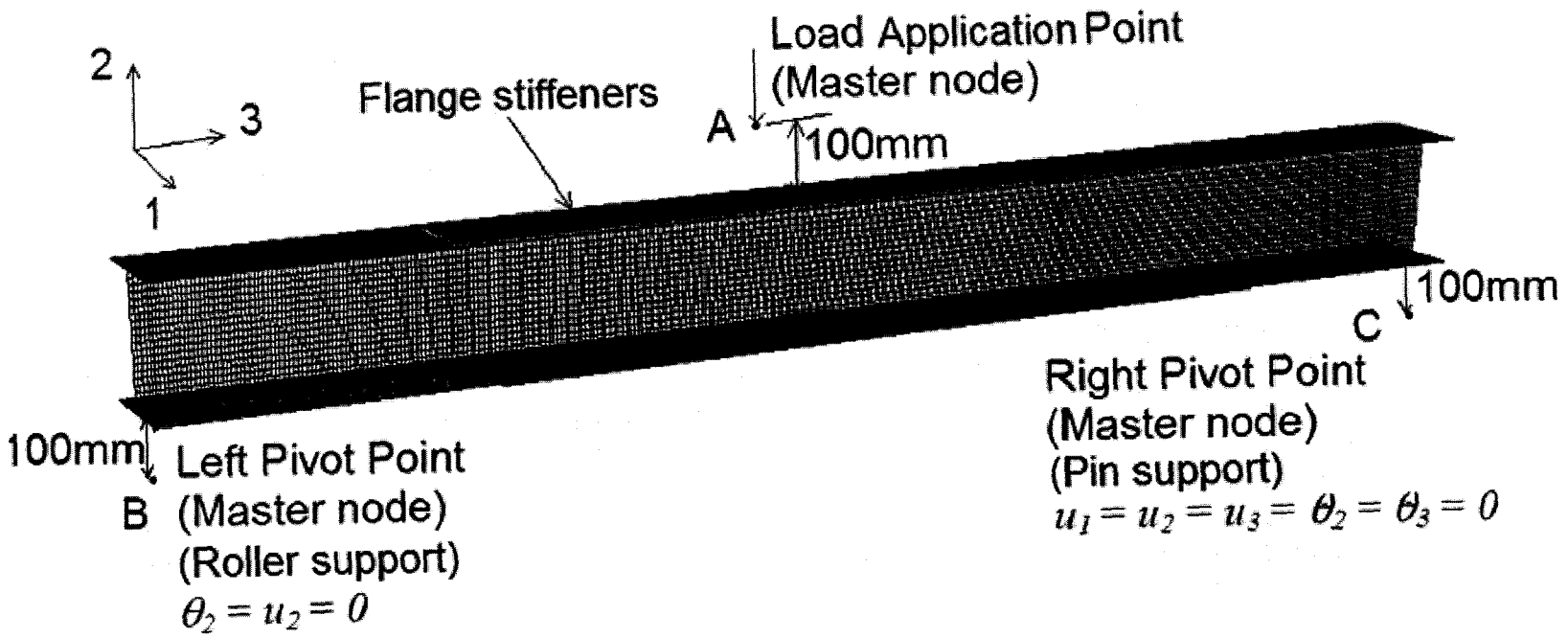

Figure 5.1: Typical geometry for the beam and Pin-Roller support

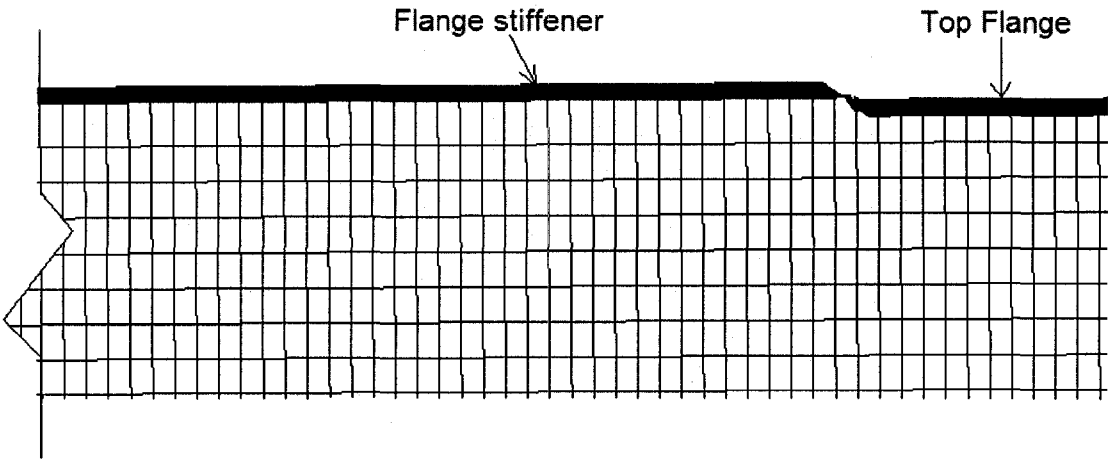

Figure 5.2 Flange stiffener

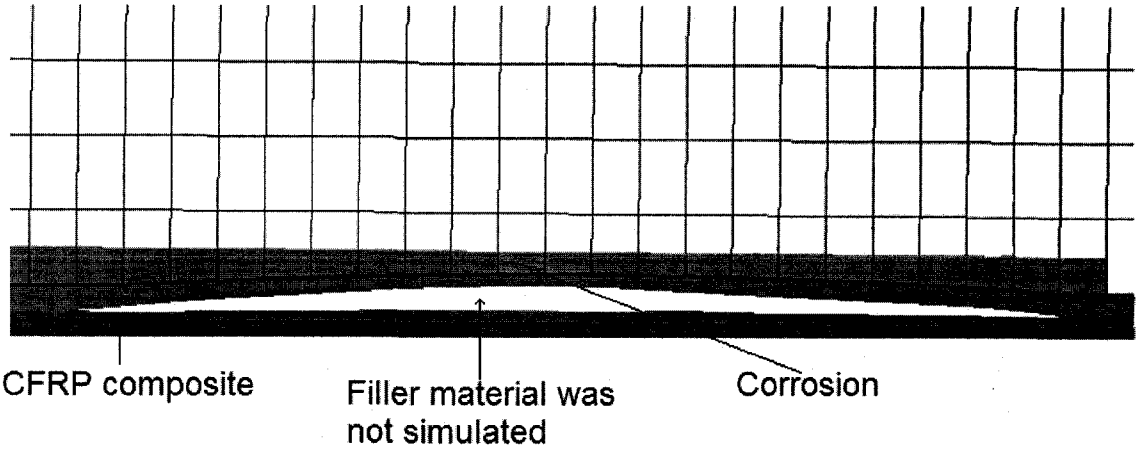

Figure 5.3: corrosion, filler material and CFRP composite

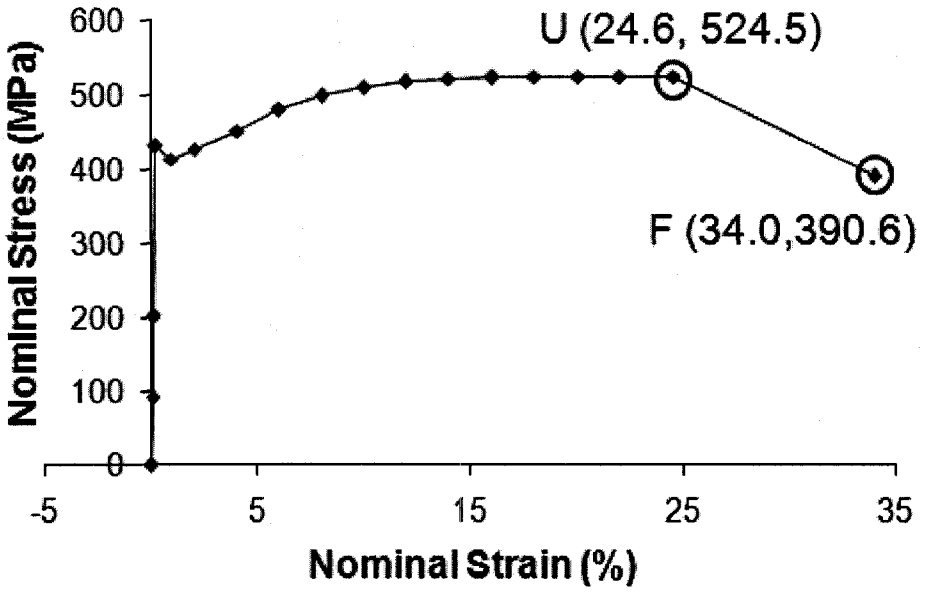

Figure 5.4: Nominal stress-strain behavior until fracture

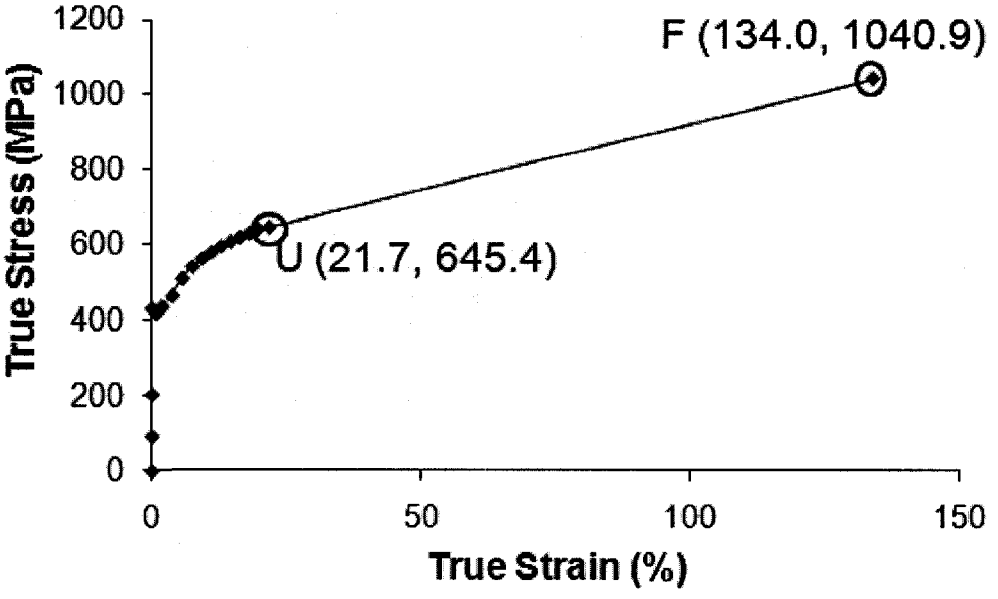

Figure 5.5: True stress-True total strain behavior until fracture

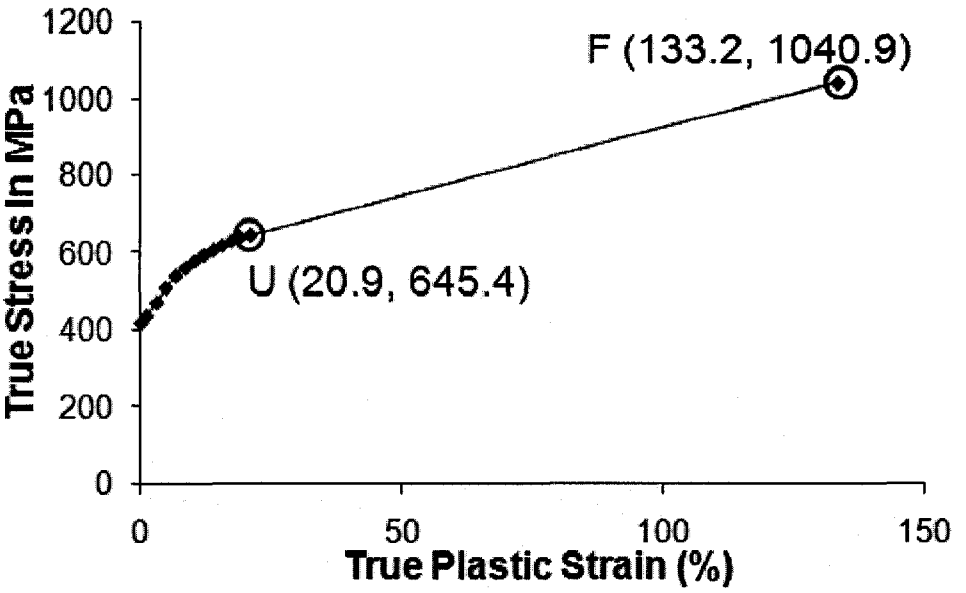

Figure 5.6: True stress-true plastic strain behavior until fracture

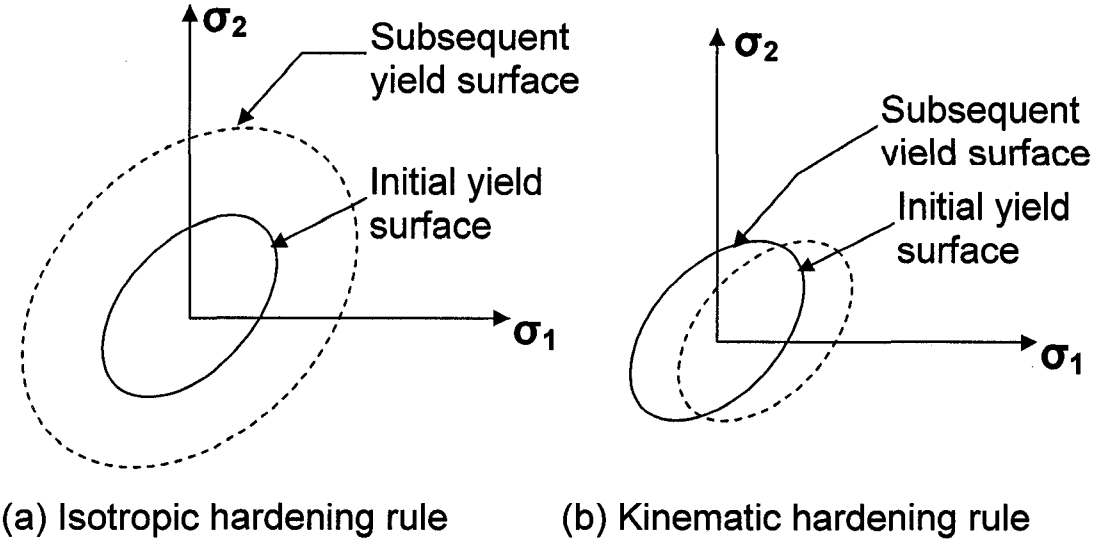

Figure 5.7: Isotropic hardening rule v.s. Kinematic hardening rule for plane stress condition

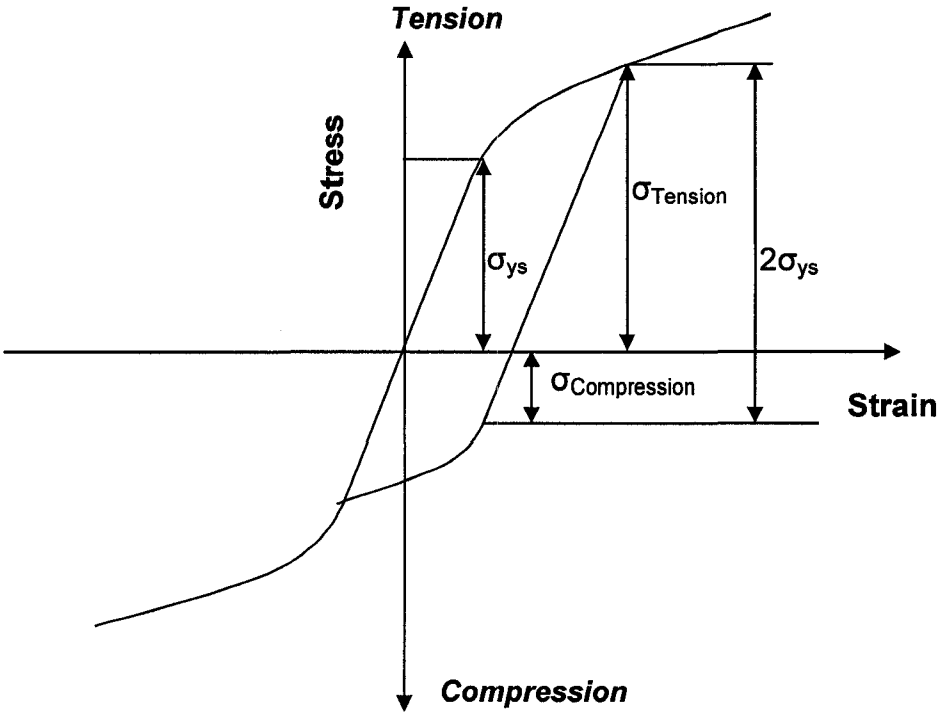

Figure 5.8: Bauschinger effect

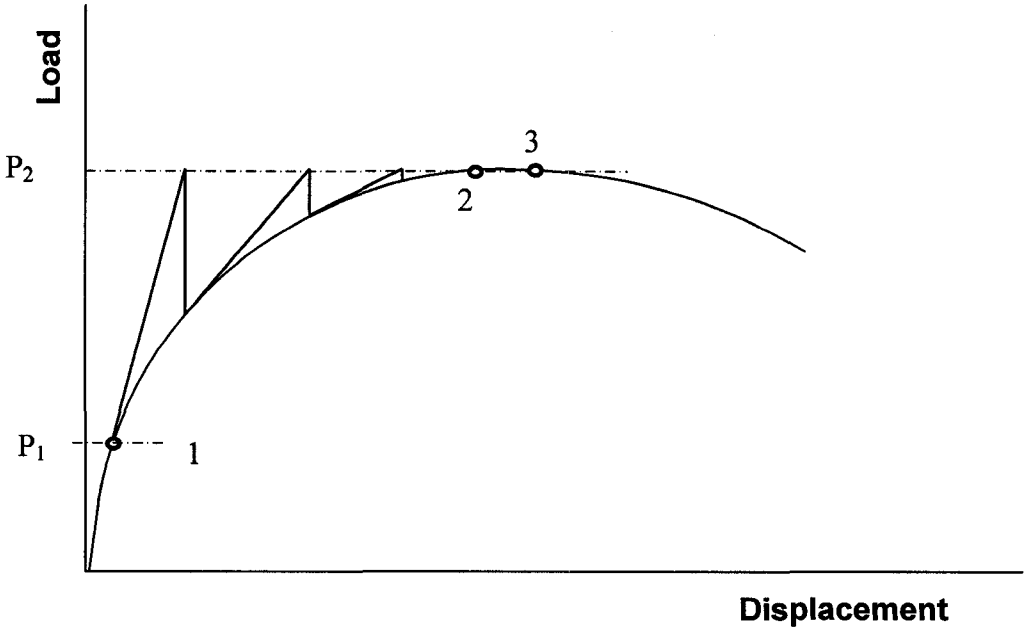

Figure 5.9: Newton's method

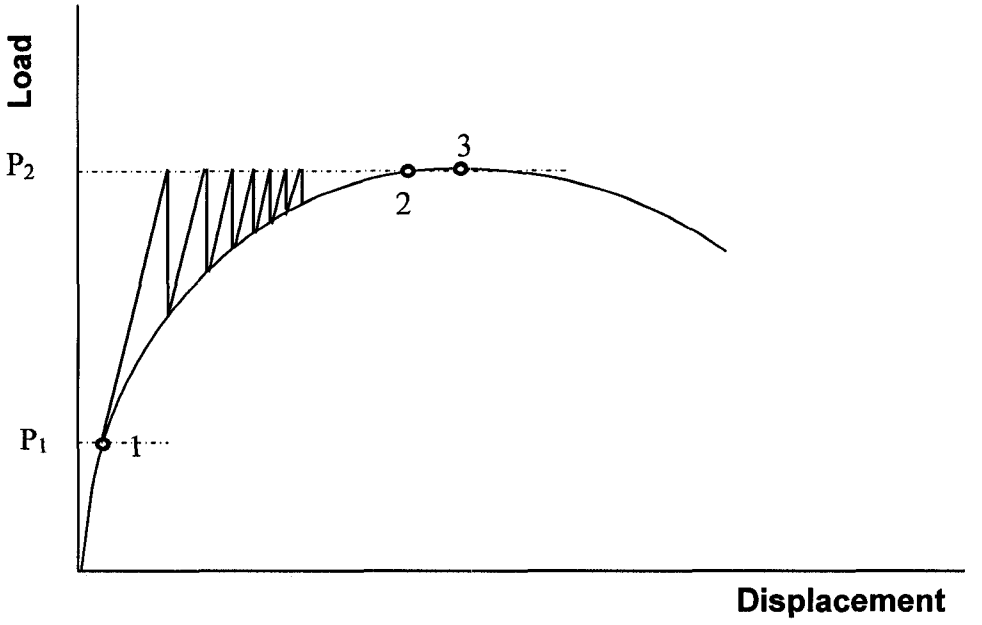

Figure 5.10: Quasi-Newton's method

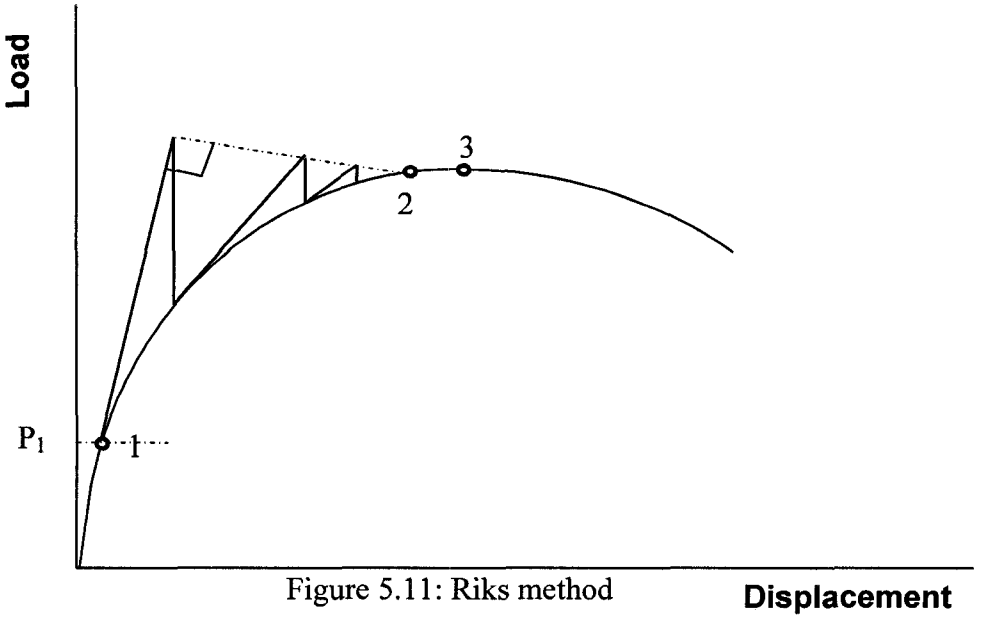

Figure 5.11: Riks method

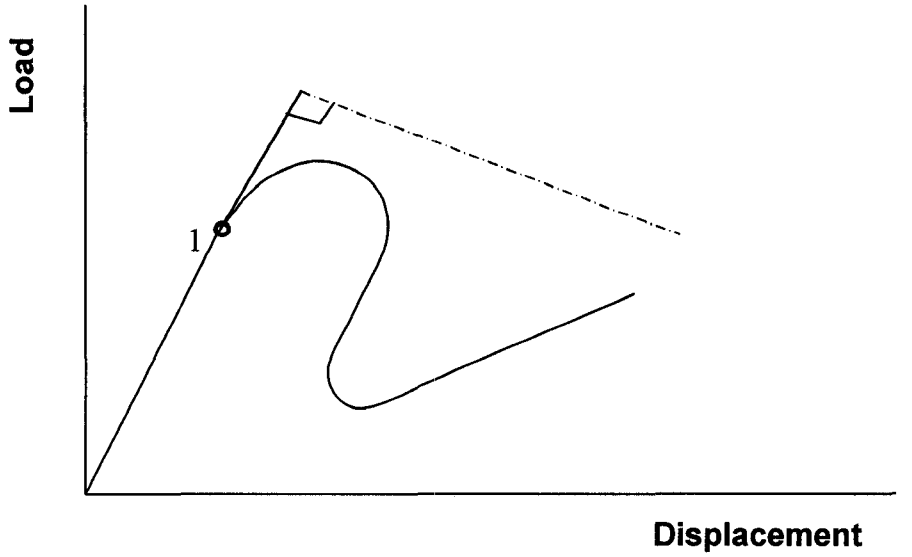

Figure 5.12: Riks method fails at snap-back behavior

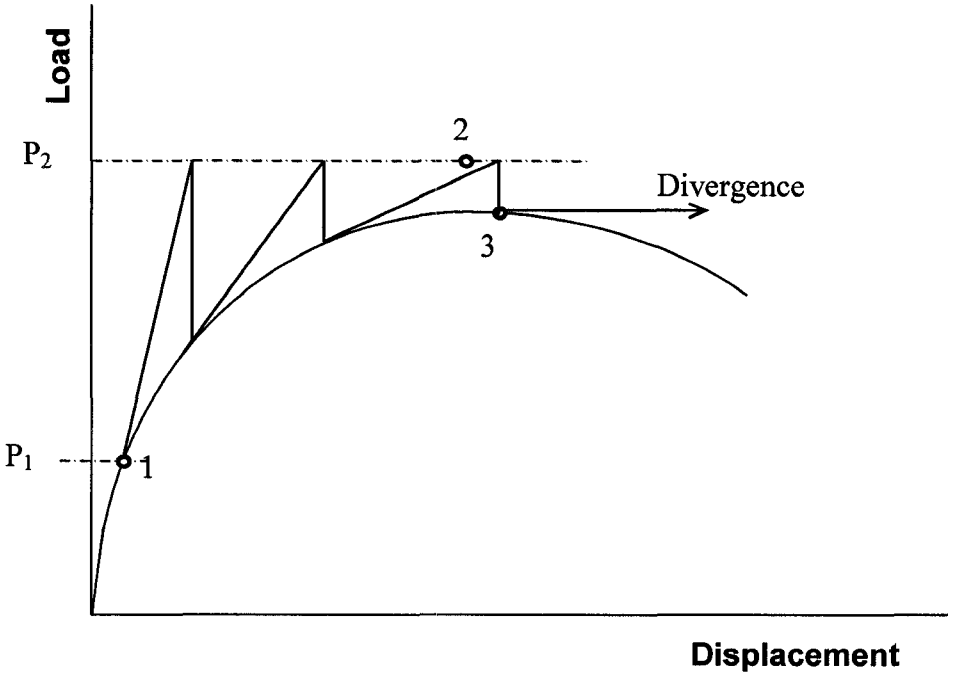

Figure 5.13: Load control process fails at limit point

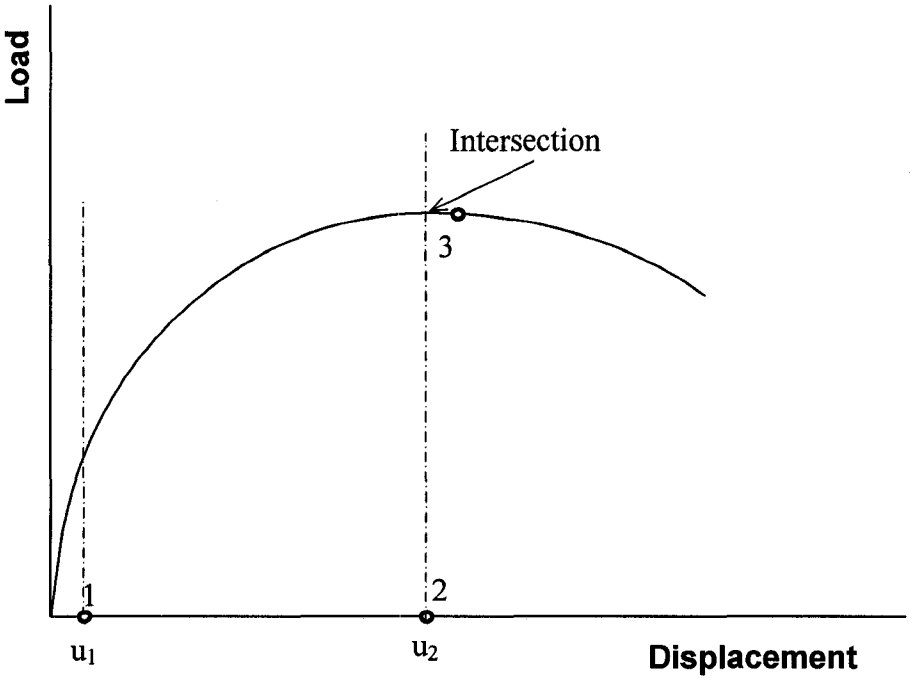

Figure 5.14: Displacement control process

6 COMPARISON OF EXPERIMENTAL AND FEA RESULTS

6.1 General

A detailed discussion on modeling techniques adopted for the numerical analyses using finite element method (FEM) is made in last chapter. This chapter discusses the results obtained from the finite element analyses (FEA) and compares these results with the test results. The primary objective of the numerical analysis was to develop a numerical tool that is able to simulate the complicated global and local behaviors observed from the test specimens. However, primary calibration of the numerical models was done based on global behavior only. A good correlation between the test and FEA models was obtained for the specimens.

6.2 Validation of FE Model

The following subsections discuss the comparisons of test behavior and numerical analyses for all group 2 specimens. As mentioned in Chapter 3, group2 contained one control virgin specimen (CV-G2), one control corroded specimen (CC-G2), and three rehabilitated specimens (RC-W133-T2.4-G2, RC-W133-T1.2-G2, and RC-W133-T0.6-G2). All specimens had web stiffeners to prevent web buckling at mid-span, and flange stiffeners to prevent top flange buckling under load as discussed in section 3.3.4. In addition, the specimens were supported at top and bottom flanges laterally using eight lateral supports to avoid lateral torsion buckling. Four steel round blocks were mounted between the top and bottom flanges under the load application point to reduce the flanges from buckling.

6.2.1 Specimen CV-G2

Specimen CV-G2 was the control virgin specimen in the series of group 2 specimens. The ultimate load for this specimen was 322 kN, and similarly, for the finite element analysis (FEA) model, the ultimate load of the specimen was 314.6 kN. The global load-deformation behaviors obtained from the test and from FEA are presented in Figure 6.1, and similar behavior was also obtained. However, in the test, sever and sudden web buckling occurred at roller supports because the lateral support system near that support

broke. Thus, the load dropped quickly and significantly. This was not simulated in the numerical modeling to keep the modeling and analysis relatively simple, and thus, sudden and quick drop in the load capacity in the numerical model was not obtained. The lateral support system in FEA model was modeled by constraining displacement u_1 at particular nodes as mention in section 5.3.2, thus was able to stop the web from buckling in FEA.

A good correlation was observed between the test and FEA global load-deformation behavior. The ultimate load obtained from numerical analysis is about 2.3% lower than the test value. The stiffness of elastic curve obtained from the numerical analysis is 17.3% higher than that obtained from the test data (Table 6.1). This is because, in the FE model, the beam's curvature at the web-flange intersection and at the tips of the flanges were not considered (Figure 6.2a). Also, in FE model, finite elements (5 mm x 5 mm and 5 mm x 6 mm) were used. Therefore, the cross-section of the beam in FEA is slightly larger than the in the test specimen as shown in Figure 6.2b. Another reason could be the beam used in the test are not perfect W200x21 beam, which means the flange of the beam was not exactly 6.4 mm thick and the web was not exactly 5 mm thick.

Figure 6.3.a and b show the final deformed shape of beam obtained from test. The final deformed shape of Specimen CV-G2 obtained from FEA is shown in Figure 6.3c. A good correlation between the deformed shapes obtained from test and finite element analysis (FEA) was found. Both figures showed that no web or flange buckling under the load application point (mid-span). Figure 6.3b shows the web buckling at the roller support for test specimen. The FE analysis did not show this web buckling (Figure 6.3c). The web buckling occurred in the test was due to large lateral force. The lateral supports in FEA model was able to stop the top flange move laterally, thus, no web buckled in FEA model.

6.2.2 Specimen CC-G2

Specimen CC-G2 was the control corroded specimen of group 2. The ultimate load for this specimen was 260 kN, and the finite element model predicted ultimate load of 261.4 kN. The global load-deformation behavior that was obtained from the test and FEA analysis are presented in Figure 6.4. Similar behavior is again observed from both test and FEA.

A good correlation was observed between the test and numerical (FEA) global load-deformation behavior. The maximum load obtained from the numerical analysis is about 0.5% higher than the test value. The stiffness of elastic curve obtained from numerical analysis is 17.2% higher than that obtained from the test data. Consequently, the deformation corresponding to the ultimate load for the analytical model is lower than that for test specimen.

The final deformed shape of Specimen CC-G2 obtained from the test is shown in Figures 6.5a and 6.5b and that obtained from the FEA is shown in Figure 6.5c. A good correlation between these two deformed shapes obtained for this specimen is observed. Both FEA and test did not show web or flange buckling for this specimen. However, the tearing of the bottom flange at center corrosion observed from test specimen (Figure 6.5b) was not modeled in numerical analysis. This would require separation of geometry in FE analysis and thus, would make the FE modeling and analysis extremely complicated.

6.2.3 Specimen RC-W133-T2.4-G2

Specimen RC-W133-T2.4-G2 was a corroded specimen repaired with 2.4 mm thick (eight layers of Sikawrap Hex 230c dry fabric) Carbon Fiber Reinforced Polymer (CFRP) composite. The ultimate load for this specimen was 354 kN, and the finite element analysis (FEA) model exhibited an ultimate load of 353.8 kN, and thus, the difference is 0.06%. The load-deformation behavior obtained from the test and FEA are presented in Figure 6.6. Similar load-deformation behavior for this specimen was also obtained from numerical analysis and test.

A good correlation was observed between the test and FEA global load-deformation behavior. The maximum load obtained from numerical analysis is about same as the test value. The stiffness of elastic curve obtained from the numerical analysis is 15.9% higher than that obtained from test data (see Figure 6.6). Consequently, the deformation corresponding to the ultimate load for the FEA model is a little lower than that for the test specimen.

The final deformed shape of Specimen RC-W133-T2.4-G2 obtained from test is shown in Figure 6.7a and b and that obtained from FEA is shown in Figure 6.7c and d. A good correlation between the deformed shapes obtained from test and FEA is found between these two deformed shapes. Both figures show that there is no web or flange buckling under the load application point for this test specimen. Both Figures 6.7b and 6.7d show the web lateral buckling at the roller support.

6.2.4 Specimen RC-W133-T1.2-G2

Specimen RC-W133-T1.2-G2 was a corroded specimen repaired with 1.2 mm thick (four layers of Sikawrap Hex 230c dry fabric) CFRP composite. The ultimate load for this specimen was 330 kN, and the finite element analysis (FEA) model exhibited the ultimate load of 330.5 kN. The load deformation behavior obtained from the test and FEA are presented in Figure 6.8 and a similar behavior is noticed.

A good correlation is observed between the test and analytical global load-deformation behavior. The maximum load obtained from numerical analysis is about 0.15% higher than the test value. The stiffness of elastic curve obtained from the numerical analysis is 14.4% higher than that obtained from test data (see Figure 6.8). Consequently, the deformation corresponding to the ultimate load for the FEA model is a little lower than that for the test specimen. The load dropped faster in the numerical model than the test specimen after reaching the ultimate load. This could be due to the friction that was present between the lateral support (LS) and beam in the test specimen, but the same was not simulated in the FE model to make the model relatively simpler.

The test specimen finally failed due to buckling of web at roller support. The final deformed shape of Specimen RC-W133-T1.2-G2 obtained from test is shown in Figure 6.9a and 6.9b. The final deformation obtained from FEM analysis is shown in Figure 6.9c and 6.9d. A good correlation between the deformed shapes obtained from test and finite element analysis (FEA) are found from these figures. Both figures show that no web or

flange buckling occurred at the mid-span. Both Figures 6.9b and 6.9d show the web buckling at the roller support.

Localized strain behaviors obtained from test and FEA are shown in Figures 6.10 to 6.19. As shown in Figures 6.10a to 6.19a, after the strain in steel increases above 0.2% (yield strain), the difference between the strain values obtained from test and FEA increased. This is primarily because of the strain values obtained from the FEA are true (logarithmic) strain values, and the strain values obtained from experimental test are not. The other reason is that the FEA assumes perfect bond between CFRP matrix and steel substrate whereas in test there was shear deformation between these two materials. Figures 6.10b to 6.19b show the strain values obtained from both test and FEA until the steel yielded (0.2% strain value). However, a small difference is found between test and FEA displacement-strain behaviors shown in these figures. A possible reason could be that the strain gauges used in the test to obtain the strain values for CFRP and steel differ in sizes to those in the FEM analysis. The actual strain gauges were 13 mm long x 7.2 mm wide for CFRP and 3.2 mm long x 2.5 mm wide for steel, while the area of the elements in the FEA was 5 mm long x 6 mm wide. Another possibility could be the strain gauges were installed slightly off the targeted locations.

6.2.5 Specimen RC-W133-T0.6-G2

Specimen RC-W133-T0.6-G2 was a corroded specimen repaired with 0.6 mm thick (two layers of Sikawrap Hex 230c dry fabric) CFRP composite. A good correlation is observed between the test and analytical global load-deformation behavior until application of ultimate load (276 kN) where the debonding of CFRP occurred in the test specimen as shown in Figure 6.20. The stiffness of elastic curve obtained from the numerical analysis is 11% higher than that obtained from test data (see Figure 6.20). In the test, the major debonding of CFRP matrix occurred after the ultimate load was applied. The CFRP was no long able to share the load and became ineffective, therefore the load dropped to the level of control corroded specimen (CC-G2). However, CFRP debonding was not modeled in FE model and therefore, the CFRP matrix was bonded perfectly to the steel

substrate all along. Therefore, the load in FE model was able to transfer to the CFRP matrix through the bonding and thus, the load in FEA continued to increase.

6.3 Parametric Study

Full-scale test data showed that bonding CFRP matrix to the beam was able to restore the ultimate load to the level of virgin (undamaged) beam specimen. However, based on test data, it could not be concluded if this rehabilitation method would still be able to restore the ultimate load to the corroded beam and of maximum ductility could be obtained when sizes (depth and length) of the corrosion changes. Thus, a detailed parametric study was undertaken to determine numbers of layers of CFRP required rehabilitating the corroded specimens with various depth and length of this circular corrosion. The depth of the corrosion was varied between 1 mm to 6 mm with 1 mm increments. The length of the corrosion was varied from 50 mm to 175 mm with 25 mm increments. A total of 36 (6x6) beam specimens were therefore analyzed using FE method for this study and the results are discussed next.

In this parametric study, it was assumed that the rehabilitation is successful if the rehabilitated corroded beam reaches its original ultimate strength (ultimate strength of virgin or undamaged beam) with a minimum 20 mm vertical deformation before failed in one of the failure modes (flange buckling, web buckling at mid-span or at the supports, or rupture of CFRP matrix). Then the thickness of CFRP matrix required to be able to make the rehabilitation successful was found for each specimen. The results are shown in Table 6.2. The graphical representation of the parametric study is shown in Figure 6.21.

Both Table 6.2 and Figure 6.21 show that length of corrosion does not influence the required thickness of CFRP matrix. This may be due to the fact that the length of CFRP composite was 100 mm and this is large enough for all the corrosion lengths chosen in this study. The other reason could be modeling of perfect bond between CFRP composite and steel substrate in the FEA model. A tri-linear relationship between the corrosion depth and required CFRP thickness was obtained (Figure 6.21). This figure shows that

optimum required thickness of CFRP composite (laminate) is less than the depth of corrosion when corrosion depth is higher.

6.4 Conclusion and recommendation

The previous chapter presented numerical modeling and solution techniques of test specimens. The model is able to simulate and predict the behavior of rehabilitated specimens if no debonding between CFRP matrix and steel substrate occurs. This chapter presents the results obtained from the FEA and compares these results with the test results. The comparisons show that a numerical tool like ABAQUS is able to simulate the tests results successfully. However, further improvement in the FE model needs to be undertaken in future studies. Some of these modifications are discussed below.

(a) Saturant needs to be modeled as an individual component in order to simulate CFRP debonding.
(b) Saturant and CFRP bonded to steel using contact modeling in order to simulate CFRP debonding.
(c) Reduction of element size at each load concentrated area to achieve results that are more accurate.
(d) Tearing of steel and CFRP matrix needs to be modeled using a suitable failure model.

Full-scale tests were carried out to study the effects of corroded beams when repaired with different thicknesses of CFRP. Detailed parametric studies were then undertaken using FE methods to study the influence of corrosion thickness and corrosion length on the minimum thickness of CFRP required to repair the corroded beam. The following conclusions are made based on the current study.

(a) Both experimental test data and numerical analysis indicate that the strength can be fully restored by using CFRP to repair the corrosion.
(b) The parametric study shows that thicker CFRP is required when a larger percentage of the bottom flange depth is lost. However, the relationship is not

directly proportional. The optimum required thickness of CFRP composite (laminate) is less than the depth of corrosion when corrosion depth is higher.

(c) The parametric study shows that the length of corrosion does not affect the required thickness of the CFRP complete.

Table 6.1: Stiffness of elastic curve

	Stiffness obtained from FEA	Stiffness obtained from test	Difference in stiffness (%)
CV-G2	42.1	34.8	17.3
CC-G2	39.0	32.3	17.2
RC-W133-T2.4-G2	45.2	38.0	15.9
RC-W133-T1.2-G2	43	36.8	14.4
RC-W133-T0.6-G2	40.0	35.6	11.0

Table 6.2: Thickness of the CFRP required (mm)

		Depth of the corrosion (mm)					
		1	**2**	**3**	**4**	**5**	**6**
Length of the corrosion (mm)	**50**	0.3	0.3	0.6	0.9	1.2	1.8
	75	0.3	0.3	0.6	0.9	1.2	1.8
	100	0.3	0.3	0.6	0.9	1.2	1.8
	125	0.3	0.3	0.6	0.9	1.2	1.8
	150	0.3	0.3	0.6	0.9	1.2	1.8
	175	0.3	0.3	0.6	0.9	1.2	1.8

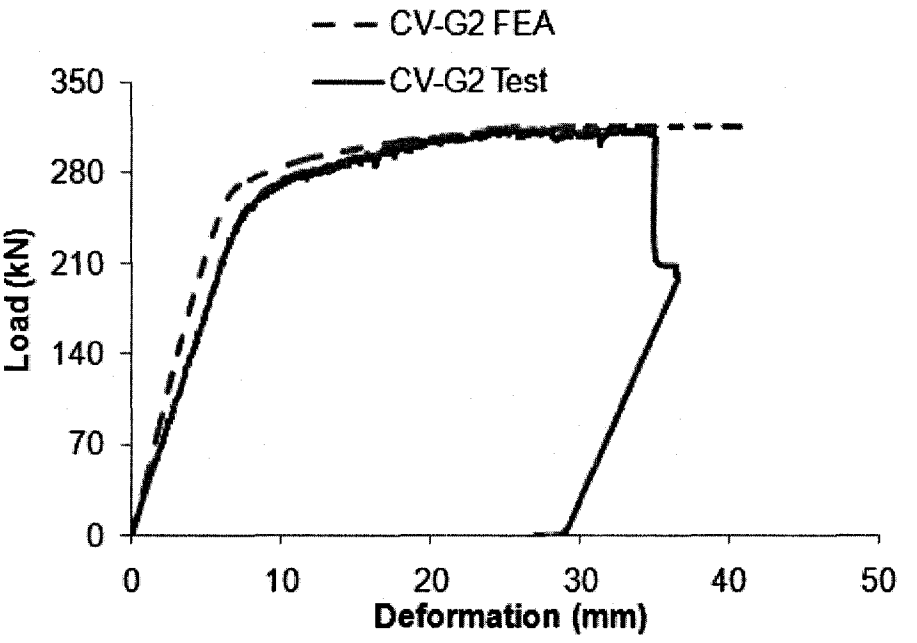

Figure 6.1: Load deformation curve for CV-G2 (FEA and Test)

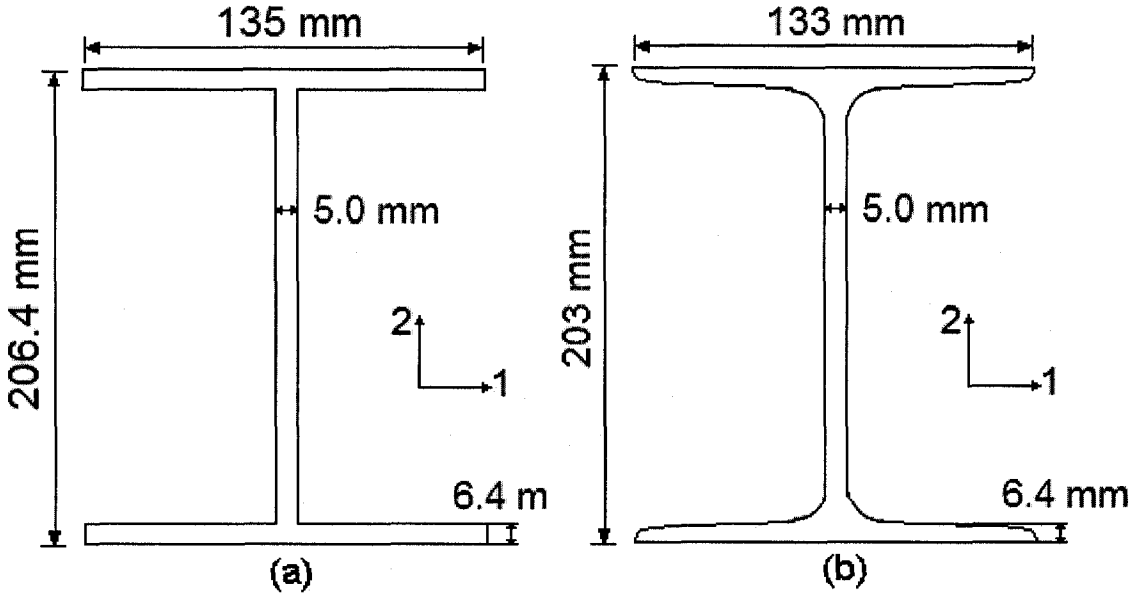

Figure 6.2: Cross-section of the beam, (a) FEA, and (b) test

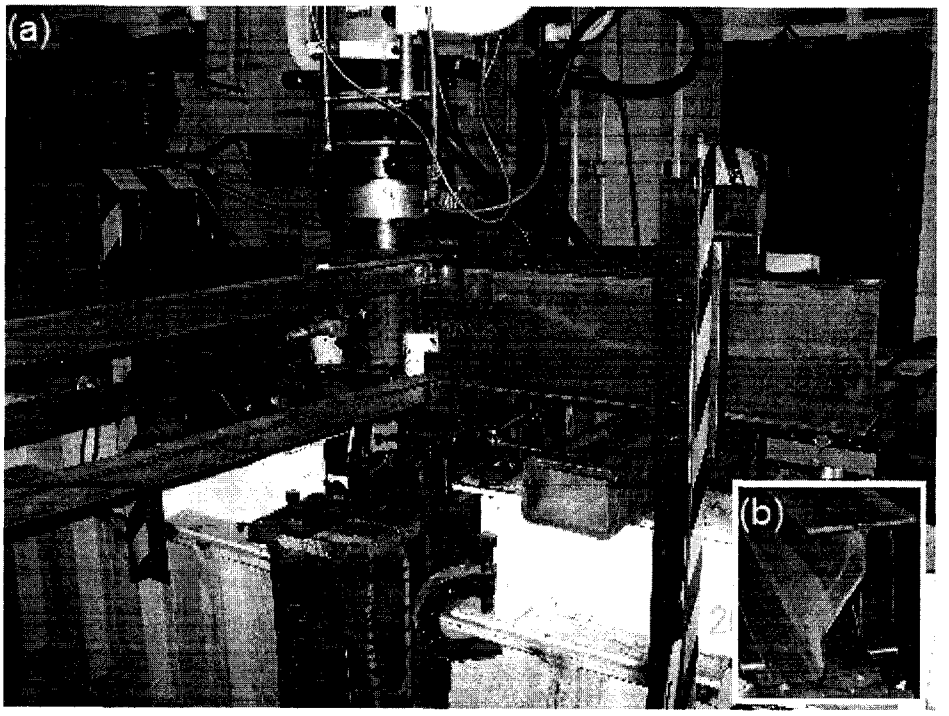

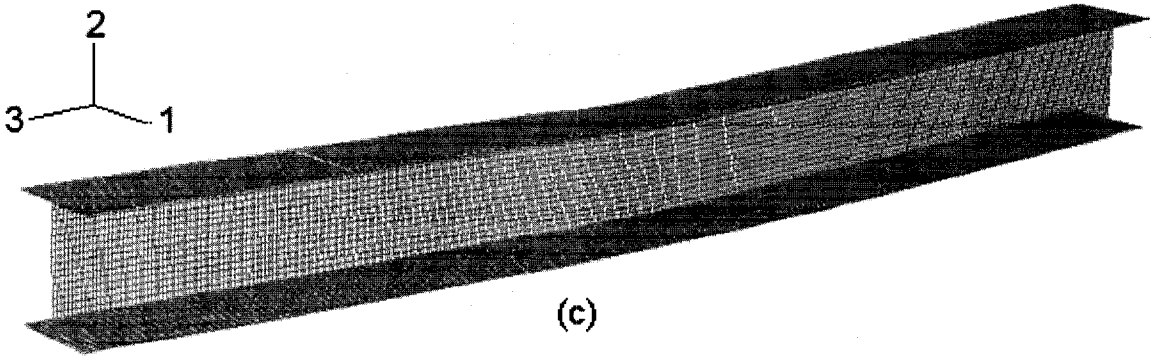

Figure 6.3: Final deformed shape of test CV-G2 specimen
(a) test, (b) web buckled at roller support, and (c) FEA

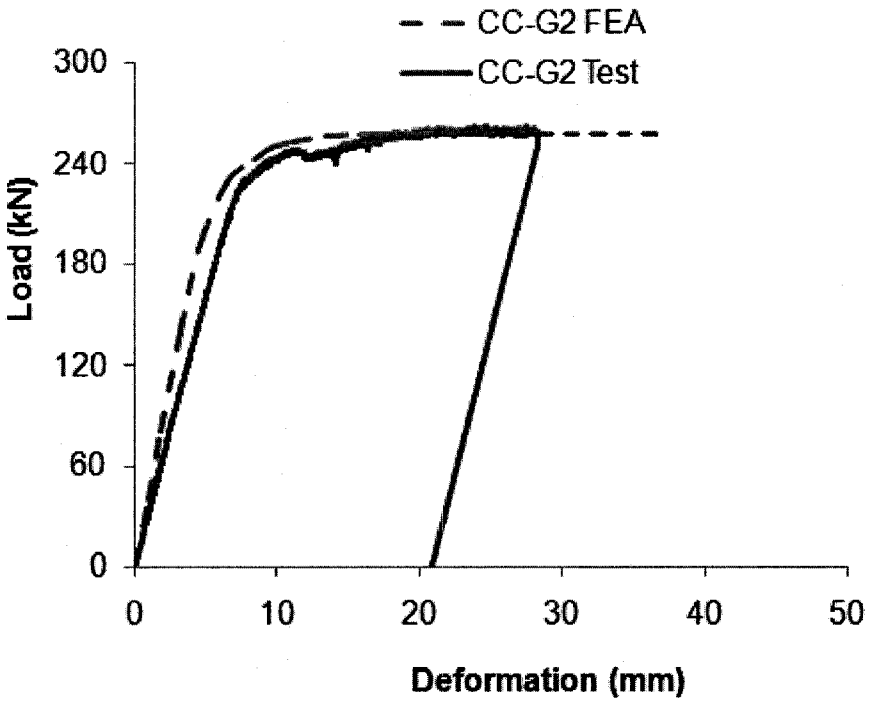

Figure 6.4: Load deformation curve for CC-G2 (FEA and Test)

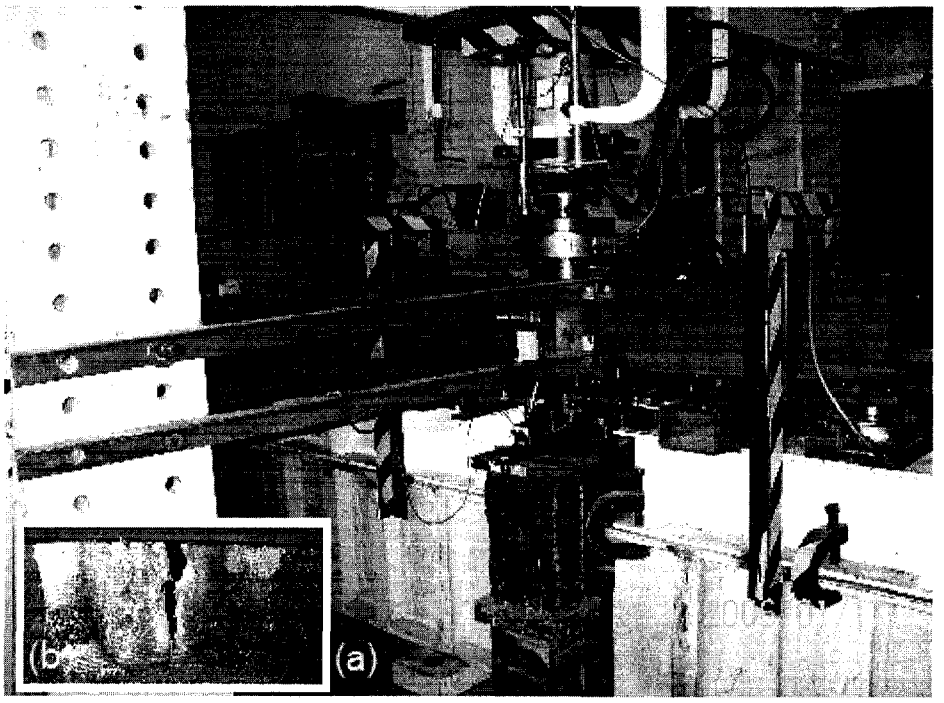

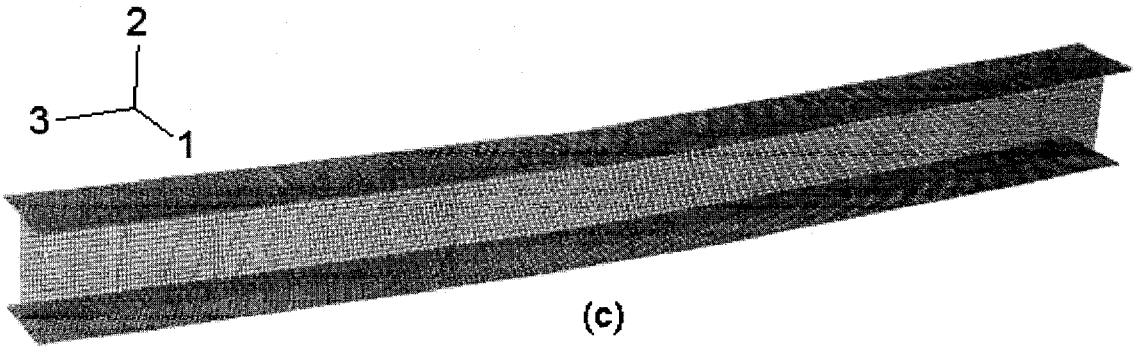

Figure 6.5: Final deformed shape of test CC-G2 specimen
(a) Test, (b) cracking at the center of corrosion, and (c) FEA

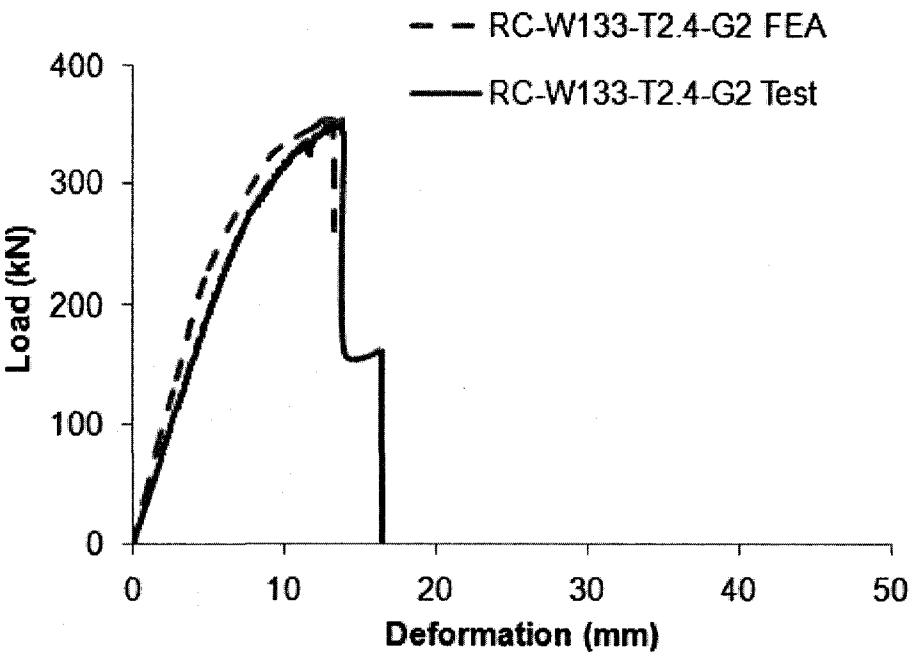

Figure 6.6: Load deformation curve for RC-W133-T2.4-G2 (FEA and Test)

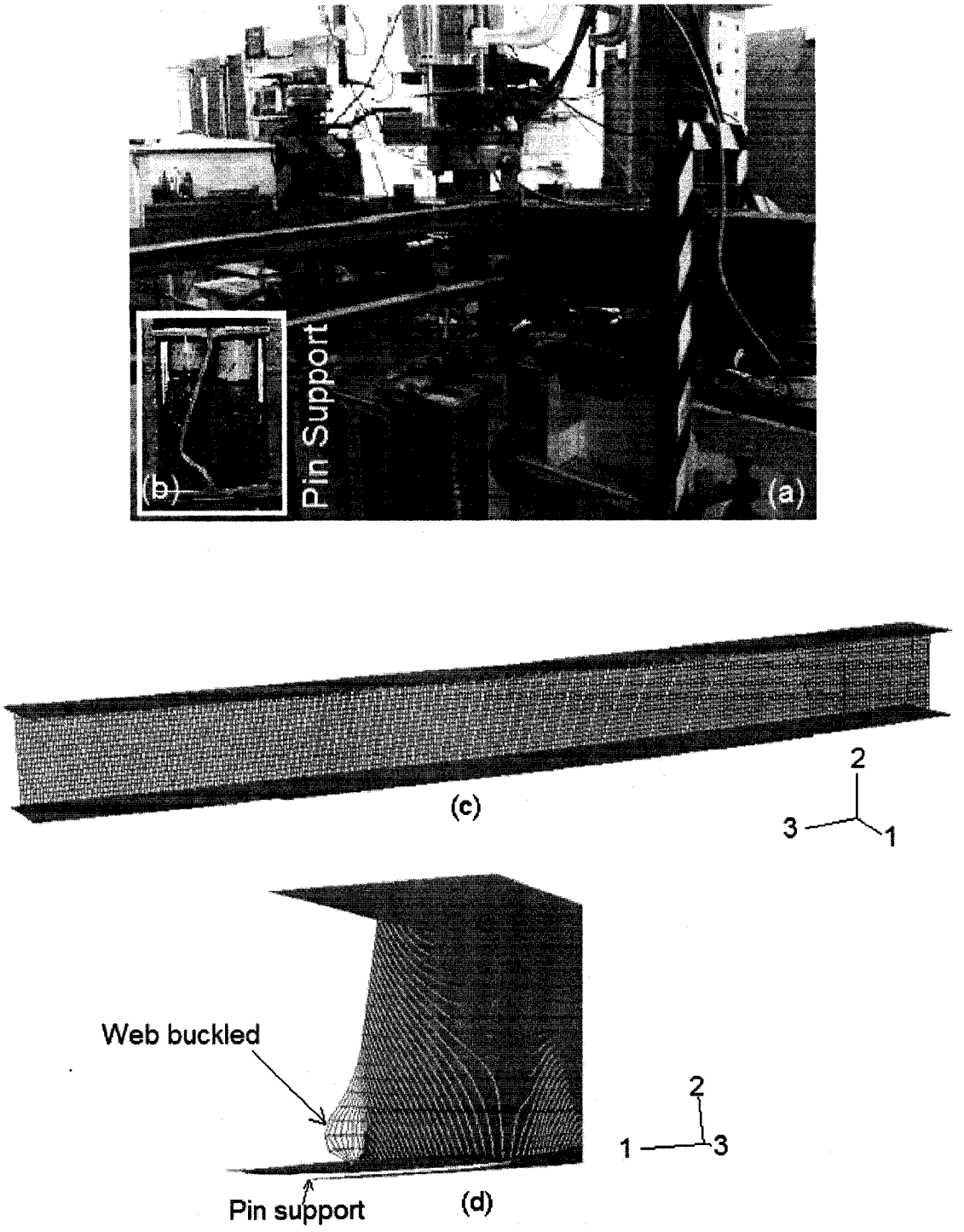

Figure 6.7: Final deformed shape of test RC-W133-T2.4-G2 specimen (a) Test, (b) web buckled at pin support (test), (c) FEA, and (d) web buckled at pin support (FEA)

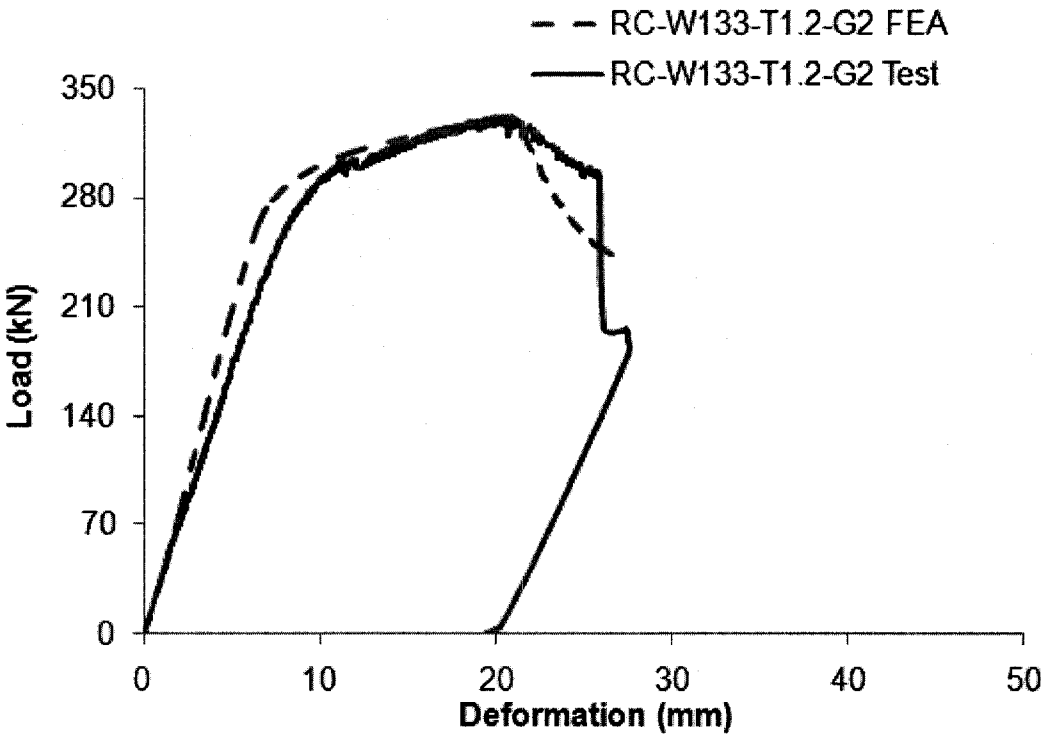

Figure 6.8: Load deformation curve for RC-W133-T1.2-G2 (FEA and Test)

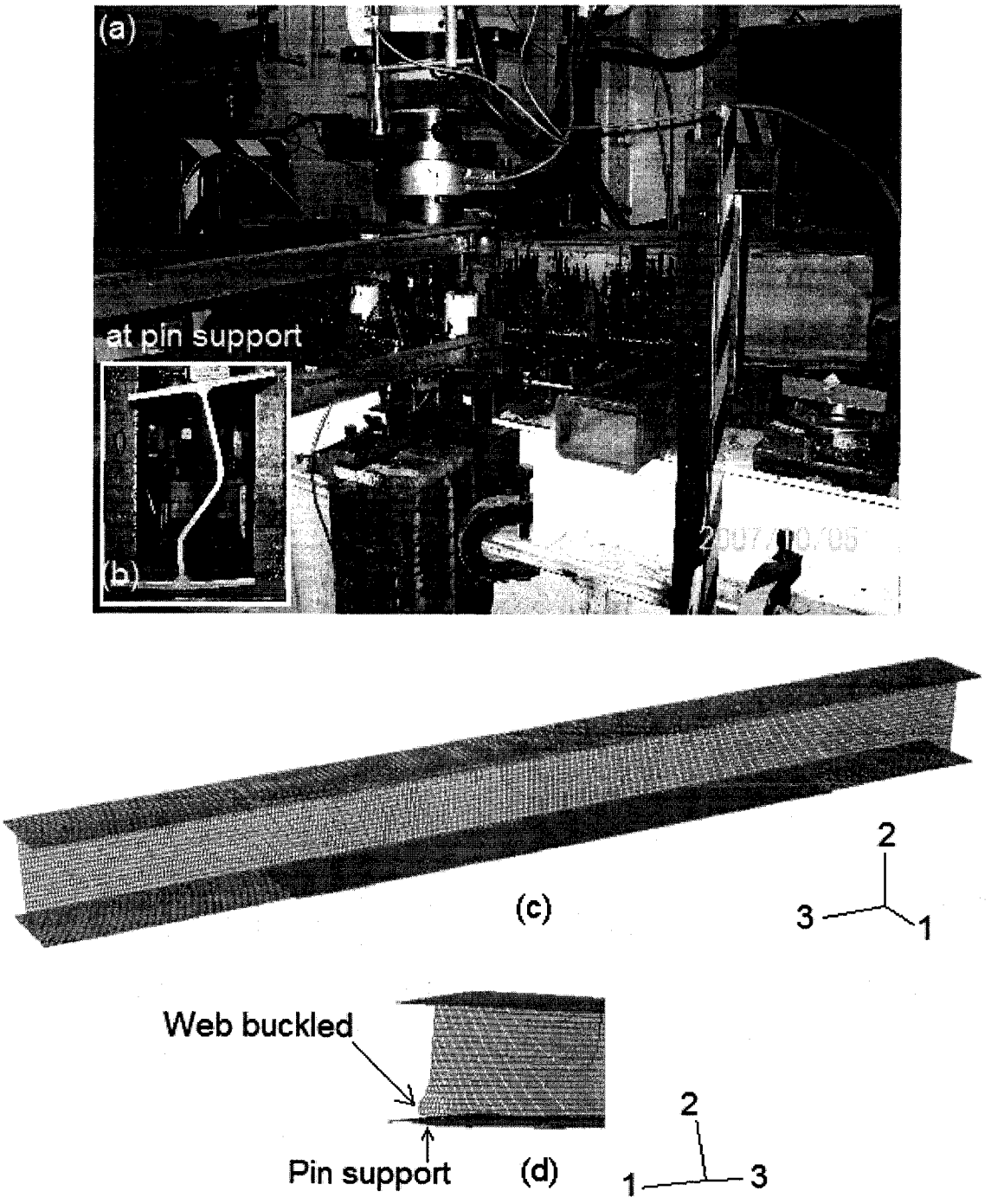

Figure 6.9: Final deformed shape of test RC-W133-T1.2-G2 specimen (a) test, (b) web buckled at pin support (test), (c) FEA, and (d) web buckled at pin support (FEA)

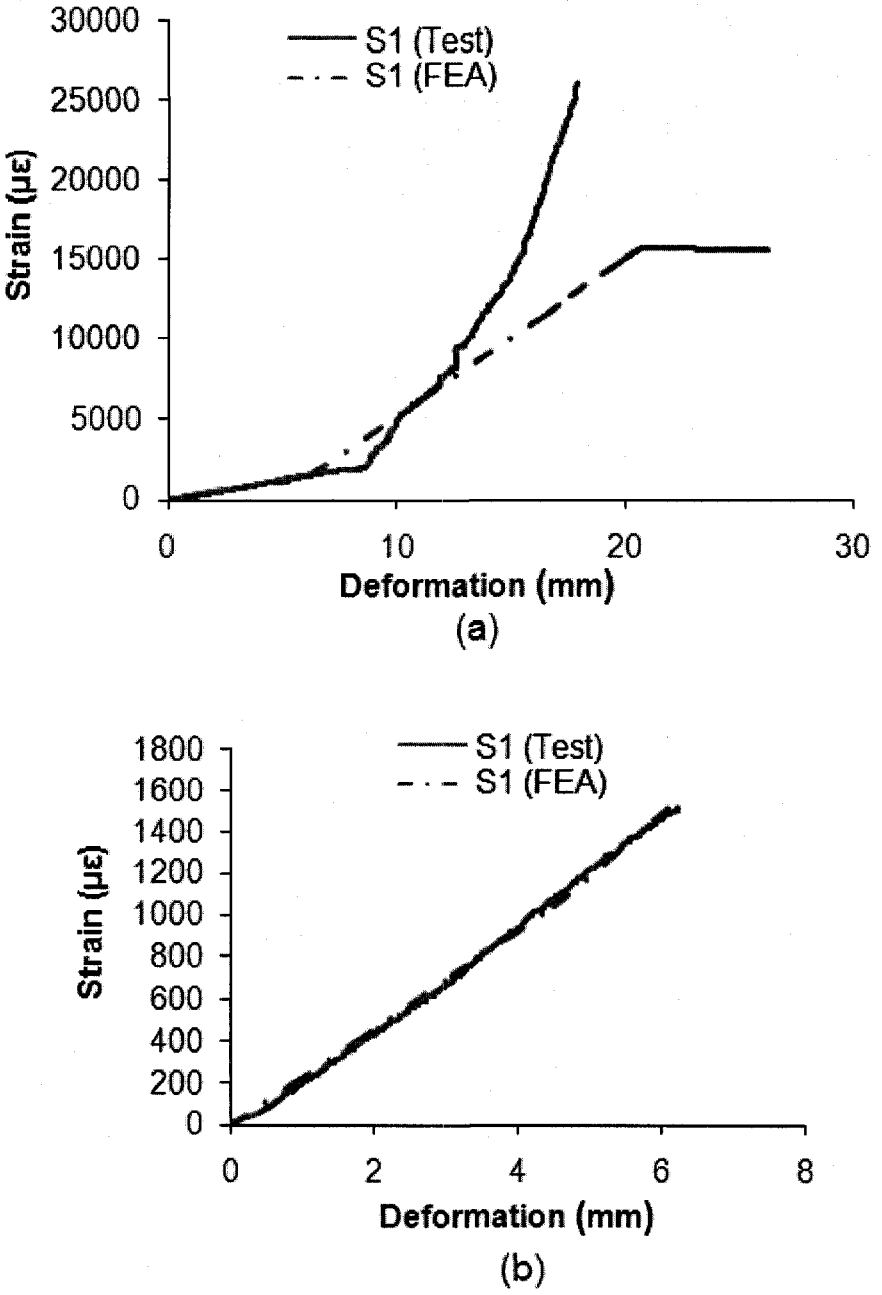

Figure 6.10: (a) Strain of steel at location 1 (FEA v.s. test) and (b) Strain before steel yield (0.2%)

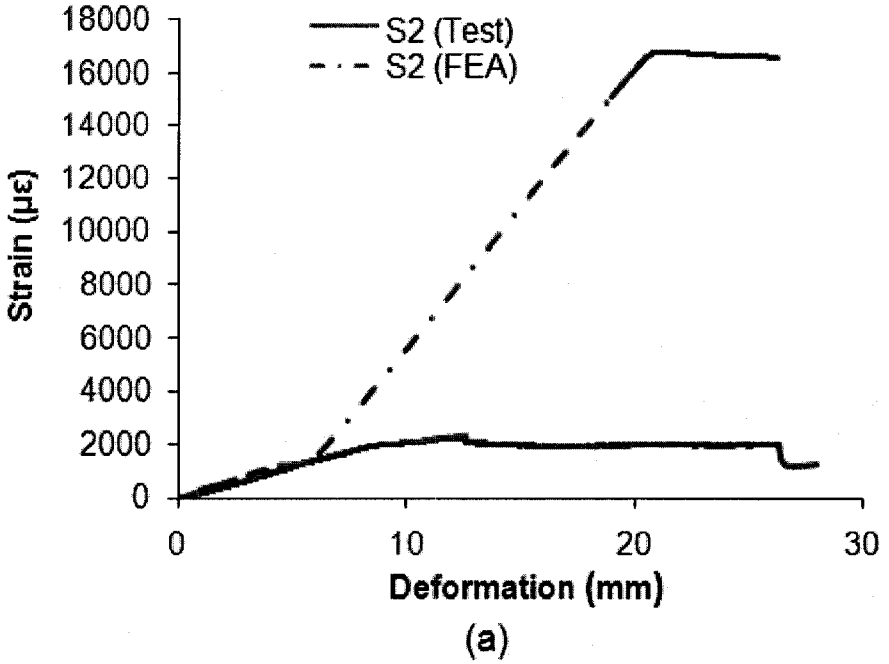

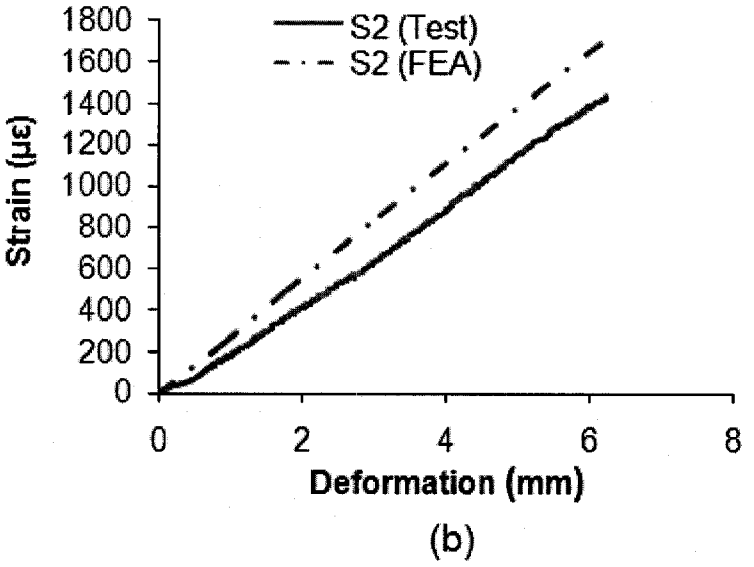

Figure 6.11: (a) Strain of steel at location 2 (FEA v.s. test) and (b) Strain before steel yield (0.2%)

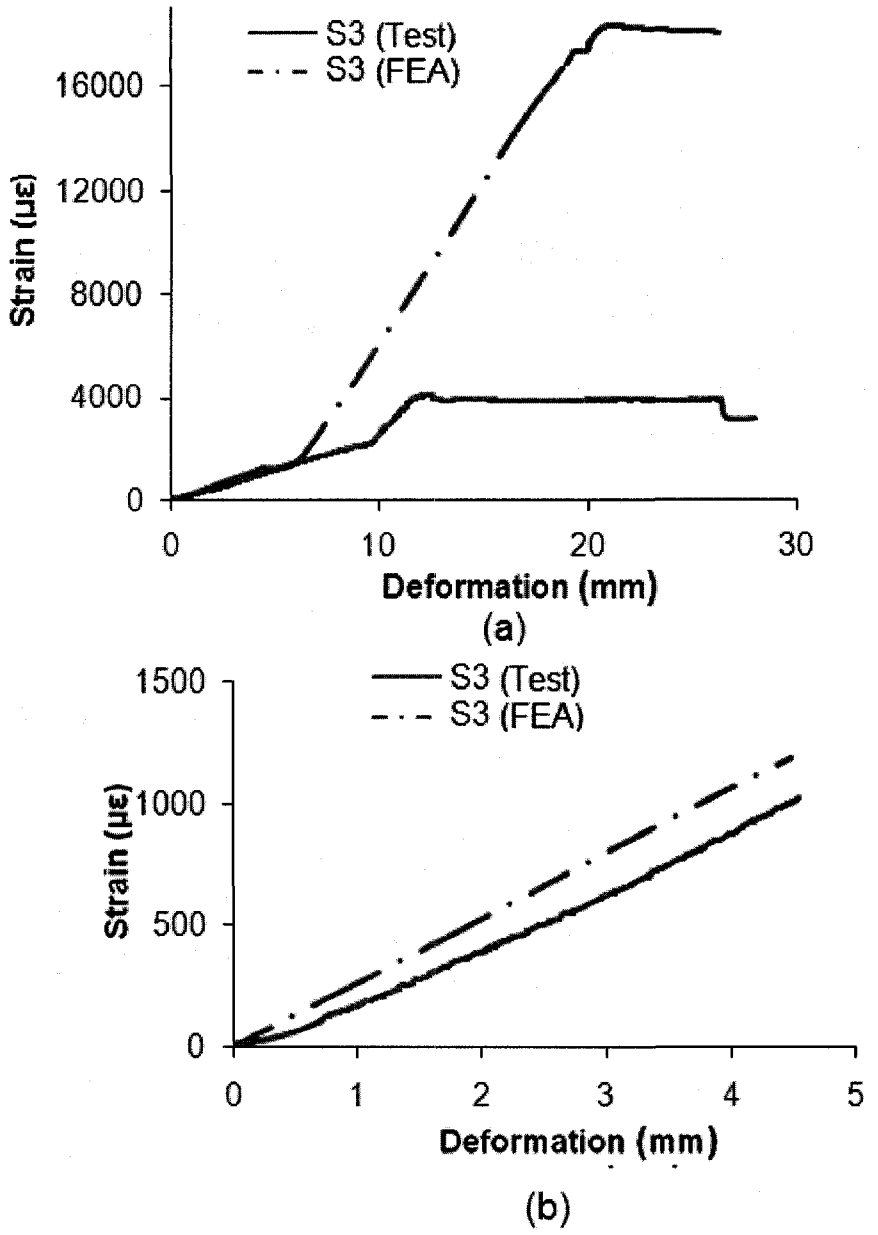

Figure 6.12: (a) Strain of steel at location 3 (FEA v.s. test)
and (b) Strain before steel yield (0.2%)

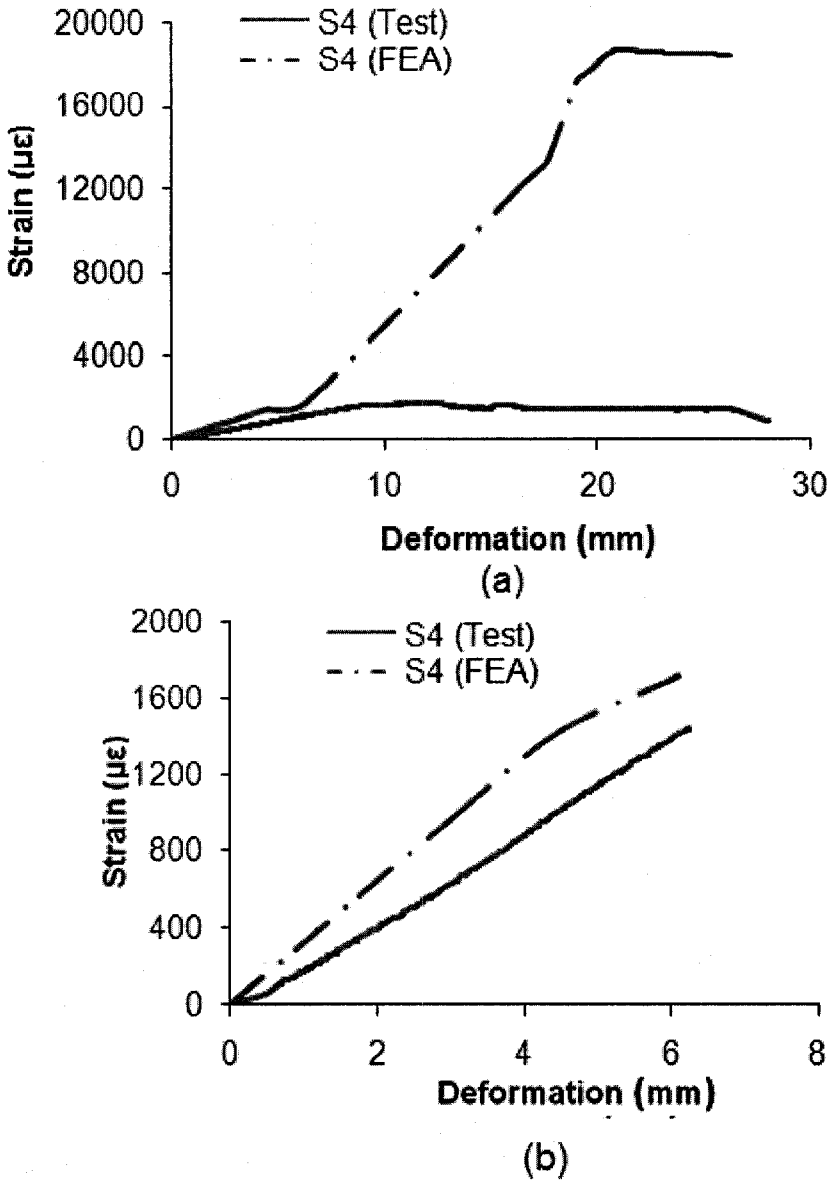

Figure 6.13: (a) Strain of steel at location 4 (FEA v.s. test) and (b) Strain before steel yield (0.2%)

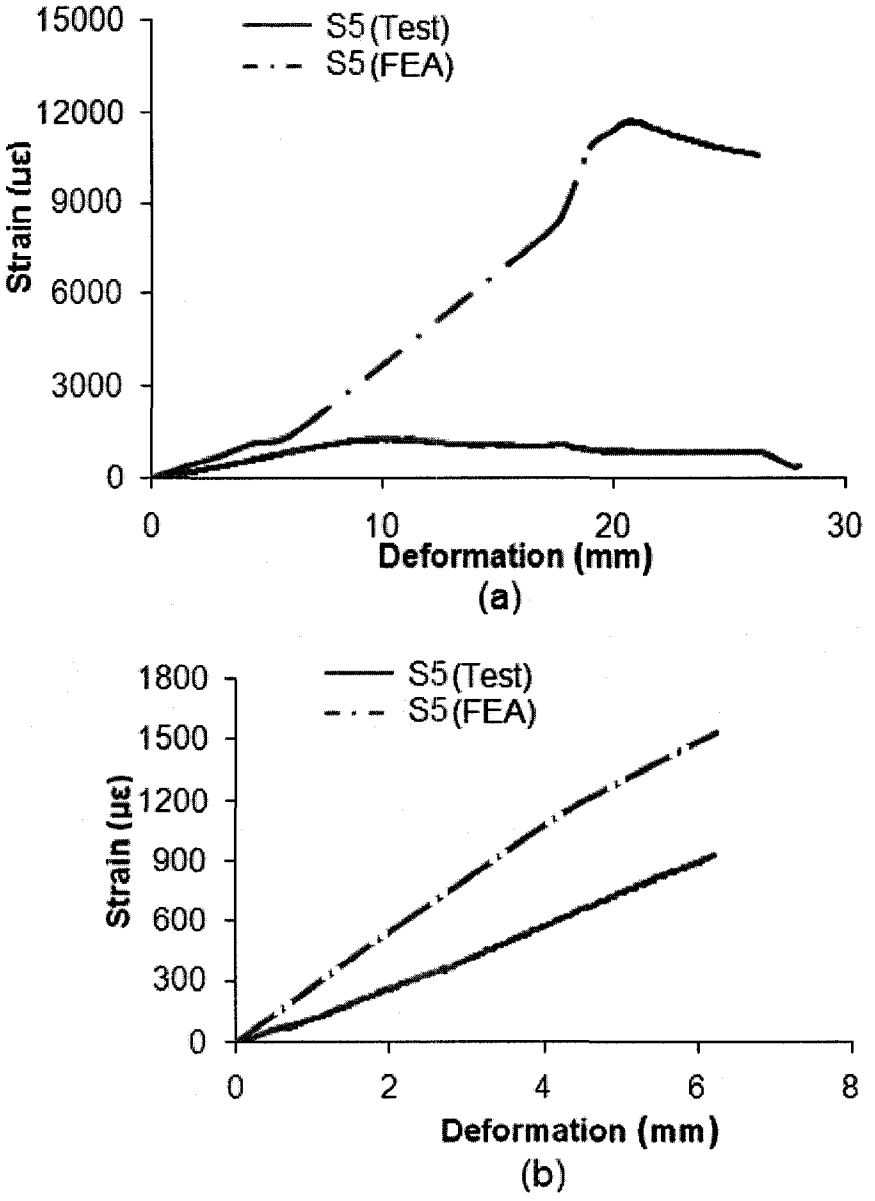

Figure 6.14: (a) Strain of steel at location 5 (FEA v.s. test)
and (b) Strain before steel yield (0.2%)

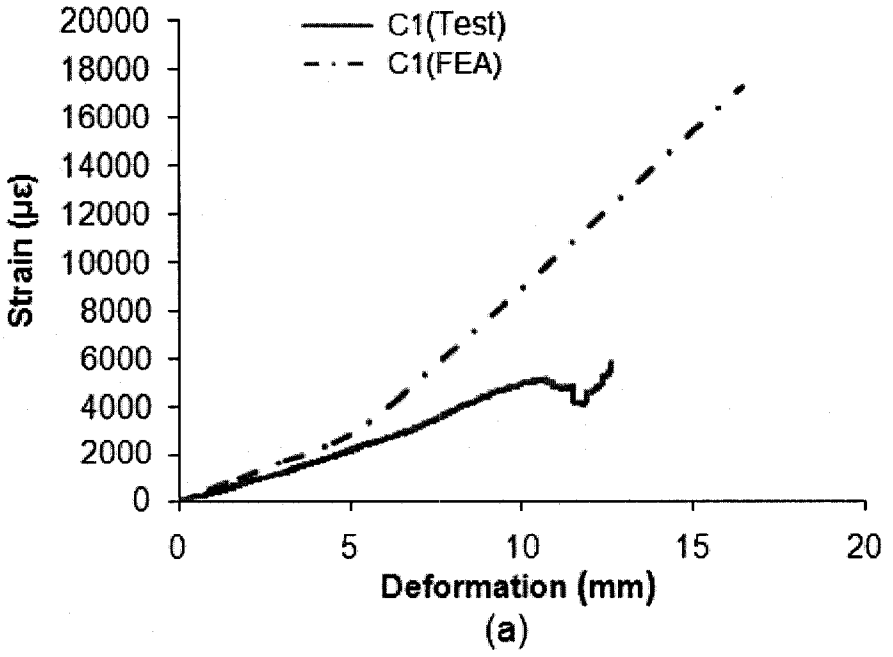

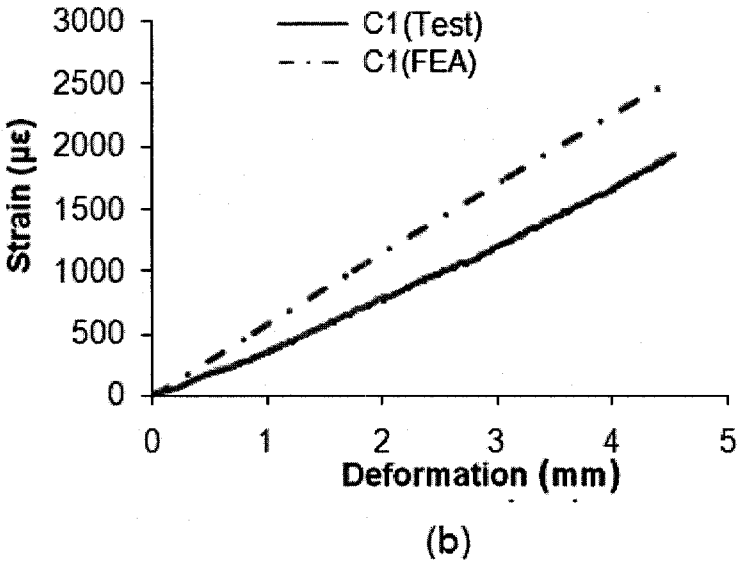

Figure 6.15: (a) Strain of CFRP at location 1 (FEA v.s. test) and (b) Strain before steel yield (0.2%)

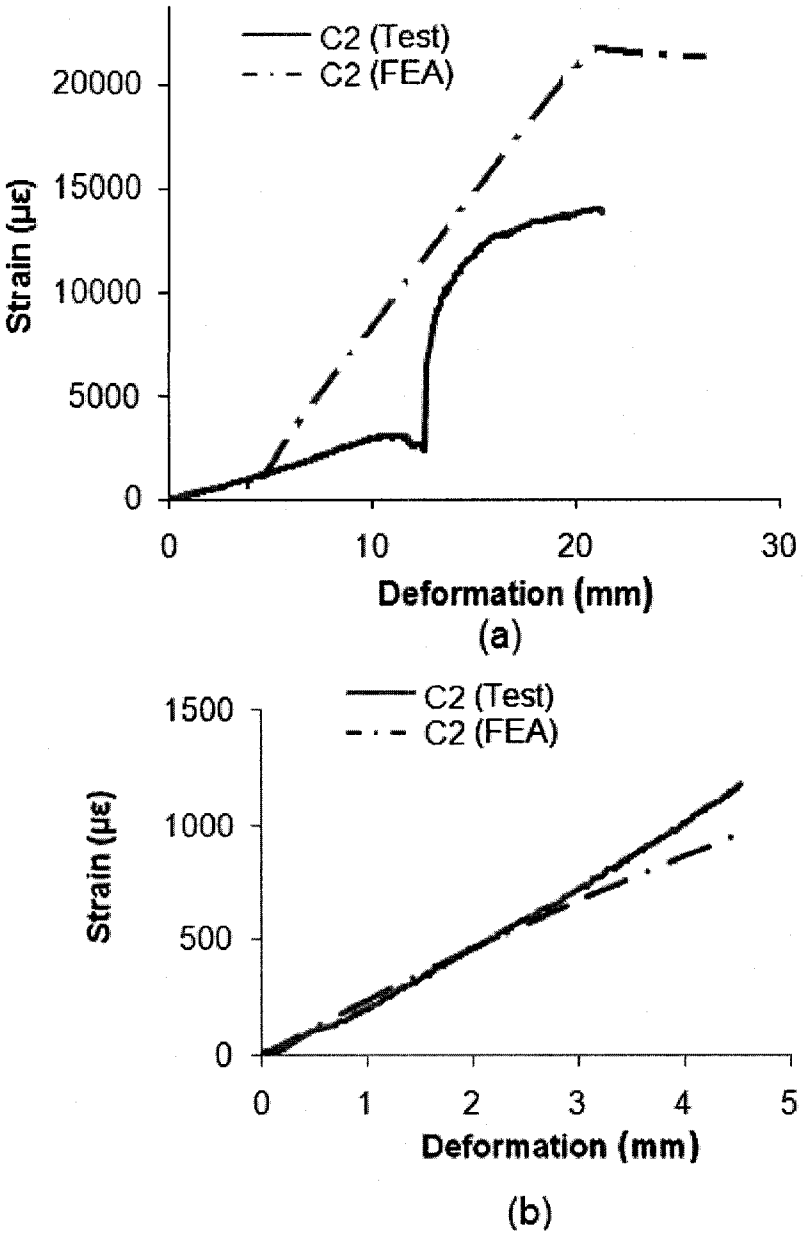

Figure 6.16: (a) Strain of CFRP at location 2 (FEA v.s. test) and (b) Strain before steel yield (0.2%)

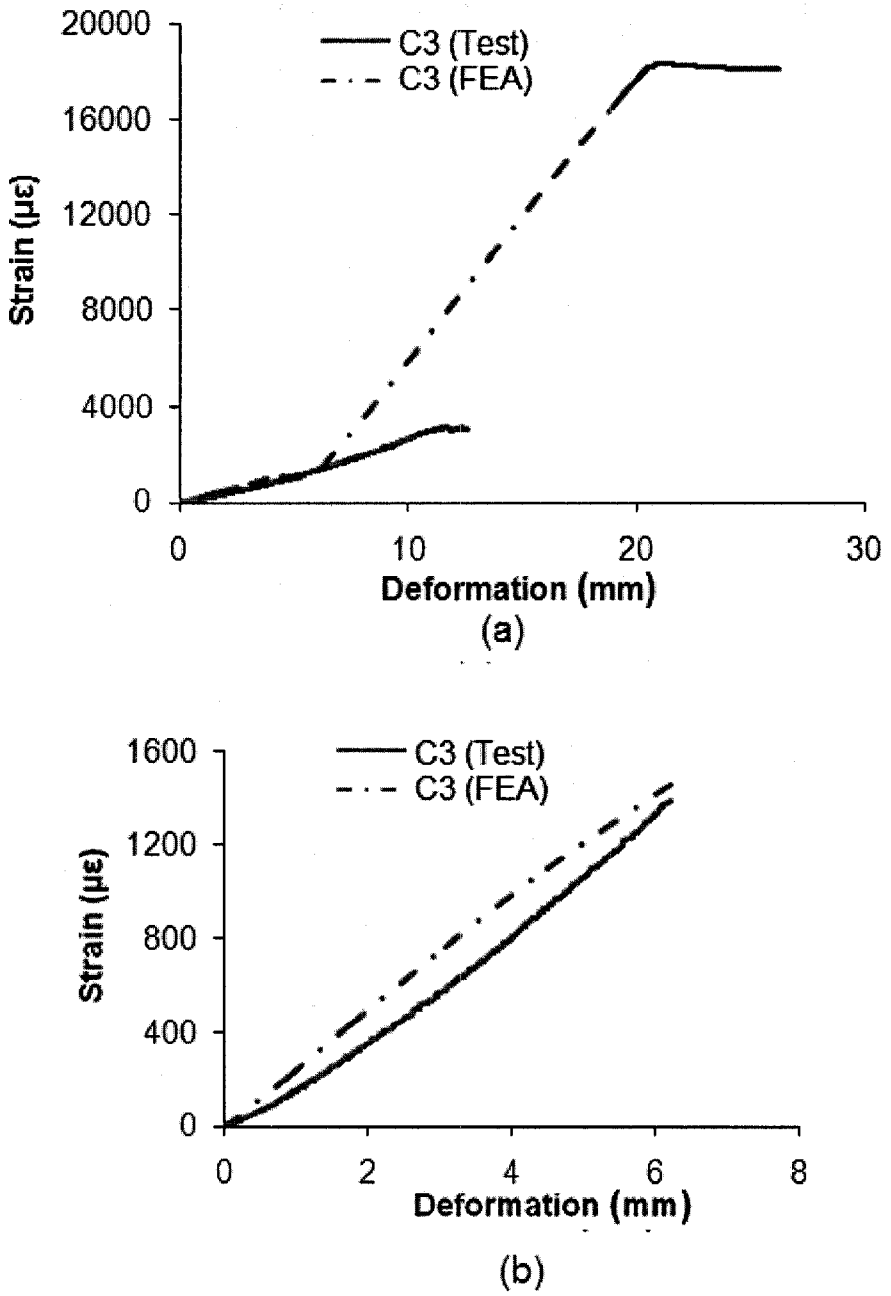

Figure 6.17: (a) Strain of CFRP at location 3 (FEA v.s. test) and (b) Strain before steel yield (0.2%)

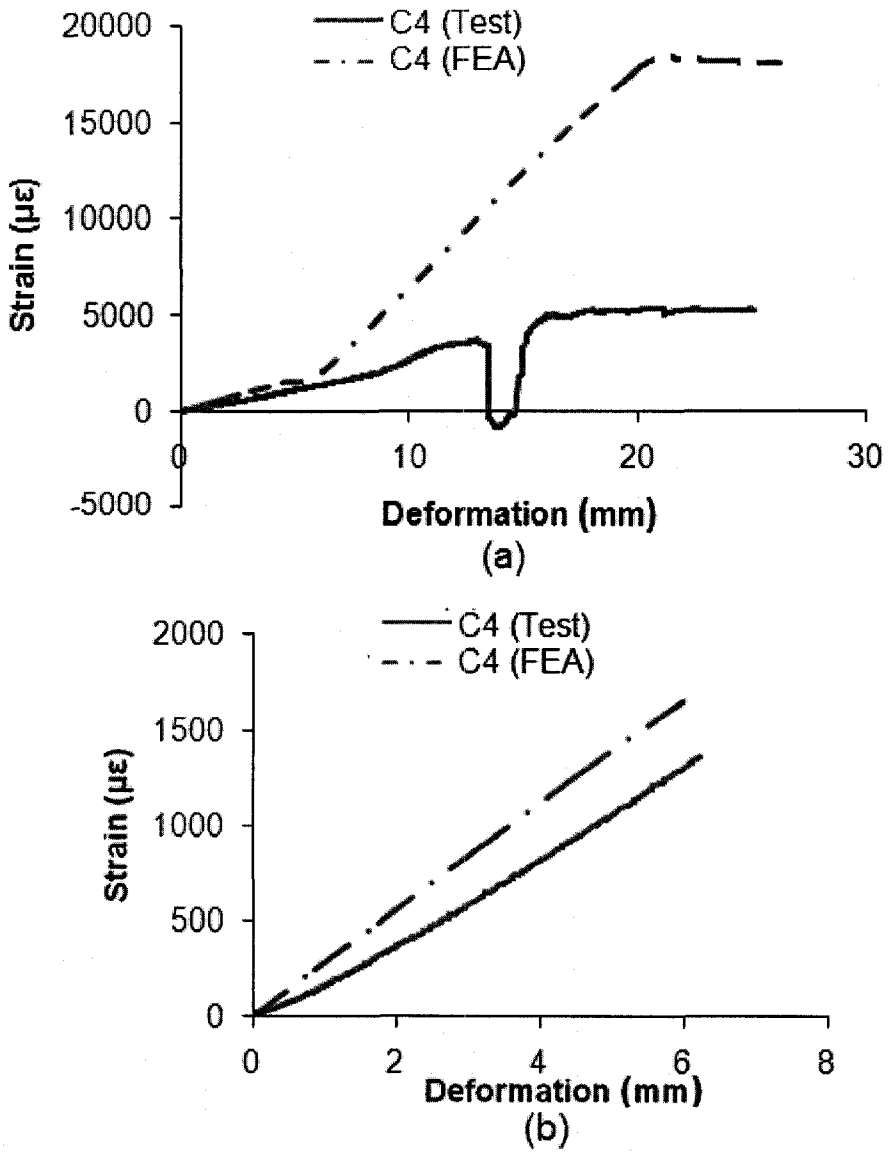

Figure 6.18: (a) Strain of CFRP at location 4 (FEA v.s. test) and (b) Strain before steel yield (0.2%)

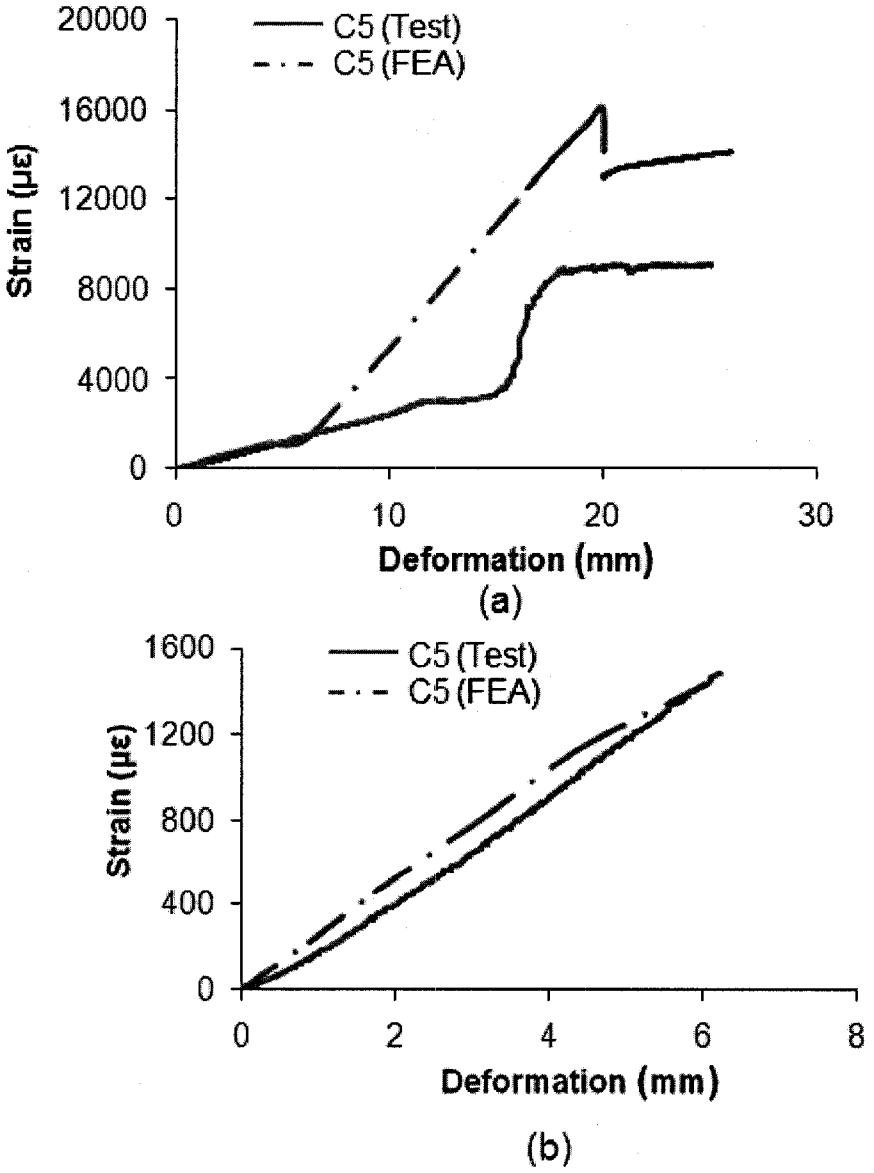

Figure 6.19: (a) Strain of CFRP at location 5 (FEA v.s. test) and (b) Strain before steel yield (0.2%)

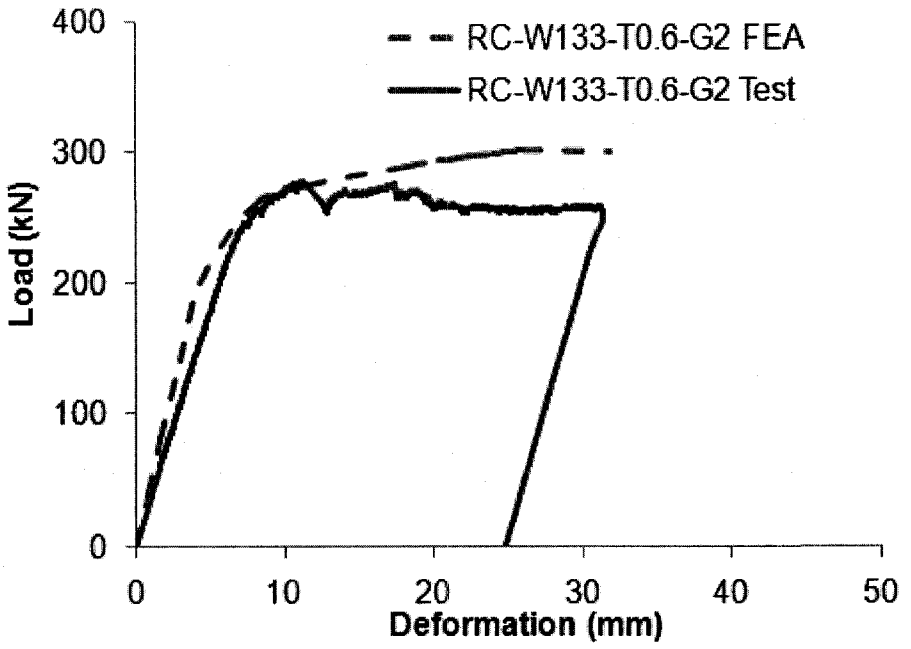

Figure 6.20: Load deformation curve for RC-W133-T0.6-G2 (FEA and test)

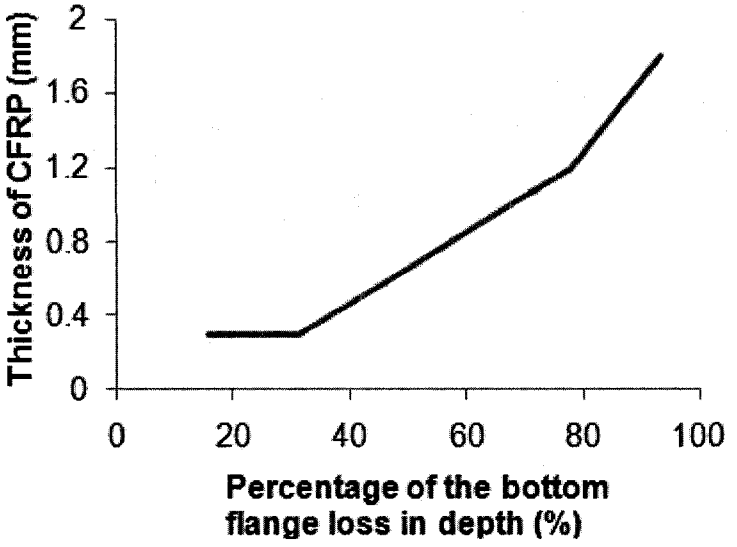

Figure 6.21: Load deformation curve for RC-W133-T0.6-G2 (Analysis and Experimental)

7 SUMMARY, CONCLUSIONS, AND RECOMMENDATIONS

This chapter summarizes the research and findings, and provides conclusions on the work completed under the scope of the thesis. This chapter also recommends further work that is necessary and can be undertaken in future studies.

7.1 Summary

Field observations found a large numbers of steel bridges with various levels of corrosion. It is understood that conventional method of repair for the corroded steel bridge could lead to other problems, such as fatigue problem, brittle failures, and galvanic corrosion. Recently, Carbon Fiber Reinforced Polymer (CFRP) and other fiber polymers have been introduced in corrosion repair of steel structural members. As a result, this research program was set to examine the rehabilitation technique of surface corroded steel beam using CFRP sheets (fabrics).

As a first step towards the examination of the rehabilitation technique of surface corroded steel beams using CFRP sheets, two groups consisting of nine steel beam specimens were undertaken and tested to understand the behaviour of the rehabilitated beams.

This experimental data indicated that the repair technique using CFRP sheets is a valid one. The global behaviour of the corroded and virgin beam specimens was stable and ductile. The rehabilitated beams were able to restore strength of un-corroded (virgin) beams but provided less ductile behaviour.

Once the experimental program was completed, a finite element (FE) model was developed to simulate the test behaviour of five beam specimens of group 2. The primary objective was to develop a numerical tool that is able to predict behaviour similar to that observed from the five test specimens in group 2. The global behaviour and deformed shapes of numerical models correlated well with the experimental results. The observations from numerical (FE) analyses were similar to the observations from experimental studies. A parameter study on thirty-six rehabilitated beam specimens were

undertaken to study the influence of corrosion depth and corrosion length on the optimum required thickness of CFRP.

7.2 Conclusions

A number of conclusions are drawn based on the experimental and analytical results of this study and these are as follows.

(a) The rehabilitation technique was successful in restoring the ultimate load capacity of corroded beam to the level of the control virgin (un-corroded) beam.

(b) The ductility of rehabilitated beams is lower than virgin beam. The ductility reduces as the total thickness of CFRP composite layers increase.

(c) The numerical parametric study shows that the optimum thickness of CFRP composite is usually less than the corrosion depth. The relationship between the required thickness of CFRP composite and depth of corrosion is tri-linear as shown in Figure 6.21.

(d) Parametric study shows that the length of corrosion has no influences on the required thickness of CFRP for restoring strength to the level of virgin (un-corroded) beam.

7.3 Recommendations

This research provided a number of significant contributions toward the objectives of the project. In order to achieve more confidence in the understanding of the behaviors of using CFRP to rehabilitate corroded steel beams, more research works are recommended.

(a) Additional experimental work and/or finite element analysis are required to examine the influence of parameters like different shapes of the corrosion, and different size (width, length, and thickness) of the corrosion.

(b) Additional experimental work and finite element analysis are required to examine the surface corrosion repair on other steel members.

(c) In FE modeling and analysis, saturant should be modeled as an individual component in order to simulate CFRP debonding.

(d) The bond between steel and saturant, as well as saturant and CFRP needs to be modeled and it may be achieved by using contact algoritm.

(e) FE model can be refined with finer mesh to reduce the stiffness of the load-deformation curve.

(f) Tearing of steel and CFRP matrix needs to be modeled.

REFERENCES

ACMA (American Composites Manufactures Association), 2004, "Definition of FRP Composites", http://www.mdacomposites.org/mda/FRP_def.html , viewed on April 16, 2007.

Al-Saidy Abdullah H.; Klaiber F. W.; and Wipf T. J., 2004, "Repair of Steel Composite Beams with Carbon Fiber-Reinforced Polymer Plates", Journal of Composites for Construction, ASCE, New York, NY, USA, Vol. 8, No. 2, April 1, 2004, P163-172

ASTM, (2006, a) "Standard test method for tensile properties for polymer matrix composite materials D3039/D 3039M – 00" Annual book of ASTM standards Vol. 15, No. 3 ASTM International, 100 Barr Harbor Drive, PO Box C700, West Conshohocken, PA, 19428-2959 USA

ASTM (2006, b) Standard test method for tension testing of metallic materials [Metric] E8M-04 Annual book of ASTM standards Vol. 3, No. 1 ASTM International, 100 Barr Harbor Drive, PO Box C700, West Conshohocken, PA, 19428-2959 USA

ASTM (2006, c) Standard test method for strength properties of adhesives in cleavage peel by tension loading (engineering plastics-to-engineering plastic) D3807-98 Annual book of ASTM standards Vol. 15, No. 6 ASTM International, 100 Barr Harbor Drive, PO Box C700, West Conshohocken, PA, 19428-2959 USA

ASTM (2006, d) Standard test method for climbing drum peel for adhesive D1781-98 Annual book of ASTM standards Vol. 15, No. 6 ASTM International, 100 Barr Harbor Drive, PO Box C700, West Conshohocken, PA, 19428-2959 USA

ASTM (2006, e) Standard test method for lap shear adhesion for fiber reinforced plastic (FRP) bonding D5868 - 01 Annual book of ASTM standards Vol. 15, No. 6 ASTM International, 100 Barr Harbor Drive, PO Box C700, West Conshohocken, PA, 19428-2959 USA

ASTM (2006, f) Standard test method for tensile properties of plastic D638 – 03 Annual book of ASTM standards Vol. 8, No. 1 ASTM International, 100 Barr Harbor Drive, PO Box C700, West Conshohocken, PA, 19428-2959 USA

Asghar Bhatti M., 2005, "Fundamental Finite Element Analysis and Applications with mathematical and matlab computations", John Wiley & Sons, Mississauga, Ontario, Canada

BASF (a), "MBrace CF160 Product Data", http://www.basfbuildingsystems.com/documents/z31_tdg.pdf, viewed on Dec 15, 2006.

BASF (b), "MBrace Primer Product Data", http://www.basfbuildingsystems.com/documents/z34_tdg.pdf, viewed on Dec 15, 2006.

BASF (c), "MBrace Putty Product Data", http://www.basfbuildingsystems.com/documents/z35_tdg.pdf, viewed on Dec 15, 2006.

BASF (d), "MBrace Saturant Product Data", http://www.basfbuildingsystems.com/documents/z36_tdg.pd, viewed on Dec 15, 2006.

Canadian Institute of Steel Construction, 2000, "Handbook of Steel Construction Seventh Edition 350W", Canadian Institute of Steel Construction, Willowdale, Ontario, Canada

Conroe Watkins, 2006, "The historic Devil's elbow bridge is in need of repair", http://www.rollanet.org/%7Econorw/cwome/article51&52combined.htm, viewed on August 25, 2006

Edberg William; Mertz Dennis; Gillespie John Jr., 1996, "Rehabilitation of steel bridge using composite materials", Proceedings of the 1996 4th Materials Engineering Conference part 1 (of 2), ASCE, Washington, DC, USA, Nov 10- 14 1996, pp.502-508

Gillespie John W. Jr.; Mertz D.R.; Kasai K.; Edberg W.M.; Demitz J.R.; Hodgson I., 1996 (a), "Rehabilitation of steel bridge girders: Large Scale Testing", Proceeding of the 1996 11th Technical Conference of American Society for Composites, Clark Atlanta University, Atlanta, GA, USA, Oct 7-9 1996, pp.231 - 240

Gillespie John W. Jr.; Mertz Dennis R.; Kasai K.; Edberg William M.; Ammar Nouredine; Kasai Kazuhiko; Ian C., 1996 (b), "Rehabilitation of steel bridge girders through application of composite materials", Proceedings of the 1996 28th International SAMPE Technical Conference, SAMPE, Seattle, WA , USA, November 4-7, 1996, pp1249-1257

Gillespie John W. Jr.; Mertz Dennis R.; Edberg William M.; Ammar Nouredine, 1997, "Steel girder rehabilitation through adhesive bonding of composite materials", Proceedings of the 1997 55th Annual Technical Conference, ANTEC, Toronto, CA, April 27 – May 2, 1997, Vol. 1 (of 3), pp1171-1175

Harajli M. H. and Soudki K.A., 2003, "Shear strengthening of interior slab-column connections using carbon fiber-reinforced polymer sheets", Journal of Composites for Construction, American Society of Civil Engineers, Reston, VA 20191-4400, United States, Vol. 7, No. 2, pp145-153

Hibbit, Karlsson, & Sorensen, Inc. (HKS), 2006, "ABAQUS Analysis User's Manual" Version 6.6-1. Hibbitt, Karlsson & Sorensen, Inc. Pawtucket, USA

Hibbit, Karlsson, & Sorensen, Inc. (HKS), 2006 (a), "ABAQUS Theory Manual" Version 6.6-1. Hibbitt, Karlsson & Sorensen, Inc. Pawtucket, USA

Hibbit, Karlsson, & Sorensen, Inc. (HKS), 2006 (b), "ABAQUS/Standard User's Manual" Version 6.6-1. Hibbitt, Karlsson & Sorensen, Inc. Pawtucket, USA

Hollaway L., 1993, "Polymer composites for civil and structural engineering" Chapman & Hall, London

Kayser Jack R; and Nowak Andrzej S.; 1989, "Capacity loss due to corrosion in steel-girder bridges", Journal of structural engineering, ASCE, Reston, VA 20191-4400, United States, Vol. 115, No. 6 pp.1525 – 1537

Lamanna Anthony J.; Bank Lawrence C.; and Scott David W.; 2004, "Flexural strengthening of reinforced concrete beams by mechanically attaching fiber-reinforced polymer strips", Journal of Composite for Construction, American Society of Civil Engineers, Reston, VA 20191-4400, United States Vol. 8, No. 3, pp 203-210

Liu X.; Silva P.F.; Nanni A., 2001, "Rehabilitation of steel bridge members with FRP composite materials", Composites in constructions, Figuerias et al (eds), Swets & Zeitlinger, Lisse, ISBN 90 2651 858 7

Matta F.; Karbhari Vistasp M; Vitaliani Renato, 2005, "Tensile response of steel/CFRP adhesive bonds for the rehabilitation of civil structures", Structural Engineering and Mechanics, Techno Press, Taejon, 305-600, South Korea, Vol. 20, No. 5 pp.589 – 608

Mertz Dennis R.; Gillespie John W., 1996, "Idea Project final report", Idea program Transportation research board, National Research Council, Washington, DC

Miller Trent C.; Chajes Michael J.; Mertz Dennis R.; Hastings Jason N., 2002, "Strengthening of a steel bridge girder using CFRP plates", Journal of Bridge Engineering, ASCE, Reston, VA 20191-4400, United States, Vol. 6, No. 6, pp.514-522

Network, 2000, "New Jersey Experience in Movable Bridge Inspection" http://www.pbworld.com/news_events/publications/network/tools/print_article.asp?referrer=/news_events/publications/network/Issue_47/47_18_KrishnagiriR_NewJerseyExperince.asp, viewed on August 25, 2006

Nozaka Katsuyoshi; Shield Carol K.; Hajjar Jerome F., 2005, "Effective bond length of carbon-fiber-reinforced polymer strips bonded to fatigue steel bridge I-girders" Journal of bridge engineering, ASCE, Reston, VA 20191-4400, United States, Vol. 10, No. 2 pp.195 - 205

Plexus Structural adhesive, 2006, "Guide to bonding Plastics – Composites – metals", http://www.itwplexus.com/Guide_To_Bonding.pdf , viewed on June 26, 2006.

Polymer Science Learning Center, 2005, "Epoxy Resins", http://pslc.ws/macrog/epoxy.htm, viewed on April 16, 200.

Sen R.; Liby L.; Spillett L.; Mullins G., 1995, "Strengthening steel composite bridge members using CFRP laminates", Proceedings of the 1995 2nd International RILEM Symposium, FRPRCS-2, Ghent, Belg, Aug 23-25 1995, pp. 551

Sen R.; Liby L.; Mullins G., 2001, "Strengthening steel bridge sections using CFRP laminates", Composites Part B: Engineering, Elsevier Science Ltd., Atlanta, USA, Vol. 32, No. 4, pp.309-322

Sika Canada Inc., "Sikawrap Hex 230C product data sheet", http://www.sika.ca/con-tds-sikawraphex230c-ca.pdf, viewed on July 15, 2007, updated in July 2007.

Soudki Khaled; Sherwood Ted, 2003, "Bond behavior of corroded steel reinforcement in concrete wrapped with carbon fiber reinforced polymer sheets", Journal of Materials in Civil Engineering, ASCE, Reston, VA 20191-4400, United States, Vol. 15, No. 4, pp. 358-370

Tam C.K.; Stiemer S.F., 1996, "Development of bridge corrosion cost model for coating maintenance", Journal of performance of constructed facilities, ASCE, New York, NY, USA Vol. 10, No. 2, pp.47-56

Tavakkolizadeh M.; Saadatmanesh H., 2001 (a), "Galvanic corrosion of carbon and steel in aggressive environments", Journal of composites for construction, ASCE, New York, NY, USA, Vol. 5, No.3 pp.200-210

Tavakkolizadeh M.; Saadatmanesh H., 2001 (b), "Repair of damaged steel-concrete composite girders using carbon fiber-reinforced polymer sheets", Journal of composites for construction, ASCE, New York, NY, USA, Vol. 7, No. 4, pp.311-321

Toray Carbon Fibers America, Inc., 2004, "Carbon Fibers and Composites Terminology" http://www.torayusa.com/cfa/terminology.html, viewed on April 16, 2007.

US DOT (U.S. Department of Transportation), 2004(a), "Questions and Answers on the National Bridge Inspection Standards 23 CFR 650 subpart C" http://www.fhwa.dot.gov/bridge/nbis/, viewed on Aug 15, 2006.

US DOT (U.S. Department of Transportation), 2004 (b), "Preventing Corrosion in Steel Bridges", http://www.tfhrc.gov/pubrds/04sep/08.htm, viewed on Aug 15, 2006.

US DOT (U.S. Department of Transportation), 2005, "National Bridge Inventory (2005)", http://www.fhwa.dot.gov/bridge/mat05.xls, viewed on Aug 15, 2006.

Vinson R J.; Sierakowski L. R., 1987, "The behavior of structures composed of composite materials", Kluwer, Dordrecht, The Netherlands

Wikimedia Foundation Inc., 2007(a), "Carbon Fiber", http://en.wikipedia.org/wiki/Carbon_fiber, viewed on April 16, 2007.

Wikimedia Foundation Inc., 2007(b), "Carbon Fiber Reinforced Plastic", http://en.wikipedia.org/wiki/Cfrp, viewed on April 16, 2007.

Wikimedia Foundation Inc., 2007(c), "Composite Material", http://en.wikipedia.org/wiki/Composite_material, viewed on April 16, 2007.

Wikimedia Foundation Inc., 2007(d), "Epoxy", http://en.wikipedia.org/wiki/Epoxy, viewed on April 16, 2007.

APPENDICES

Appendix I

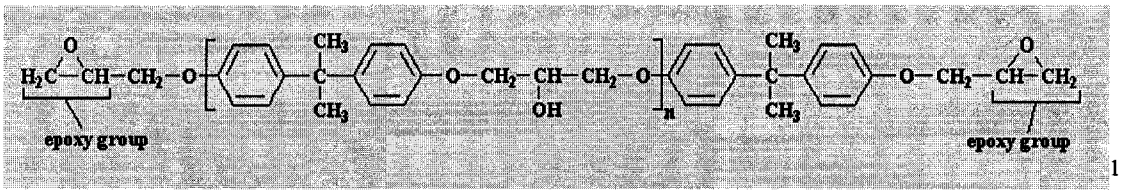

1

One of the common type epoxy molecule, n is in the range between 0 and 25.

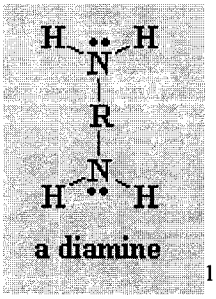

1

A catalyst could be used with the epoxy shown above.

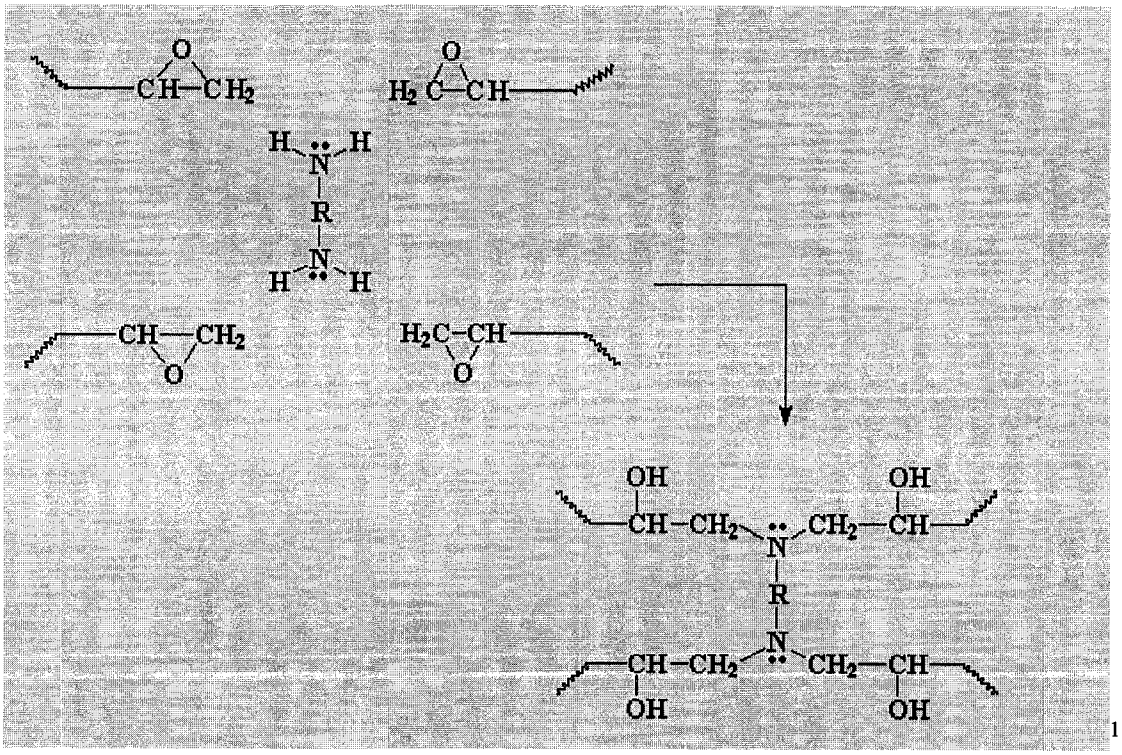

1

When the epoxy and catalyst mixed together, the exothermic reaction will occur, and link the epoxy molecule and catalyst molecule together.

Wikimedia Foundation Inc. 2007a

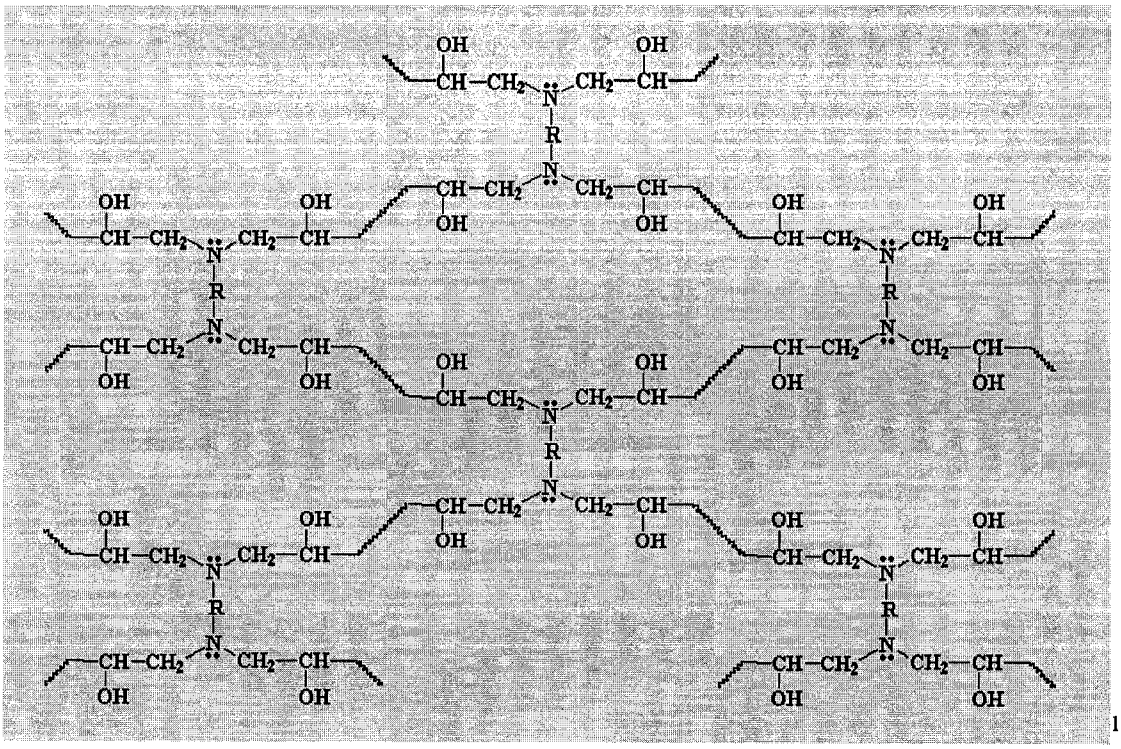

1

The reaction occurs through out the epoxy and the final product is a cross linked network.

Appendix II

All pages are refer to Handbook of Steel Construction Seventh Edition (Canadian Institute of Steel Construction, 2000)

W200*21

1.

Page 1 – 25

Type 3 *Beam*

2.

Page 5 – 98

$L_u = 1930\,mm > 1600\,mm$ *OK*

No lateral torsion buckling

No lateral sup *port needed*

3.

Page 1 – 43 *web stiffener*

$B_r = \phi_{bi} \times w \times (N + 10t) F_y = 0.80 \times 5 \times (100 + 10 \times 6.4) \times 350$

$= 229600\,N = 230\,kN > ultimate\ load = 208\,kN$

$B_r = 1.45 \phi_{bi} \times w^2 \times (F_y E)^{0.5} = 1.45 \times 0.8 \times 5^2 \times (350 \times 200000)^{0.5}$

$= 242631\,N = 242.6kN > ultimate\ load = 208\,kN$

No web stiffener is needed

$133mm\ wide \times 75mm\ long \times 12mm\ thick$ *plate is required*

4.

Page 5 – 98 *Failure load* (*at yield po*int)

$M_r = {}^{60.5kNm}/_{0.9} = 67.22kNm$

$\frac{PL}{4} = 67.22kNm$

$P = 134.22kN$

Appendix III

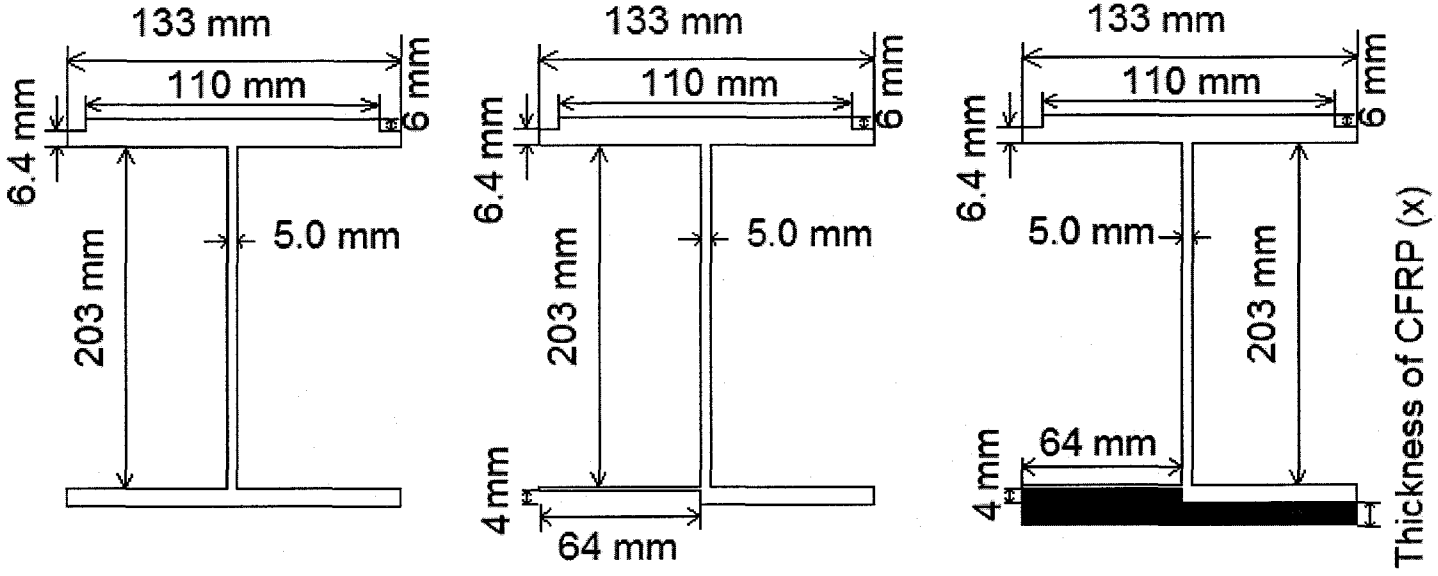

Original W200x21 Cut W200x21 Fixed W200x21

E_{steel} = 200 GPa, E_{CFRP} = 200 GPa

	Area1	Area2	Area3	Area4	Sum
A(mm^2)	110*6 = 660	133*6.4 = 851.2	203*5 = 1015	133*6.4 = 851.2	3377.4
Y (mm)	218.8	212.6	107.9	3.2	
AY(mm^3)	144408	180965.12	109518.5	2723.84	437615.46
Y (mm)					**129.6**

$$I_{control} = 110 \times 6^3 + 110 \times 6 \times (218.8 - 129.6)^2 + 133 \times 6.4^3 + 133 \times 6.4 \times (212.6 - 129.6)^2 + 5 \times 203^3 + 5 \times 203 \times (107.9 - 129.6)^2 + 133 \times 6.4^3 + 133 \times 6.4 \times (3.2 - 129.6)^2$$
$$= 67.1 \times 10^6 mm^4$$

1. **CV-G2**

   $$EI_{control} = E_{steel} \times I_{control} = 200GPa \times 67.1 \times 10^6 mm^4 = 13420\,Nm^2$$

2. **CC-G2**

   $$I_{cut} = 64 \times 4^3 + 64 \times 4 \times (2 - 129.6)^2 = 4.2 \times 10^6 mm^4$$
   $$I_{corroded} = I_{control} - I_{cut} = 62.9 \times 10^6 mm^4$$
   $$EI_{corroded} = E_{steel} \times I_{corroded} = 200GPa \times 62.9 \times 10^6 mm^4 = 12580\,Nm^2$$

3. **RC-W133-T2.4-G2**

   $$Thickness\ of\ CFRP = 2.4mm$$
   $$I_{CFRP\,2.4mm} = 133 \times 2.4^3 + 133 \times 2.4 \times 129.6^2 = 5.4 \times 10^6 mm^4$$
   $$EI_{corroded} = E_{steel} \times I_{corroded} + E_{CFRP} \times (I_{corroded} + I_{CFRP\,2.4mm})$$
   $$= 200GPa \times 62.9 \times 10^6 mm^4 + 227GPa \times (4.2 \times 10^6 mm^4 + 5.4 \times 10^6 mm^4)$$
   $$= 14759.2Nm^2$$
   10% incensement

4. **RC-W133-T1.2-G2**

   $$Thickness\ of\ CFRP = 1.2mm$$
   $$I_{CFRP\,1.2mm} = 133 \times 1.2^3 + 133 \times 1.2 \times 129.6^2 = 2.7 \times 10^6 mm^4$$
   $$EI_{corroded} = E_{steel} \times I_{corroded} + E_{CFRP} \times (I_{corroded} + I_{CFRP\,1.2mm})$$
   $$= 200GPa \times 62.9 \times 10^6 mm^4 + 227GPa \times (4.2 \times 10^6 mm^4 + 2.7 \times 10^6 mm^4)$$
   $$= 14146.3Nm^2$$
   5.4% incensement

5. **RC-W133-T0.6-G2**

   $$Thickness\ of\ CFRP = 0.6mm$$
   $$I_{CFRP\,0.6mm} = 133 \times 0.6^3 + 133 \times 0.6 \times 129.6^2 = 1.3 \times 10^6 mm^4$$
   $$EI_{corroded} = E_{steel} \times I_{corroded} + E_{CFRP} \times (I_{corroded} + I_{CFRP\,1.2mm})$$
   $$= 200GPa \times 62.9 \times 10^6 mm^4 + 227GPa \times (4.2 \times 10^6 mm^4 + 1.3 \times 10^6 mm^4)$$
   $$= 13828.5Nm^2$$
   3% incensement

	Stiffness (Nm^2)	Incensement (%)
CV-G2	13420	--
RC-W133-T2.4-G2	14759.2	10
RC-W133-T1.2-G2	14146.3	5.4
RC-W133-T0.6-G2	13828.5	3

Appendix IV

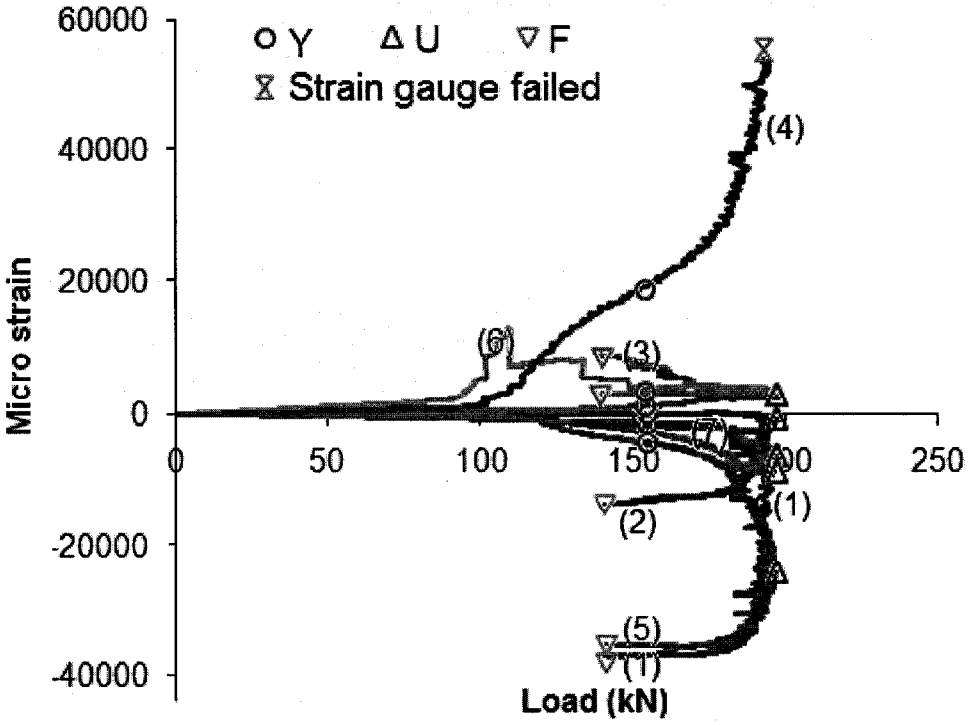

Figure A4.7: Local strain vs. load CC-G1 (Strain Gauge 1-7)

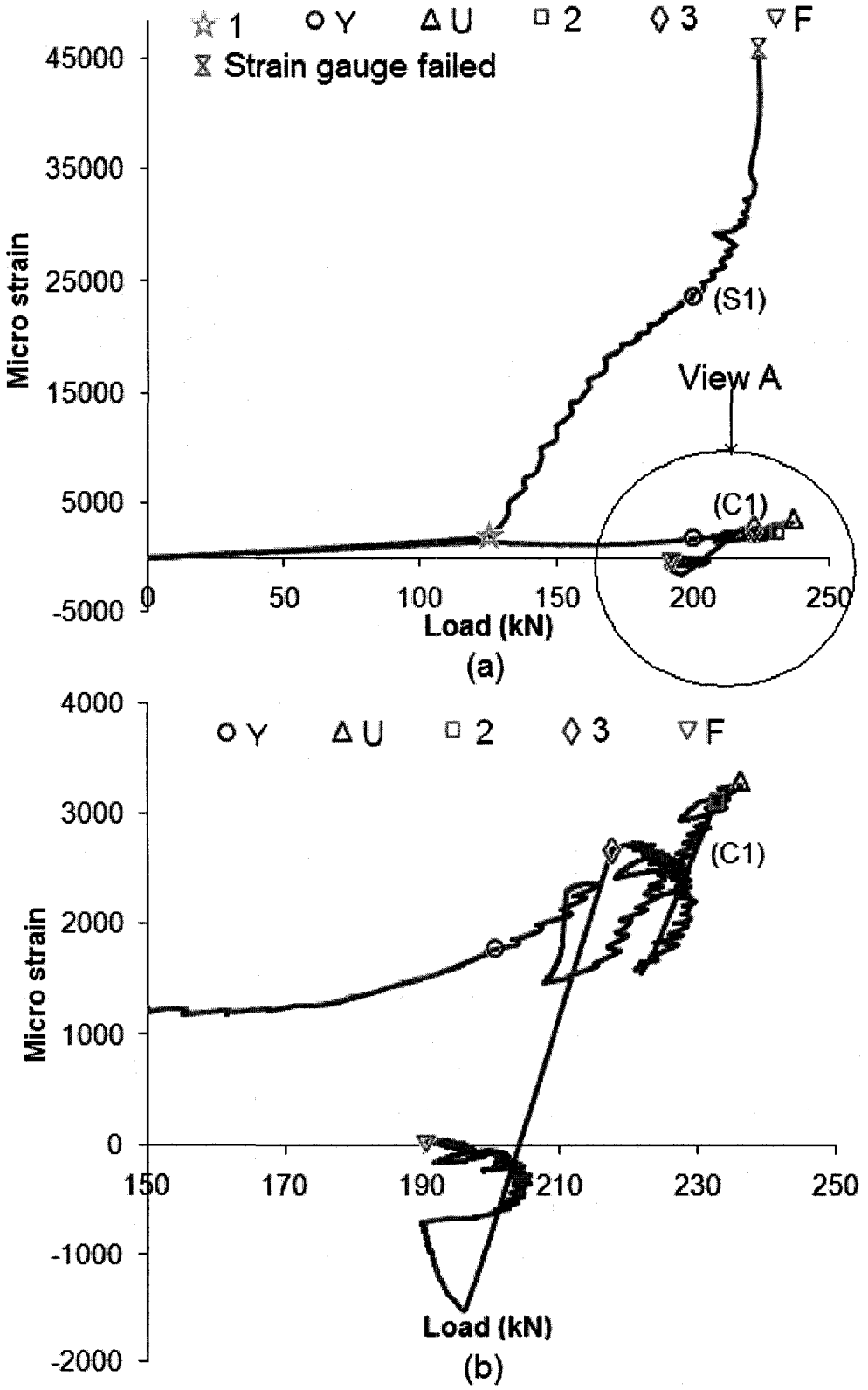

Figure A4.14: (a) Local strain from SG C1 & S1 vs. load for RC-W67-T2.4-G1 and (b) Details of View "A"

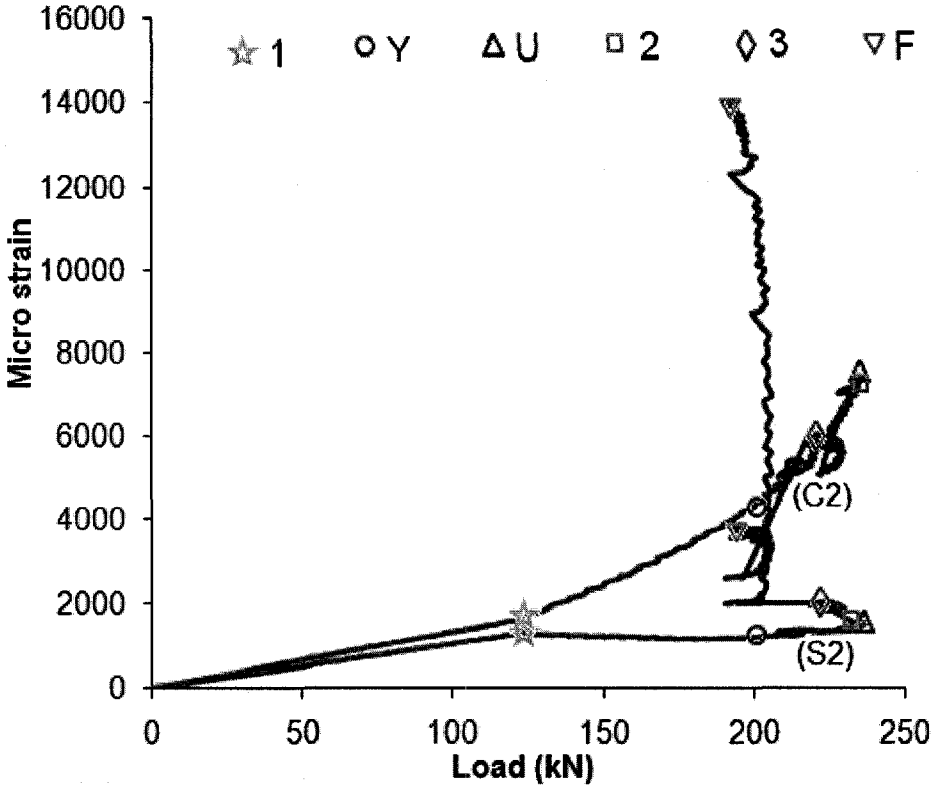

Figure A4.15: Local strain from SG C2 & S2 vs. load for RC-W67-T2.4-G1

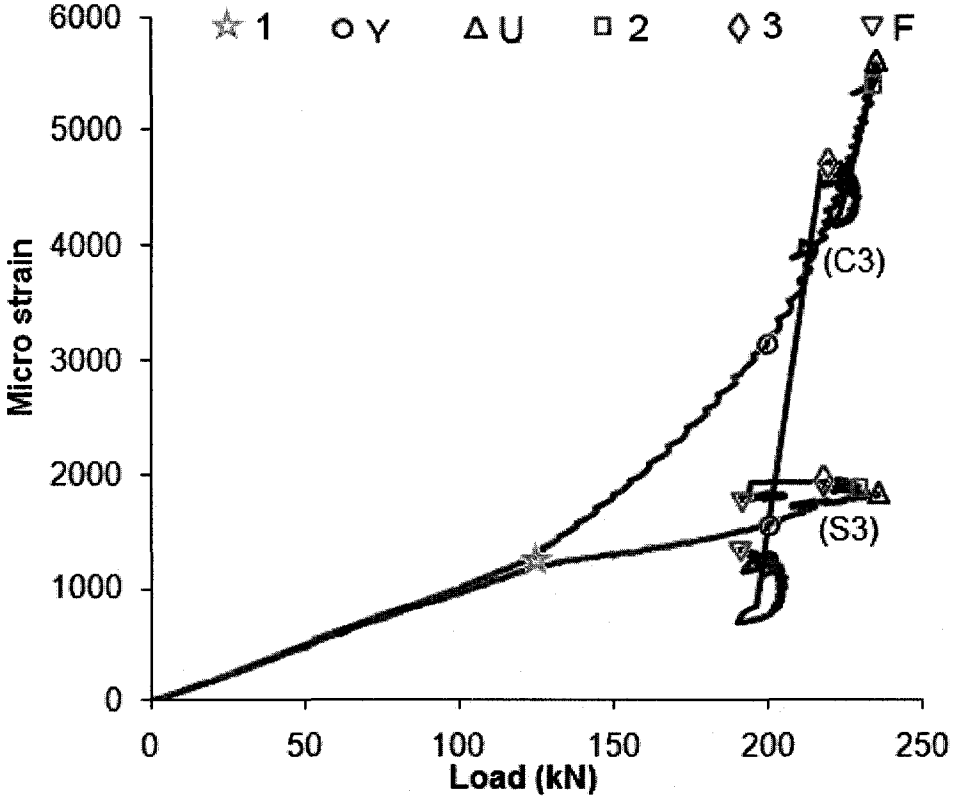

Figure A4.16: Local strain from SG C3 & S3 vs. load for RC-W67-T2.4-G1

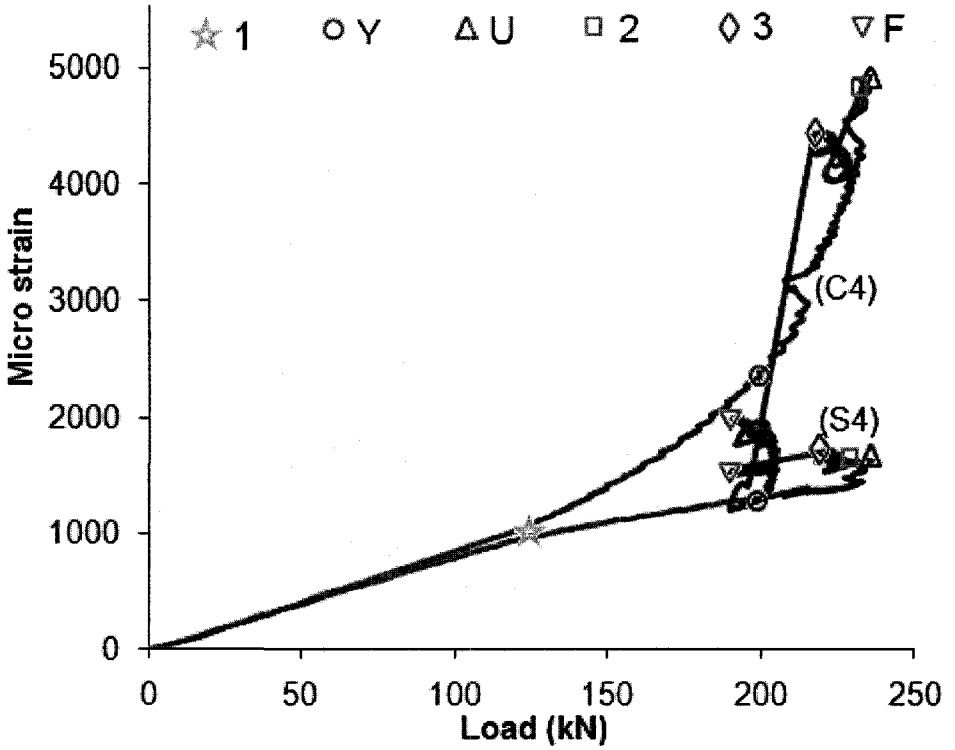

Figure A4.17: Local strain from SG C4 & S4 vs. load for RC-W67-T2.4-G1

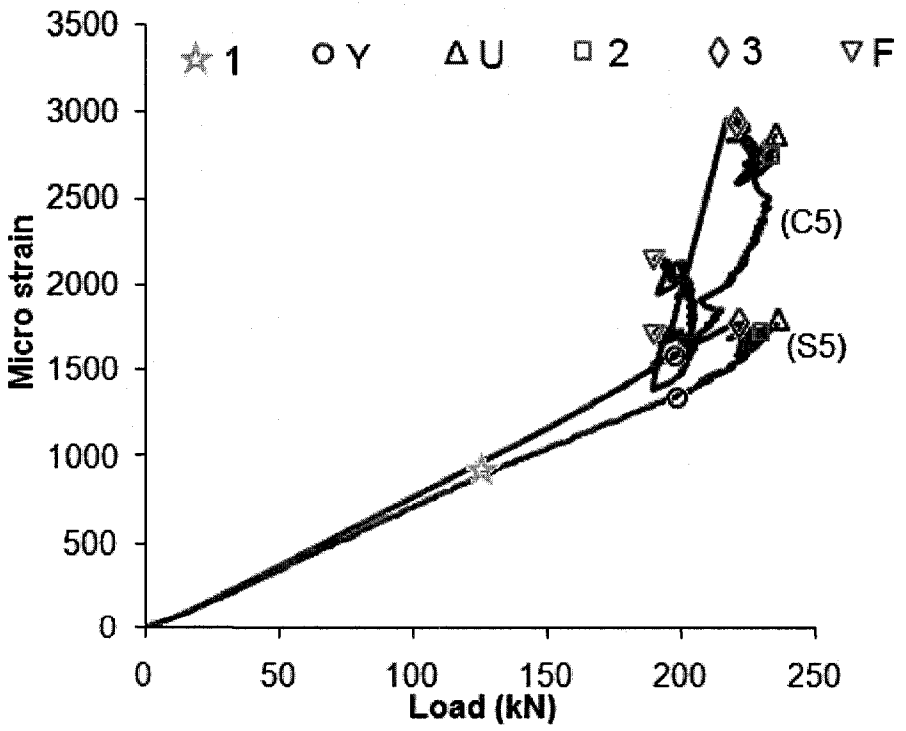

Figure A4.18: Local strain from SG C5 & S5 vs. load for RC-W67-T2.4-G1

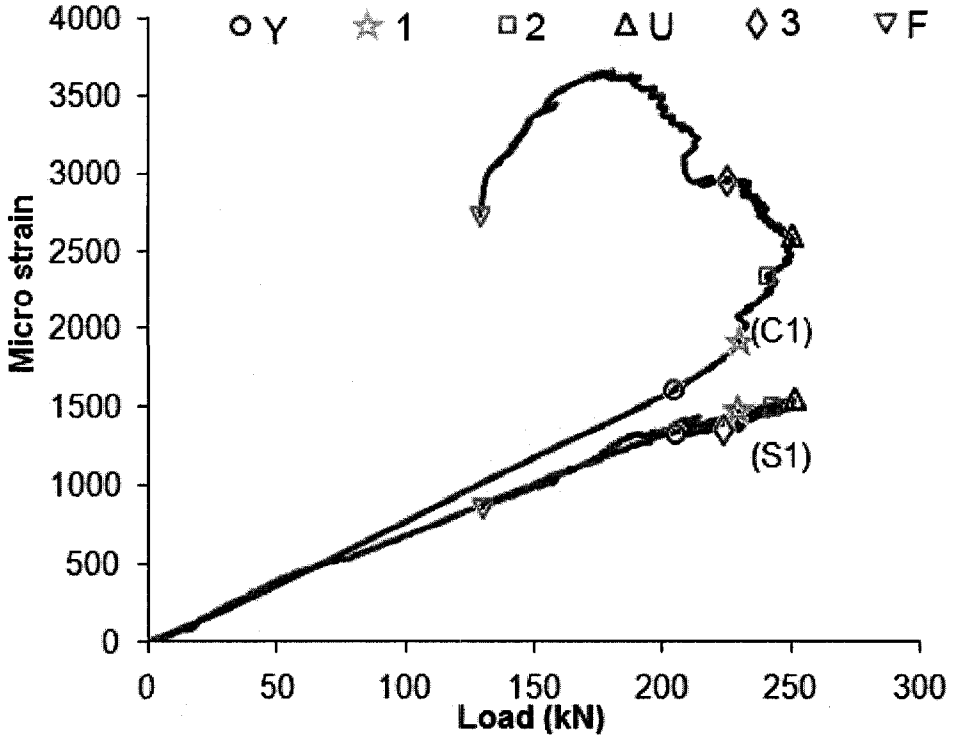

Figure A4.23: Local strain from SG C1 & S1 vs. load for RC-W133-T2.4-G1

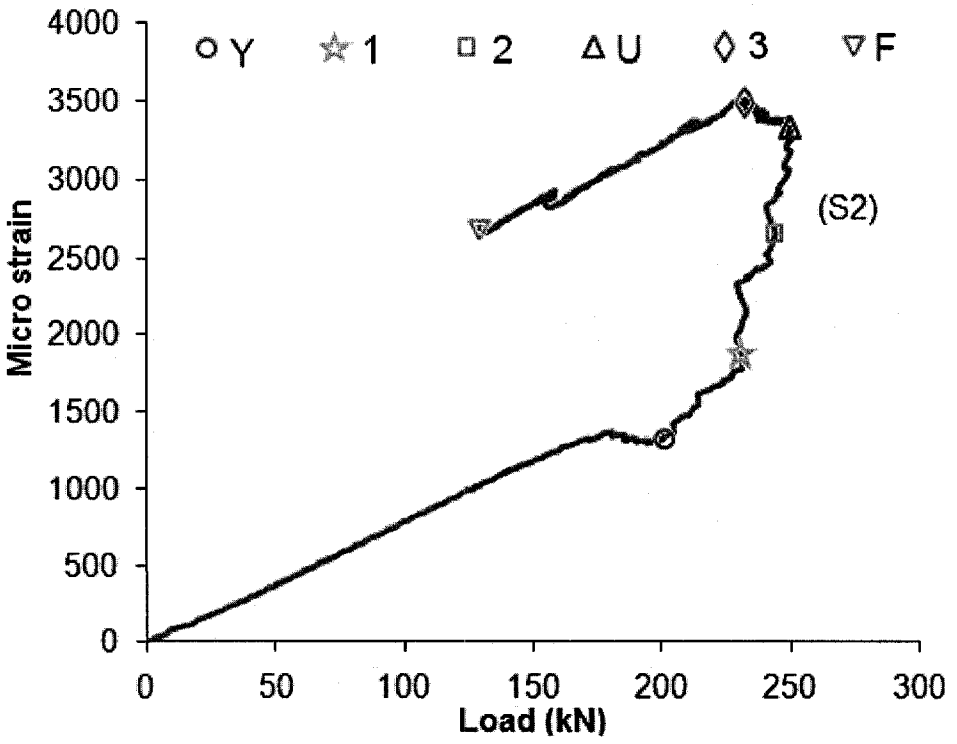

Figure A4.24: Local strain from SG S2 vs. load for RC-W133-T2.4-G1

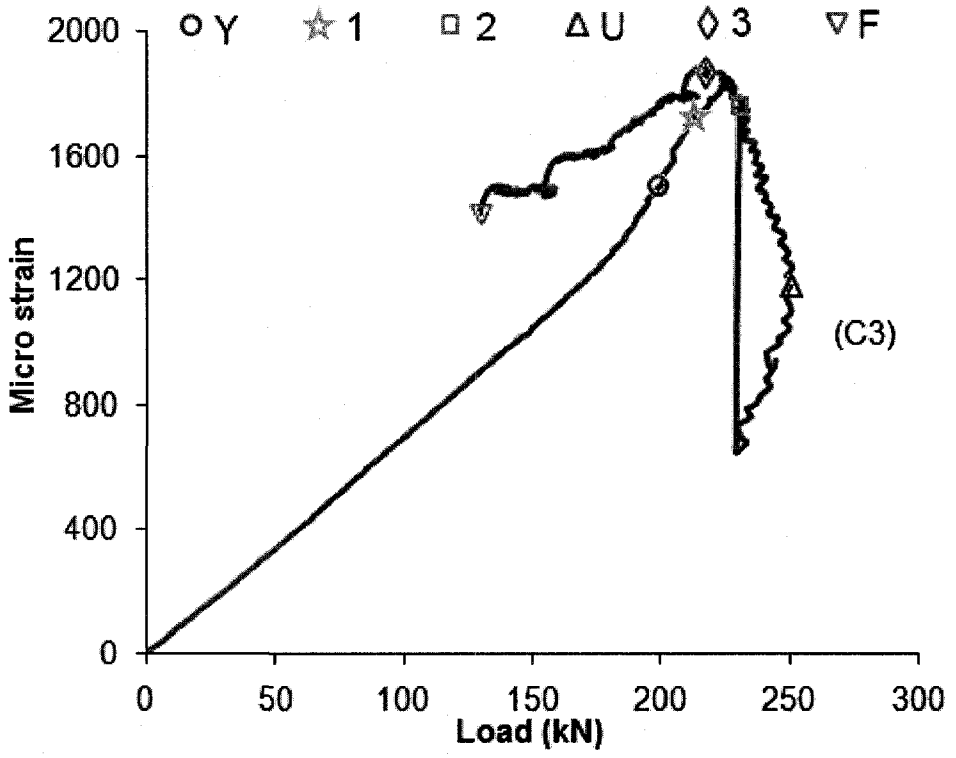

Figure A4.25: Local strain from SG C3 vs. load for RC-W133-T2.4-G1

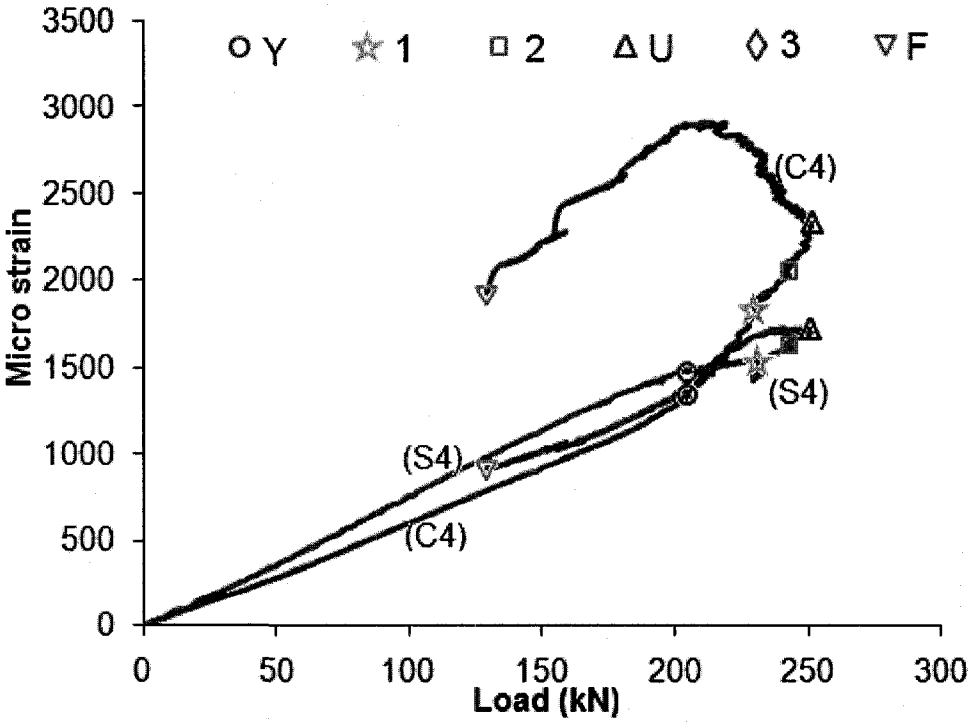

Figure A4.26: Local strain from SG C4 & S4 vs. load for RC-W133-T2.4-G1

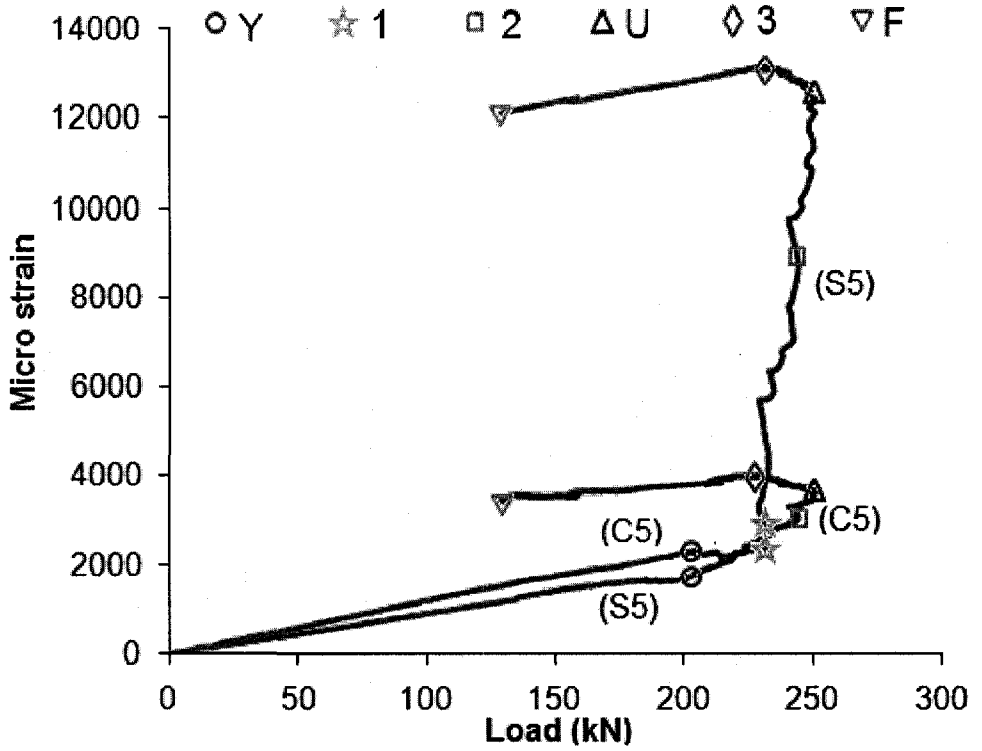

Figure A4.27: Local strain from SG C5 & S5 vs. load for RC-W133-T2.4-G1

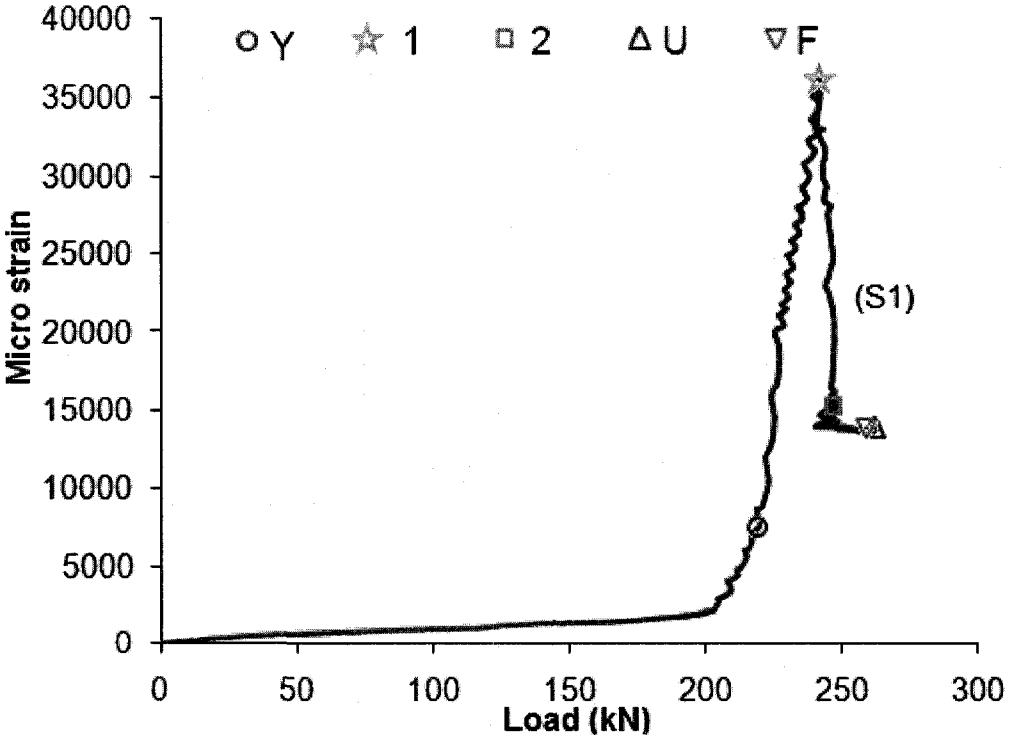

Figure A4.36: Local strain from SG S1 vs. load for CC-G2

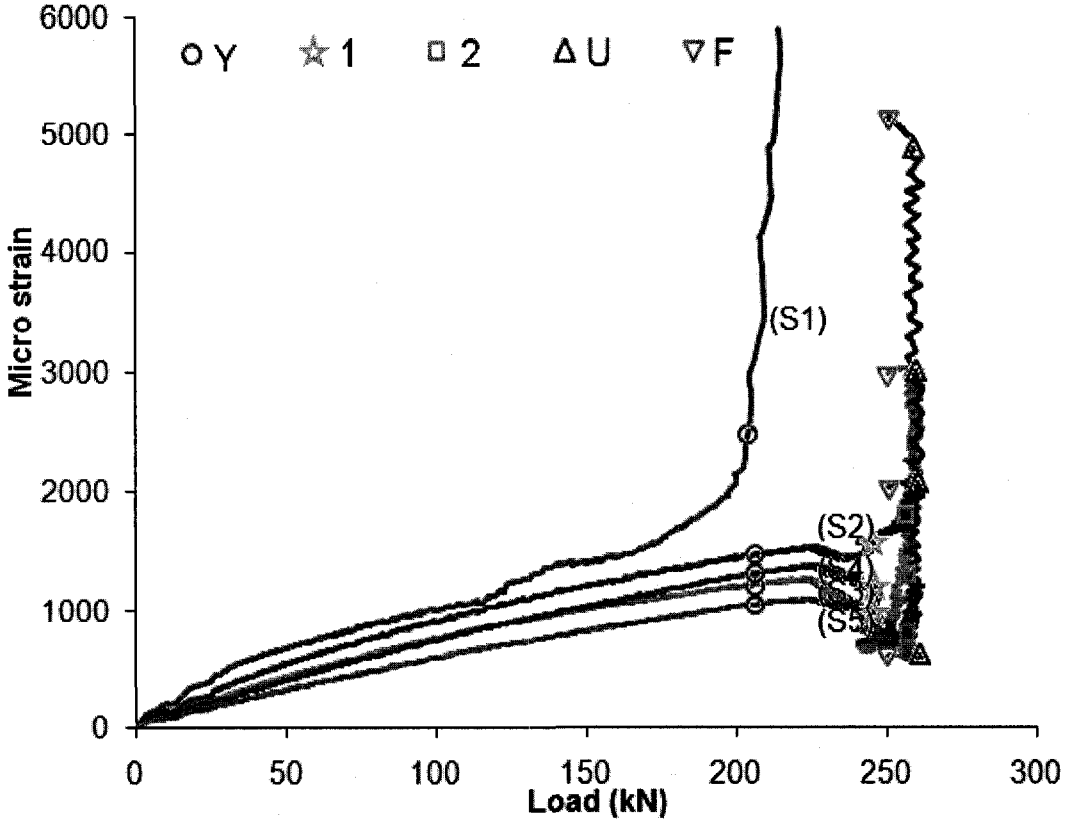

Figure A4.37: Local strain from SG S2 to S5 vs. load for CC-G2

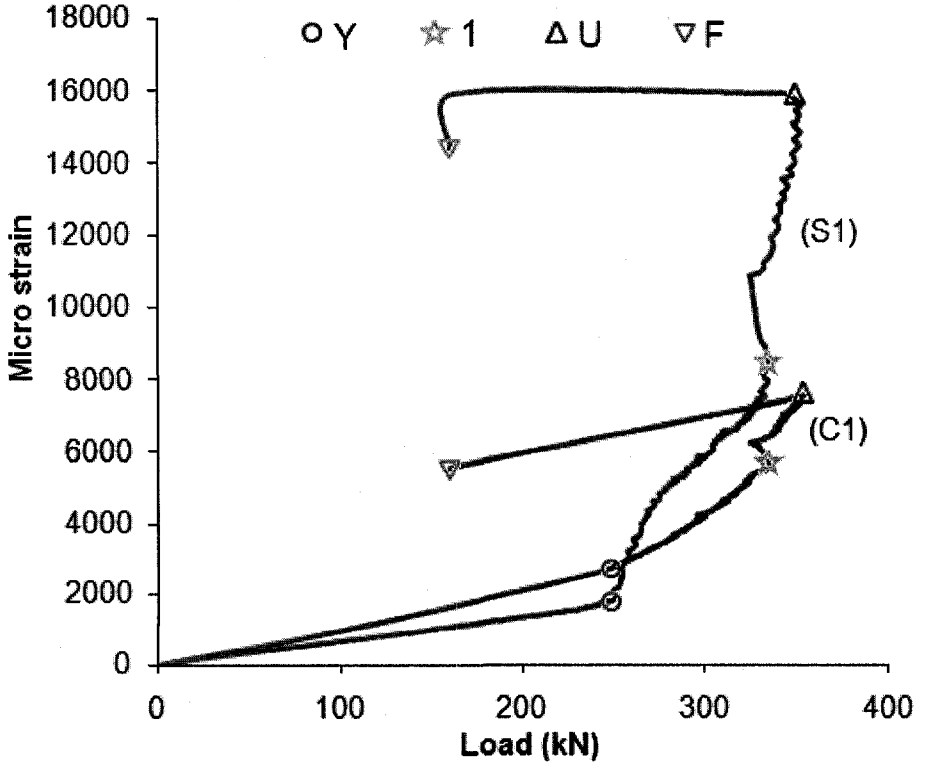

Figure A4.44: Local strain from SG C1 & S1 vs. load for RC-W133-T2.4-G2

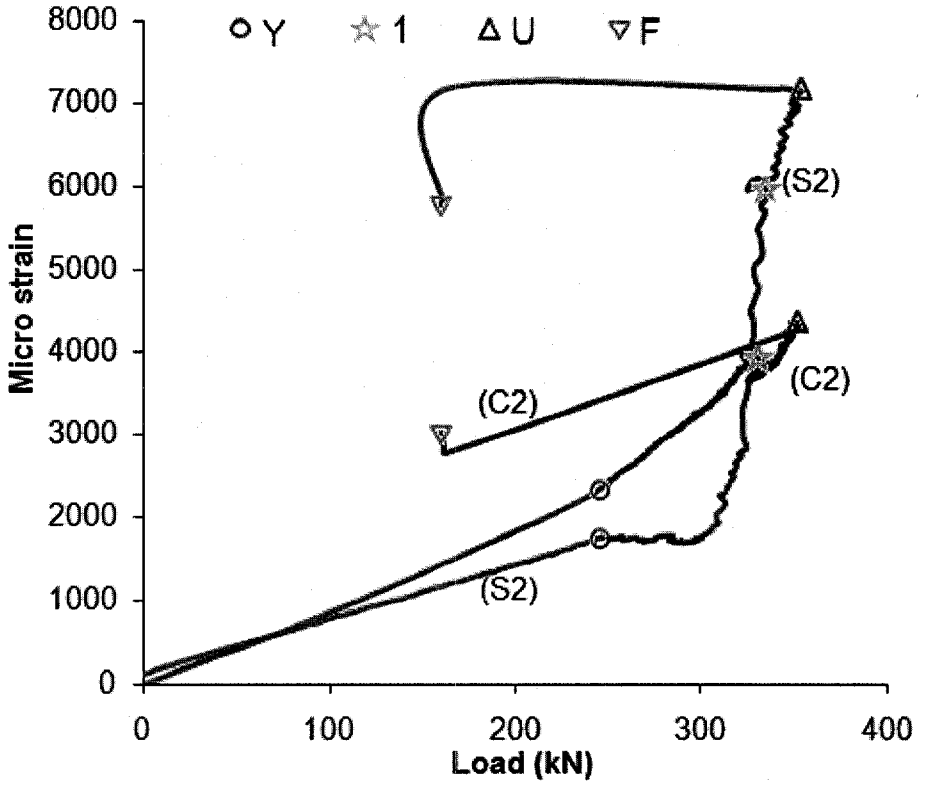

Figure A4.45: Local strain from SG C2 & S2 vs. load for RC-W133-T2.4-G2

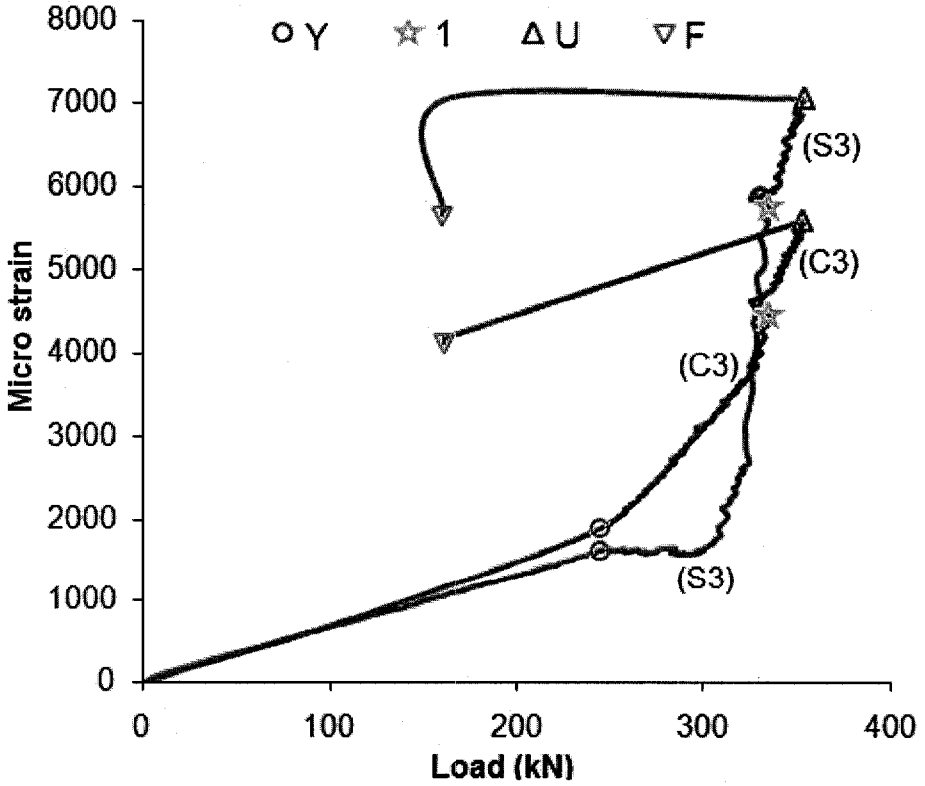

Figure A4.46: Local strain from SG C3 & S3 vs. load for RC-W133-T2.4-G2

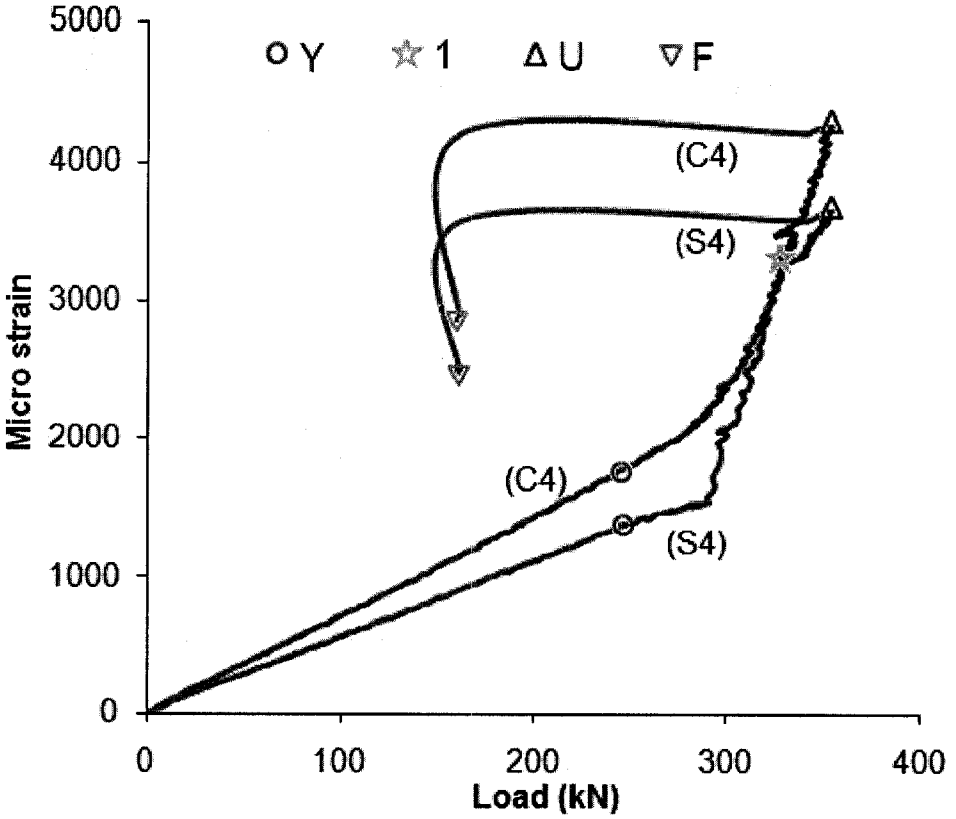

Figure A4.47: Local strain from SG C4 & S4 vs. load for RC-W133-T2.4-G2

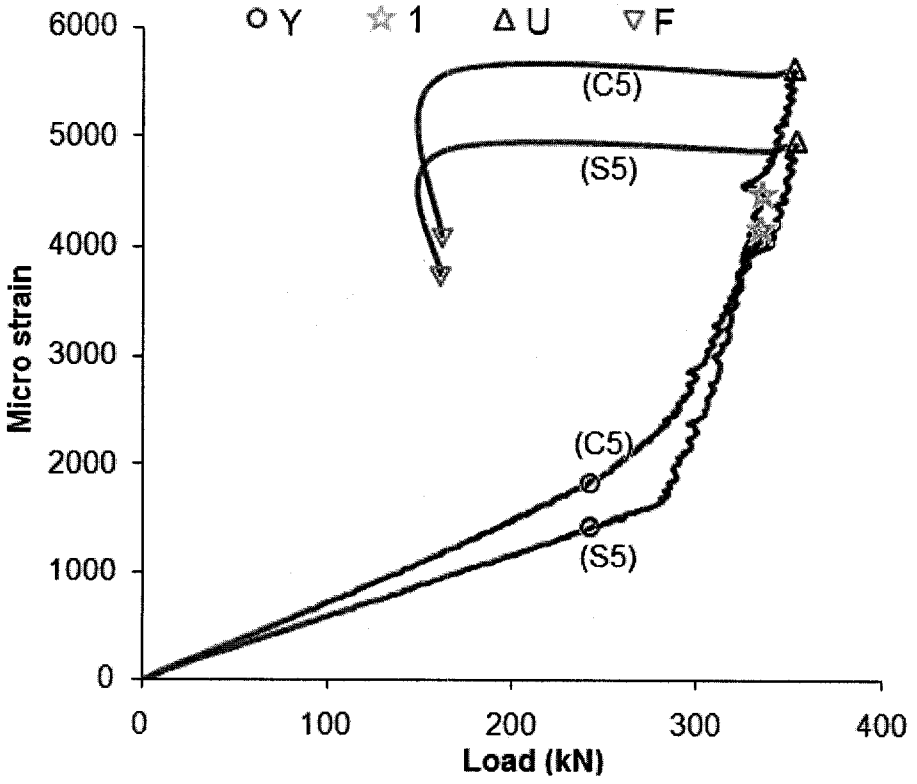

Figure A4.48: Local strain from SG C5 & S5 vs. load for RC-W133-T2.4-G2

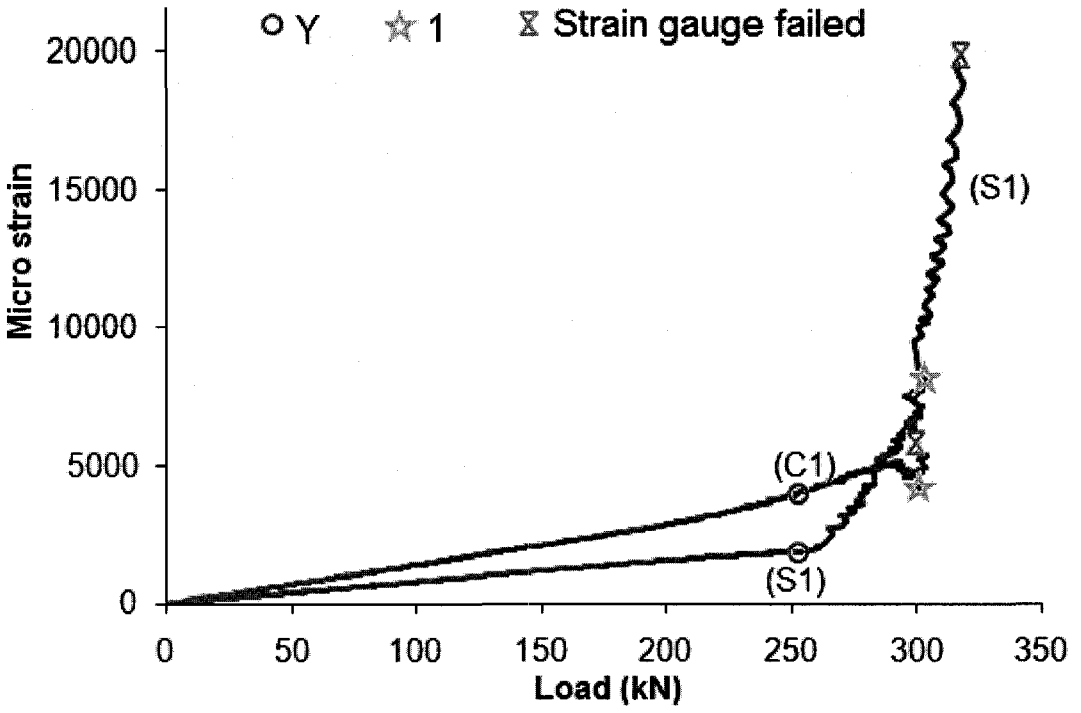

Figure A4.55: Local strains from SG C1 & S1 vs. load for RC-W133-T1.2-G2

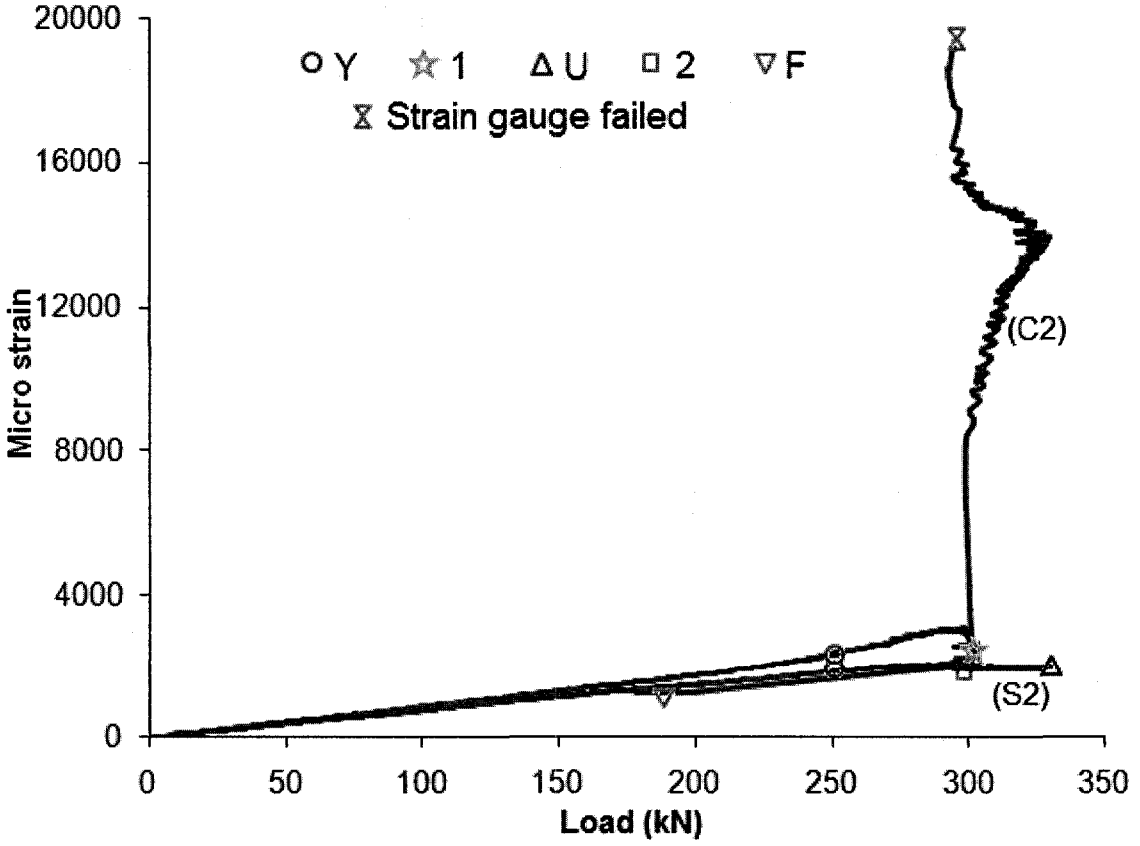

Figure A4.56: Local strain from SG C2 & S2 vs. load for RC-W133-T1.2-G2

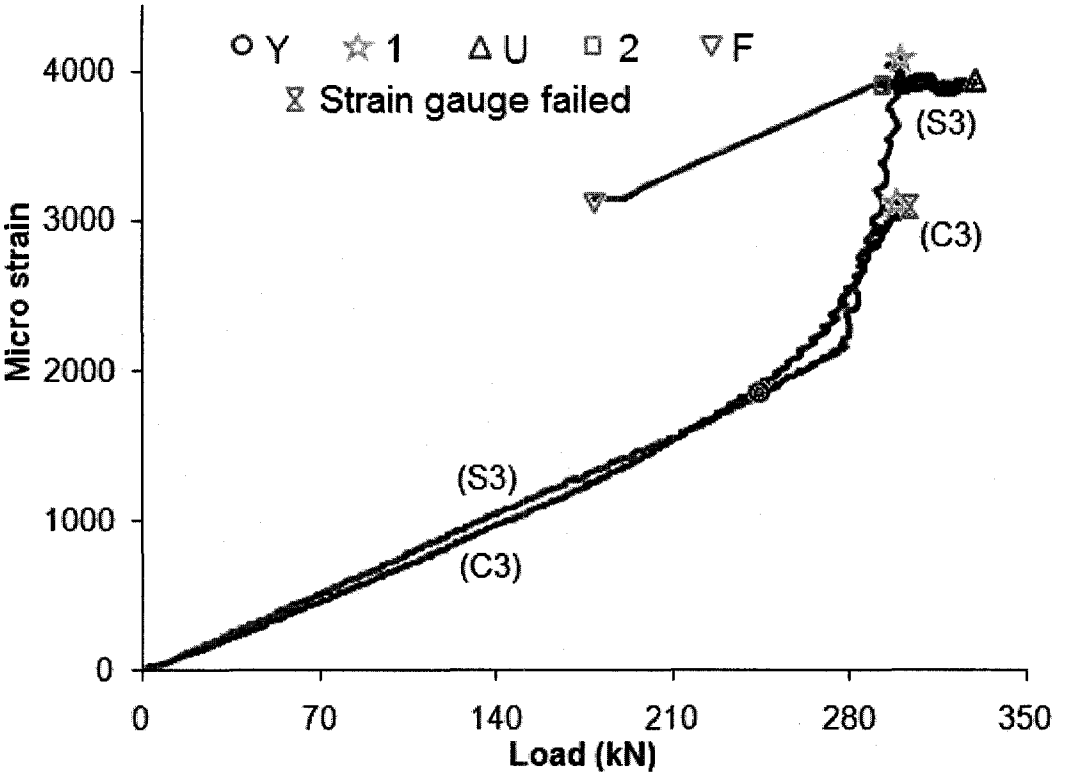

Figure A4.57: Local strain from SG C3 & S3 vs. load for RC-W133-T1.2-G2

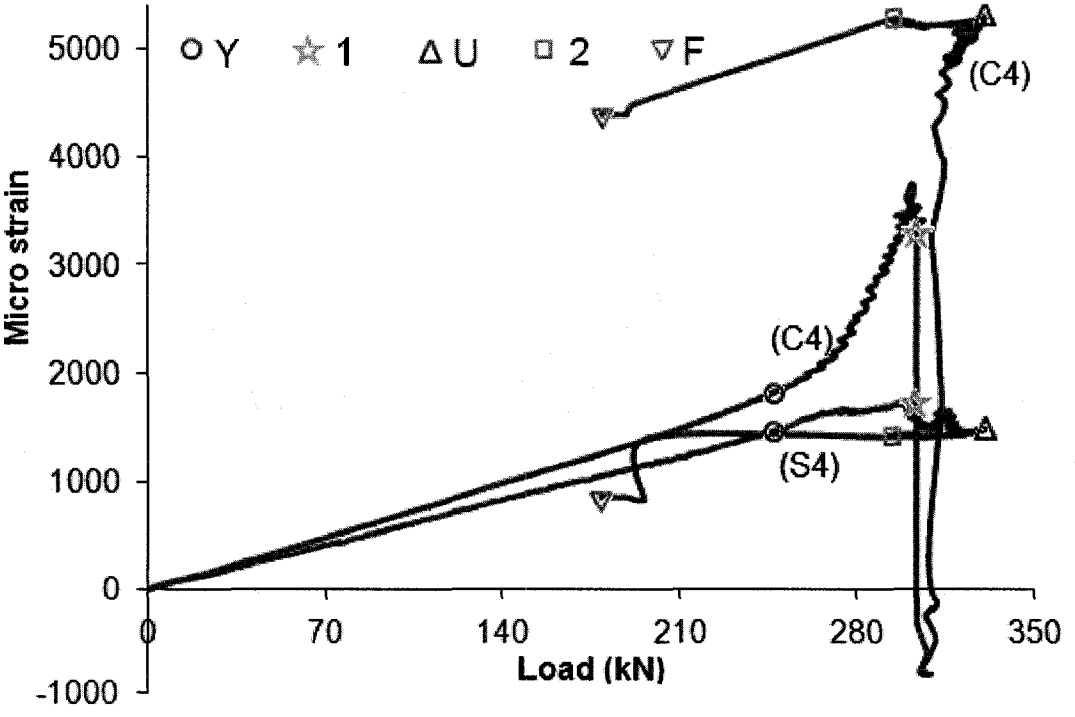

Figure A4.58: Local strain from SG C4 & S4 vs. load for RC-W133-T1.2-G2

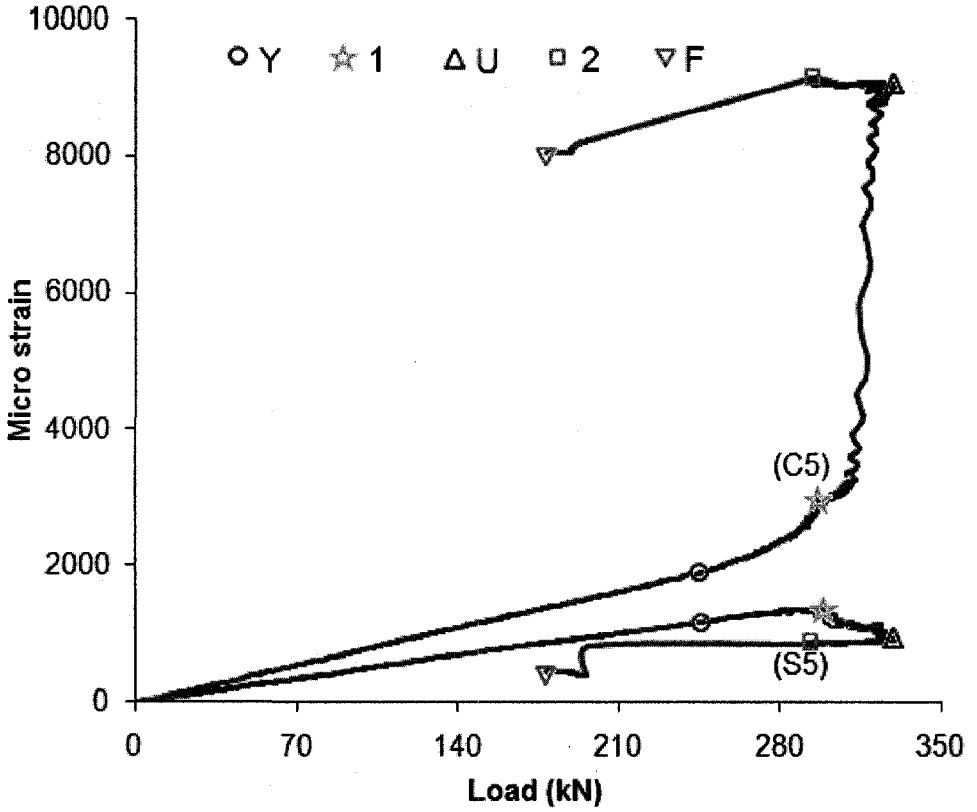

Figure A4.59: Local strain from SG C5 & S5 vs. load for RC-W133-T1.2-G2

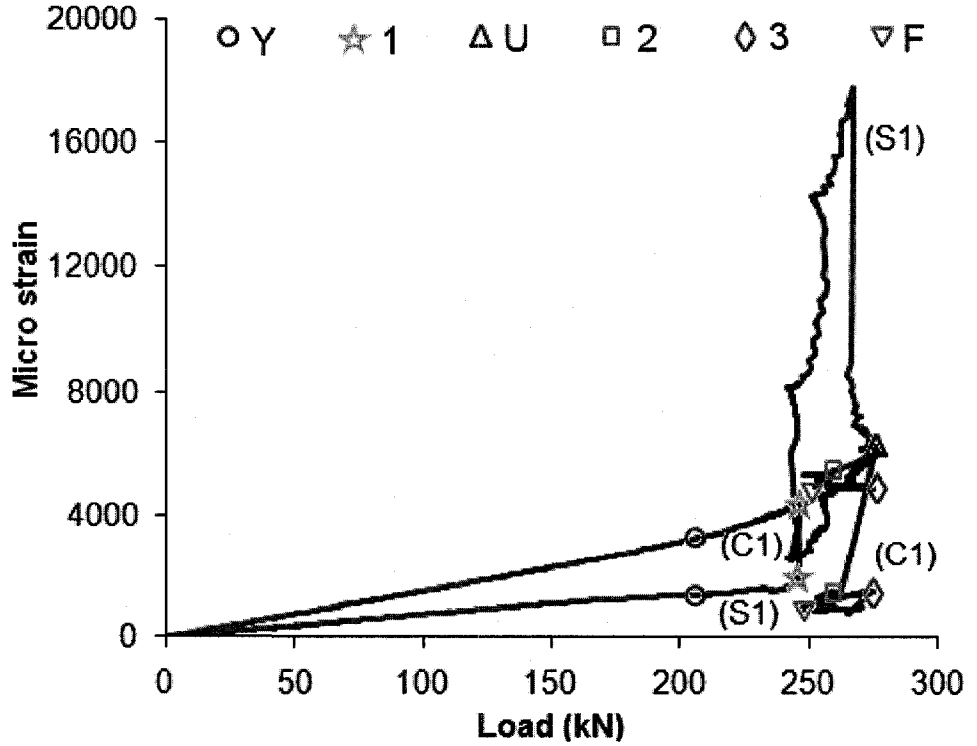

Figure A4.66: Local strain from SG C1 & S1 vs. load for RC-W133-T0.6-G2

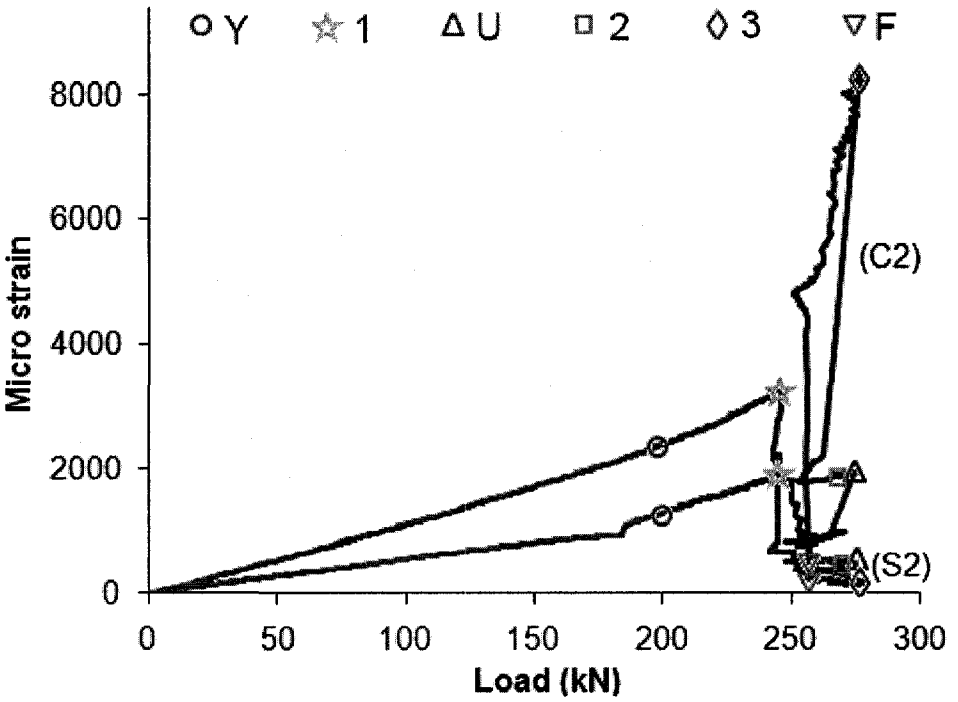

Figure A4.67: Local strain from SG C2 & S2 vs. load for RC-W133-T0.6-G2

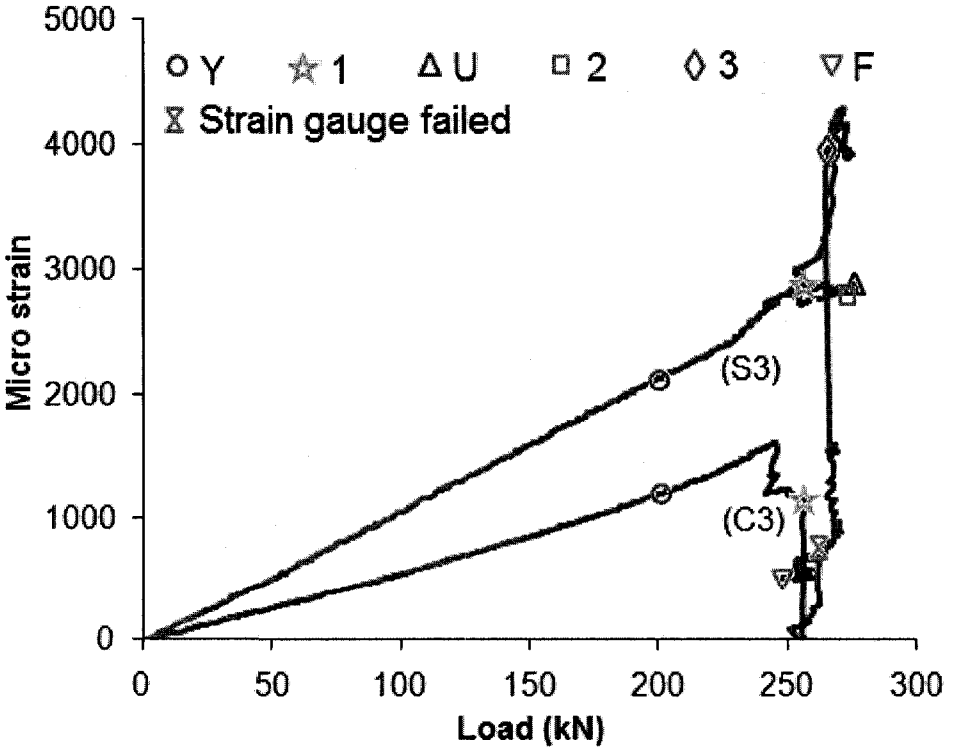

Figure A4.68: Local strain from SG C3 & S3 vs. load for RC-W133-T0.6-G2

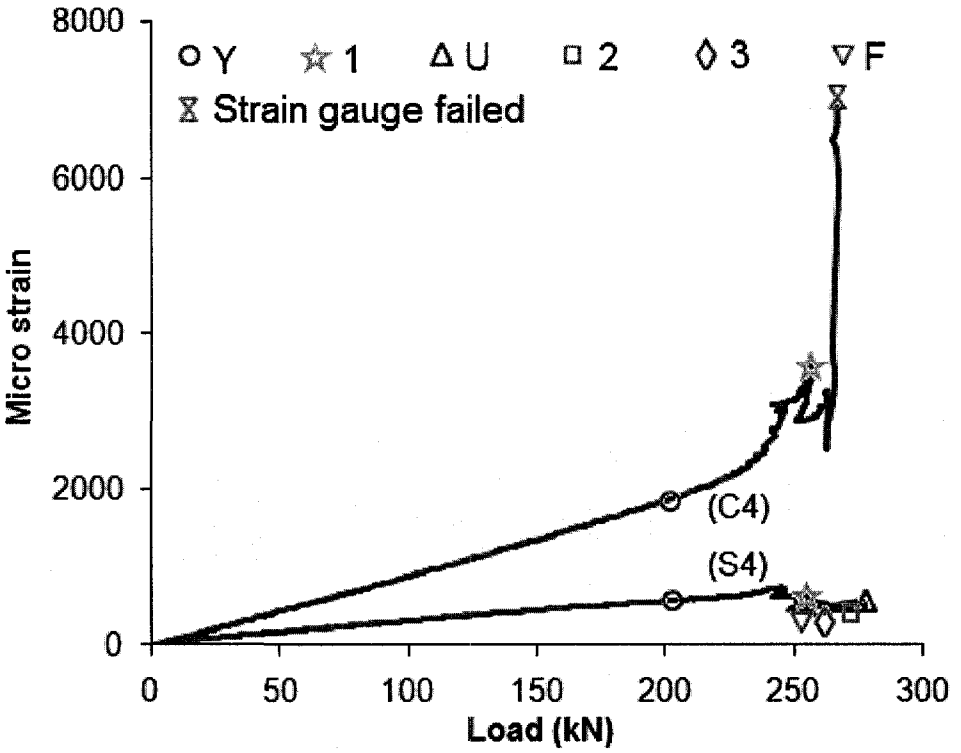

Figure A4.69: Local strain from SG C4 & S4 vs. load for RC-W133-T0.6-G2

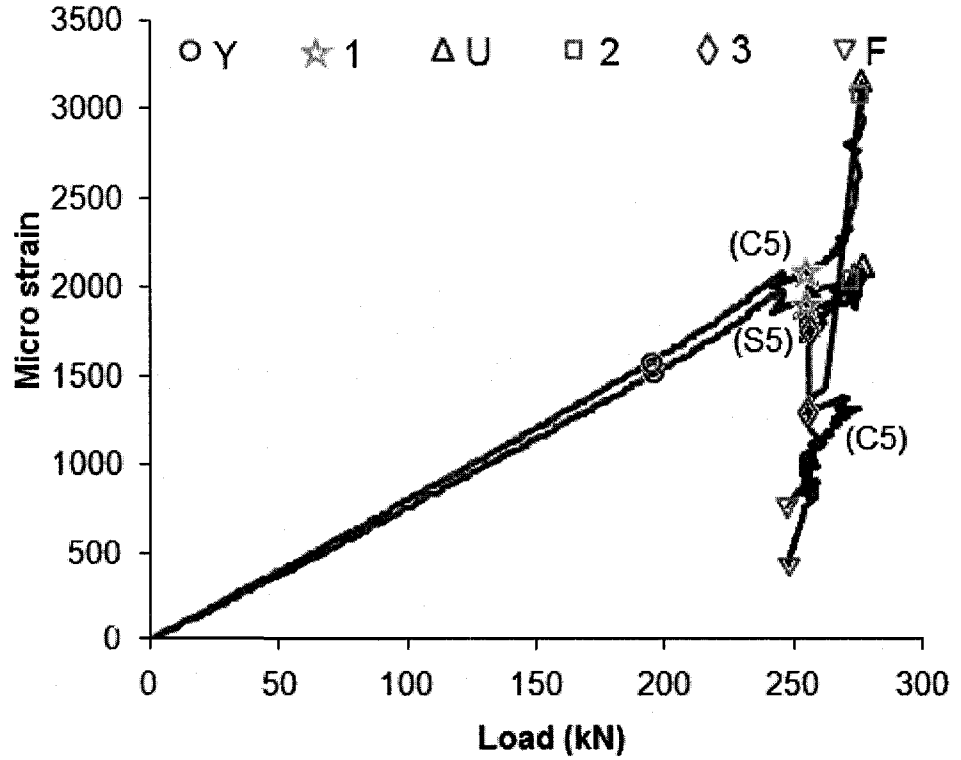

Figure A4.70: Local strain from SG C5 & S5 vs. load for RC-W133-T0.6-G2

VITA AUCTORIS

Name: Meiling Chen

Education: University of Windsor, Windsor, Ontario
2001-2005 BACHELOR OF APPLIED SCIENCE Co-op

University of Windsor, Windsor, Ontario
2005-2007 MASTER OF APPLIED SCIENCE, Civil Engineering